ALMACAL: The Evolution of Gas and Dust in Galaxies Using ALMA Calibrator Observations

KLITSCH, ANNE

ALMACAL: The Evolution of Gas and Dust in Galaxies Using ALMA Calibrator Observations

Anne Klitsch

A thesis presented in accordance with the regulations for admittance to the degree of Doctor of Philosophy

Centre for Extragalactic Astronomy
Department of Physics
University of Durham
United Kingdom

July 2019

Dedicated to

Those Who Dare to Dream

ALMACAL: The Evolution of Gas and Dust in Galaxies Using ALMA Calibrator Observations

Anne Klitsch

Abstract

A fundamental question in astronomy is how galaxies form and evolve. How does gas flow into and out of galaxies? What physical processes drive the evolution of the star formation rate history? What is the role of dusty star formation at high redshift? To answer these questions we must understand the complex interplay between galaxies and the surrounding circum-galactic medium and we have to study the evolution of molecular gas and dust in galaxies.

We present the ALMACAL survey utilizing ALMA calibration observations for science. We use this unique dataset to study the evolution of molecular gas and dust in galaxies with cosmic time.

Using this survey, we select a sample of CO emission line detections in gas-rich galaxies first identified as intervening absorbers. From this parent sample we select the three galaxies detected in multiple CO emission lines for a further analysis and follow up observations. Ultimately we are aiming for a better understanding of the population of gas-rich galaxies.

As a pilot study, we use VLT/MUSE to follow up one absorption-selected system at $z \sim 0.5$ detected in multiple CO transitions. We find in total four galaxies at the absorber redshift, one of which was detected in CO. This provides further evidence that the connection between absorber and host galaxy is more complex than a simple one-to-one relation. We find that most probably the absorbing gas is tracing intra-group medium.

Next we focus on the multiple CO transitions and study for the first time the CO spectral line energy distribution of absorption-selected galaxies. We find evidence for more excited ISM conditions compared to the Milky Way. This indicates that previous studies of absorption-selected systems might overestimate the molecular gas mass in some galaxies. Furthermore, we suggest that absorption-selected galaxies may preferentially trace group environments.

In addition to the local baryon cycle in single objects, we study the global baryon cycle over cosmic time. To understand the processes that drive the evolution of the star

formation rate history, we trace the evolution of the molecular gas mass density over cosmic time using intervening molecular absorption. In the currently largest available dataset of quasar spectra in the submillimetre regime, ALMACAL, we do not detect intervening CO absorption. We place constraints on the evolution of the molecular gas mass density. This suggests, combined with complementary measurements from the literature, a strong evolution following that of the star formation rate history.

Finally, half of the star formation activity in the Universe is expected to take place in dusty star-forming galaxies. We use our ALMACAL dataset to search for dusty star-forming galaxies observed at 680μm. We determine the first high-frequency number counts at 680μm free of source blending and cosmic variance effects. At this wavelength we find that we resolve the majority of the extragalactic background light.

Declaration

The work described in this thesis was undertaken between October 2016 and July 2019 while the author was a research student under the supervision of Dr Ian Smail in the Department of Physics at the University of Durham. No part of this thesis has been submitted for any other degree at the University of Durham or any other University. Two sections of this work have appeared in the following peer-reviewed papers:

- *Chapter 3:* **ALMACAL - III. A combined ALMA and MUSE survey for neutral, molecular, and ionized gas in an H I-absorption-selected system** Klitsch, A.; Péroux, C.; Zwaan, M. A.; Smail, I.; Oteo, I.; Biggs, A. D.; Popping, G.; Swinbank, A. M.; 2018 MNRAS, 475, 492.

- *Chapter 4:* **ALMACAL V: absorption-selected galaxies with evidence for excited ISMs** Klitsch, A.; Zwaan, M. A.; Péroux, C.; Smail, I.; Oteo, I.; Popping, G.; Swinbank, A. M.; Ivison, R. J.; Biggs, A. D.; 2019, MNRAS, 482, 65.

The following sections of this work appear in the following paper which has recently been submitted for peer review:

- *Chapter 5:* **ALMACAL VI: Molecular gas mass density across cosmic time via a blind search for intervening molecular absorbers** Anne Klitsch, Céline Péroux, Martin A. Zwaan, Ian Smail, Dylan Nelson, Gergö Popping, Chian-Chou Chen, Benedikt Diemer, R. J. Ivison, James R. Allison, Sébastien Muller, A. Mark Swinbank, Aleksandra Hamanowicz, Andrew D. Biggs, Rajeshwari Dutta, 2019 MNRAS (Submitted)

The author carried out the work in this thesis with the following exceptions: (1) the ALMACAL data retrieval and reduction described in Chapter 2 was carried out by Martin A. Zwaan, (2) the column density distribution function predictions from IllustrisTNG presented in Chapter 6 were derived by Dylan Nelson, (3) the ALMA Band 6 maps presented in Chapter 7 were created by Martin A. Zwaan.

In addition to the work presented in this thesis, the author has also either worked on, or been involved in, the following work during the period of their PhD:

- **ALMACAL IV: a catalogue of ALMA calibrator continuum observations** Bonato, M.; Liuzzo, E.; Giannetti, A.; Massardi, M.; De Zotti, G.; Burkutean, S.; Galluzzi, V.; Negrello, M.; Baronchelli, I.; Brand, J.; Zwaan, M. A.; Rygl, K. L. J.; Marchili, N.; *Klitsch, A.*; Oteo, I.; 2018, MNRAS, 478, 1512.

- **Multiphase circumgalactic medium probed with MUSE and ALMA** Péroux, Céline; Zwaan, Martin A.; *Klitsch, Anne*; Augustin, Ramona; Hamanowicz, Aleksandra; Rahmani, Hadi; Pettini, Max; Kulkarni, Varsha; Straka, Lorrie A.; Biggs, Andy D.; York, Donald G.; Milliard, Bruno; 2019, MNRAS, 485, 1595.

Acknowledgements

After so many years of continuous progress I finally reached the end of my PhD. I am looking back at an unbelievable evolution from a naive kid taking up studies to a maybe still naive but hopefully a bit more grown up person. I want to take this opportunity and thank everyone who supported me and made this PhD such a unique experience.

First and foremost, I want to thank my supervisory team, Martin Zwaan, Céline Péroux, Ian Smail, Mark Swinbank, and Rob Ivison. Your critical questions when the rate of progress was high and your continuous guidance, advice, and support also when times got rough have been invaluable for me. Thank you for always believing in my abilities, having my back, and allowing me to follow my dream. I want to especially thank Martin Zwaan: you have been the best supervisor I could have wished for.

I want to thank my mentors, Gergö, Allison, and TC for supporting me, and giving me valuable advice. Special thanks to Gergö for asking the uncomfortable questions and helping me to see the big picture when I could not.

A big thanks should also go to the rest of my little academic family, Ramona and Alex. Daily science life, celebrating smaller and bigger milestones in the PhD, and travelling to various places in the world with you has been a great adventure. Especially, I want to thank Alex for being the best academic little sister I could have ever imagined, and for providing the coffee that I turned into this thesis. I spent most of my PhD at ESO, where students, fellows, and staff created a friendly, and inspiring environment that made my PhD so enjoyable. Many other people deserve to be named here: Harald Kuntschner, Dominik Elsässer, Maryam Arabsalmani, and everyone who supported me on the way with or without me realising, thank you all.

I shall not forget those who have always been with me during these years — my wonderful familiy — unconditionally backing me up, believing in me and my dreams and supporting me in everything I do. Mama, Papa, Michael, Omas und Opas, ich bin euch unendlich dankbar. Mein größter Dank gilt Peter. Ohne dich an meiner Seite hätte ich das nicht geschafft.

Mein Dank gilt auch Peter's Familie: Anke, André, Ingrid, Monika, Helmut und Manfred. Für eure Unterstützung und euern Glauben an meine Fähigkeiten.

I also want to thank Peter, Anke, André, and all Mountainmen and Mountainwomen for regularly pulling me away from the laptop to be reborn as heroes of the mountains.

Contents

Abstract iii

Declaration v

Acknowledgements viii

1 Introduction 1

1.1 Extragalactic Astronomy 1

1.2 Galaxy Evolution and the Cosmic Baryon Cycle 2

1.2.1 Composition of the Universe 2

1.2.2 Early Understanding of Galaxies 4

1.2.3 The Need for Gas Flows into and out of Galaxies 6

1.2.4 Galactic Baryon Cycle 7

1.3 The Circum-Galactic Medium 9

1.3.1 Lyman α Absorbers 9

1.3.2 Absorber Host Galaxy Identification 12

1.4 Molecular Gas 14

1.4.1 Measuring Molecular Gas Masses 14

1.4.2 CO Spectral Line Energy Distribution 16

1.4.3 Molecular Gas in Absorber Host Galaxies 17

1.5 Global Baryon Cycle 20

1.5.1 The Peak of the Star-Formation Rate History 20

1.5.2 The High Redshift Slope of the Star-Formation Rate History . . . 23

1.6 Thesis Overview 24

2 ALMACAL — Overview 27

2.1 The Philosophy of an ALMA Calibrator Survey (ALMACAL) 27

2.2 ALMA Observing Schedule 28

2.3 ALMA Calibrator Properties 29

2.4 A Broad Dynamic Range 32

2.5 Data Reduction 32

2.6 The ALMACAL Survey Characteristics 33

2.7 Comparison to Conventional Large Programs and Other Studies 39

2.7.1 Conventional Large Programs and Other Studies 39

2.7.2 Number Counts of Dusty Star-Forming Galaxies in ALMACAL . 41

3 Molecular Gas in Absorber Host Galaxies 45

3.1 Sample Selection 46

3.2 ALMACAL Data Reduction 47

3.3 CO Emitter Search at the Absorber Redshifts 49

3.4 Summary 55

3.5 Appendix 56

4 A Combined ALMA and MUSE Survey for Neutral, Molecular, and Ionised Gas in an HI-Absorption-Selected System 59

4.1 Introduction 60

4.2 Observations and Data Reduction 62

4.2.1 ALMACAL 62

4.2.2 New MUSE Observations 65

4.2.3 Ancillary Data 66

4.3 Analysis 69

4.3.1 ALMA Source Detection and Flux Measurement 69

4.3.2 MUSE Source Detection and Flux Measurement 73

4.3.3 Broad-band Photometry and Stellar Mass 78

4.3.4 Molecular Gas Mass . . . 78
4.3.5 Star-Formation Rates . . . 80
4.3.6 Morphology and Kinematics . . . 81
4.3.7 Neutral Gas Properties . . . 87
4.3.8 Metallicities . . . 89
4.4 Discussion . . . 91
4.4.1 The Nature of the Galaxy J0423B . . . 91
4.4.2 Assessing the Possibility of a Misidentification . . . 92
4.4.3 The Nature of the Absorbing Gas . . . 94
4.5 Summary and Conclusion . . . 96

5 Absorption-Selected Galaxies with Evidence for Excited ISMs 99
5.1 Introduction . . . 100
5.2 Sample and Reduction . . . 101
5.3 Analysis . . . 104
5.4 Discussion and Conclusion . . . 107

6 Cosmic Molecular Gas Mass Density Constraints from a Blind Search for Intervening Molecular Absorbers 111
6.1 Introduction . . . 112
6.2 ALMACAL Observations and Data Reduction . . . 115
6.3 Analysis and Results . . . 120
6.3.1 Blind Search for Intervening Absorbers . . . 120
6.3.2 The Column Density Distribution Function Based on Intervening Absorbers . . . 122
6.3.3 Predicting the Column Density Distribution Function from IllustrisTNG . . . 127
6.3.4 Cosmic Evolution of the Molecular Gas Mass Density . . . 128
6.4 Discussion . . . 128
6.5 Summary and Conclusions . . . 132

7 First High-Frequency Number Counts Free of Blending 134

7.1 Introduction . . . 134
7.2 ALMACAL Data Reduction . . . 136
7.3 Analysis . . . 138
7.3.1 Source Detection . . . 138
7.3.2 Spurious Detections and Jets . . . 139
7.3.3 Completeness . . . 140
7.3.4 Flux Deboosting . . . 142
7.3.5 Source Catalogue . . . 143
7.3.6 Band 6 Counterparts and Redshift Distribution . . . 149
7.3.7 Challenges . . . 152
7.3.8 Effective Area . . . 155
7.4 Results and Discussion . . . 155
7.4.1 Number Counts . . . 155
7.4.2 Resolving the 680μm Background Light . . . 159
7.5 Summary and Conclusion . . . 160
7.6 Appendix . . . 161
7.6.1 Details of the Observations . . . 161

8 Conclusions and Future Work 168

8.1 Summary of the Presented Work . . . 169
8.1.1 The Baryon Cycle in an Absorption-Selected System . . . 169
8.1.2 Evidence for More Excited ISMs in Absorption-Selected Galaxies . . . 169
8.1.3 Estimating the Molecular Gas Mass Density Over Cosmic Time from Intervening Molecular Absorbers . . . 170
8.1.4 High-Frequency Submillimetre Number Counts Free of Source Confusion . . . 170
8.2 Ongoing and Future Work . . . 171
8.2.1 Understand the Gas Flows in the Population of Gas-Rich Galaxies . . . 172
8.2.2 Evolution of the Molecular Gas Mass Density . . . 174

8.2.3 Deciphering the Population of Galaxies in which Half of the Star formation Activity in the Universe Takes Place 175

8.3 Concluding Remarks 176

Appendix **204**

A Appendix **204**

A.1 ALMACAL 204

List of Figures

1.1 The shape of the Milky Way estimated by William Herschel. 2
1.2 The baryon budget of the Universe. 3
1.3 Physical properties of galaxies as a function of $M_\star$. 5
1.4 A schematic overview of the circum-galactic medium. 10
1.5 Schematic comparison of associated and intervening absorption. 11
1.6 Observed frequency of CO emission lines as a function of redshift. 16
1.7 Predicted CO spectral line energy distribution. 17
1.8 CO spectral line energy distribution of galaxies. 18
1.9 Molecular gas properties of absorption-selected galaxies. 19
1.10 The cosmic star formation rate history. 21
1.11 Cosmic HI gas mass density. 21
1.12 The cosmic molecular gas mass density. 22
1.13 The cosmic star formation rate history as presented by Casey et al. (2018). 24

2.1 Flux distribution of the ALMA calibrators. 30
2.2 Positions of the ALMACAL fields. 31
2.3 Redshift distribution of the ALMA calibrators. 31
2.4 Observation time distribution of ALMA calibrator fields per Band. 34
2.5 Proportion of the total ALMA frequency coverage in Band 3, 4, 6, 7, 8 and 9 observed per field. 36
2.6 Histograms of the number of calibrators as a function of the fraction of the Band covered in ALMACAL. 37
2.7 Example of the frequency coverage per calibrator. 38

2.8 ALMA Band 6 (1.2 mm) images of the dusty star-forming galaxies detected in ALMACAL, reproduced from Oteo et al. (2016b). 42
2.9 Cumulative number counts of DSFGs in ALMACAL Band 6 and 7 (Oteo et al., 2016b). 42
2.10 High resolution imaging of the two SMGs in the field of J1058+0133. . . 43

3.1 Distribution of the channel rms noise in the 93 image cubes used to search for CO emission in the absorber host galaxy. 47
3.2 Distribution of the spatial resolution in kpc of the 93 image cubes used to search for CO emission in the absorber host galaxy. 48
3.3 Search radius for CO emission from absorber host galaxies in ALMACAL in kpc in the different Bands as a function of redshift. 48
3.4 An example of the diagnostic plot used to identify CO line emitter candidates 50
3.5 Spectra and integrated flux maps of an unbiased sample of CO emission from absorption-selected systems with only one CO emission line detected. 53
3.6 Fig. 3.5 continued. 54

4.1 Overview of the detected sources in the field of J0423−0130. 63
4.2 CO spectra in our ALMACAL data cubes centred in position on the quasar J0423–0130. 70
4.3 Zoom in on J0423B in Fig. 4.1. 71
4.4 Rest frame optical spectra of the four group members identified from our MUSE observation. 74
4.5 The intensity weighted line-of-sight velocity field of the ^{12}CO(2–1) emission from the ALMA observations for J0423B. 82
4.6 Results from the morpho-kinematic fitting. 83
4.7 Fits to the FeII2382Å, FeII2600Å, MgII2796Å, MgII2803Å, MgI2852Å absorption lines in the QSO spectrum. 88
4.8 Column density of intervening absorbers as a function of impact parameter. 92
4.9 Comparison of all spectra of detected systems. 93

5.1 Spectra and integrated flux maps of the absorption-selected galaxies with multiple ALMACAL CO lines. 104

5.2 CO Spectral line energy distribution of the three absorption-selected galaxies with multiple CO emission lines detected in ALMACAL. 105
5.3 CO(2-1) luminosity as a function of impact parameter and CO(2-1) luminosity as a function of HI absorption column density. 108

6.1 A flowchart describing our methodology to efficiently process the large data volume of ALMACAL while maintaining the highest spectral resolution. 116
6.2 Example of the first data reduction step. 117
6.3 Illustration of the application of a low-pass filter in the data processing. . 118
6.4 Key quantities of the ALMACAL spectra. 120
6.5 Examples of detected absorption lines. 121
6.6 CO column density distribution functions in the two redshift bins. 122
6.7 Cumulative number of molecular absorbers per comoving path length interval ΔX with a column density greater than N. 123
6.8 An example of a molecular gas disk in a z=0.5 galaxy. 126
6.9 Redshift evolution of the H_2 column density distribution function as predicted from the IllustrisTNG simulation and from observations by Zwaan & Prochaska (2006). 129
6.10 Cosmic evolution of the molecular and atomic gas densities. 130

7.1 The cumulative number of spurious detections in the inverted maps as a function of the pear SNR. 139
7.2 Completeness of ALMACAL Band 8 as a function of the SNR. 141
7.3 The ratio between the output and input flux densities of the simulated sources as a function of the input SNR. 142
7.4 Band 8 and Band 6 maps of the 0.3″ resolution detections. 143
7.5 Ratio of the fluxes measured in the low and high resolution maps as a function of resolution in the high resolution maps. 149
7.6 The ratio between the primary beam corrected flux densities at 680μm and 1.2mm for the DSFGs. 150
7.7 The redshift distribution of the DSFGs detected at 680μm based on the average SED from ALESS. 153

7.8 The redshift of the DSFGs based on the SED as a function of the redshift of the calibrator in the field. 154
7.9 The effective area covered by the current ALMACAL Band 8 observations as a function of the flux density of detected sources. 156
7.10 Cumulative number counts of DSFGs at 680μm. 157
7.11 The integrated surface brightness of the 680μm emitters relative to the CIB. 159

List of Tables

1.1 Rest emission line frequencies (ν [GHz]) of the ^{12}CO $J = 1 - 0$ to $9 - 8$ rotational transitions. 14
1.2 Details of the AMA observing Bands. 14

2.1 ALMACAL observing time statistics. 35
2.2 Versions of the ALMACAL survey and the related projects. 36
2.3 The key properties of comparable ALMA Large Programs and other relevant major telescope projects. 40

3.1 Summary of the detected single CO emission lines for our sample of absorption-selected CO emitters. 51
3.2 Summary of the detected multiple CO emission lines for our sample of absorption-selected CO emitters. 52
3.3 ALMA calibrators with known absorbers. 56

4.1 Summary of the used ALMACAL observations of J0423−0130. 64
4.2 Summary of the final J0423−0130 ALMA data cube properties. 64
4.3 Summary of all previously detected galaxies connected to the absorber towards J0423–0130. 67
4.4 ALMA detection of the galaxy J0423B. 69
4.5 Observed properties of the galaxies from the MUSE observation and the broad-band imaging. 76
4.6 Summary of the physical properties of the galaxies at the absorber redshift based on our MUSE data and the SED fitting. 84

4.7 Summary of the morphological parameters from 2D fitting and morpho-kinematic parameters from 3D fitting. 85
4.8 Fit parameters for the absorption line Voigt profile fitting using VPFIT. . . 87
4.9 Metallicity of the galaxies and expected metallicity based on extrapolation using a constant slope at the absorber position assuming an extended gas disk. 90

5.1 Summary of the ALMA observations of J0238+1636. 101
5.2 ALMA detections of multiple CO emission lines towards J0238+1636 and J0423–0120. 102
5.3 The derived physical properties of the CO-detected galaxies associated with two absorbers from our ALMA observations. 106

6.1 Redshift path surveyed, Δz, and comoving pathlength, ΔX, for each CO transition. 123

7.1 DSFGs detected at 680μm up to December 2019 in our ALMACAL survey. 147
7.2 Cumulative 680μm number counts. 158
7.3 Summary of the ALMACAL Band 8 (680μm) and Band 6 (1.2mm) observations. 162

Chapter 1

Introduction

1.1 Extragalactic Astronomy

The term galaxy is derived from the Greek word γαλαξιαζ (galaxias, literally: "milky") which was used to describe the Milky Way. Already the ancient Greek philosophers as well as medieval Arabic astronomers speculated about the nature of the bright band on the night sky (e.g. Plutarch, 2006; Al-Biruni & Wright, 2004). However, only in the year 1610 Galileo Galilei, using one of the first telescopes, could prove that the Milky Way consists of many faint stars (Galilei, 1610). 175 years later, William Herschel was the first to determine the shape of the Milky Way by counting the number of stars in different regions on the sky (see Fig. 1.1).

More powerful telescopes enabled Charles Messier as well as William Herschel and his wife Caroline Herschel to compile the first catalogues of extended nebulae and clusters of stars (Messier, 1781; Herschel, 1786). However, the relative position of these objects with respect to the Milky Way remained unknown even 150 years later. The astronomer Thomas Wright of Durham was the first to propose that these nebulae are distant galaxies (Wright, 1750). This idea was taken up and elaborated on by Immanuel Kant who speculated that the Milky Way is just one 'Island Universe' of many (Kant, 1755). The discussion whether these objects are unresolved structures within the Milky Way or extra-galactic objects culminated in the "Great Debate" between Heber Curtis and Harlow Shapley at the Annual Meeting of the National Academy of Sciences (Shapley & Curtis, 1921). Shapley argued that the whole universe consists of only one galaxy while Curtis opposed that it

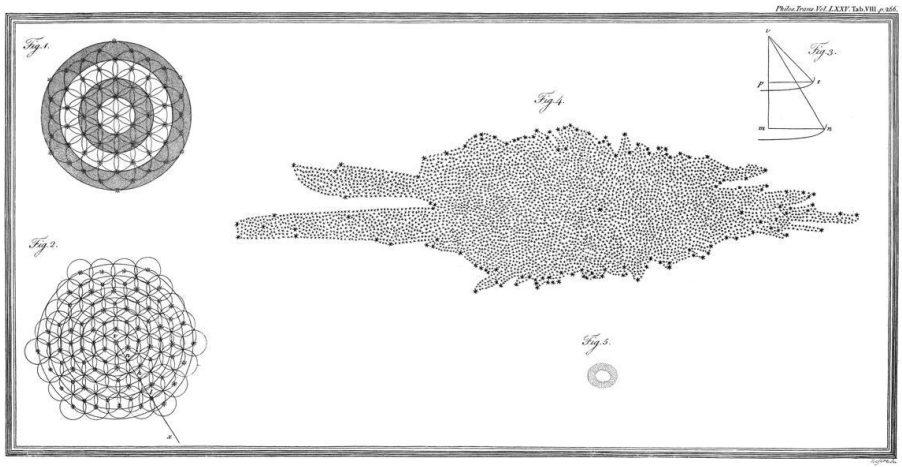

Figure 1.1: The shape of the Milky Way as estimated from stellar counts by William Herschel (Herschel William, 1785). The left hand side of the figure shows different homogeneous distributions of stars Herschel used to calculate the length of the visual ray.

contains many galaxies. Shapley thought that the unresolved structures were inside the Milky Way and were made of gas. Later it turned out that Curtis was right arguing that these structures were separate galaxies. Shapley on the other hand was correct arguing that the Milky Way was much larger than previously thought and that the Sun is not at its centre.

Resolving the outskirts of these nebulae into separate stars and measuring their distance using Cepheid variable stars, Edwin Hubble was finally able to close the debate (Hubble, 1929). Using the tight period-luminosity relation of the Cepheids discovered by Leavitt (1908) he could determine the distance to the nebulae placing them outside of the Milky Way. This finding revolutionized the understanding of the universe as well as the view on our place in it. The discovery of extragalactic objects opened up and laid the foundation for the new field of study: *extragalactic astronomy*.

1.2 Galaxy Evolution and the Cosmic Baryon Cycle

1.2.1 Composition of the Universe

When studying the evolution of galaxies it is important to understand the mass budget of the different components of the universe. At $z \sim 0$ the majority ($> 90\%$) of the baryons

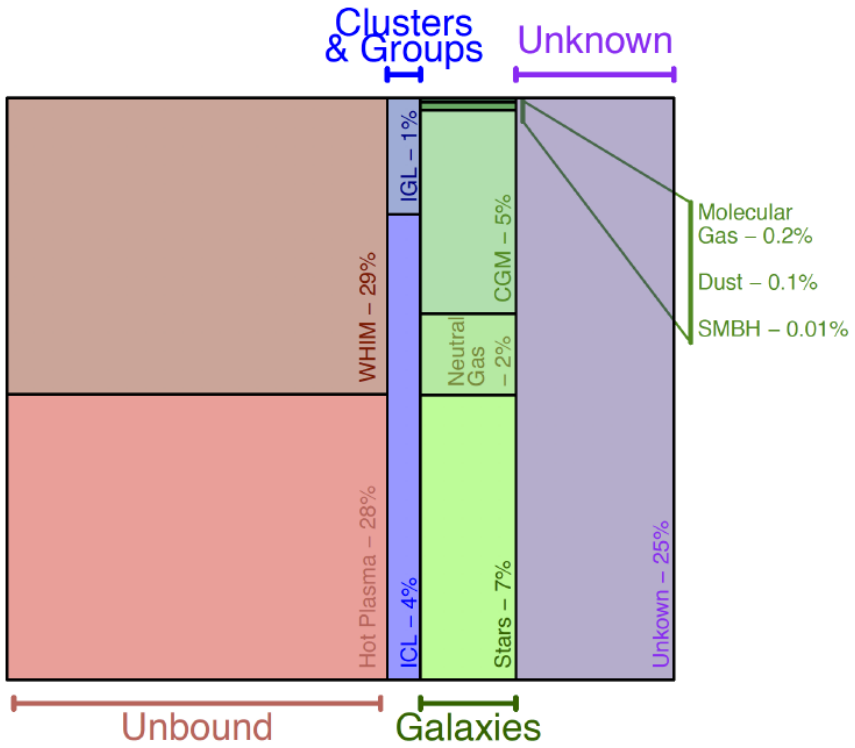

Figure 1.2: The baryon budget of the universe at $z \sim 0$ compiled by Driver et al. (2018) mostly from data presented by Shull et al. (2012). The majority of baryons is in the gas phase which is therefore the key component fo galaxy formation and evolution.

exist in the form of molecular, neutral and ionized gas which together form the essential component in the evolution of galaxies. A very small fraction ($\sim$ 2%) of this gas is condensed into galaxies (Fukugita et al., 1998), while most of the gas is in the diffuse reservoir of the circum-galactic, intra-group or intra-cluster medium or unbound to any halo. An updated overview of the total baryon budget is shown in Fig. 1.2. Observing the stellar light of the galaxies is only accounting for half of the baryons in a galaxy and therefore it is important to also study the gas in the disk and halo of galaxies. Furthermore, the stellar component is not representative of the bulk of the baryons as the stars only make up $\sim$ 7% of the baryons in the universe at $z \sim 0$ (Baldry et al., 2008, 2012; Peng et al., 2010; Moffett et al., 2016; Wright et al., 2017). The majority ($\sim$ 85%) of the baryons are not found to be condensed in galaxies but rather outside in the ICM, IGM (Shull et al., 2012; Driver et al., 2016), WHIM (Shull et al., 2012) and hot plasma (Fukugita et al., 1998; Shull et al., 2012). To get a full picture of galaxy evolution it is therefore key to observe all phases in which baryons exist.

1.2.2 Early Understanding of Galaxies

The simplest model to describe the chemical evolution of galaxies is that of a closed box, describing a galaxy as a closed system of gas and stars whose evolution is not affected by the surrounding medium. Talbot & Arnett (1971) used this model to determine analytic expressions for the galactic chemical evolution. The closed-box model was used to predict the chemical enrichment of galaxies based on stellar evolution and the pollution of the ISM with metals produced in stars. It was recognized, however, that the metal abundance distribution of stars in the Milky Way is more strongly peaked than predicted by the simple closed-box model. This is known as the G dwarf problem in the Milky Way (van den Bergh, 1962; Schmidt, 1963; Pagel & Patchett, 1975; Sommer-Larsen, 1991) and external galaxies (Worthey et al., 1996). These observations were the first indications for the need of gas accretion onto galaxies in galaxy evolution models.

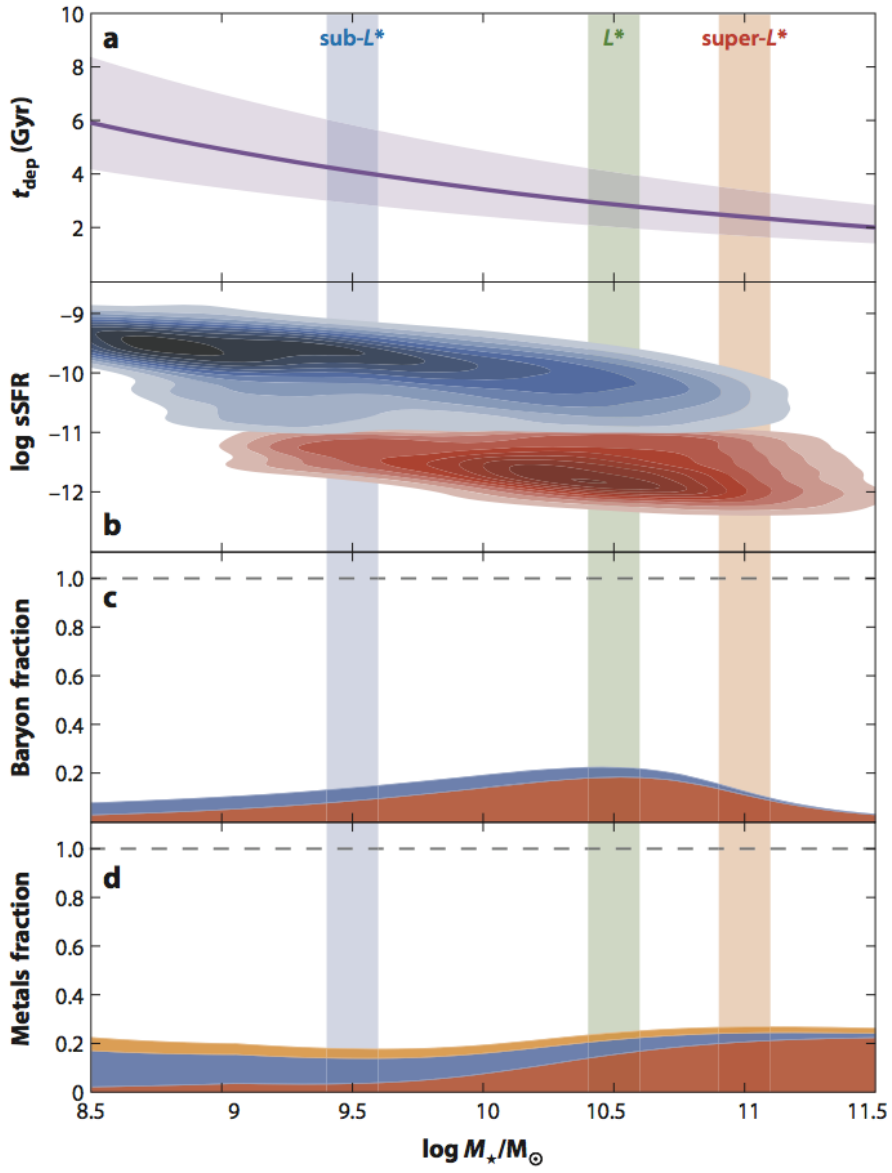

Figure 1.3: Physical properties of galaxies at $z \sim 0$ as a function of their stellar mass $M_\star$ (taken from Tumlinson et al. (2017)). Depletion time ($M_{\rm gas}/\dot{M}_{\rm SFR}$) based on $M_{\rm gas}$ from Peeples et al. (2014) and $\dot{M}_{\rm SFR}$ from Whitaker et al. (2012) (a), specific star formation rate (b), observed baryon fraction (c) and observed metal fraction of galaxies (d). These results challenge our current understanding of galaxy evolution and suggest that the circumgalactic medium is the key ingredient in galaxy formation and evolution. For a detailed discussion see text.

1.2.3 The Need for Gas Flows into and out of Galaxies

Over time more evidence for the interaction between the galaxies and their surroundings was collected. It was found that the gas depletion time is short for all galaxies, that galaxies come in two distinct types of star-forming and quiescent galaxies, that only ∼30% of the predicted baryons are observed (Behroozi et al., 2010) and that only ∼30% of the predicted metals are observed (Peeples et al., 2014).

Gas Depletion Time The depletion time is defined as the time in which current star formation consumes all gas available in a galaxy: $t_{\rm depl} \sim M_{\rm gas}/\dot{M}_{\rm SFR}$. This time scale varies by a factor of two between sub-$L^\star$ and super-$L^\star$ galaxies (see Fig. 1.3a). Since the depletion timescale is shorter than the age of the universe galaxies should have used up all their fuel for star formation already. However, galaxies are still observed to form stars. Therefore, the galaxies have to acquire new gas to serve as star-forming fuel.

Star-Forming vs. Quiescent Galaxies Galaxies are observed as two distinct types, actively star-forming and passive galaxies (see Fig. 1.3b). However, how and if galaxies evolve from being star-forming to being passive is still unknown. Proposed scenarios involve a change in the gas supply be either stopping accretion from the IGM or keeping the CGM hot so it cannot cool and accrete onto the ISM.

The Missing Baryon Problem The currently most successful model to describe the evolution of the universe is the ΛCDM model (Blumenthal et al., 1984; Carroll et al., 1992, and references therein). In this model, the universe contains three major components: a cosmological constant (Λ) associated with dark energy, cold dark matter (CDM) and ordinary matter. Based on this cosmological model baryons follow the dominant gravitational pull from the dark matter into halos. The gas dissipates its energy via radiation and cools into the centre of the halo. Observations of galaxies, however, only recover a small fraction of the predicted baryonic mass in stars and the ISM (e.g. Behroozi et al., 2010, see Fig. 1.3c). These missing baryons could either be in a hot and diffuse phase and have therefore not been detected yet, could have been expelled from the halo, or could have never been accreted onto the halo. Any of these explanations require a study

of the CGM to search for a not yet detected cold or hot gas phase, or evidence for the past ejection of gas. Recent studies using the absorption towards background quasars suggest that depending on the photo-ionization models between half and all missing baryons are in the cold and warm-hot phase of the CGM (Werk et al., 2014; Prochaska et al., 2017).

The Missing Metals Problem Contrary to the pristine gas being accreted from the IGM, metals are formed within the galactic disk via stellar evolution processes. The surrounding CGM is polluted by metals from stellar winds and supernovae. However, based on observations star-forming galaxies from sub-$L^\star$ to super-$L^\star$ retain only 20–25% of the metals they have produced (Peeples et al., 2014, see also Fig. 1.3d). The remaining 75–80% of the metals are expelled through outflows (Tremonti et al., 2004), but the scaling of the outflows with galaxy mass is unknown. It is also unclear whether the expelled metals leave the halo completely or whether they fall back onto the disk in a fountain process (Oppenheimer & Davé, 2008). Furthermore, details like the metal recycling timescale and the metal loading factor are input to state-of-the-art simulations.

These four observations together with the G dwarf problem are pieces of evidence for the importance of interactions between galaxies and their surroundings which need to be taken into account in galaxy evolution models. More specifically the four observations listed in this section demonstrate that the CGM is a key component in understanding gas flows into and out of galaxies. A detailed understanding of the CGM will help to improve models of galaxy evolution.

1.2.4 Galactic Baryon Cycle

In contrast to the early closed-box models, the modern paradigm of galaxy evolution is governed by the exchange of mass, energy and metals between galaxies and their surroundings, the CGM and IGM (e.g. Davé et al., 2012; Lilly et al., 2013). Accretion of pristine gas from the IGM is required for galaxies to sustain their observed star formation (e.g. Erb, 2008; Tacconi et al., 2010; Putman et al., 2012; Sánchez Almeida et al., 2014). However, accretion is notoriously difficult to observe. The Milky Way is known to accrete through the Magellanic Stream (Fox et al., 2014). Given our position inside the Galaxy, it is difficult to detect inflowing gas except from high-velocity clouds (Zheng et al., 2015). The

net inflow rate detected in galaxies beyond the local universe is low at $\sim 5\%$ (Martin et al., 2012; Rubin et al., 2012). The velocity of gas seen in absorption aligned with the major axis of the host galaxy can be modelled as a co-rotating disk with an inflowing component (Bouché et al., 2016; Bowen et al., 2016; Ho et al., 2017). For a review on gas accretion studied in both observations and simulations see Fox & Davé (2017). Stellar feedback powered outflows, on the other hand, are ubiquitously observed at all redshifts (e.g. Martin, 2005; Rupke et al., 2005; Veilleux et al., 2005; Weiner et al., 2009; Steidel et al., 2010; Martin et al., 2012; Newman et al., 2012; Chisholm et al., 2015, 2016; Heckman et al., 2015; Pereira-Santaella et al., 2018; Fluetsch et al., 2019). Outflowing gas is enriched by the mass loss of massive stars as well as the ejecta from supernovae explosions. Enriched outflows transport gas to large radii explaining the metal abundances observed in the CGM (e.g. Tumlinson et al., 2011a; Shen et al., 2012; Muzahid et al., 2015a; Lehner et al., 2013; Ford et al., 2014; Turner et al., 2014; Werk et al., 2014, 2016). Outflow velocities are often smaller than the escape velocity and a fraction of the gas is therefore not ejected from the halo but recycled (e.g. Tumlinson et al., 2011b; Rubin et al., 2012; Bouché et al., 2012a; Stocke et al., 2013; Mathes et al., 2014; Bordoloi et al., 2014; Emonts et al., 2015; Pereira-Santaella et al., 2016; Zheng et al., 2017; Tremblay et al., 2018a). This recycling provides a secondary source of accretion fuelling future star formation (e.g. Oppenheimer et al., 2010; Ford et al., 2014; van de Voort, 2017). This whole process of accretion, star formation, outflow and recycling together makes the *baryon cycle* of galaxy evolution. An illustration of the baryon cycle is shown in Fig. 1.4.

Much work has focused on studying the details of the baryon cycle from simulations (e.g. Brook et al., 2014; Shen et al., 2014; Mitra et al., 2015; Anglés-Alcázar et al., 2017; Tollet et al., 2019). An ideal tool to study the cycling of baryons between galaxies and their surroundings is offered by cosmological hydrodynamical simulations. In simulations accretion from the cosmic web on the one hand feeds galaxies with fresh fuel for star formation (e.g. Kereš et al., 2005; Brooks et al., 2009; Dekel et al., 2009; Kereš et al., 2009; Faucher-Giguère et al., 2011; van de Voort et al., 2011; Romano-Díaz et al., 2014). Winds on the other hand evacuate gas from galaxies (e.g. Oppenheimer & Davé, 2008; Anglés-Alcázar et al., 2014; Muratov et al., 2015, 2017; Sadoun et al., 2016). Furthermore, outflowing gas is found to often re-accrete onto the galaxies (e.g. Oppenheimer et al., 2010;

Übler et al., 2014; Hobbs et al., 2015; Christensen et al., 2016; Anglés-Alcázar et al., 2017).

Using observations to study the baryon cycle is more challenging, because the halo gas is not directly observable with current instrumentation because of its low surface brightness (see Section 1.5). Furthermore, the time evolution of gas flows cannot be directly studied in observations as it is possible in simulations.

1.3 The Circum-Galactic Medium

The CGM is a loosely defined region of a few hundred kpc around a galaxy filled with diffuse gas. For practical purposes the virial radius could be taken as the outer boundary of the CGM Tumlinson et al. (2017). However, there is no evidence for a special behaviour of the gas at this radius. Furthermore, the extent of the CGM depends on the environment, since tidal interactions can significantly impact the distribution of the gas around galaxies (Morris & van den Bergh, 1994; de Blok et al., 2018). The CGM is a key ingredient to galaxy evolution since all gas flows into and out of a galaxy pass through this region. As described above it holds the answer to many open questions in galaxy evolution and hosts an important part of the baryons in the gas phase. A schematic view of the CGM is shown in Fig. 1.4. It shows a disk galaxy onto which gas from the cosmic web is accreted and from which outflows are launched that either leave the halo or are recycled in a fountain process. The CGM is multi-phase with a hot, warm-hot and cold component and possibly also harbours cold molecular gas.

1.3.1 Lyman α Absorbers

Studying the CGM directly via its emission remains challenging with currently available instrumentation because of the low gas density resulting in a low emissivity (Cantalupo et al., 2005; Arrigoni Battaia et al., 2016; Gallego et al., 2018, Augustin et al. subm.). Successful observations of Ly α halos were achieved by using long exposure times (Wisotzki et al., 2016, 2018), stacking a large number of objects (Steidel et al., 2011; Momose et al., 2014) or targeting objects with boosted Ly α emission due to the presence of a quasar (e.g. Cantalupo et al., 2014; Borisova et al., 2016; Arrigoni Battaia et al., 2019). The main avenue to study the CGM is through the absorption it imprints on the

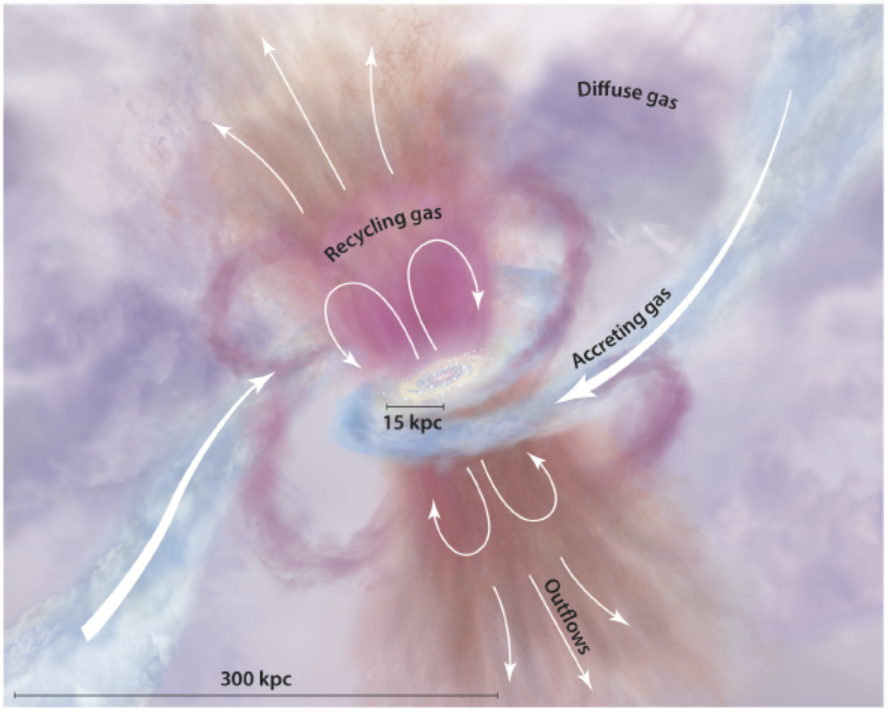

Figure 1.4: A schematic overview of the circum-galactic medium (Tumlinson et al., 2017). A typical galaxy is embedded in a halo of low density gas fuelled by accretion and outflows. This low-density gas is with currently available instrumentation mostly observable via absorption lines imprinted on background quasar spectra.

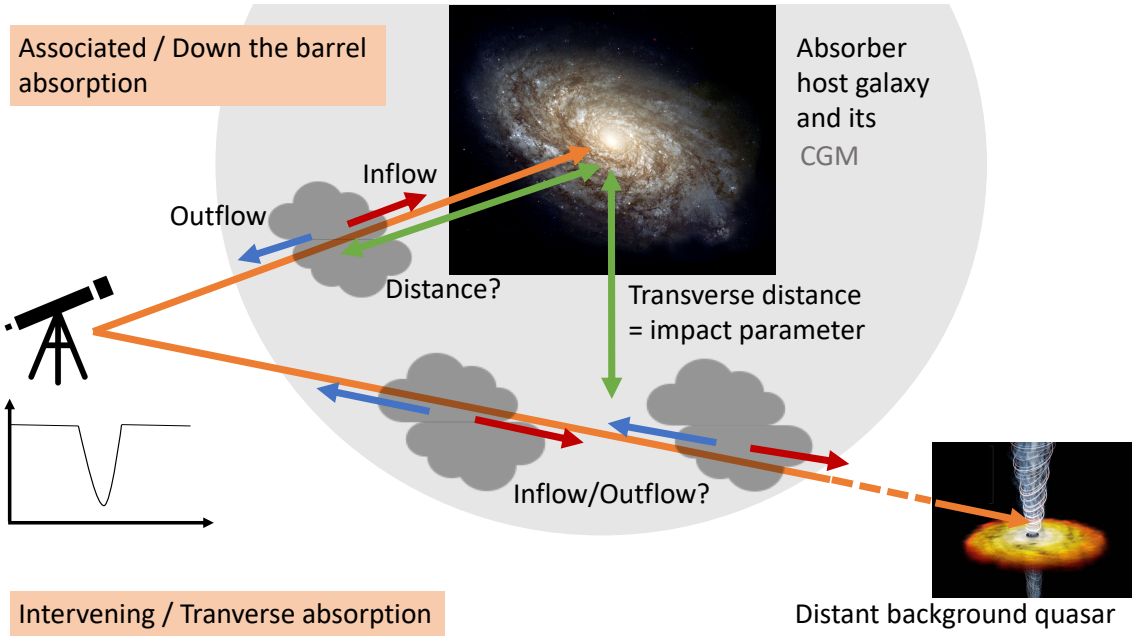

Figure 1.5: Schematic comparison of intrinsic (*top*) and intervening (*bottom*) absorption (not to scale). For details see text.

spectra of bright background galaxies at much higher redshift that align by chance with the galaxy line of sight.

Damped Ly α absorbers were discovered in the 1970s in the spectra of distant quasars (Beaver et al., 1972; Carswell et al., 1975). Ly α absorbers are broadly divided into three main categories: Lyman Limit Systems, subDamped Ly α systems (subDLAs) and Damped Ly α systems (DLA). These absorber types are defined by their column density (LLS: $10^{17.3}$ atoms cm^2 $< N$(HI) $< 10^{19}$ atoms cm^2, sLLS: 10^{19} atoms cm^2 $< N$(HI) $< 2 \times 10^{20}$ atoms cm^2, DLAs: N(HI) $> 2 \times 10^{20}$ atoms cm^2) (Wolfe et al., 2005). At the column densities of DLAs the gas is mostly neutral, while in subDLAs the gas can have a range of ionization stages (Péroux et al., 2002, 2003a) and in LLS the gas is mostly ionized. Furthermore, the DLAs contain the majority of the neutral gas in the Universe (Wolfe et al., 1986; Lanzetta et al., 1995; Zafar et al., 2013) while the contribution of subDLAs, especially at high redshift, might be non-negligible (Péroux et al., 2003b). A connection between the absorber and the host galaxy will provide vital clues on the link between the gas supply in form of neutral hydrogen and the star formation. For a detailed review on DLAs see Wolfe et al. (2005).

The background object towards which the absorption is observed can either be the host

galaxy itself, or an unrelated distant background quasar. Absorption observed towards the host galaxy itself is called intrinsic or "down the barrel" absorption and towards a background quasar is called intervening or transverse absorption. A schematic comparison to the two cases is shown in Fig. 1.5. In the case of intrinsic absorption, the absorbing gas is known to be in front of the host galaxy. A blueshift or redshift of the absorbing material relative to the galaxy redshift unambiguously relates to outflow or infall of the absorbing gas. The distance from the galaxy, however, cannot be determined. In the case of intervening absorption, the projected distance (also known as impact parameter) is a direct observable. Whether the redshifted/blueshifted gas is in front of a galaxy and infalling/outflowing or behind and outflowing/infalling is not directly distinguishable. More sophisticated techniques such as measuring the metallicity of the absorbing gas and the host galaxy or component by component kinematic analysis are needed to determine the relation between the galaxy and the absorbing gas. Gas with a metallicity higher than that of the host galaxy represents material preprocessed and enriched by previous star formation and therefore indicates an outflow, while pristine or low metallicity gas indicates an inflow. Another technique to disentangle inflows and outflows is measuring the azimuthal angle (angle between the major axis of the galaxy and the quasar sight line). Outflowing gas leaves the galaxy preferentially along the path of least resistance, the minor axis, while infalling gas is co-planar with the disc, along the major axis (Shen et al., 2012). However, combining the azimuthal angle with the metallicity relative to the host galaxy Péroux et al. (2016) find no clear correlation between the two which might be due to the limited sample size.

Furthermore, absorption can only trace the gas properties along a single sight line. Therefore, we require a large sample of absorbers with known host galaxies to draw firm conclusions on the processes in the CGM.

1.3.2 Absorber Host Galaxy Identification

Understanding the gas flows in the CGM based on the absorption line technique requires the identification of the absorber host galaxy assuming this is a unique host. In the case of intervening absorption, the much-needed host galaxy identification remains a challenge. Early studies used ground-based telescopes as well as the Hubble Space

TELESCOPE (Warren et al., 2001; Møller et al., 2004). However, despite decades of ongoing research, progress has remained slow. Only recently, building on the identification of the galaxy mass-metallicity relation (Tremonti et al., 2004; Maiolino et al., 2008) searches for absorber host galaxies using X-shooter long-slit triangulation became more successful yielding tens of DLA host galaxies (Fynbo et al., 2010, 2013; Krogager et al., 2017). The spectroscopic follow-up of absorption detections was also facilitated by optical and infrared integral field spectrographs such as SINFONI at the VLT (e.g. Péroux et al., 2011) and OSIRIS at the Keck Observatory (e.g. Jorgenson & Wolfe, 2014) and multi-object spectrographs such as MOSFIRE at the Keck Observatory (Rudie et al., 2019) becoming available.

The single host galaxy identification paradigm is challenged by an increasing number of studies finding absorbers associated with intra-group medium (Rao et al., 2003; Whiting et al., 2006; Kacprzak et al., 2010; Gauthier, 2013). With the development of large field of view integral field spectrographs such as the Multi Unit Spectroscopic Explorer (MUSE) on the VLT evidence for absorbers being associated with multiple galaxies is ever-increasing (Bielby et al., 2017; Fumagalli et al., 2017; Péroux et al., 2017; Rahmani et al., 2018; Klitsch et al., 2018; Peroux et al., 2019; Chen et al., 2019, Hamanowicz et al. in prep).

The most successful studies identifying DLA host galaxies target the high-metallicity absorbers that might preferentially trace the high mass end of the absorber host galaxy population. Simulations, however, suggest that DLAs trace the faint end of the luminosity function (Haehnelt et al., 1998; Fynbo et al., 1999; Pontzen et al., 2008; Barnes & Haehnelt, 2009). An unbiased approach targeting the genuinely gas-rich rather than metal-rich and thus massive galaxies is crucial to understand the underlying galaxy population probed by absorption. Furthermore, the picture arising from the current observations is more complicated than a one-to-one match of absorber and host galaxy. A more careful component-by-component analysis is crucial to get the full context of the gas flows into and out of galaxies selected by absorption.

1.4 Molecular Gas

1.4.1 Measuring Molecular Gas Masses

Table 1.1: Rest emission line frequencies (ν [GHz]) of the ^{12}CO $J = 1 - 0$ to $9 - 8$ rotational transitions.

J	1–0	2–1	3–2	4–3	5–4	6–5	7–6	8–7	9–8
ν	115.27	230.54	345.80	461.04	576.27	691.47	806.65	921.80	1036.9

Molecular gas is the key to study star-formation. It can cool via line emission of rotational and vibrational transitions more efficiently than atomic gas and is thought to be the direct fuel for star-formation (McKee & Ostriker, 2007). However, this important ingredient to the baryon cycle is notoriously difficult to observe. H_2 is a symmetric, homonuclear molecule with no dipole moment and is therefore radiating inefficiently. The lowest allowed rotational transition is the quadrupole transition tracing gas warmer ($\sim$ 500K (Dabrowski, 1984)) than the typical cold gas in giant molecular clouds with temperatures of $10 - 20$K. Thus, the cold molecular hydrogen vital to star formation and making up most of the molecular ISM in galaxies is invisible to us. A resolution to this problem is to use carbon monoxide (^{12}CO, CO hereafter), the second most abundant molecule in the universe, to trace H_2. CO is easily excited with the excitation energy of the lowest transition CO(1–0) being $h\nu/k \sim 5.53$K. The emission frequencies of the lowest nine rotational transitions of CO are listed in Table 1.1. To determine the total molecular gas mass it is then necessary to measure the conversion factor between CO and H_2. The standard methodology uses a simple linear relation between the observed

Table 1.2: Details of the AMA observing Bands.

ALMA Band	Frequency [GHz]	Wavelength [mm]	Primary Beam FWHM [″]
Band 3	84–116	2.6–3.6	56
Band 4	125–163	1.8–2.4	48
Band 5	163–211	1.4–1.8	35
Band 6	211–275	1.0–1.4	27
Band 7	275–373	0.8–1.0	18
Band 8	385–500	0.6–0.8	12
Band 9	602–720	0.4–0.5	9
Band 10	787–950	0.3–0.4	7

CO integrated line intensity ($W(\mathrm{CO}J = 1-0)$[K km s^{-1}]) and the molecular gas column density ($N(\mathrm{H_2})$):

$$N(\mathrm{H_2}) = X_{\mathrm{CO}} \times W(\mathrm{CO}J = 1-0) \tag{1.4.1}$$

Integrating over the emitting area and correcting for the mass contribution of heavier elements in the molecular gas leads to the following expression:

$$M_{\mathrm{mol}} = \alpha_{\mathrm{CO}} \times L'_{\mathrm{CO}}, \tag{1.4.2}$$

where M_{mol} is the molecular gas mass in $M_\odot$ and L'_{CO} is the CO line luminosity defined by Solomon et al. (1992):

$$L'_{\mathrm{CO}} = 3.25 \times 10^7 \times S_{\mathrm{CO}}\Delta v \ \frac{D_{\mathrm{L}}^2}{(1+z)^3 \nu_{\mathrm{obs}}^2} [\mathrm{K\ km\ s^{-1}\ pc^2}], \tag{1.4.3}$$

where $S_{\mathrm{CO}}\Delta v$ is the integrated line flux density in Jy km s^{-1}, D_{L} is the luminosity distance to the source in Mpc and ν_{obs} is the observed frequency in GHz. α_{CO} can be seen as a mass-to-light ratio.

Both α_{CO} and X_{CO} are referred to as the CO-to-$\mathrm{H_2}$ conversion factor. The recommended conversion factor in the Milky Way disk is $X_{\mathrm{CO}} = 2 \times 10^{20} \mathrm{cm^{-2}(K\ km\ s^{-1})^{-1}}$ with a ±30% uncertainty (Bolatto et al., 2013). This corresponds to $\alpha_{\mathrm{CO}} = 4.3 M_\odot (\mathrm{K\ km\ s^{-1}})^{-1}$. However, this conversion factor is a global value determined for the Milky Way and is not necessarily applicable in external galaxies. Among other factors, the metallicity and the cosmic ray incidence are found to strongly affect the conversion factor (Schruba et al., 2012; Bisbas et al., 2017). For a detailed review on this topic see Bolatto et al. (2013). Despite molecular gas being the key ingredient in the baryon cycle the exact measurement of the molecular gas mass is still challenging. A game changer in the studies of molecular gas at all redshift is ALMA becoming available which offers an order-of-magnitude higher sensitivity and resolution (Wootten & Thompson, 2009).

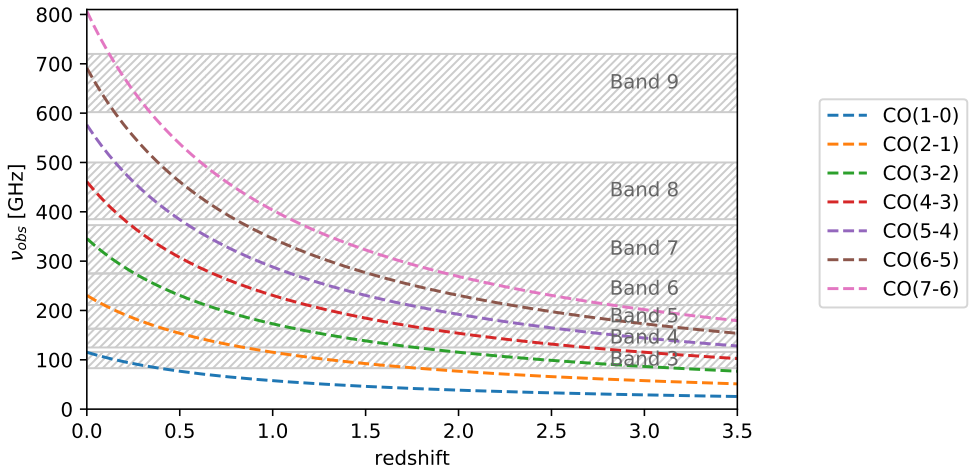

Figure 1.6: Observed frequency of CO emission lines as a function of redshift. ALMA Bands are indicated with the grey areas. In most combinations of redshift and ALMA observing frequencies only one CO transition can be covered. In this case the redshift and line identification are degenerate.

1.4.2 CO Spectral Line Energy Distribution

The CO-to-H_2 conversion factor is defined as the conversion of the CO line flux in the $J = 1 - 0$ transition. However, for two reasons the CO(1–0) transition is not always the first line to target in observing projects. First the CO(1–0) transition is not always accessible. In Fig. 1.6 we show the redshifted observed frequencies of CO transitions with the ALMA observing bands overlayed. The CO(1–0) transition is only accessible with ALMA for galaxies at low redshifts $z \lesssim 0.4$. For higher redshifts one has to revert to higher J transitions.

The relative strength of these CO transitions in a galaxy is referred to as the CO spectral line energy distribution (SLED) or CO excitation ladder. The exact shape of the CO SLED depends on the temperature and density of the emitting gas and can therefore be used to study the ISM conditions in external galaxies (see Fig. 1.7). Another reason to observe higher J transitions is therefore that based on the CO SLED a higher flux is expected in the higher J lines making observations more time efficient. The brightest transition that is observable depends on the ISM conditions. For a detailed review see Carilli & Walter (2013).

The CO-to-H_2 conversion factor relates the CO(1–0) line flux with the molecular gas

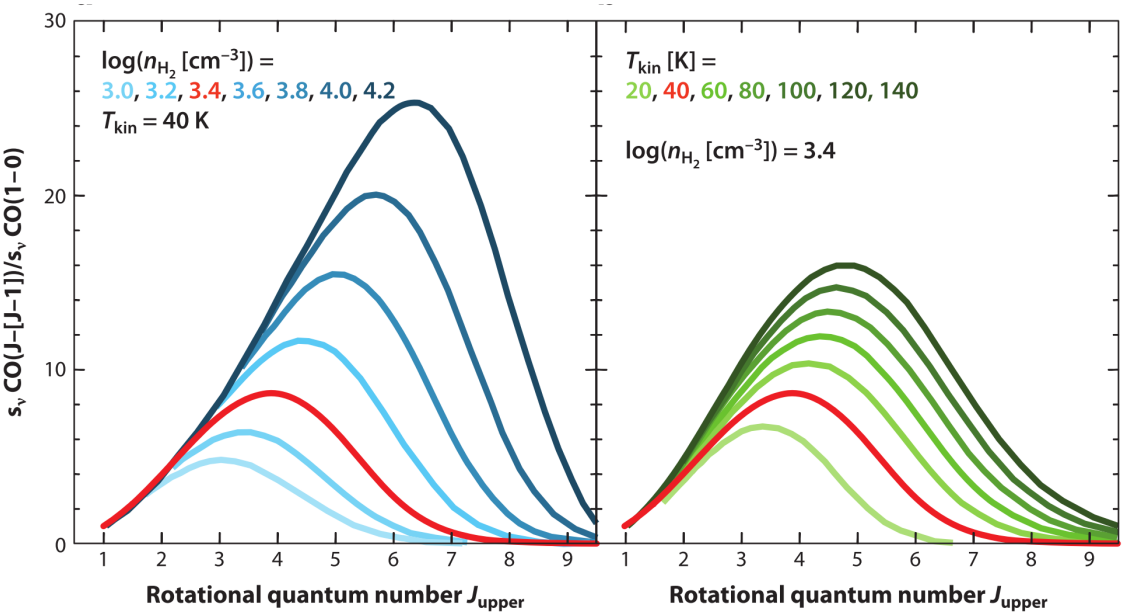

Figure 1.7: The line flux of a CO rotational transition relative to the CO(1–0) transition as a function of the rotational quantum number presented by Carilli & Walter (2013). *Left panel:* Predicted CO SLED for a fixed temperature of 40K and a varying density. *Right panel:* Predicted CO SLED for a fixed density of $\log(n_{H2}[\mathrm{cm}^{-3}]) = 3.4$ and a varying temperature. If the CO SLED is completely populated it is possible to measure the temperature and density of the emitting gas.

mass. If a higher J line is observed, it is necessary to convert to the CO(1–0) line flux using a line ratio based on the expected CO SLED. For most SLEDs, moderately high J CO transitions might be expected to be brightest and therefore the CO SLED can be used to plan observations in a more time-efficient way. However, detailed knowledge of the CO SLED is vital for the conversion to a molecular gas mass. Normal star-forming galaxies have flatter CO SLEDs than star-burst galaxies or quasars (see Fig. 1.8). If the line ratio for the Milky way is assumed while the CO SLED is more similar to that of a star-burst galaxy, the molecular gas mass can be overestimated.

1.4.3 Molecular Gas in Absorber Host Galaxies

Only recently a new avenue for absorber host galaxy detection was opened with ALMA. Targeting the high-metallicity end of the absorbers led to high detection rates of molecular gas emission lines at the absorber redshift in pioneering studies by Neeleman et al. (2016, 2017); Kanekar et al. (2018); Møller et al. (2018); Fynbo et al. (2018a); Neeleman et al.

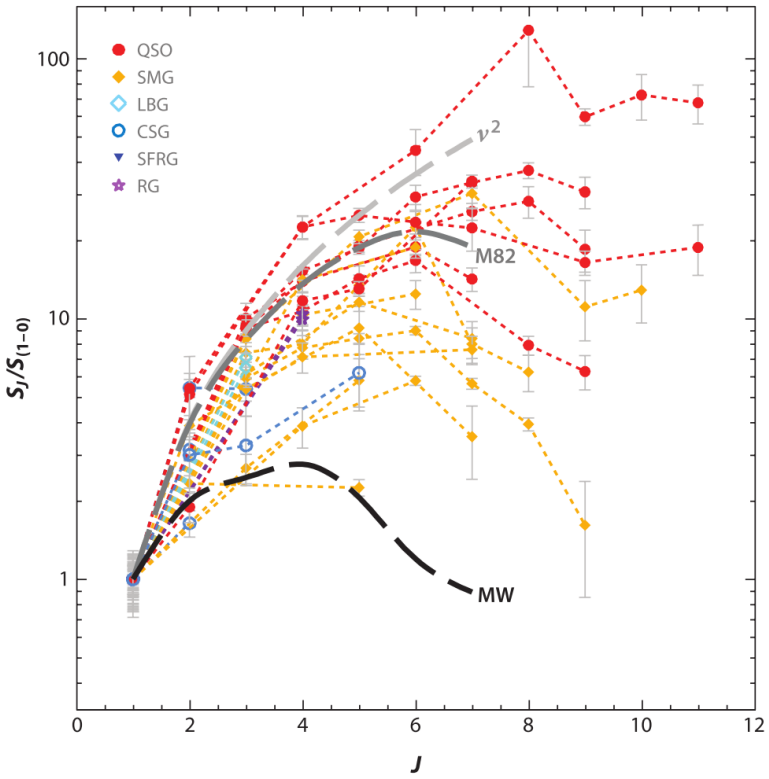

Figure 1.8: The CO SLED as presented in Fig. 1.7 as measured for the Milky Way, the star-burst galaxy M82, quasars and submillimetre galaxies (SMGs) (Ivison et al., 2011). (Credit: Carilli & Walter, 2013).

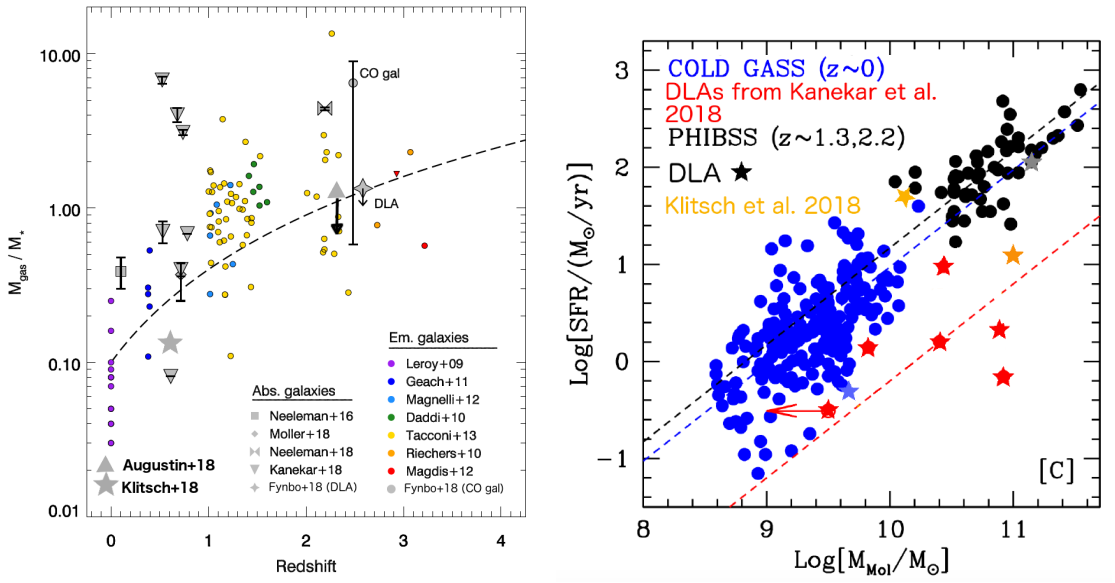

Figure 1.9: Molecular gas properties of absorption-selected galaxies. *Left Panel:* Molecular gas mass fraction as a function of redshift for emission (circles) and absorption (grey symbols) selected galaxies (adapted from Fynbo et al. (2018b)). Both samples follow the same evolution of decreasing molecular gas fraction with decreasing redshift. *Right panel:* The SFR as a function of molecular gas mass for emission- (circle) and absorption-selected (stars) galaxies (adapted from Kanekar et al. (2018)). Dashed lines mark constant SFE. The absorption-selected galaxies at redshift $z \sim 0.5$ seem to have a lower SFE. The orange stars show the results for J0423B using conversion factors appropropriate for a LIRG (light orange) and for a normal spiral (dark orange) as discussed in Chapter 4.

(2019). In Fig. 1.9 we show the characteristics of the molecular gas masses of absorption-selected galaxies compared to emission-selected galaxies. The right panel shows that the molecular gas fraction is decreasing with decreasing redshift for both samples. As shown in Fig. 1.9 (right panel) it was also found that while emission-selected galaxies at high ($z \sim 1,2$) and low ($z \sim 0$) redshift have a roughly constant SFE, absorption-selected galaxies at $z \sim 0.5$ seem to have a lower SFE meaning that either the SFR is low given their molecular gas mass or the molecular gas mass is high given the SFR. However, as described in Section 1.4.1 and 1.4.2, the Milky Way-type conversion factor and line ratios might not be applicable to these galaxies and the molecular gas mass may be overestimated by a factor of a few. Furthermore, the emission-selected galaxy observations clearly outnumber the observations of absorption-selected galaxies. The field is still in its infancy and more progress will be made soon.

1.5 Global Baryon Cycle

In addition to the local baryon cycle in individual objects, it is important to study the global baryon cycle in the universe as a whole. This will offer a global connection between the gas reservoirs and star formation and a deeper understanding of the physical mechanisms driving galaxy evolution.

The cosmic star-formation rate history is well-established out to high redshift. In Fig. 1.10 a recent compilation of cosmic star formation rate density measurements from a review by Madau & Dickinson (2014) is shown. This figure includes observations from ultraviolet, infrared, submillimetre, and radio wavelengths tracing non-dust-obscured as well as dust-obscured star formation. The star formation rate density increased with decreasing redshift reaching a peak at $z \sim 2$ and declined until the present by a factor of $20-30$. The physical processes driving this evolution, however, remain poorly understood.

1.5.1 The Peak of the Star-Formation Rate History

Understanding the peaked shape of the SRH is one of the outstanding open questions in galaxy evolution. It can be explained if the amount of fuel for star-formation available over cosmic time followed the same evolution. Measurements of the cosmic HI density

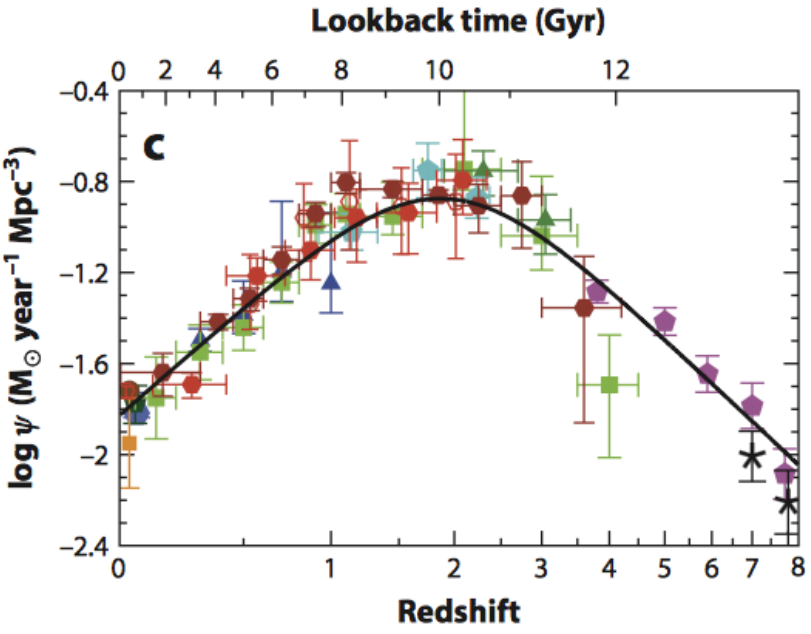

Figure 1.10: The cosmic star formation rate history (Madau & Dickinson, 2014). The SFH shows a peak at $z \sim 2$ and declined by a factor of $20 - 30$ until the present. The physical processes driving this evolution are not fully understood.

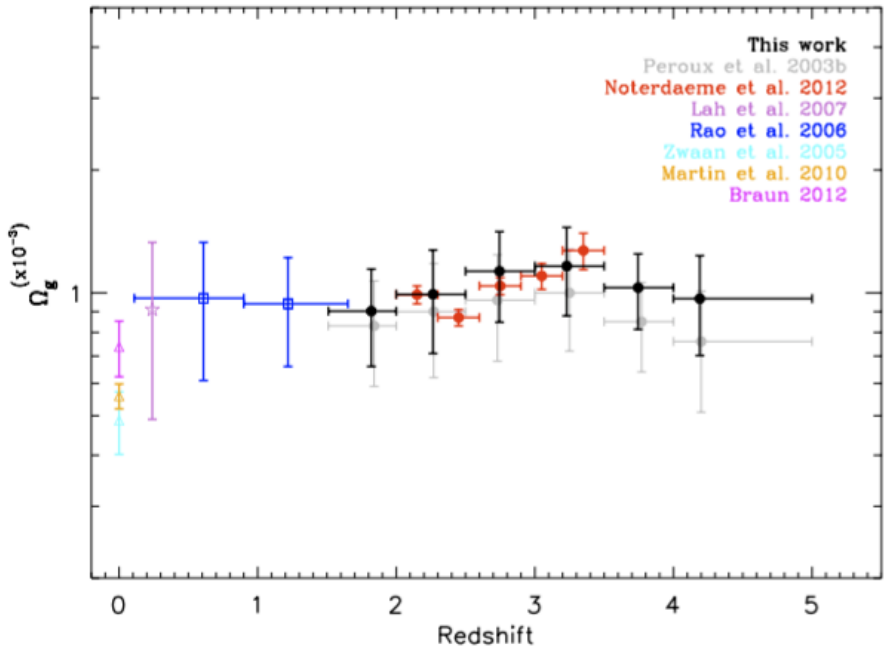

Figure 1.11: Cosmic HI gas mass density (Zafar et al., 2013). While the SFH decreases by a factor of $20 - 30$ since $z \sim 2$, $\Omega_{\rm HI}$ decreased only by $\sim 15\%$.

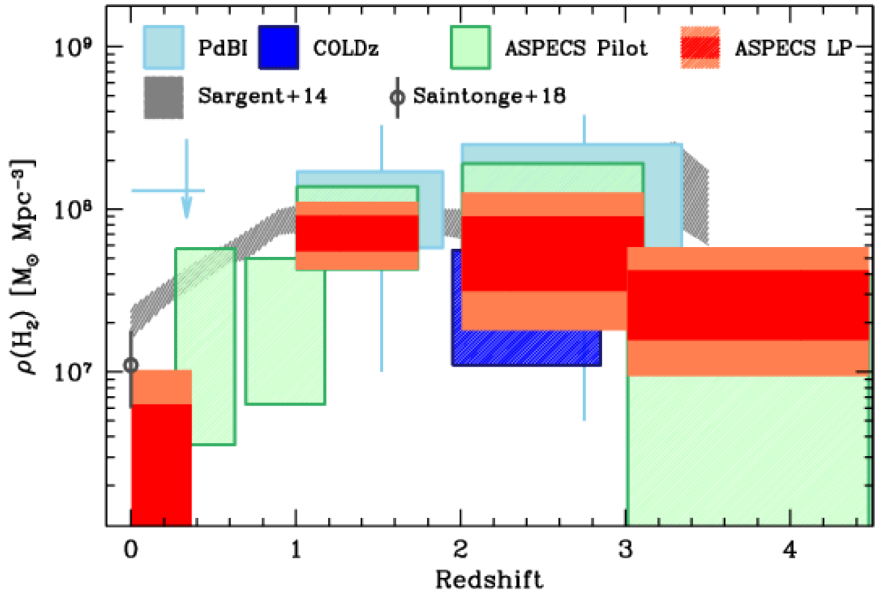

Figure 1.12: The cosmic molecular gas mass density (Decarli et al., 2019). While the SFH decreases by a factor of 20 – 30 since $z \sim 2$, Ω_{H2} decreased by about one order of magnitude.

traced by the damped Lyman alpha absorbers shown in Fig. 1.11 show no strong evolution and decreased only by $\sim 15\%$ since $z = 2$.

However, it is widely believed that the direct fuel for star formation is the molecular hydrogen (McKee & Ostriker, 2007). Only since ALMA became available have statistically significant observations of molecular hydrogen traced by CO rotational transitions in galaxies at low and high redshifts become available. A compilation of the most recent measurements of the cosmic molecular gas mass density from large observing programs is shown in Fig. 1.12. These measurements indicate a decrease of the molecular gas mass density by about one order of magnitude, which is similar to the decrease of the cosmic star formation rate history. However, the uncertainties on the measurements are still large. Emission line studies are mostly sensitive to the high mass end of the CO luminosity function missing the possibly non-negligible contribution of the faint end. Another uncertainty of the large observing programs ASPECS and COLDz is that these surveys target relatively few small fields on the sky making them sensitive cosmic variance. Furthermore, the choice of the CO-to-H_2 conversion factor is uncertain.

1.5.2 The High Redshift Slope of the Star-Formation Rate History

The field of galaxy formation and evolution was revolutionized by the discovery of submillimetre galaxies, a population of dusty star-forming galaxies with submillimetre flux densities of a few mJy. These so-called SMGs were discovered about 20 years ago (Smail et al., 1997; Barger et al., 1998; Hughes et al., 1998; Ivison et al., 1998). Initially such galaxies were identified in surveys using bolometer cameras such as the Submillimetre Common-User Bolometer Array (SCUBA - Holland et al., 1999) mounted on the 15m single dish James Clerk Maxwell Telescope (e.g. Coppin et al., 2006; Weiß et al., 2009; Wardlow et al., 2011; Casey et al., 2013; Geach et al., 2013).

It was established that SMGs are predominantly found at $z \sim 1-3$ with a tail to $z \sim 6$ (Chapman et al., 2005; Wardlow et al., 2011; Smolčić et al., 2012; Weiß et al., 2013; Simpson et al., 2014; Chen et al., 2016) and that SMGs dominate the high redshift star formation history (Barger et al., 2012; Swinbank et al., 2014) with SFRs $100-1000 \mathrm{M}_{\odot}\ \mathrm{yr}^{-1}$ (Blain et al., 2002; Chapman et al., 2005; Magnelli et al., 2012; Casey et al., 2013; Swinbank et al., 2014). These high SFRs suggest that SMGs can build up high stellar masses larger than $M_{\star} = 10^{11} \mathrm{M}_{\odot}$ and might be the progenitors of massive elliptical galaxies in the local universe (Lilly et al., 1999; Fu et al., 2013; Simpson et al., 2014).

Despite being a key ingredient in the stellar mass growth in the most massive galaxies measuring the physical properties of SMGs has been challenging due to the lack of angular resolution in single dish studies. In fact, it turned out that between 15 and 90% of the SMGs detected in single dish observations at 850μm are composed of multiple galaxies blended together in the large beam (e.g. Wang et al., 2011; Karim et al., 2013; Simpson et al., 2015; Hill et al., 2018).

Models of galaxy formation and evolution aim to reproduce the number of observed galaxies per deg^2 on the sky at a certain flux level. This is referred to as submillimetre number counts. To determine accurate submillimetre number counts from observations it is crucial to resolve the emission into individual galaxies since even small changes in the form of the number counts can have a significant impact on the evolution of high-redshift dust-obscured star-burst galaxies (e.g. Cowley et al., 2015; Lacey et al., 2016).

Models of galaxy formation and evolution also try to reproduce the high redshift slope of the SFH (as shown in Fig. 1.13 Casey et al., 2018). However, the SFH at high redshift is

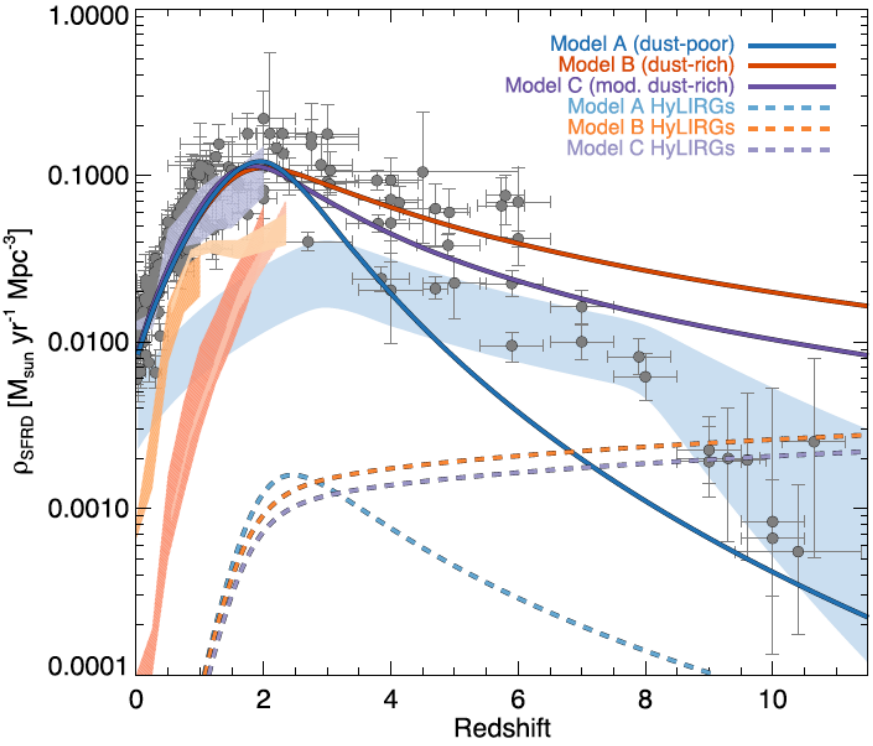

Figure 1.13: The cosmic star formation rate history as presented by Casey et al. (2018). The grey points are taken from Madau & Dickinson (2014). Thick solid lines mark three different models of galaxy evolution with a dust-poor early universe (Model A), a dust-rich early universe (Model B) and a modified dust-rich early universe (Model C). The contribution of hyper luminous infrared galaxies (HyLIRGs) is shown as the dashed curve. From the currently available observations at high redshift it is not yet possible to exclude even the most extreme models.

not as well constrained as the low redshift part. The models overlayed in this figure assume different amounts of dust in high redshift galaxies. With the current measurements it is not possible to discard even the most extreme models. A statistically significant sample of high redshift DSFGs is needed to constrain the importance of dust in galaxy evolution models and the high redshift slope of the cosmic star formation rate density.

1.6 Thesis Overview

The aim of this thesis is to probe the evolution of gas flows in the CGM, and molecular gas and dust in galaxies using ALMA calibrator observations.

- In *Chapter 2* we summarize the ALMACAL survey. We describe the survey characteristics such as observing time, observed frequencies and the basic data

reduction. The nature of the ALMA calibrators is discussed and we compare this novel approach to traditional large programs with similar science goals. We furthermore discuss recent scientific results obtained with ALMACAL data and present a search for absorber host galaxies targeting the CO emission line at the respective redshift. Parts of this chapter are published in Oteo et al. (2016b); Bonato et al. (2018).

- In *Chapter 3* we carry out an unbiased survey of CO emission lines from absorption-selected galaxies. In this work we have utilized the ALMACAL database to carry out a search for CO emission from absorber host galaxies without pre-selecting on absorption properties.

- In *Chapter 4* we present a pilot project studying the neutral, molecular and ionized gas in an absorption-selected system detected in Chapter 3 using ALMA and MUSE observations. This work has been published in a first-author paper, Klitsch et al. (2018).

- In *Chapter 5* we analyse the first measurements of the CO spectral line energy distribution in absorption-selected galaxies using ALMACAL observations. Here we use three galaxies identified in Chapter 3, that are detected in multiple CO emission lines. The indication of low star formation efficiencies discussed in Section 1.4.3 might be challenged if the CO spectral line energy distribution in absorption-selected galaxies is deviating from that of the Milky Way. This work has been published in a first-author paper, Klitsch et al. (2019).

- In *Chapter 6* we put constraints on the molecular gas mass density over cosmic time via a blind search for intervening molecular absorbers. This alternative approach is complementary to the emission-selected studies presented in Section 1.2.5 as it is also sensitive to the faint end of the column density distribution function and free of cosmic variance. This work has been submitted in a first-author paper, Klitsch et al. subm..

- In *Chapter 7* we present the first high-frequency number counts free of source blending and cosmic variance effects. We have used the most recent ALMACAL

version December 2018 to derive high spatial resolution number counts. Using the simultaneous Band 6 coverage we derive spectral indices and determine the redshift distribution of the population of DSFGs detected at 680μm. Furthermore, whether our observations resolve the extra-galactic background light at 680μm.

- Finally, in *Chapter 8* we summarize the main results and describe future directions of this work. We discuss ongoing and future projects and identify remaining open questions to be addressed.

Chapter 2

ALMACAL — Overview

2.1 The Philosophy of an ALMA Calibrator Survey (ALMACAL)

ALMA becoming available revolutionized the field of submillimetre astronomy given both its high sensitivity and its high spatial resolution. Compared to previously available telescopes such as the Submillimeter Array (SMA Ho et al., 2004) on Hawaii or the Combined Array for Research in Millimeter-wave Astronomy (CARMA Bock, 2007) in California, the sensitivity and spatial resolution increased by a factor of $10 - 100$. ALMA was designed to answer three main science questions: *i)* the origins of galaxies, *ii)* the origins of stars and *iii)* the origins of planets. Outstanding scientific results besides extragalactic astronomy are the observation of protoplanetary disks (e.g. Andrews et al., 2018) and recent observations of our Sun (e.g. Loukitcheva, 2019). See also Wootten (2001); Bachiller & Quintanilla (2008) for an overview of the ALMA science goals. The versatility of this telescope combined with the strong user support results in an on average 5 times higher demand of observing time relative to the available observing time (referred to as the telescope pressure). The channel to obtain a larger amount of observing time ($>$ 50h) is via a Large Program. We choose an alternative approach to obtain even more observing time "for free". Approximately 20% of the total ALMA observing time is spent on calibration observations of solar system bodies and extra-galactic targets. According to 'ALMA User Policies' the data are publicly available without proprietary time. To

date (until June 2019) the calibration observations amount to ~ 2100h of observation time which is similar to ~ 20 Large Programs or half of all observing time awarded to observers in cycle 7 (one cycle is equivalent to one year). This calibrator survey can be used to study both the calibrators themselves and the galaxies in the field. A caveat with this kind of observations is that the frequency setup and spatial resolution of the calibrator observations are the same as for the science target of the corresponding observations. Therefore, we have no influence on what is exactly observed. Furthermore, a single integration of a calibrator is about 5 min and therefore usually multiple observations have to be combined to reach a significant depth. Overall ALMACAL is a good way to make use of the 20% of ALMA observing time that is used only for calibration. It is also an effective way to obtain large amounts of observing time at a highly demanded telescope. However, it comes at the price of short individual integration times, limited observed fields and random frequency setups and spatial resolutions. An overview of the ALMACAL observing strategies and first science results is also given by Oteo et al. (2016a).

2.2 ALMA Observing Schedule

For the ALMACAL survey we make use of the calibration observations that are carried out together with every ALMA observation. The ALMA observing time is divided in so-called execution blocks. Each execution block comprises observations of a science target and observations of two or three bright, compact sources for calibration purposes. These calibrators are usually planets or extragalactic sources. The flux densities of these calibrators are typically of the order of 1 Jy. The observations of bright calibrators are used to calibrate the amplitude and phase of the science targets' visibilities, to set the flux density scale, and to determine the bandpass response. These calibration observations comprise on average 20% of the observing time in one execution block. In most cases, each calibrator is observed with the same observational set-up (array configuration, frequency set-up) as for the science observations.

Some calibrators are used in multiple observing programs and are therefore observed multiple times, with different array configurations and different frequency set-ups. These multiple observations increase the depth as well as potentially the frequency coverage.

The multiple observations also offer the opportunity to study light curves.

2.3 ALMA Calibrator Properties

ALMA calibrators were chosen as radio-bright compact sources. The objects used for calibration observations are millimetre-bright relatively compact sources from the Australia Telescope 20 GHz (AT20GHz) survey (Ekers et al., 2007). Planets and moons can also be used as flux calibrators, but those are not used in ALMACAL. The extragalactic sample is dominated by flat-spectrum radio quasars (FSRQs, 46%), blazars of uncertain type (38.3%) and BL-Lac objects (11.3%). In total 97% of the extragalactic ALMA calibrators are found to be blazars (Bonato et al., 2018).

The distribution of calibrators on the sky is shown in Fig. 2.2. Since the calibrators are distributed randomly on the sky, any study based on this dataset will be free of cosmic variance effects.

A key property for studies of the calibrators themselves or intervening absorbers is the redshift of the calibrator. However, only a sub-sample of the ALMA calibrators have known redshifts. We have compiled a database of physical properties of the calibrators in Bonato et al. (2018) which we have combined with updated redshift measurements from the AT20G sources (E. Mahony private comm.). Furthermore, we have conducted an additional query to the Simbad and NED databases. In total this results in redshift measurements for 622 calibrators. A redshift distribution is shown in Fig. 2.3. The majority of the calibrators are at $z < 1.5$ and the highest known redshift is $z \sim 3.2$. Since the known redshift is crucial for the blind molecular absorption line survey described in Chapter 6 we have initiated an "any weather" program to obtain VLT X-shooter spectra for 50 additional quasars. We aim to detect CIV and MgII emission lines in 15 – 45 minutes observing time to determine spectroscopic redshifts. Half of the targets are observed and the data analysis is currently in progress.

A detailed study of the ALMA calibrators including a SED fitting and light curve analysis is presented by Bonato et al. (2018) incl. Klitsch.

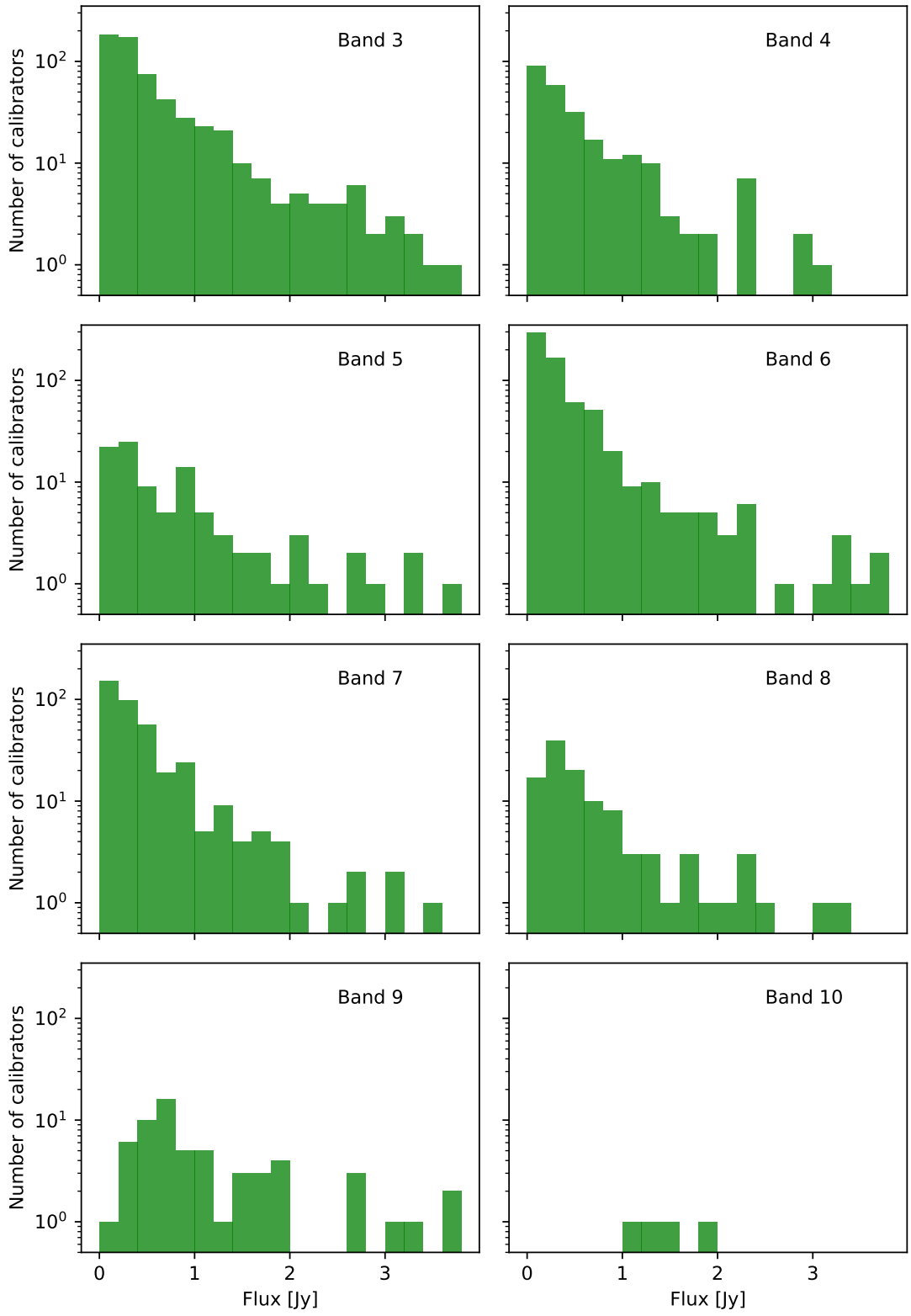

Figure 2.1: Flux distribution of the ALMA calibrators in the different observing Bands. The calibrators are bright at the observed wavelength making them ideal targets to search for intervening absorption. At the same time the bright source in all ALMACAL observations requires the detectors to be sensible to a large dynamic range.

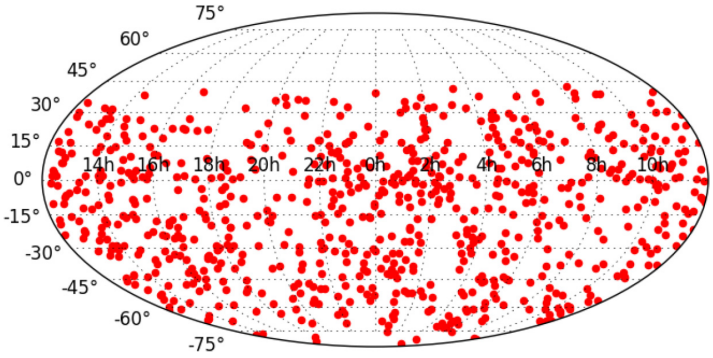

Figure 2.2: Positions of the ALMACAL fields in Mollweide projection as shown by Bonato et al. (2018). The ALMA calibrator fields are distributed randomly over the southern sky up to a declination of ~ 45 deg and therefore statistical studies using all ALMACAL fields will be free of cosmic variance.

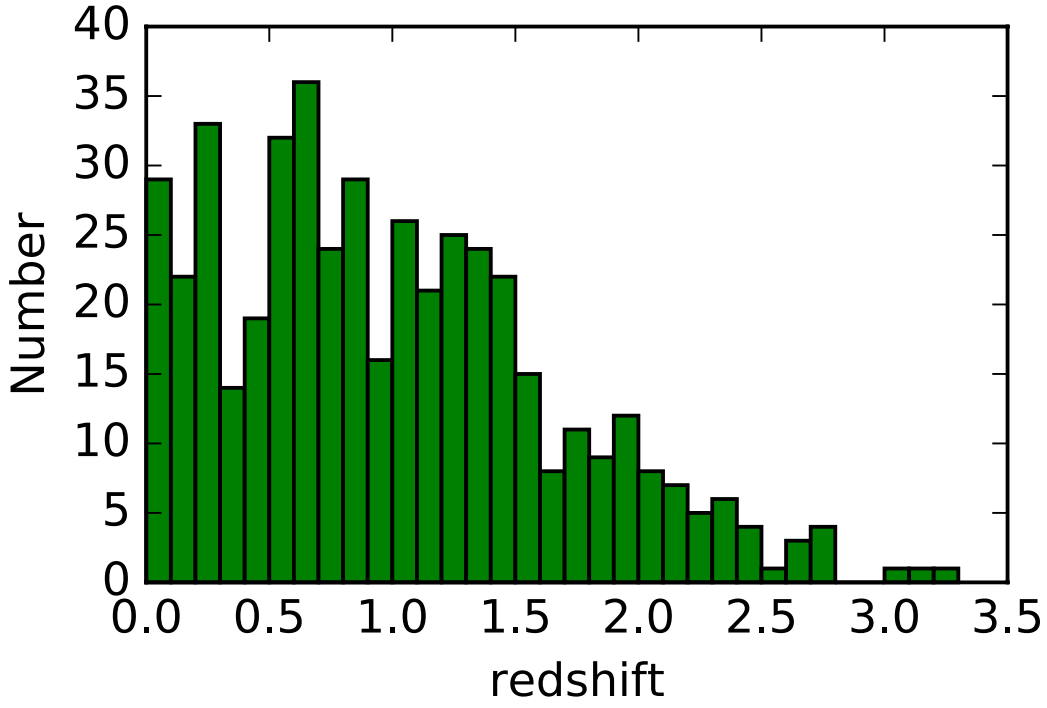

Figure 2.3: Redshift distribution of the ALMA calibrators included in ALMACAL with redshifts available from the literature.

2.4 A Broad Dynamic Range

A key requirement for calibrator sources is submillimetre brightness. This is a challenge for our survey since we need to make sure the dynamic range in the final image is large enough to be able to detect faint sources close to the bright calibrators. We measure the flux of the calibrator in the data reduction and subtract a point source with the given flux from the data. These flux measurements can also be used to construct light-curves and study the variability in different Bands. We calculate the mean flux per Band and calibrator and show the flux distribution of all ALMA calibrators in Fig. 2.1. The majority of the calibrators have fluxes between $\sim$ 0.5 and 3.5 Jy at all but the highest frequencies observed with ALMA. Oteo et al. (2016b) has detected flux densities down to 0.2 mJy exceeding a dynamic range of 18,000. Other studies find similar results. For example, Meyer et al. (2018) found in their observations of M84 a peak flux of 0.187 Jy and a secondary bright knot of $\sim$ 1 mJy and reach an rms noise of $\sim$ 10 μJy in the continuum image. This translates to a dynamic range of $\sim 20,800$.

We conclude therefore that the presence of the calibrator in the centre of the image does not put strong limitations on the detectability of faint sources in our survey.

2.5 Data Reduction

The usual ALMA data reduction pipeline was developed to reduce the science observations in an optimal way. For ALMACAL, however, we use the calibrator observations which are not fully reduced in the standard pipeline. We therefore developed a specific data reduction pipeline designed to produce calibrated data on which we can do science. Therefore, we extend the standard data reduction to taking also advantage of the calibrator being in the field of view of the observations and do a self-calibration.

We retrieve the calibrator observations from the ALMA archive. In the standard ALMA calibration scripts from the earlier cycles not all calibrators are always fully calibrated. The calibration tables obtained from the phase calibrator are usually only applied to the science target but not to the bandpass calibrator. To remedy this, the flux density scale of the bandpass calibrator is retrieved from the delivered flux table and the calibration tables are applied to the bandpass calibrator.

To keep the data volume manageable the spectral resolution of the data is kept fixed at 15.625 MHz. This is sufficient for extra-galactic emission line surveys. For projects focussed on intervening molecular absorption lines presented in Chapter 5 an alternative data reduction is used to achieve higher spectral resolution without drastically increasing the data volume or processing speed. This technique is described in detail in Chapter 5.

When a bright point source is detected in a field it is possible to use it to calibrate the phase and amplitude for this observation. Since every ALMACAL field includes by definition a bright point source, namely the calibrator itself, it is possible to perform the so-called "self-calibration". It takes advantage of the fact that interferometric observations are over-constrained because the number of baselines is larger than the number of antennas. The self-calibration yields nearly optimal calibration results. To enable a fast self-calibration a so-called 'pseudo-continuum' measurement set is created by averaging all channels per spectral window. The self-calibration is applied twice, once only in the phase calibration and once in both phase and amplitude calibration. The solution interval is always chosen to be equal to the integration time. For the majority of datasets these two rounds of self-calibration produce adequate results. For all studies not reliant on the central continuum emission a point source model is subtracted from the visibility data from each observation separately. The subtraction is done for every observation separately to take into account possible variability of the calibrator. The fully calibrated visibility data is stored for further processing. This amounts to $\sim$ 26Tb of reduced raw data processed up until June 2019.

2.6 The ALMACAL Survey Characteristics

As explained above we have no influence on the observed targets and frequency setups. Therefore, the depth and frequency coverage of the ALMACAL observations vary strongly between the different calibrator fields.

The distribution of observations in the different Bands is illustrated in Table 2.1. Band 3, 6 and 7 are used most extensively and have total integration times $\geq$ 500h. We find 20, 24 and 15 fields respectively, with integration times longer than 10h in these Bands. Remarkable is also the longest integration time in a single field per Band which amounts

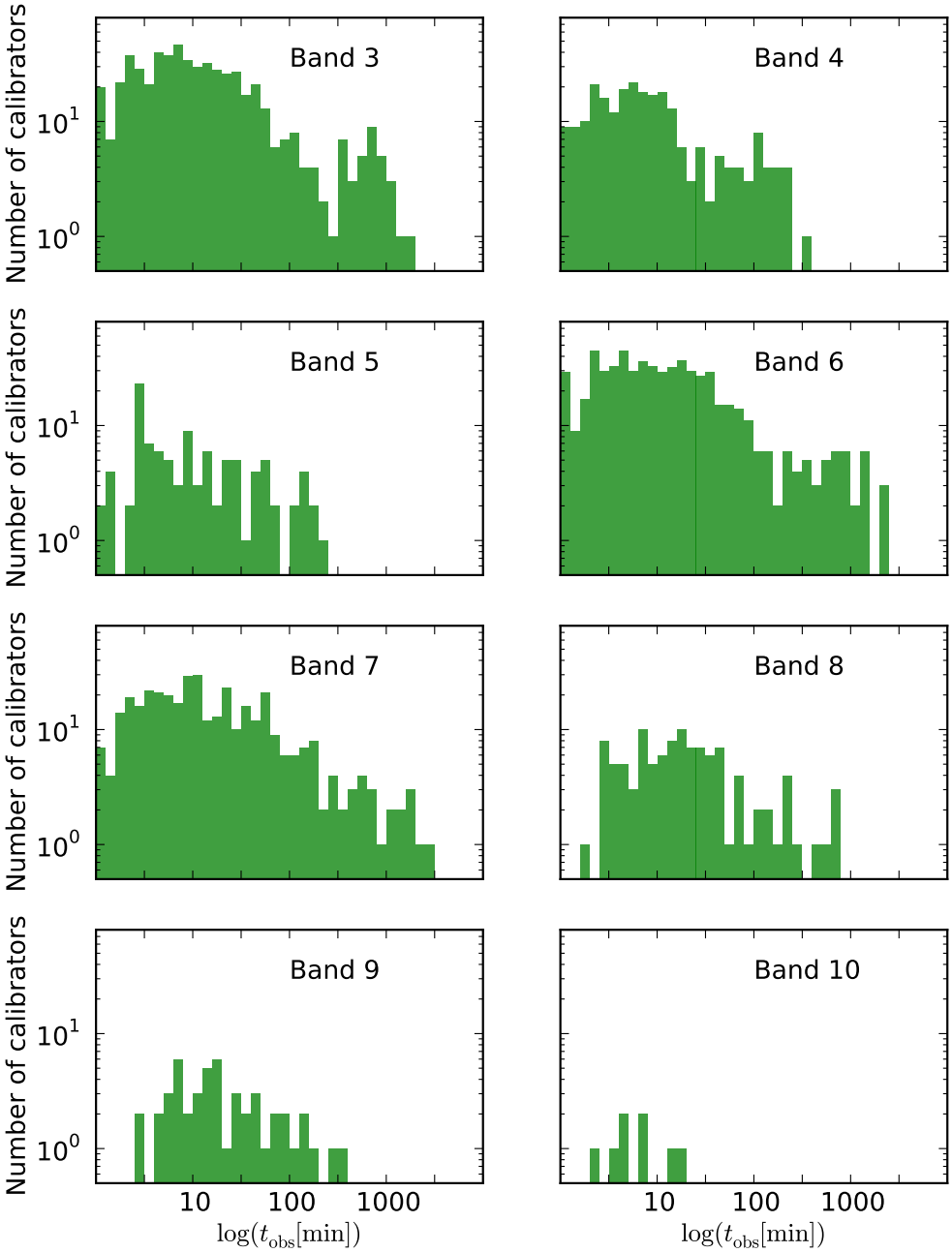

Figure 2.4: Observation time distribution of ALMA calibrator fields per ALMA Band. The most frequently used ALMA Bands with the deepest observations per field are Band 3 and 6. Higher frequency Bands 8, 9 and 10 are observed far less frequently. ALMA Band 5 started operations only in Cycle 5 and therefore also in this Band observations are shallower.

Table 2.1: ALMACAL observing time statistics.

Band	$t_{\mathrm{int\,tot}}$ [h]	#cal	$t_{\mathrm{int\,max}}$ [min]	$t_{\mathrm{int\,mean}}$ [min]	#($t_{\mathrm{int}} > 10$ h)
3	570	590	1611	58	20
4	97	252	344	23	0
5	43	103	202	25	0
6	762	626	2450	73	24
7	558	374	2693	90	15
8	113	109	743	62	3
9	36	49	339	45	0
10	1	8	16	8	0

up to $\sim$ 30 – 45h in Band 3, 6 and 7. Histograms of the observing times per field in the 8 ALMA Bands are shown in Fig. 2.4. We find that the observing time for the bulk of the fields is $\sim$ 10min with an extended tail up to several hours. Overall, we notice that the higher frequency Bands are used less frequently. The first light of Band 5 was only in 2016 and therefore the total observing time in this Band is shorter compared to the other Bands that are available since 2009 – 2013.

The frequency setup for the calibrator observations is usually the same as for the science target, the frequency coverage is varying between the different fields. To perform line searches at specific redshifts this is challenging since the observed frequencies may or may not be the ones required for a specific science goal. In Fig. 2.5 we show the number of calibrators for which more than 10 % of the total ALMA frequency coverage are observed (except Band 5 and Band 10). The same characteristic is shown in Fig. 2.6 split into the 8 ALMA Bands. We find that for a significant number of calibrators more than half of the width of Band 3, 4 and 6 are observed. This offers the opportunity to search for emission lines in the calibrator fields as well as to study the spectra of the calibrators. An example of the frequency coverage for all calibrators is shown in Fig. 2.7. The full list of ALMA calibrators is shown in the appendix A.1.

Since ALMACAL is an ongoing project we use observations up until different dates for the different projects. The details of the different "versions" of ALMACAL and the corresponding projects carried out are listed in Table 2.2.

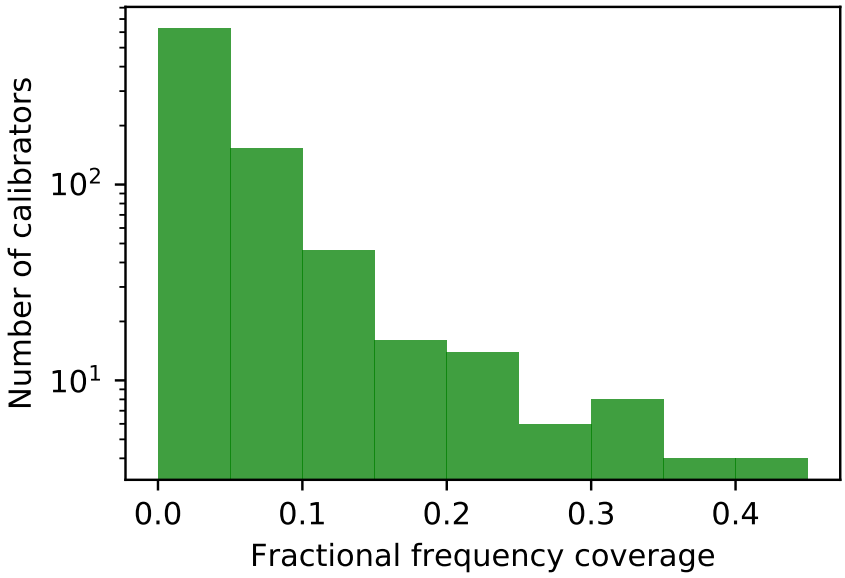

Figure 2.5: Histogram of the proportion of the total ALMA bandwidth (including Band 3, 4, 6, 7, 8 and 9) observed per field. For a large number of calibrators a substantial fraction of the total ALMA observing frequencies is covered making those ideal targets for blind emission of absorption line searches.

Table 2.2: Versions of the ALMACAL survey and the related projects.

No.	processed up to	total # fields	ALMACAL projects
1	July 2015	69	I: Dual Band number counts (Oteo et al., 2016b)
2	March 2017	350	II: High resolution imaging of two z = 3.442 SMGs (Oteo et al., 2017)
3	July 2017	749	III: Study of the neutral, molecular and ionized gas in an absorption-selected galaxy (Klitsch et al., 2018) unpublished: CO emission from absorber host galaxies an unbiased survey (see Section 3) V: Absorption selected galaxies with evidence for excited ISMs (Klitsch et al., 2019)
4	September 2017	754	IV: Catalogue of ALMA continuum observations (Bonato et al., 2018)
5	December 2018	880	VI: blind search for intervening molecular absorbers Klitsch et al. subm. VII: Band 8 number counts Klitsch et al. in prep

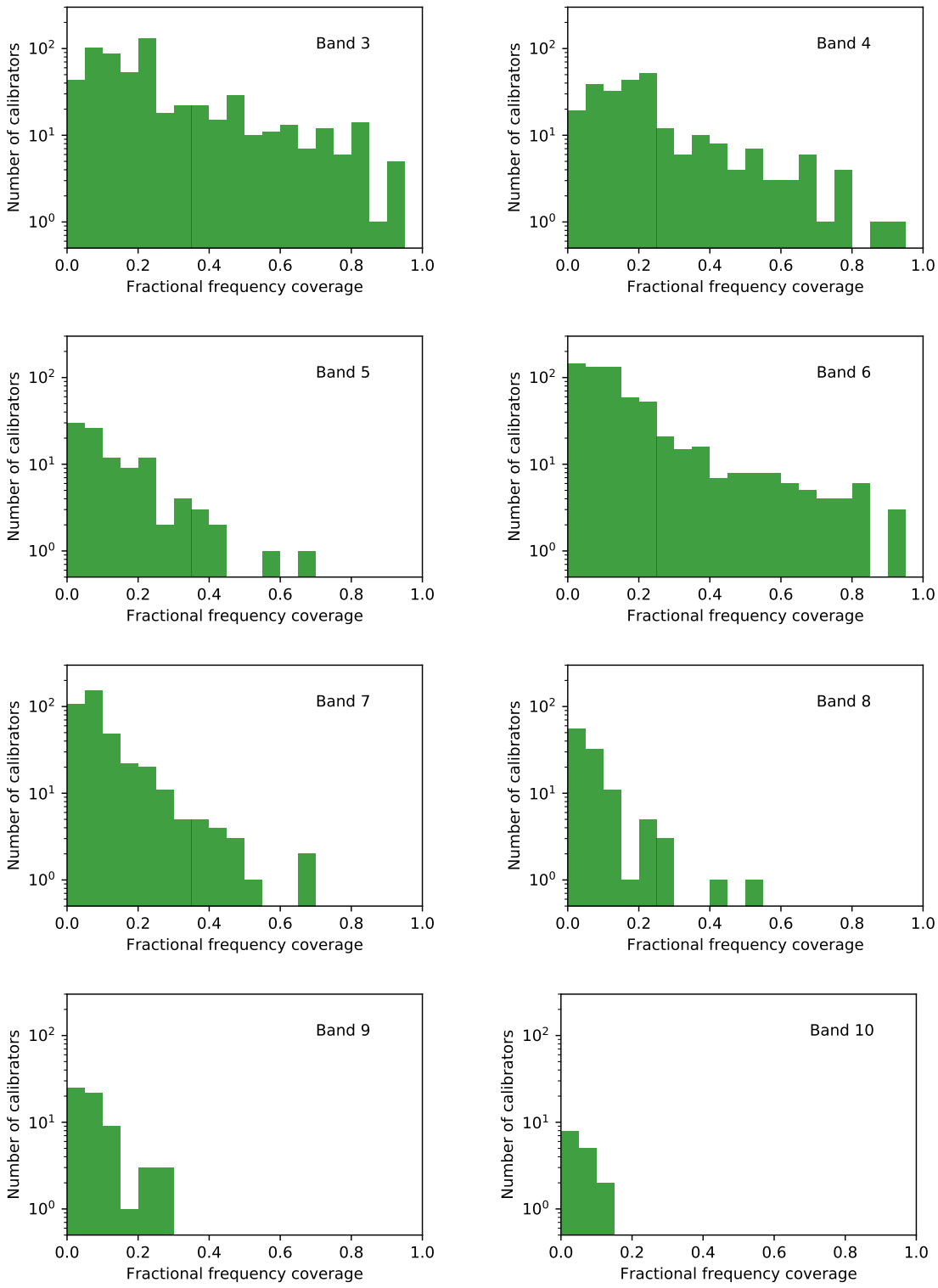

Figure 2.6: Histograms of the number of calibrators as a function of the fraction of the Band covered in ALMACAL. More than half of the total bandwidth of Band 3, 4 and 6 are observed for a large number of calibrators. This makes them ideal targets for blind emission and absorption line searches.

Figure 2.7: An example of the frequency coverage per calibrator. The full figure is shown in the appendix.

2.7 Comparison to Conventional Large Programs and Other Studies

ALMACAL is an efficient way of obtaining a large dataset of ALMA observations. The amount of observing time is more than one order of magnitude higher than that of ordinary Large Programs. However, it is lacking a handle on the observed field, frequency or spatial resolution. We want to showcase the success of dedicated ALMA Large Programs and highlight the differences and similarities between the Large Programs and ALMACAL. An overview of the details of ALMA and VLA major projects with similar science goals is shown in Table 2.3. Here we give a short summary of the projects and the respective science goals.

2.7.1 Conventional Large Programs and Other Studies

ASPECS (pilot and LP): The ALMA SPECtral line Survey in the HUDF was carried out as a pilot study and a Large Program in ALMA cycle 2 and 4, respectively. In the pilot a region of 1 arcmin^2 in the HUDF was observed at high sensitivity. In the Large Program the observations were extended to the whole eXtremely Deep field in HUDF (4.5 arcmin^2). The aim of this program was to search for 1.2 and 3mm continuum detections as well as for low and high redshift CO and [CII] line emitters. The authors published measurements of the continuum number counts (Aravena et al., 2016b) as well as the molecular gas evolution across cosmic time (Decarli et al., 2016, 2019, see Fig. 1.12).

COLDz: The aim of this study is to detect low J CO transitions in high redshift galaxies with the VLA to measure the evolution of the molecular gas mass density over cosmic time. In Riechers et al. (2018) the authors published a high redshift measurement of the cosmic molecular gas mass density (see 1.12).

HUDF: This study is comparable to the ansatz of the ASPECS team. Dunlop et al. (2017) observed the eXtremely Deep Field in the HUDF. The difference between the two studies is that Dunlop et al. (2017) chose to observe a wider field of view at the cost of a shallower depth. The aim was to measure ALMA Band 6 number counts of continuum

Table 2.3: The key properties of comparable ALMA Large Programs and other relevant major telescope projects.

Name	PI	Telescope and cycle	$t_{\rm obs}$ [h]	Area [arcmin^2]	Band	line or cont.	σ [mJy b^{-1}]	Ref.
ASPECS pilot	F. Walter	ALMA 2	40	1	3	both	0.004	Walter et al. (2016)
					6		0.013	Aravena et al. (2016a)
ASPECS	F. Walter	ALMA 4	150	4.6	3 & 6	both		e.g. Decarli et al. (2019)
COLDz	D. Riechers	VLA	122	~ 60	Ka	cont		Pavesi et al. (2018)
HUDF	J. Dunlop	ALMA 1&2	20	4.5	6	cont	0.034	Dunlop et al. (2017)
Lensing	K. Kohno	ALMA 6		88	6	both	0.08	
ALPINE	O. Le Fèvre	ALMA 5	70		7	line		

emitters.

ALMA Lensing Cluster Survey: The goal of this study is to determine the nature of faint submillimetre galaxies and line emitters. This will be achieved by observing 33 lensing clusters which are the best-studied clusters to date with coverage in the HST treasury programs.These observations will probe the origin of the extragalactic background light, measure the [CII] luminosity functions near the Epoch of Reionization, and help to constrain the evolution of the molecular gas mass density up to the peak epoch of cosmic star formation.

ALPINE: ALPINE stands for The ALMA Large Program to INvestigate CII at Early times. The aim of this project is to study mechanisms that fuel the initial growth of galaxies and the ISM properties of galaxies in the early universe. This will be achieved by measuring the CII and FIR continuum emission from 122 known main sequence star-forming galaxies at redshifts of $z = 4.4 - 5.9$.

2.7.2 Number Counts of Dusty Star-Forming Galaxies in ALMACAL

We give an overview of the dual band number counts from Oteo et al. (2016b) and the detailed study of the two SMGs in the field of J1058+0133 as examples of the capabilities of ALMACAL.

The cosmic SFH is well-established at low redshift. At high redshift, however, the slope of the SFH is not well constrained. As shown in Fig. 1.13, it is currently not possible to constrain the amount of dust in the early universe from the available observations. It is therefore crucial to expand the number of SFR measurements at high redshift.

To measure the influence of dust in the early universe a tool commonly used are cumulative number counts of DSFGs, the number of galaxies above a given flux limit at a given observed frequency per deg^2. Models of galaxy evolution attempt to match these number counts at different frequencies.

In a pilot study Oteo et al. (2016b) have shown the power to constrain cumulative number counts of DSFGs with ALMACAL. Example detections are shown in Fig. 2.8. The derived cumulative number counts are shown in Fig. 2.9. The number counts are lower

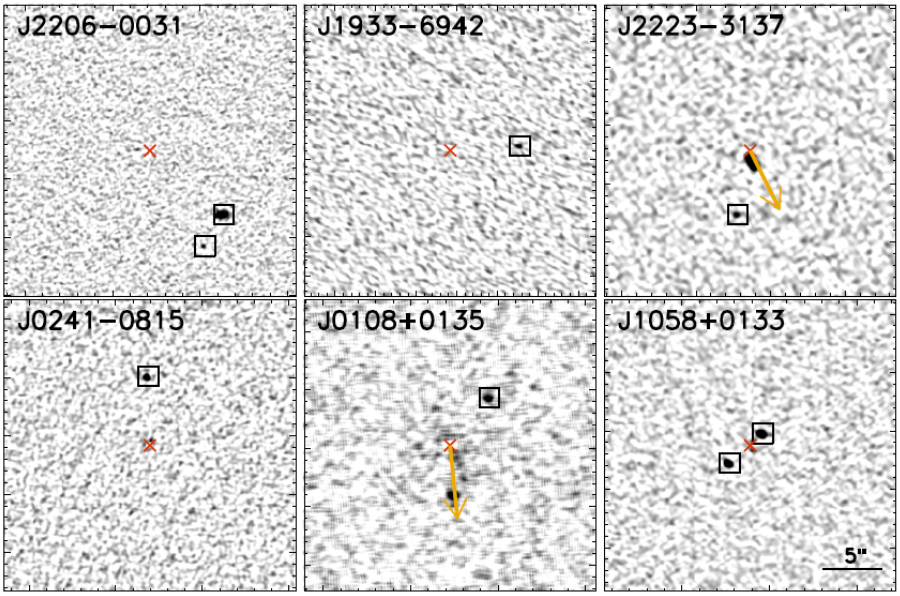

Figure 2.8: ALMA Band 6 (1.2 mm) images of the dusty star-forming galaxies detected in ALMACAL, reproduced from Oteo et al. (2016b). The position of the detection is marked by a black square, the position of the subtracted calibrator is marked by a red cross. Jets emanating from the quasar are marked by yellow arrows. We can identify jets via simultaneously available Band 3 (3 mm) imaging.

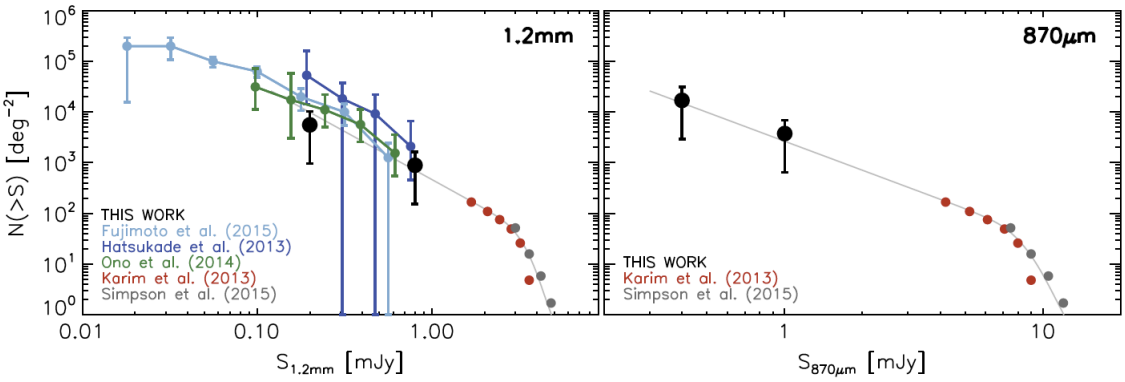

Figure 2.9: Cumulative number counts of DSFGs in ALMACAL Band 6 (left) and 7 (right) (Oteo et al., 2016b).

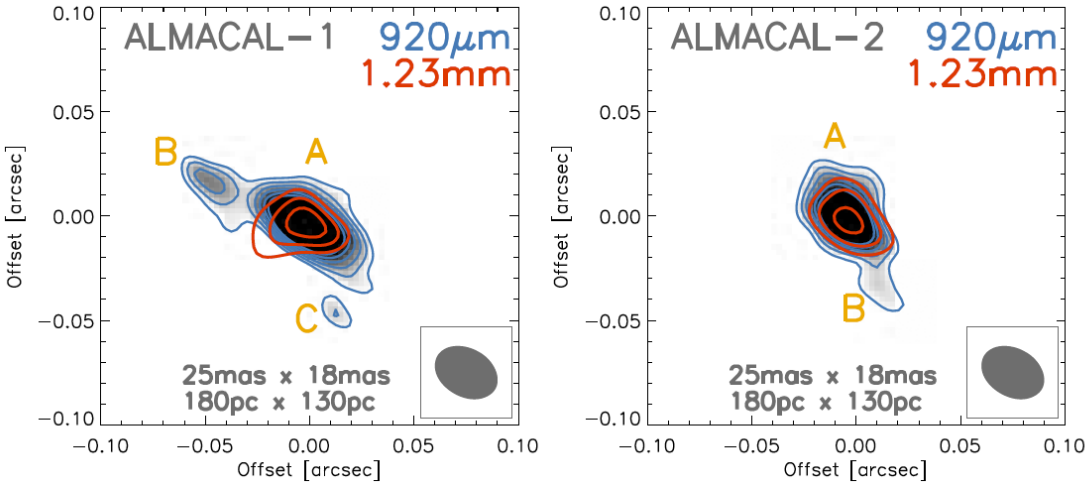

Figure 2.10: High resolution imaging of the two SMGs in the field of J1058+0133.

than derived from previous studies (Hatsukade et al., 2013; Ono et al., 2014; Fujimoto et al., 2016). This might be due to different observing strategies, as well as differences in the detection thresholds. Previous works observe mostly overdensities and tend to choose low detection thresholds, which increases the number of detections at the price of risking a higher contamination from spurious detections. This would artificially increase the observed number counts.

In summary this early work proved the possibility to detect even faint DSFGs in ALMACAL. Oteo et al. (2016b) detected 8 and 11 DSFGs in Band 6 and 7, respectively. Among these six were detected in Band 6 and Band 7. The average population of DSFGs traced in this study is fainter than the typical SMGs detected in single dish observations and would have been missed also in the deepest *Herschel* extragalactic surveys. The number counts derived by Oteo et al. (2016b) are lower than those previously reported.

In Oteo et al. (2017) the authors have undertaken a detailed study of the two SMGs in the field of the calibrator J1058+0133 presented by Oteo et al. (2016b) including all available ALMACAL data. The authors have used the high resolution imaging revealing multiple-clumps of star formation (see Fig. 2.10). Furthermore, it was possible to detect multiple ^{12}CO and H_2O emission lines ($z = 3.442$). All star-forming clumps have extremely high star formation rate surface densities of up to $\sim 6000 M_\odot$ yr^{-1} kpc^{-2}.

These project highlight the possibility to study statistical samples of submillimetre galaxies using ALMACAL. The total area probed in this early work was 16/6 arcmin^2

in ALMA Band 6/7. Today (June 2019) the survey area of ALMACAL increased to 80/50/24/3 arcmin^2 in Band 4/6/7/8. This is comparable or larger than many dedicated science observations listed in Table 2.3. We have shown that the total observation time in some fields that amount up to 30 – 45h in Band 3, 6 and 7. This is comparable or even exceeding that in the dedicated science observations. A caveat though is that non-uniform usage of the calibrators resulting in varying noise levels per field.

As shown in Fig. 2.6, a substantial number of calibrator fields are observed in more than half of the frequency range in Band 3, 4 and 6. In such cases it is possible to perform line searches as presented by Oteo et al. (2017). Such fields can be used for projects similar to some of the dedicated science observations. ALMACAL is an innovative way of using archival data. The number of observations per field will continue to grow as long as ALMA is operational.

Chapter 3

Molecular Gas in Absorber Host Galaxies

The first project using ALMACAL focuses on the detection of CO emission from absorption-selected galaxies presented in Chapter 1.3. As outlined in that Chapter, the identification of absorber host galaxies has been challenging. Only recently a new perspective on absorption-selected galaxies opened up by observing the molecular gas content of these galaxies or indeed by identifying the galaxies by their molecular gas content (Neeleman et al., 2016, 2017; Kanekar et al., 2018; Møller et al., 2018; Fynbo et al., 2018a; Klitsch et al., 2018, 2019; Neeleman et al., 2019). Current samples are high-metallicity absorbers and therefore likely introduce a bias towards high-mass galaxies (e.g. Krogager et al., 2018). Surveys for molecular gas in absorber host galaxies targeting high column density and high metallicity absorbers yielded high detection rates. Results based on the limited sample, indicate that absorption-selected galaxies at intermediate redshifts have a lower star formation efficiency than emission-selected galaxies at high ($z \sim 1-2$) and low ($z \sim 0$) redshift (Kanekar et al., 2018).

Motivated by these early studies, we decide to follow a complementary approach of selecting absorbers regardless of the absorption properties. Our aim is to study the underlying population of absorption-selected galaxies in an unbiased way. A representative sample of absorption-selected galaxies will be key to gain insights in gas flows and the baryon cycle.

3.1 Sample Selection

The aim of this work is to identify and characterize galaxies connected to intervening quasar absorbers with a particular focus on the molecular gas content of the host galaxies. We have performed a cross-matching of ALMACAL quasars with previously identified absorbers in the optical, regardless of HI column density or metallicity. Here, we use the 749 quasar fields observed up until July 2017 (ALMACAL version July 2017).

To select possible targets, we first create a non exhaustive list of known intervening absorbers from catalogues of Lyα absorbers with a column density of $16 \leq \log[N(\mathrm{HI})/\mathrm{cm}^{-2}] \leq 22.35$ published by Péroux et al. (2003b), Prochaska et al. (2005), Rao et al. (2006), Prochaska et al. (2008), Guimarães et al. (2009), Noterdaeme et al. (2009), Prochaska et al. (2010), O'Meara et al. (2011), Noterdaeme et al. (2012), Fumagalli et al. (2013), Zafar et al. (2013), Noterdaeme et al. (2014), and Turnshek et al. (2015). Furthermore, we use the strong metal line absorbers identified in a sample of $\sim 10^5$ quasar spectra from the Sloan Digital Sky Survey (SDSS) DR7 (Zhu & Ménard, 2013). We perform a coordinate based query in the Simbad database for DLAs ($N(\mathrm{HI}) \geq 2 \times 10^{20}$atoms cm^{-2}), subDLAs (10^{19}atoms cm^{-2} $< N(\mathrm{HI}) < 2 \times 10^{20}$atoms cm^{-2}), and metal absorption lines where we use the positions of all ALMA calibrators included in ALMACAL. The Simbad query provides new systems that were not part of the larger surveys listed above and metal line absorbers without known HI column densities. The resulting cross-matched list contains 108 absorbers towards 49 quasars that are part of ALMACAL and which have between one and eight unique intervening absorbers. Out of these 108 known absorbers 57 absorbers towards 26 quasars were observed at a frequency range covering one or more CO emission lines. These absorbers are listed in Table 3.3. The redshift range of the intervening absorbers is $0.06 < z < 3.0$. We define unique absorbers as absorbers with a separation of less than 1000 km s^{-1} or 0.005 in redshift.

To study the molecular gas content of galaxies first identified by an intervening absorber at an optical wavelength we are at this stage mainly interested in the CO emission lines, because these are bright tracers of the molecular gas that can be observed at $z \leq 1$. Therefore, we match the available frequency coverage from ALMACAL with the expected CO rotational transition frequency redshifted to the respective absorber redshift. We identify a sample of quasars with one or more known absorbers, for which one or more

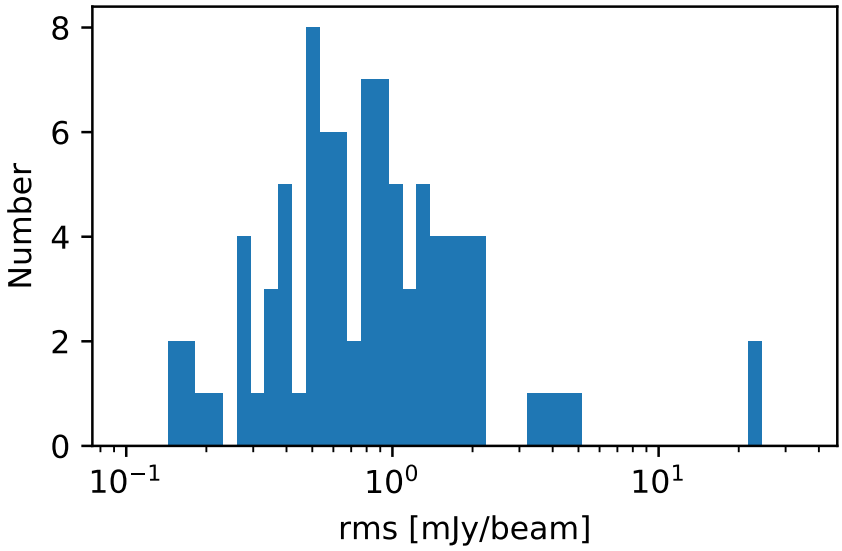

Figure 3.1: Distribution of the channel rms noise in the 93 image cubes used to search for CO emission in the absorber host galaxy.

CO transition is covered by the ALMACAL data.

3.2 ALMACAL Data Reduction

The imaging of the calibrator-subtracted visibility data is carried out using the Common Astronomy Software Applications (`CASA`) software package version 4.7.0. The *uv*-datasets for one calibrator covering a specific line are concatenated using the task `CONCAT`. We use the task `CLEAN` to image the data. A natural weighting scheme is applied to the visibilities ensuring a maximum signal-to-noise ratio. We assume that the typical extent of the molecular gas is < 1 kpc. Thus, for the detection experiment, we apply to the visibility data an outer taper of 1 kpc at the absorber redshift in order to at most marginally resolve the emission. We define a cleaning window with a size of 1.5 times the FWHM of the primary beam of the respective Band.

In the resulting cubes, we reach a median rms noise level of 0.8 mJy beam^{-1} per channel, the maximum and minimum rms noise levels are 33 mJy beam^{-1} and 0.3 mJy beam^{-1}. A histogram of the channel rms noise in all image cubes is shown in Fig. 3.1. The angular resolution ranges between 0.22" and 11" with a median of 0.87". This converts to 0.6 kpc to 72 kpc and a median of 3.7 kpc at the respective absorber

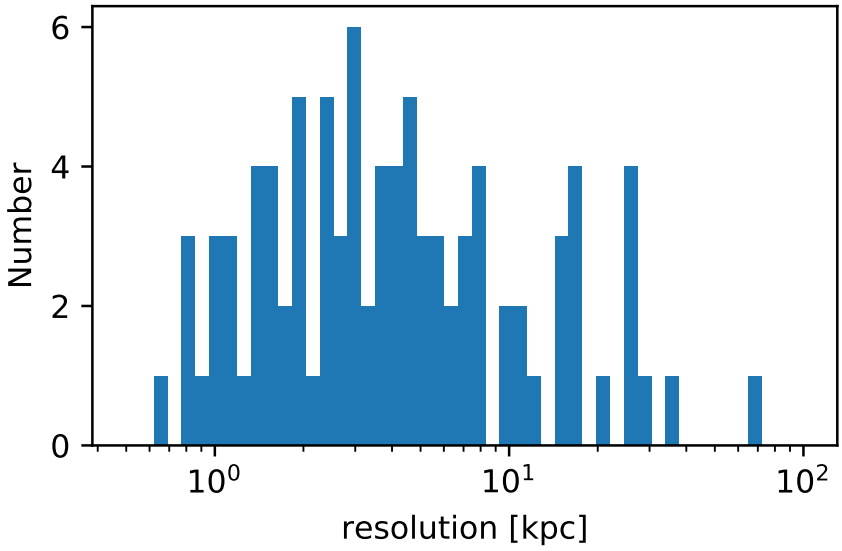

Figure 3.2: Distribution of the spatial resolution in kpc (at the corresponding absorber redshift) of the 93 image cubes used to search for CO emission in the absorber host galaxy.

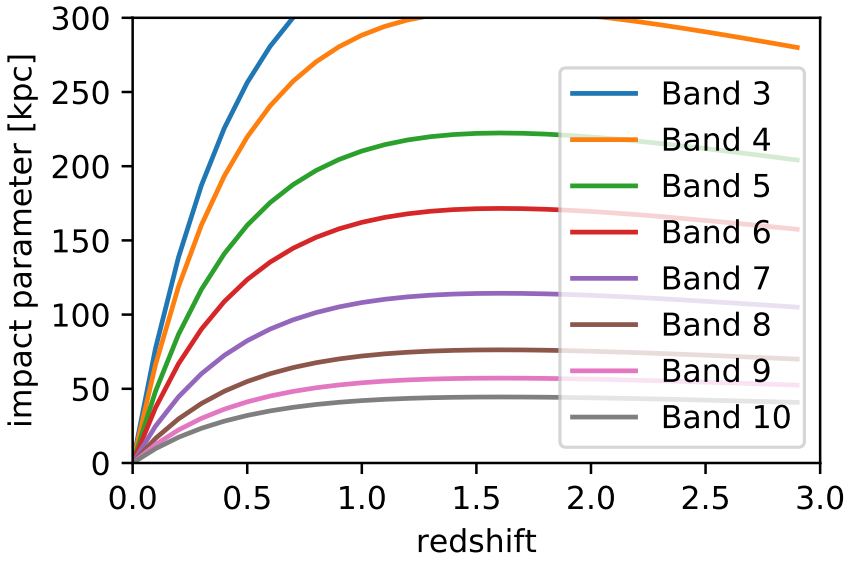

Figure 3.3: Search radius for CO emission from absorber host galaxies in ALMACAL in kpc in the different Bands as a function of redshift. The diameter of the field in which we search for emission is defined as 1.5× the FWHM of the ALMA primary beam. At $z < 0.3$ a limitation is introduced due to the limited field of view at high frequencies. At low frequencies the field of view even covers impact parameters of 300 kpc, which is the typical maximum size of the CGM in groups (Bordoloi et al., 2011).

redshift. A histogram of the resolution in kpc is shown in Fig. 3.2.

The integration time and therefore the depth of the observations at a particular frequency varies from field to field. Here we search for emission within a velocity range of ± 1000 km s^{-1}. Since we are combining all available data for a given ^{12}CO transition regardless whether the data covers the full velocity window or not, the resulting data cubes can have a varying resolution and rms noise as a function of frequency. Such cubes are cut to ensure uniform resolution and noise per cube.

The primary beam size varies as a function of observed frequency. In Fig. 3.3, we show the expected search radius as a function of redshift for all ALMA receiver bands. At $z \lesssim 0.3$ and for high frequency observations we note that we are sensitive to the impact parameters smaller than the typical CGM size in groups, which can have radii up to 300 kpc (Bordoloi et al., 2011).

3.3 CO Emitter Search at the Absorber Redshifts

The aim of this project is to identify ^{12}CO line emission from galaxies associated with known absorbers. We use the DUCHAMP source finder (Whiting, 2012) to identify emission lines in the data cubes.

This source finder has a wavelet reconstruction method implemented that reconstructs the low spatial frequency features of the cube and removes the high spatial frequency noise in the data cube. We use the default parameters for the wavelet reconstruction and apply a reconstruction threshold of 2.5 σ. Channels that are flagged in the data cube are masked for the emission line search. Finally a SNR threshold of 2.5σ is applied for an initial source detection. The noise level is determined as the median absolute deviation from the median for the entire cube. We keep all other input parameters at their default values.

Additionally to the wavelet reconstruction described above, we perform a second round of source finding using the smoothing option in DUCHAMP. Since the channel width in the input cubes is varying we use a 3, 5, 7 and 9 channels wide kernel for the Hanning smoothing.

We select CO emission-line candidates by comparing the physical parameter space

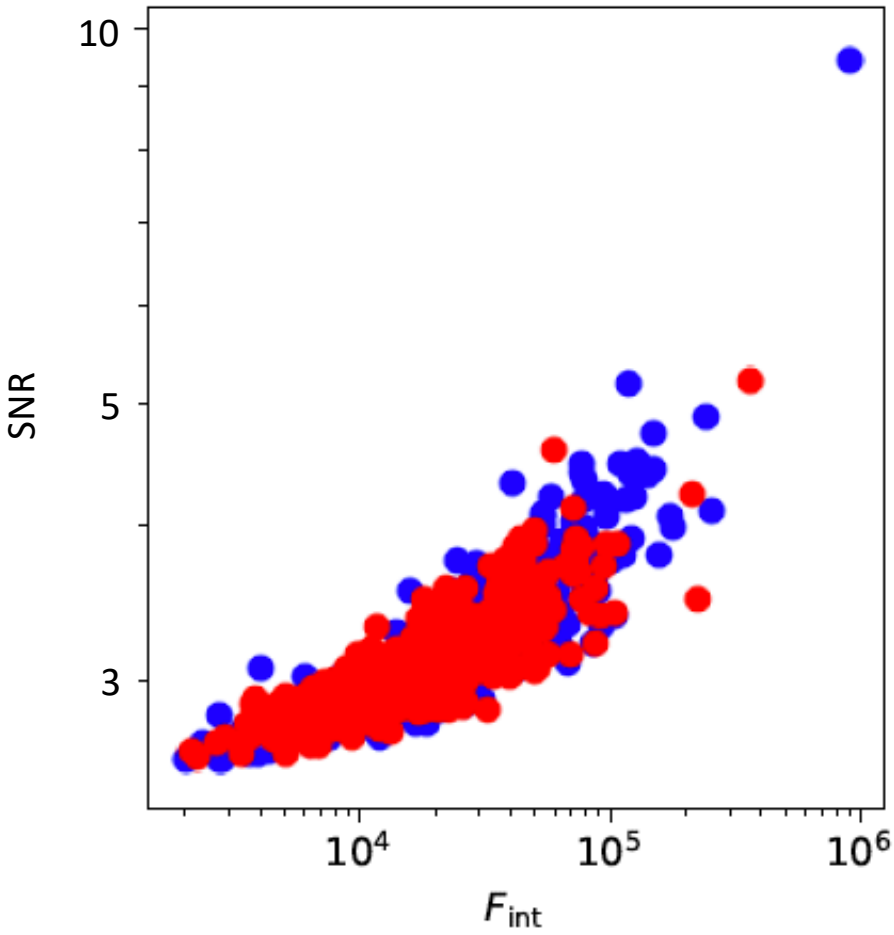

Figure 3.4: An example of the diagnostic plot used to identify CO line emitter candidates at the absorber redshift. We compare the detection in the positive (blue) and negative (red) image cube in the SNR vs. integrated flux (in arbitrary units) plane.

Table 3.1: Summary of the detected single CO emission lines for our sample of absorption-selected CO emitters. The molecular gas mass is calculated assuming conversion factors appropriate for the Milky Way (Carilli & Walter, 2013).

QSO name	z_{abs}	$\log(N_{HI})$	other abs lines	CO trans.	F_{int} [Jy km s^{-1}]	w_{50} [km s^{-1}]	M(H_2) [$\times 10^{10} M_\odot$]	Ref.
J1229+0203	0.029	13.55	OVI, CIII	2-1	0.24 ± 0.04	~ 80	$(2 \pm 0.3) \times 10^{-3}$	Sembach et al. (2001)
J1415+1320	0.247	22.3	OH, HCO+	3-2	4 ± 2	~ 50	2 ± 1	Kanekar et al. (2002)
J1415+1320	0.247	22.3	OH, HCO+	3-2	3 ± 1	~ 50	1.6 ± 0.5	Kanekar et al. (2002)
J0635–7516	0.417		HI, SiIII	3-2	1.1 ± 0.6	~ 150	1.7 ± 1.0	Jannuzi et al. (1998)
J2148+0657	0.791	18.43	MgII, FeII	5-4	0.6 ± 0.2	~ 100	4 ± 1	Tappe & Black (2004)
J0125–0005	0.953		OIV, CIV	5-4	0.5 ± 0.1	~ 120	5 ± 1	Bahcall et al. (1996)
J0217+0144	1.254		HI, CIV	2-1	3 ± 1	~ 260	50 ± 20	Blades et al. (1985)
J1150–0023	1.986		CIV	9-8	1.2 ± 0.5	~ 100		Sargent et al. (1988),
J0108+0135	2.098		CIV	3-2	0.59 ± 0.07	~ 150	22 ± 2	Vestergaard (2003)
J1007+1356	2.592		SiII, CII,	7-6	0.4 ± 0.1	~ 50		Lanzetta et al. (1991)
J1007+1356	2.592		*CIV, AlII	7-6	0.8 ± 0.4	~ 100		Lanzetta et al. (1991)

Table 3.2: Summary of the detected multiple CO emission lines for our sample of absorption-selected CO emitters. The Galaxies listed in this table are presented separately in Chapter 4 and 5.

QSO name	z_{abs}	$\log(N_{HI})$	other abs lines	CO trans.	F_{int} [Jy km s^{-1}]	w_{50} [km s^{-1}]	$M(H_2)$ [$\times 10^{10} M_\odot$]	Ref.
J0423–0130	0.633	18.54	MgI, MgII, FeII	2-1	3.6 ± 0.2	590 ± 30	2.1 ± 0.1	Chapter 4
				3-2	5.2 ± 0.3	610 ± 40		
J0238+1636	0.5253	21.70	MgI, MgII, FeII, MnII	2-1	0.32 ± 0.06	350 ± 20	0.13 ± 0.02	Chapter 5
				3-2	0.70 ± 0.09	380 ± 40		
				4-3	1.2 ± 0.4	420 ± 30		
J0238+1636	0.5253	21.70	MgI, MgII, FeII, MnII	2-1	0.2 ± 0.05	350 ± 40	0.08 ± 0.02	Chapter 5
				3-2	0.43 ± 0.04	380 ± 40		
				4-3	< 0.9			

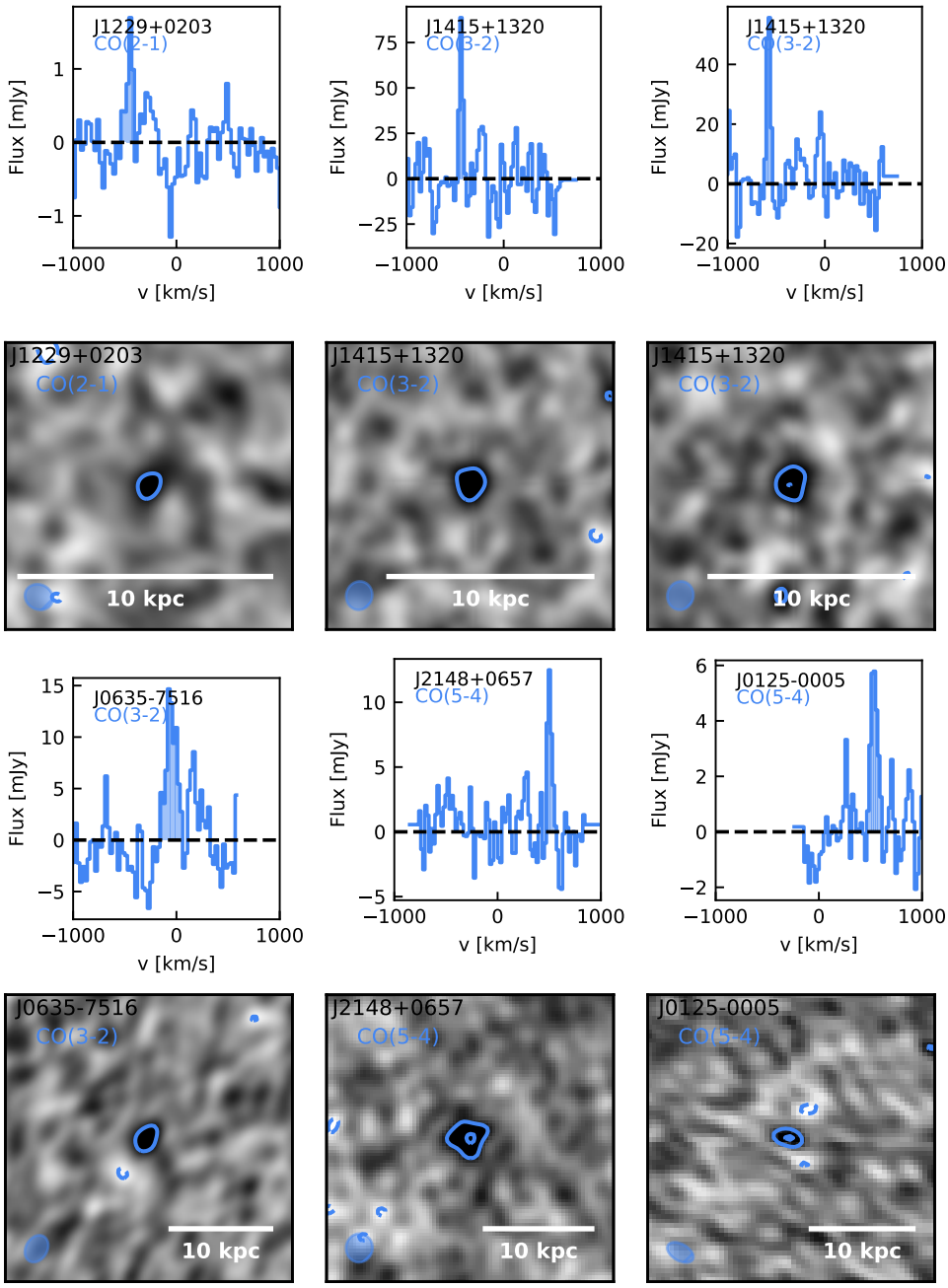

Figure 3.5: Spectra and integrated flux maps of an unbiased sample of CO emission from absorption-selected systems with only one CO emission line detected. The sample resulted from a search in 109 quasar fields with known absorbing systems. The contours mark the $3, 4, 5\sigma$ levels in the maps. Once confirmed by a second CO transition this will double the total number of absorption-selected galaxies with known molecular gas mass as well as a measurement of the ISM conditions. Detections of multiple CO transitions are presented in Chapter 3 and 4.

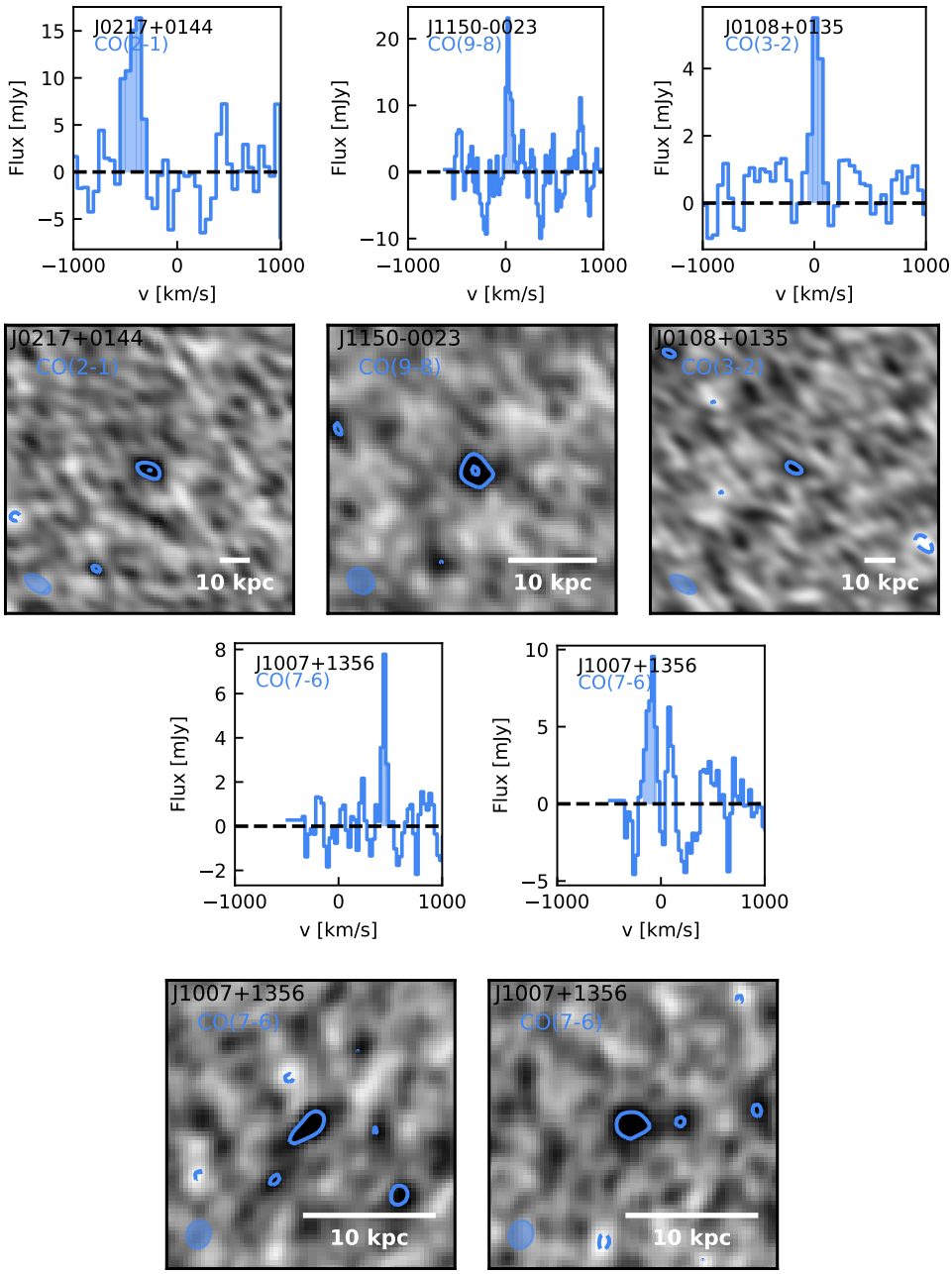

Figure 3.6: Fig. 3.5 continued.

covered by the detections in the data cube and the inverted datacube. Detections in the inverted data cube are expected to be false positive detections. We assume that by applying low thresholds we probe a significant fraction of the physical parameter space covered by pure noise detections. Emission-line candidates are chosen from the integrated flux vs. peak SNR plane (see Fig. 3.4). The spectra and integrated flux density maps of outliers in the peak SNR and integrated flux are visually inspected separately by several people (AK, CP, MZ). This results in the detection of three galaxies with multiple CO lines detected and eleven galaxies with only one CO transition detected. The properties of the CO detections are listed in Table 3.1 and 3.2, spectra and integrated intensity maps of single line detections are shown in Fig. 3.5. The CO detections with multiple J transitions are analysed in more detail in Chapter 4 and 5. We find that all single line detections have a FWHM of $100 - 300$km s^{-1}, lower than the FWHM of the CO emission lines from galaxies with multiple transitions.

3.4 Summary

We conduct a blind search for CO emission from absorption-selected galaxies using the ALMACAL database version July 2017. We identify 57 known absorbers towards 26 ALMA calibrators that have been observed at a frequency at least partially covering at least one CO line at the absorber redshift.

The absorbers covered in this study are not pre-selected by HI column density or metallicity. We make use of the ALMACAL database putting no constraints on the absorption properties. Furthermore, observations sometimes cover only part of the expected velocity range of absorber host candidates. A statistical analysis of the sample is beyond the scope of this detection experiment. The goal of this survey is to benefit from the available data.

We find eleven single line emission candidates and three galaxies detected in multiple CO emission lines. The three multi-line detections are subject to further analysis presented in Chapter 4 and 5. The remaining eleven candidates have no counterpart at other wavelengths. Furthermore, these candidate emission lines have FWHMs of $100 - 300$km s^{-1}, smaller than the FWHM of CO lines in galaxies detected in multiple

lines. We note that single-line detections at a significance of $\geq 6\sigma$ presented in the literature turned out to be false detections in deeper follow-up observations (Hayatsu et al., 2019). Therefore, we conclude that we need follow-up observations of the eleven candidate emission lines before drawing further conclusions.

We have submitted an ALMA cycle 7 follow-up proposal to confirm these absorber host galaxy candidates by observing a second CO transition. This will also yield the first systematic measurements of the CO SLEDs from an unbiased sample of absorption-selected galaxies.

3.5 Appendix

Table 3.3: ALMA calibrators with known absorbers.

Name	Ra	Dec	$z_{\rm abs}$	$z_{\rm QSO}$
J0051–4226	00h51m09.5084s	–42d26m33.342s	1.483	1.749
J0108+0135	01h08m38.8s	+01d35m00s	2.0983	2.099
J0125–0005	01h25m28.8438s	–00d05m55.933s	0.9531	1.07454
			0.9667	
J0217+0144	02h17m48.9547s	+01d44m49.699s	1.2542	1.715
			1.345	
			1.491	
			1.55	
			1.644	
			1.649	
			1.6855	
			1.719	
J0238+1636	02h38m38.9301s	+16d36m59.274s	0.5253	0.94
			0.852	
J0423–0120	04h23m15.8007s	–01d20m33.065s	0.6331	0.915
J0440–4333	04h40m17.1729s	–43d33m08.619s	2.347	2.852
J0457–2324	04h57m03.1792s	–23d24m52.019s	0.606	1.003

. . . Table 3.3 continued.

Name	Ra	Dec	z_{abs}	z_{QSO}
			0.752	
J0501–0159	05h01m12.8098s	–01d59m14.256s	1.999	2.285998
			2.02	
			2.028	
			2.04	
			2.069	
			2.089	
			2.204	
J0635–7516	06h35m46.5144s	–75d16m16.74s	0.152	0.651
			0.4168	
J0909+0121	09h09m10.089s	+01d21m35.6111s	0.535778	1.024
J1007+1356	10h07m41.4981s	+13d56m29.6s	1.045	2.72115
			2.592	
J1112+3446	11h12m38.771s	+34d46m39.0455s	1.44265	1.953
J1118+1234	11h18m57.3018s	+12d34m41.717s	1.949	2.12528
			1.9768	
			2.1279	
J1130–1449	11h30m07.0473s	–14d49m27.424s	0.313	1.187
			0.382	
J1145+0455	11h45m21.3151s	+04d55m26.687s	1.343	1.34133
J1150–0023	11h50m43.8712s	–00d23m54.218s	1.4669	1.97956
			1.9861	
J1229+0203	12h29m06.6951s	+02d03m08.662s	0.00338	0.158339
			0.00526	
			0.02947	
			0.04898	
			0.06655	
			0.09012	
			0.12007	

. . . Table 3.3 continued.

Name	Ra	Dec	z_{abs}	z_{QSO}
			0.1466	
J1331+3030	13h31m08.2956s	+30d30m32.9015s	0.692	0.85
J1357–1744	13h57m06.0661s	–17d44m01.696s	3.00694	3.147
J1415+1320	14h15m58.8175s	+13d20m23.713s	0.24671	0.2467
J1707+0148	17h07m34.4153s	+01d48m45.698s	2.1888	2.576
J1833–2103	18h33m39.871s	–21d03m39.78s	0.192	2.51
			0.88582	
J2148+0657	21h48m05.4586s	+06d57m38.604s	0.7908	0.99
J2225–0457	22h25m47.2592s	–04d57m01.39s	0.4925	1.404
			0.702	
J2253+1608	22h53m57.7479s	+16d08m53.561s	0.1538	0.859001

Chapter 4

A Combined ALMA and MUSE Survey for Neutral, Molecular, and Ionised Gas in an HI-Absorption-Selected System

Abstract

As outlined in Chapter 1, studying the flow of baryons into and out of galaxies is an important part of understanding the evolution of galaxies over time. In this chapter we present a detailed case study of the environment around an intervening Ly α absorption line system identified in Chapter 3. It is seen towards the quasar J0423−0130 ($z_{\rm QSO}$ = 0.915, $z_{\rm abs}$ = 0.633). We detect with ALMA the ^{12}CO(2–1), ^{12}CO(3–2) and 1.2 mm continuum emission from a galaxy at the redshift of the Ly α absorber at a projected distance of 135 kpc. From the ALMA detections, we infer ISM conditions similar to those in low redshift Luminous Infrared Galaxies. DDT MUSE integral field unit observations reveal the optical counterpart of the ^{12}CO emission line source and three additional emission line galaxies at the absorber redshift, which together form a galaxy group. The ^{12}CO emission line detections originate from the most massive galaxy in this group. While we cannot exclude that we miss a fainter host, we reach a dust-uncorrected star-formation rate (SFR) limit of > 0.3 $M_\odot$ yr^{-1} within 100 kpc from the sight line to the background quasar. We measure the dust-corrected SFR (ranging from 3 to 50 $M_\odot$ yr^{-1}), the morpho-kinematics and the metallicities of the four group galaxies to understand the relation between the group

and the neutral gas probed in absorption. We find that the Ly α absorber traces either an outflow from the most massive galaxy or intra-group gas. This case study illustrates the power of combining ALMA and MUSE to obtain a census of the cool baryons in a bounded structure at intermediate redshift.

4.1 Introduction

A key part of understanding the evolution of galaxies is to determine how gas is accreted onto galaxies and how it is exchanged with their surroundings via outflows. Since ultimately the respective evolutions of gas, stars, and metals are connected through the stellar life cycle, gas flows have an immediate impact on the history of star formation and the chemical enrichment. Inflows of pristine gas might dilute the metal content of galaxies and certainly fuel their star formation, whereas outflows take away the metals, chemically enriching the circum-galactic medium (CGM). High column density gas lying along a quasar line of sight is an ideal tool to study the CGM. These gas clouds characterized by Ly α or metal absorption profiles can probe not only a static CGM, but also flows of gas through the halo. To obtain a full picture of the CGM and its interplay with galaxies, it is important to study the location, kinematics, and metallicity of both the absorbing gas and the nearby galaxy.

Using integral field spectroscopy it is possible to efficiently identify galaxies at the redshift of absorbers as well as determine their star-formation rate (SFR), kinematics and metallicity (e.g. Bouché et al., 2007; Péroux et al., 2011; Jorgenson & Wolfe, 2014; Péroux et al., 2017). Interestingly, recent studies have shown that the identification of the Ly α absorber host galaxy is not always unique. In some cases, the absorber can be linked to one galaxy, but in other cases, it is associated with intra-group gas (Whiting et al., 2006; Kacprzak et al., 2010; Gauthier, 2013; Bielby et al., 2017; Fumagalli et al., 2017; Péroux et al., 2017; Rahmani et al., 2018).

Recent studies have shown that the CGM extends to at least 100 kpc for isolated galaxies (Prochaska et al., 2017) and 140 kpc in groups of galaxies (Bordoloi et al., 2011). These distances convert to a radial angular extent of $\sim 20''$ at intermediate redshifts of $z \sim 0.5$ requiring a large field of view integral field unit such as MUSE to cover the full

potential extent of the CGM.

Large surveys aiming to understand the connection between absorption line systems and their host galaxies either use galaxy-quasar pairs searching for absorption from the known galaxy in the quasar spectrum (e.g. Tumlinson et al., 2013) or target known absorbers and search for the associated galaxies using integral field spectroscopy (e.g. Schroetter et al., 2016; Bielby et al., 2017; Fumagalli et al., 2017; Péroux et al., 2017; Rahmani et al., 2018). Outflows are frequently observed at all redshifts (e.g. Rupke et al., 2005; Veilleux et al., 2005; Tremonti et al., 2007; Weiner et al., 2009) while direct observations of inflows are less commonly found (e.g. Martin et al., 2012; Bouché et al., 2013), possibly because they are more difficult to observe.

A completely new perspective is opened by studying the molecular gas of the Ly α absorber host galaxy traced by ^{12}CO emission lines. Recently, Neeleman et al. (2016) reported the first detection of ^{12}CO(1-0) emission from such a host galaxy at $z = 0.101$. Moreover, the combination of ^{12}CO emission line detections with IFS, potentially allows us to get a complete census of the stars and the cool gas in such systems. This is the next important step towards a better understanding of such systems and therefore the flow of baryons through galaxies.

In our (sub)mm survey ALMACAL version July 2017 presented in Chapter 2, we detect additionally to the eleven single CO emission line detections for the first time multiple ^{12}CO transitions from two galaxies first identified as intervening absorbers. Here we focus on the absorber towards the quasar J0423−0130 ($z_{\rm QSO} = 0.915$, $z_{\rm abs} = 0.633$. We have obtained additional MUSE observations revealing a group of four galaxies at the absorber redshift, where one of these is coincident with the ^{12}CO emission seen in the ALMA observations. The immediate aim of this study is to identify the origin of the absorption seen towards the quasar. In a broader perspective, this system serves us as a reference system to demonstrate the need for a multi-wavelength study of intervening absorbers and their environment.

This chapter is organized as follows: In Section 4.2 we describe our dataset from the ALMA archive, the new MUSE observations, the ancillary archival data and previous work. We describe the source detections and measurements from the ALMA and MUSE observations, the broad-band photometry based on archival data, and the analysis of the

measurements in Section 4.3. In Section 4.4 we discuss possible scenarios explaining the absorption. A summary and the conclusions are given in Section 4.5. Throughout the chapter, we adopt an $H_0 = 70$ km s^{-1} Mpc^{-1}, $\Omega_M = 0.3$, and $\Omega_\Lambda = 0.7$ cosmology.

4.2 Observations and Data Reduction

The aim of this work is to identify and characterize galaxies connected to the intervening quasar absorber with a particular focus on the molecular gas content of the host galaxies.

As discussed in Chapter 3, we have identified a particular absorber at $z = 0.633$ towards the quasar J0423−0130 (04h23m15.8s −01d20m33s, $z = 0.915$) from our parent sample. The absorber is a Lyman Limit System with an HI column density of $\log(N(\mathrm{HI})/\ \mathrm{atoms\ cm^{-2}}) = 18.54^{+0.07}_{-0.10}$. This source is chosen for our pilot study, because we detect two ^{12}CO emission lines in our ALMACAL data. We have obtained MUSE PI DDT follow-up observations of the field. We show that combining these two datasets with other ancillary data yields a more complete picture of such systems.

4.2.1 ALMACAL

The data used in this work are taken from the ALMACAL survey. The characteristics of the survey and the details of the data reduction are presented in Chapter 2.

In the ALMACAL version July 2017 the quasar J0423−0130 was observed four times at frequencies corresponding to possible ^{12}CO emission lines at the absorber redshift. Two observations are available in Band 4 covering the frequency of the redshifted ^{12}CO(2–1) emission line and two observations in Band 6 covering the frequency of the redshifted ^{12}CO(3–2) emission line. The details of these observations are given in Table 4.1. The total integration time is 1333 s in Band 4 and 605 s in Band 6 for the observations covering the ^{12}CO emission lines. Furthermore, we use all well calibrated Band 6 observations that do not cover the ^{12}CO(3–2) emission line to search for continuum emission. The corresponding datasets are listed in Table 4.1.

We carry out the calibration and data reduction using the Common Astronomy Software Applications (CASA) software package version 4.7. Each individual dataset used for the emission line search is first examined in the *uv* plane to apply further interactive flagging

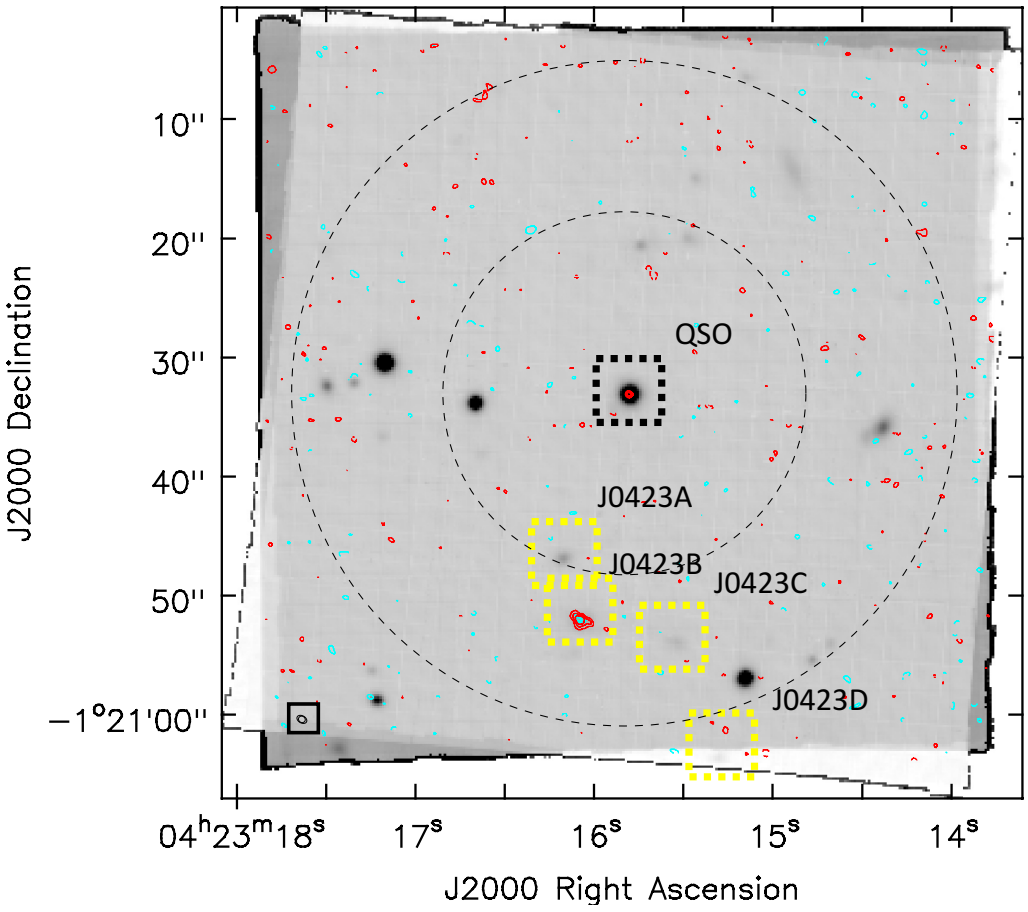

Figure 4.1: Overview of the detected sources in the field of J0423−0130. The reconstructed white-light image from our MUSE observations is shown in grey-scales, the red and cyan contours show the ^{12}CO(2–1) and ^{12}CO(3–2) emission, respectively. Contours show the −3, 3, 5, and 7σ levels in the respective maps, where negative contours are dashed. Galaxies identified to be at the absorber redshift based on our MUSE and ALMA observations are marked with the yellow boxes, the quasar is marked with the black box. The galaxies 1 and 2 in Table 4.3 are not detected in our observations and therefore not shown in the figure and not considered in the analysis presented here. Dashed large and small circles mark the ALMA half power beam width in Band 4 and Band 6, respectively. Small black circles in the bottom left corner show the synthesized beams of the ALMA Band 4 and Band 6 observations which have a comparable size. A zoom in on J0423B is shown in Fig. 4.3. The second OB of the MUSE observations was rotated by 5° with respect to the first OB due to a technical problem.

Table 4.1: Summary of the used ALMACAL observations of J0423−0130.

Project code	Date	Scan Intent	Band	^{12}CO Trans.	t_{exp} [s]
2015.1.00920.S	09.01.2016	B	4	2−1	604.8
2015.1.00262.S	22.08.2016	B	4	2−1	728.5
2012.1.00350.S	04.12.2013	B	6	3−2	302.4
2013.1.00403.S	13.06.2014	B	6	3−2	302.4
2013.1.00111.S	05.07.2015	B	6	-	302.4
2013.1.01175.S	19.07.2015	B	6	-	605.8
2013.1.01175.S	19.07.2015	F	6	-	302.4
2013.1.01225.S	05.08.2015	B	6	-	302.4
2012.1.00146.S	28.05.2015	F	6	-	151.2
2015.1.00350.S	27.10.2015	B	6	-	302.4
2013.1.00198.S	06.06.2015	B	6	-	302.4
2013.1.01172.S	30.06.2014	B	6	-	483.8
2013.1.00815.S	28.06.2014	F	6	-	151.2
2013.1.00815.S	16.06.2014	B	6	-	604.8
2013.1.00710.S	12.12.2014	F	6	-	151.2
2015.1.00920.S	01.01.2016	B	6	-	302.4
2016.1.00724.S	27.12.2016	F	6	-	151.2
2016.1.00683.S	29.11.2016	F	6	-	151.2
2016.1.00627.S	03.12.2016	F	6	-	151.2
2016.1.00627.S	01.12.2016	F	6	-	302.4
2016.1.01453.S	22.11.2016	F	6	-	151.2
2016.1.01262.S	30.11.2016	F	6	-	151.2
2015.1.00296.S	22.06.2016	F	6	-	151.2

Note: Scan intent B denotes the bandpass calibrator, and F denotes the flux calibrator.

Table 4.2: Summary of the final J0423−0130 ALMA data cube properties.

Band	Freq [GHz]	med. Ang. Res. [″]	rms [mJy beam^{-1}]	Δv [km s^{-1}]	PB FWHM [″]
4	141.166	0.43	0.28	66	48
6	211.742	0.70	0.37	44	27

if necessary. We reduce the spectral resolution to a maximum of 15.625 kHz. This results in a velocity resolution of 33 km s^{-1} (and 66 km s^{-1} after Hanning smoothing) for the Band 4 observations and a velocity resolution of 22 km s^{-1} (and 44 km s^{-1} after Hanning smoothing) for the Band 6 observations. The spectral resolution ensures that an emission line with a width of $\gtrsim$ 300 km s^{-1} is covered by at least 5 and 7 channels in the respective bands. Before the imaging, we concatenate the two datasets in each band.

For the image cubes and the continuum image, the imaging was done using the standard 'clean' algorithm. A 'robust' weighting scheme was applied, in which a Briggs weighting parameter is used to allow for a flexible weighting of long and short baselines. Here we use a Briggs parameter of 0.5, which guarantees a nearly optimal sensitivity while still providing a high spatial resolution and a well-behaved synthesized beam. In Band 4 we have two observations with a spatial resolution of 1.84″ and 0.39″ and therefore we use an outer taper of 0.5″ to prevent too high a weighting of the higher resolution data. The final parameters of the image cubes are given in Table 4.2. The resulting mean rms noise level in Band 4 is measured to be $\sim$ 0.28 mJy beam^{-1} per 66 km s^{-1} and the median angular resolution of the final data cube is $\sim$ 0.43″. The rms noise level in the Band 6 image cube is $\sim$ 0.37 mJy beam^{-1} per 44 km s^{-1} and the median angular resolution of the final data cube is $\sim$ 0.70″. The rms noise level in the 1.2 mm continuum image is $\sim$ 96 μJy beam^{-1} and the median angular resolution is $\sim$ 0.75″. We use a pixel size of 0.15″ in the Band 4 image cube, 0.24″ in the Band 6 image cube covering the ^{12}CO(3–2) emission line and 0.15″ in the Band 6 continuum image cube.

4.2.2 New MUSE Observations

We obtain Multi Unit Spectroscopic Explorer (MUSE) observations in the field of J0423−0130 through Director's Discretionary Time. Although the previously identified galaxies from our ALMACAL observations and another galaxy identified in the broad-band imaging by Rao et al. (2011) are located south of the quasar, we centre the field of view on the quasar in order to not exclude a priori the possibility to find a galaxy north of the quasar. The observations were carried out in service mode under programme ESO 298.A-5017 at the European Southern Observatory using MUSE at the Nasmyth focus of the 8.2 m Very Large Telescope UT4. Two "Observing Blocks" (OBs) were taken on the

23 and 24 December 2016. The field is rotated by 180 degrees between these two OBs. OBs are further divided into two sub-exposures, with an additional rotation of 90 degrees and a sub-arcsec dithering pattern. The exposure time of each sub-exposure is 1405s with a seeing of $0.55'' - 0.7''$ resulting in a total exposure time of 5620 s. The spectral coverage is $\sim$ 4800–9300 Å. At the redshift of the absorber ($z_{\rm abs} = 0.633$) we, therefore, cover all emission lines between [OII] and [OIII], but not H α.

We reduce the data with v1.6.1 of the ESO MUSE pipeline and use the Zurich Atmosphere Purge (ZAP) code for the sky subtraction (Soto et al., 2016). We use the master bias, master flat field and arc lamp exposures taken closest in time to the science observations to correct the raw data cubes. This is done with the SCIBASIC recipe. We do the correction to a heliocentric reference system using the SCIPOST recipe. In this step, we do not perform a sky-removal since ZAP is best performing on non-sky-subtracted cubes. We check the wavelength solution using the position of the brightest sky lines and find it to be accurate to 10 km s^{-1}. The offset table is created for each cube by comparing the positions of point sources in the field using the recipe EXP_ALIGN. In the final step, the cubes are combined using the recipe EXP_COMBINE. The seeing of the final cube measured from the quasar and other point sources is $0.71''$ at 7000 Å. To ensure a precise astrometry, we match the position of the quasar with its high precision position known from Very Long Baseline Array (VLBA) (Lanyi et al., 2010).

We remove the sky emission lines using the ZAP code (Soto et al., 2016). To determine regions with pure sky emission a mask is created from the reconstructed white light image. In this step, we set the flux levels accordingly to include bright objects in the mask. ZAP isolates the emission lines caused by sky emission using a principal component analysis and removes them from the data cube.

The quasar in this field is highly variable at optical wavelengths and we do not cover any other standard star with our field, so we estimate the flux error to be $\pm 10\%$ based on our previous experience (Péroux et al., 2017; Rahmani et al., 2018).

4.2.3 Ancillary Data

The target studied in this chapter is the intervening metal line absorber initially detected by Wills et al. (1980) as an FeII and MgII absorber at $z_{\rm abs} = 0.6320$ towards the quasar

Table 4.3: Summary of all previously detected galaxies connected to the absorber towards J0423–0130.

ID	RA (J2000)	Dec (J2000)	θ [kpc]	Previous Detection	Ref.	Detected in this Work
1	n.a.	n.a.	14.7	broad-band	Churchill et al. (1996)	No
2	04 23 15.58	−01 20 34.6	24.7	broad-band	Rao et al. (2011)	No
3	04 23 16.18	−01 20 46.9	102	[OII]	Yanny & York (1992), Rao et al. (2011)	Yes - J0423A
4	04 23 16.07	−01 20 52.1	133	[OII]	Yanny & York (1992)	Yes - J0423B
5	04 23 15.54	−01 20 54.0	146	[OII]	Yanny & York (1992)	Yes - J0423C
6	04 23 15.30	−01 21 03.7	216	[OII]	Yanny & York (1992)	Yes - J0423D

Note: For galaxy 1 Churchill et al. (1996) only report the impact parameter, but not the coordinates. Yanny & York (1992) do not give the coordinates of the detected galaxies. Therefore, we match the galaxies with our observations and quote the coordinates based on this.

QSO J0423−0130 ($z_{\rm QSO}$ = 0.915).

Early Observations This system was observed by several authors using narrow-band [OII] filters (Yanny et al., 1990; Yanny & York, 1992) and broad-band imaging (Churchill et al., 1996; Rao et al., 2011) to determine the galaxy associated with the intervening absorber. In total six systems were reported with an impact parameter $\lesssim$ 200 kpc. However, no consensus was reached on what is causing the absorption. The coordinates of these galaxies are listed in Table 4.3.

Quasar Spectroscopy The strong FeII and MgII absorber was reobserved by Churchill et al. (1996) as part of a program to study the spatial and velocity distribution of absorbing systems with known galaxy counterparts. A high-resolution spectrum of J0423−0130 was obtained in January 1995 using the HIRES echelle spectrometer (Vogt et al., 1994) on the Keck 10m telescope. The spectral resolution is 6.6 km s^{-1}.

The absorber towards J0423−0130 was also part of an MgII-FeII absorber sample, which was followed up by Rao et al. (2006) using the *Hubble Space Telescope (HST) Space Telescope Imaging Spectrograph (STIS)* spectrograph in Cycle 9 (PID 8569). The HI column density was determined to be $\log(N(\mathrm{HI})/\ \mathrm{atoms\ cm^{-2}}) = 18.54^{+0.07}_{-0.10}$.

Imaging of the Field of J0423–0130 Churchill et al. (1996) obtained broad-band imaging for the field of J0423−0130 and reported a galaxy associated with the absorber at an impact parameter of 14.7 kpc.

Furthermore, Rao et al. (2011) observed this field using the MDM Observatory 2.4 m Hiltner telescope. They analysed a 30″ × 30″ wide region of their images corresponding to a field of view of 205 × 205 kpc at the absorber redshift. The images were taken in the *B*, *R*, *I*, *J*, *H*, and *K* bands. The PSF of the quasar was only subtracted in the optical bands. Rao et al. (2011) performed a stellar population synthesis modelling for the five sources they detected within a 100 kpc radius around the quasar. It was found that only one galaxy has a photometric redshift of $z = 0.637 \pm 0.031$ consistent with the absorber ($z_{\rm abs}$ = 0.6331). The impact parameter of this galaxy is 14.5″ or 99.6 kpc. Furthermore, it was reported that another source might be at an impact parameter of 3.6″, which would translate to 25 kpc at the absorber redshift. However, it was only visible in the infrared

Table 4.4: ALMA detection of the galaxy J0423B.

Line	z	$S_{\rm peak}$ [mJy]	$S_{\rm int}$ [Jy km s^{-1}]	$L'_{\rm CO}$ [$\times 10^{10}$ K km s^{-1} pc^2]	FWHM [km s^{-1}]
^{12}CO(2–1)	0.63317	8.4 ± 0.7	3.6 ± 0.2	1.9 ± 0.1	590 ± 30
^{12}CO(3–2)	0.63335	10 ± 1	5.2 ± 0.3	1.2 ± 0.1	610 ± 40

data and the spatial resolution prevented the isolation of the object from the quasar in these frames. Therefore, Rao et al. (2011) could not perform stellar population synthesis modelling for this source. The coordinates of the detected galaxies are given in Table 4.3. In the analysis we use the broad-band images to obtain broad-band photometry of the MUSE detected galaxies.

4.3 Analysis

4.3.1 ALMA Source Detection and Flux Measurement

We aim to detect ^{12}CO emission from galaxies connected to the Lyman Limit System (LLS) at $z = 0.633$. Thus, we search for emission lines in the ALMA Band 4 and Band 6 image cubes using the Source Finding Application (`SoFiA`)[1] (Serra et al., 2015) that incorporates a number of different source detection algorithms to find emission lines in radio data cubes. We use the "Smooth + Clip Finder", which uses an algorithm developed by Serra et al. (2012). It smooths the data in both spatial and spectral direction using a number of different 3D smoothing kernels. A search of emission lines is performed on each smoothed cube by detecting spaxels above a user-defined threshold. The complete discussion of the relative strengths and weaknesses of all possible source finding strategies is presented by Popping et al. (2012). We chose the "Smooth + Clip Finder" since it offers the highest completeness and reliability for finding sources on a variety of scales. This is appropriate in our case since we do not know a priori whether our sources are spatially resolved. We use twelve smoothing kernels between 0.7″ and 4.2″ in the spatial dimension and between 66 km s^{-1} and 990 km s^{-1} for the Band 4 data cube and 44 km s^{-1} and 660 km s^{-1} for the Band 6 data cube in the spectral dimension. The detection threshold is 4σ for both data cubes.

[1] `https://github.com/SoFiA-Admin/SoFiA`

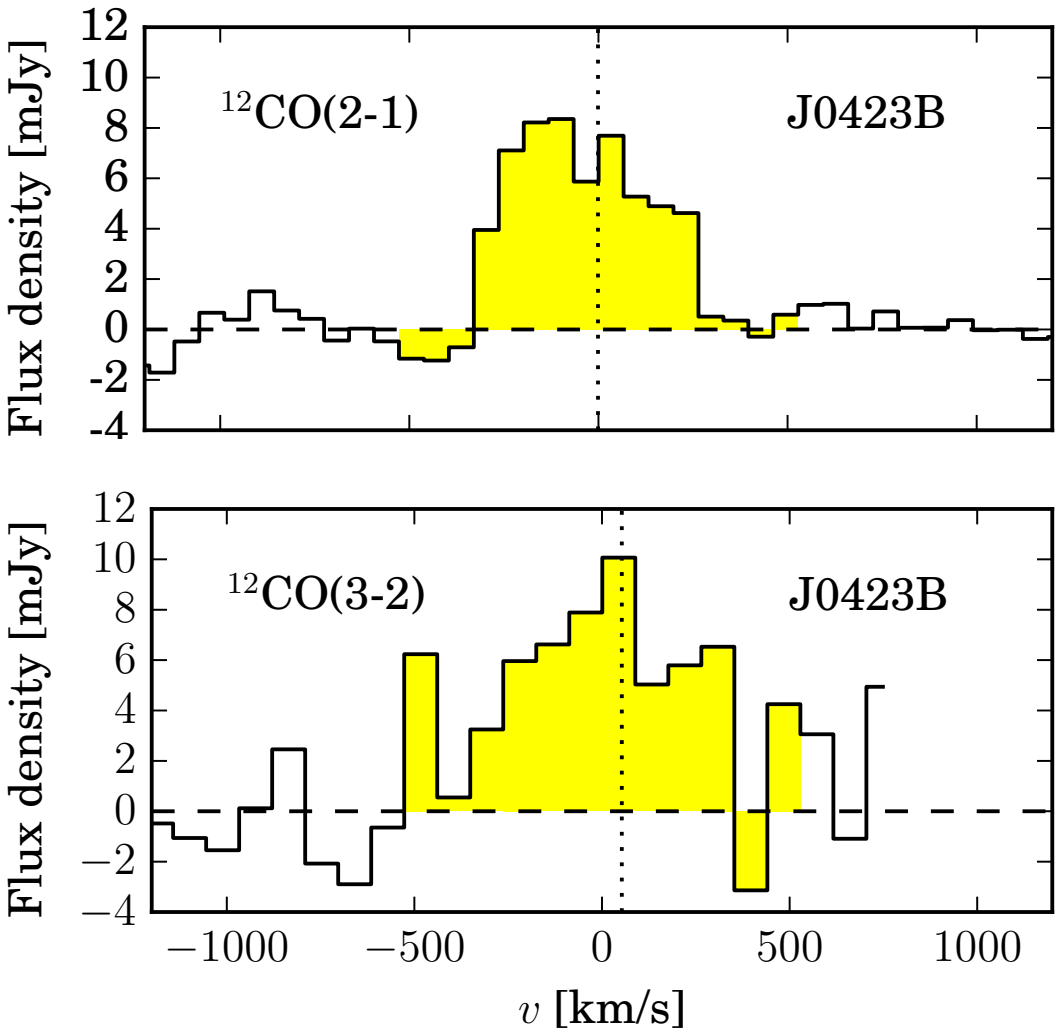

Figure 4.2: ^{12}CO(2–1) (top) and ^{12}CO(3–2) (bottom) emission lines observed in our ALMACAL data cubes centred in position on the quasar J0423–0130. Zero velocity corresponds to the redshift determined from the respective ^{12}CO emission line. The yellow region marks velocity range over which we integrate the total flux. Dotted lines show the position of the main absorption component at a redshift of 0.633174. The peak in the ^{12}CO emission line redshift corresponds exactly with that of the Ly α absorption line, which signifies the clear association between the absorption system and the ^{12}CO gas. The spectra are binned to a resolution of 66 and 88 km s^{-1} for the ^{12}CO(2–1) and ^{12}CO(3–2), respectively.

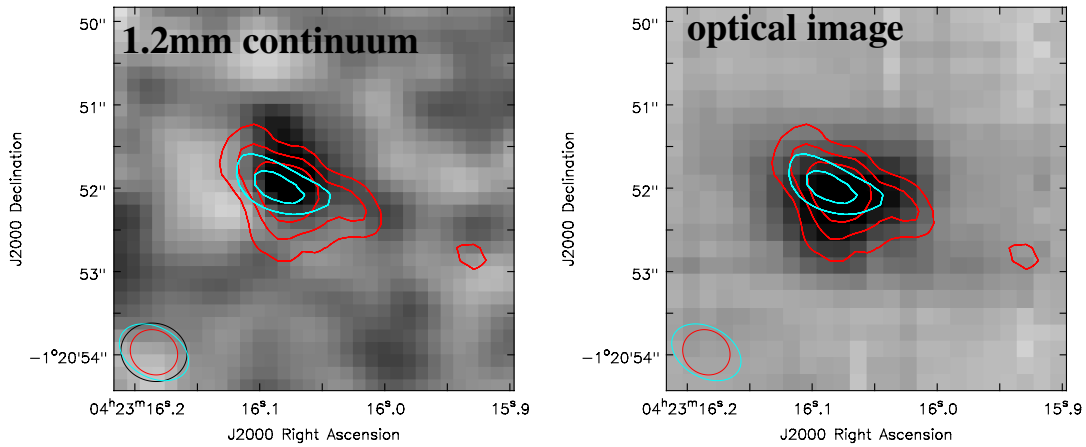

Figure 4.3: Zoom in on J0423B in Fig. 4.1. The 1.2 mm continuum emission is shown in grey scales on the left and the MUSE reconstructed white light image is shown in grey scales on the right. In both panels we show the ALMA ^{12}CO(2–1) in red contours, ALMA ^{12}CO (3–2) in cyan contours at 3, 5, 7 sigma of the respective maps overlaid. The ellipses in the lower left corner show the beam size in the Band 4 and Band 6 observations where the red ellipse corresponds to the beam in the ^{12}CO(2–1) line map, the cyan ellipse corresponds to the beam in the ^{12}CO(3–2) emission line map and the black ellipse corresponds to the beam in the 1.2 mm continuum map. Negative contours are marked with dashed lines, but are not present in this close-up. 1" in these images corresponds to 6.8 kpc at the galaxy redshift.

We require the detection to be within a range of ±2000 km s^{-1} relative to the absorber redshift, because we are targeting ^{12}CO emission at the absorber redshift. We run the source finder on the non-primary beam corrected cubes to ensure a constant noise level throughout the cube.

Using the detection method described above, we find ^{12}CO(2–1) and ^{12}CO(3–2) emission at the same position in the Band 4 and Band 6 cubes. We find no other emission lines which are detected in only one of the two data cubes. The emission lines are shown as contours in Fig. 4.1. The source is named J0423B throughout the chapter. To our knowledge, this is the first time that multiple ^{12}CO transitions have been observed from one galaxy associated with a Ly α absorber. This allows us to investigate the properties of the interstellar-medium in this galaxy.

We determine the size of the emission by fitting a two-dimensional Gaussian function to the integrated intensity maps. Here, we report the FWHM along the major axis deconvolved with the beam. The size of the ^{12}CO(2–1) emission is 1.3 ± 0.2″ which converts to 8.9±1.4 kpc at this redshift, the ^{12}CO(3–2) emission and the 1.2 mm continuum emission are not resolved.

Before extracting the spectra, we perform a primary beam correction on the image cube using IMPBCOR to account for the primary beam response function. We note that the primary beam correction at the position of our detected ^{12}CO lines in Band 6 is large because the ^{12}CO detection lies at 19.4″ from the centre of the field, and the Band 6 primary beam width is only 13.5″. We determine the redshift of the ^{12}CO emission lines from the mean of the two frequencies at which the flux reached 50% of the maximum flux density. The emission line spectra are shown in Fig. 4.2.

The flux is measured by integrating the spectra over two times the FWHM indicated by the yellow shaded region shown in Fig. 4.2. We have subtracted the continuum from the image cube using the task IMCONTSUB with a linear fit to the spectrum. We determine the width of the line profiles from the 50% level of the maximum flux density. The observed line flux densities are converted to line luminosities using the following equation (Solomon et al., 1992):

$$L'_{\rm line} = 3.25 \times 10^7 \times S_{\rm line}\Delta v \frac{D_L^2}{(1+z)^3 \nu_{\rm obs}^2} \text{K km s}^{-1} \text{ pc}^2, \tag{4.3.1}$$

where $S_{\rm line}\Delta v$ is the observed velocity integrated line flux density in Jy km s^{-1}, D_L is the luminosity distance to the galaxy in Mpc, and $\nu_{\rm obs}$ is the observed line frequency in GHz. A summary of the emission line properties is given in Table 4.4. We estimate the error of the integrated line flux to be 5% based on the expected accuracy of the flux calibration. The FWHM of the ^{12}CO emission lines is within the observed range of $60 - 800$km s^{-1} for dusty star-forming galaxies at $z < 0.35$ (Villanueva et al., 2017). The projected impact parameter between the ^{12}CO detection and the quasar sight line is 133 kpc and the position of the ^{12}CO detection is aligned with that of one of the galaxies detected in the MUSE cube. We discuss this in more detail in Section 4.3.2.

Furthermore, we combine all Band 6 observations from ALMACAL to search for continuum emission from the CO-detected galaxy. Hence, we can compare the total far-infrared luminosity based SFR with the SFR based on the dust-uncorrected [OII] emission line flux. We show in Fig. 4.3 (left) the Band 6 continuum map with the ^{12}CO (2–1) and ^{12}CO (3–2) emission line contours overplotted. We exclude any contamination from the ^{12}CO(3-2) emission line by excluding the datasets covering the relevant frequency. The total flux density at 1.2 mm is (0.8 ± 0.2) mJy and the peak intensity is (0.56 ± 0.09) mJy beam^{-1}.

Finally, we explore the possibility to observe molecular absorption lines towards the quasar in our Band 4 and Band 6 observations. The 3σ detection limit for the integrated optical depth is 0.01 km s^{-1} and 0.003 km s^{-1} for ^{12}CO (2–1) and ^{12}CO (3–2), respectively. We note, however, that the velocity resolution is very coarse and might be not sufficient to detect absorption lines. We present a blind search for intervening molecular absorption lines on the full ALMACAL high spectral resolution sample in Chapter 4. Also in this study we do not detect molecular absorption towards J0423−0130.

4.3.2 MUSE Source Detection and Flux Measurement

We blindly search for line and continuum emission from galaxies in our MUSE cube. To this end, we search for emission line and continuum sources using the MUSELET source finding algorithm included in MPDAF[2]. MUSELET runs SExtractor (Bertin & Arnouts,

[2]http://mpdaf.readthedocs.io/en/latest/

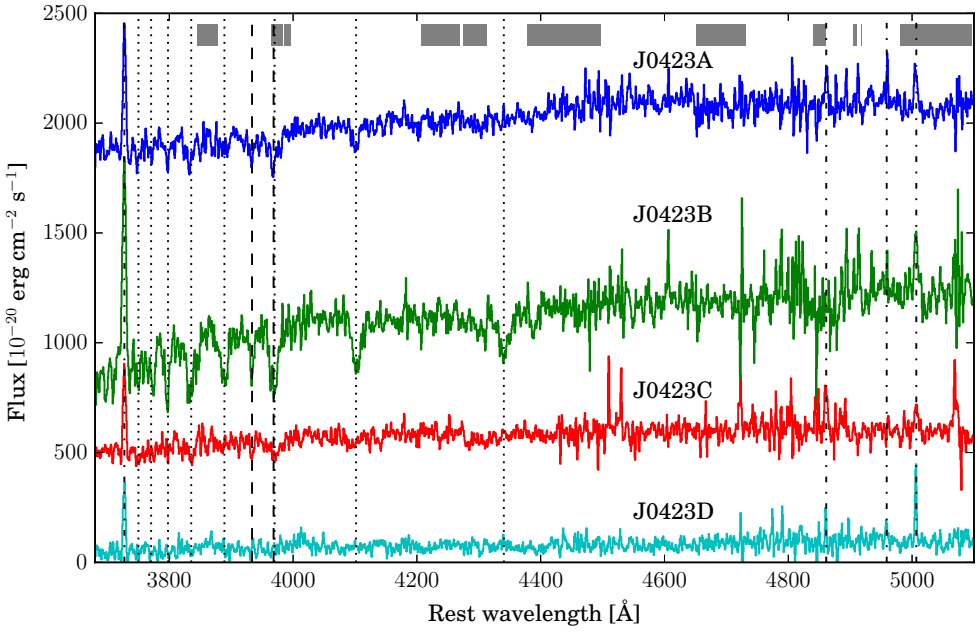

Figure 4.4: Rest frame optical spectra of the four group members identified from our MUSE observation (offset by an arbitrary number for clarity). Spectra are shifted to rest wavelength using the redshift determined from the emission lines quoted in Table 4.5. The grey area marks the regions possibly contaminated by telluric absorption and emission. The strongest emission line in all spectra is [OII] at λ = 3727 Å. The dashed-dotted line marks with increasing wavelength the [OII], H β, [OIII]4959Å, and [OIII]5007Å emission line. Dotted lines mark the Balmer absorption lines from H γ to H 12 with decreasing wavelength. Dashed lines mark the Ca H&K absorption lines. We note, that the features at the [OIII]4959Å and H β wavelength in J0423D as well as the narrow feature at the [OIII]4959Å wavelength in J0423A are marginal given the SNR of the spectrum.

1996) on each 1.25 Å-wide slice of the cube to find any source of emission. We detect 50 emission line sources and continuum sources in the MUSE cube with this method. The galaxies at the absorber redshift ($z = 0.633$) are selected based on two criteria: 1) searching for emission line sources, and 2) by searching for the 4000 Å break at the rest frame of the absorber in all 50 spectra. We find four emission line sources at the absorber redshift, but we do not detect continuum sources at the absorber redshift. The full spectra of the four emission line galaxies are shown in Fig. 4.4. In Fig. 4.1 we mark the positions of these galaxies: J0423A, J0423B, J0423C and J0423D.

We determine the redshift of the galaxies by fitting a Gaussian to the detected emission lines. Since we detect multiple lines for all galaxies, we determine the redshift of each galaxy as the median redshift from the Gaussian fit to the detected lines. The respective redshifts and emission line fluxes are shown in Table 4.5. We do not detect [OIII]4959Å for any of our galaxies and therefore give only upper limits on the line flux. This is consistent with the expected line-flux assuming a doublet flux-ratio of 3 (Storey & Zeippen, 2000). Furthermore, we detect H β in only two of the galaxies. The given upper limits are calculated from a maximum emission of 3σ and the FWHM measured from the sky emission lines corresponding to 3 Å. The line width of the detected lines determined from the Gaussian fitting is listed in Table 4.5.

In Fig. 4.3 (right) we show a comparison of the ALMA collapsed ^{12}CO emission line map and the MUSE pseudo-white-light image. It can be seen that the ^{12}CO gas is coincident with the optical position of galaxy J0423B. No emission from the other MUSE-detected galaxies is found in the ALMA cubes. Furthermore, comparing the FWHM of the [OIII] lines and the ^{12}CO emission lines, we find that the molecular gas disk seems slightly more extended than the ionized gas.

Table 4.5: Observed properties of the galaxies from the MUSE observation and the broad-band imaging.

Name		J0423A	J0423B	J0423C	J0423D
Ra (J2000)		04 23 16.18	04 23 16.07	04 23 15.54	04 23 15.30
Dec (J2000)		−01 20 46.9	−01 20 52.1	−01 20 54.0	−01 21 03.7
θ [″]		14.9	19.4	21.3	31.6
θ [kpc]		102	133	146	216
z		0.6332 ± 0.0005	0.6331 ± 0.0005	0.6338 ± 0.0003	0.6323 ± 0.0005
Line Width	σ([OII])	170 ± 10	220 ± 10	170 ± 10	140 ± 10
	FWHM([OII])	400 ± 20	520 ± 30	390 ± 30	330 ± 30
	σ([H β])	120 ± 50	-	120 ± 40	-
	FWHM([H β])	290 ± 110	-	290 ± 90	-
	σ([OIII]5007Å)	150 ± 20	170 ± 30	160 ± 40	70 ± 20
	FWHM([OIII]5007Å)	360 ± 50	400 ± 70	380 ± 90	160 ± 40
Line Fluxes	[OII]	5.3 ± 0.5	11.0 ± 1.1	3.6 ± 0.4	3.0 ± 0.3
[10^{-17} erg s^{-1} cm^{-2}]	H β	1.7 ± 0.2	< 0.9	1.7 ± 0.2	< 2
	[OIII] 4959	< 0.9	< 1	< 0.6	< 1
	[OIII] 5007	2.1 ± 0.2	2.9 ± 0.3	1.3 ± 0.1	2.2 ± 0.2

Note: θ is the impact parameter given here in ″ and kpc.

. . . Table 4.5 continued.

Name	J0423A	J0423B	J0423C	J0423D
B [mag]	23.8 ± 0.4	25.2 ± 0.5	24.6 ± 0.3	< 25.82
R [mag]	22.10 ± 0.18	21.68 ± 0.18	22.72 ± 0.15	23.75 ± 0.17
I [mag]	21.0 ± 0.3	20.0 ± 0.2	21.8 ± 0.2	< 25.15
J [mag]	20.43 ± 0.12	19.64 ± 0.09	20.90 ± 0.13	21.67 ± 0.11
H [mag]	19.83 ± 0.19	18.91 ± 0.12	20.3 ± 0.2	20.90 ± 0.19
K [mag]	19.87 ± 0.13	18.78 ± 0.08	20.34 ± 0.15	20.80 ± 0.11

Note: θ is the impact parameter given here in $''$ and kpc.

4.3.3 Broad-band Photometry and Stellar Mass

We estimate the stellar mass of the four galaxies, to infer the molecular gas mass ratio of J0423B and determine the total dynamical mass of the group. For this purpose, we use the broad-band imaging from Rao et al. (2011) to measure the broad-band photometry which we use as input for the spectral energy distribution (SED) fitting. The apparent magnitudes of the detected galaxies are determined using SExtractor and are listed in Table 4.5.

This broad-band photometry is used as input for the SED fitting with Le Phare[3] (Arnouts et al., 1999; Ilbert et al., 2006) to estimate the stellar masses of the galaxies. To perform the SED fitting the algorithm compares the observed colours with the ones predicted from a set of template SEDs. We fix the redshift for the SED fitting to the spectroscopic redshift determined from our MUSE spectra described in Section 4.3.2. The template SEDs are convolved with standard B, R, I, J, H, and K filter functions and a χ^2 minimization is performed. We quote the stellar mass of the galaxies in Table 4.6. Comparing our stellar masses to the galaxy stellar mass function at redshift $0.4 < z < 0.6$ and $0.6 < z < 0.8$ for which Drory et al. (2009) report a log(M*) of $10^{10.91-10.95}$, we find that the CO-detected, most massive galaxy J0423B has a stellar mass of almost 2 M*, while the other galaxies J0423A, J0423C and J0423D have stellar masses below M*.

4.3.4 Molecular Gas Mass

Until now the molecular gas content of galaxies associated with intervening Ly α absorbers has been determined only once (Neeleman et al., 2016). We combine the molecular gas mass with the stellar mass from the SED fitting to determine a census of the molecular gas and stars in galaxies associated with intervening absorbers. In the following, we determine the molecular gas mass using the two ^{12}CO emission lines. We use the following conversion:

$$M_{\rm mol} = \alpha_{\rm CO} \times L'_{\rm CO(1-0)}, \tag{4.3.2}$$

[3] http://www.cfht.hawaii.edu/~arnouts/lephare.html

where $L'_{\mathrm{CO(1-0)}}$ is the luminosity of the ^{12}CO(1-0) emission line and the conversion factor α_{CO} depends on the temperature, density, metallicity, and column density of the interstellar medium.

To apply the above mentioned conversion to the total molecular gas mass, we need to convert the ^{12}CO(2–1) line flux to the ^{12}CO(1-0) line flux using a suitable conversion factor. The ratio of $L'_{\mathrm{CO(3-2)}}/L'_{\mathrm{CO(2-1)}}$ is 0.63 ± 0.09 suggesting a ^{12}CO excitation ladder similar to that of a Luminous Infrared Galaxy (LIRG) (Papadopoulos et al., 2012b). We note that this value is also consistent with the expected ratio of 0.54 for Milky Way-type galaxies (Carilli & Walter, 2013). However, based on further evidence presented in Section 4.4.1 we believe that the LIRG-type conversion factor is more appropriate. Therefore, we adopt a conversion factor of $L'_{\mathrm{CO(2-1)}}/L'_{\mathrm{CO(1-0)}} = 0.9$, yielding an $L'_{\mathrm{CO(1-0)}}$ of $(2.1 \pm 0.1) \times 10^{10}$ K km s^{-1} pc^2. Furthermore, we use $\alpha_{\mathrm{CO}} = 0.6\mathrm{M}_\odot$ (K km s^{-1}pc^2)$^{-1}$, appropriate for LIRGs derived by Papadopoulos et al. (2012a) including a factor of 1.36 to account for the presence of helium. This yields a molecular gas mass of $M_{\mathrm{mol}} = (1.27 \pm 0.07) \times 10^{10}$ M$_\odot$. However, we note this low conversion factor might be an extreme value for the population of LIRGs. Papadopoulos et al. (2012a) find a higher conversion factor, similar to that of the Milky Way, in LIRGs for which also observations of dense gas tracers are available. To indicate the uncertainty in the derived H_2 mass, we also apply a conversion factor of $\alpha_{\mathrm{CO}} = 4.3\mathrm{M}_\odot$ (K km s^{-1}pc^2)$^{-1}$ typical for Milky Way-type galaxies and including a factor of 1.36 to account for the presence of helium (Bolatto et al., 2013). This yields a molecular gas mass 9×10^{10} M$_\odot$ and so we adopt a molecular gas mass of $1 - 9 \times 10^{10}$ M$_\odot$.

We have also extracted spectra from our ALMA cubes at the positions of J0423A and J0423C, but we could not find any clear sign of emission. For these two galaxies, we calculate upper limits for $L'_{\mathrm{CO(2-1)}}$ based on the 3σ noise level and assuming a width of the line of 500km s^{-1} based on the w_{50} measured from the ^{12}CO detections for J0423B. This yields an upper limit for the integrated flux of $S_{\mathrm{int}} = 0.4$ Jy km s^{-1}, assuming that the flux is evenly distributed over the full width of the profile. Therefore, the upper limit on the line luminosity of $L'_{\mathrm{CO(2-1)}}$ is 2×10^9 K km s^{-1} pc^2. We assume a Milky Way-type $L'_{\mathrm{CO(2-1)}}/L'_{\mathrm{CO(1-0)}}$ emission line ratio of 0.5 (Carilli & Walter, 2013) and a Milky Way-type CO-to-H_2 conversion factor of $\alpha_{\mathrm{CO}} = 4.3\mathrm{M}_\odot$ (K km s^{-1} pc^2)$^{-1}$ including a factor of 1.36

to account for the presence of helium (Bolatto et al., 2013). This yields an upper limit for the molecular gas mass of $M_{\rm mol} < 1.7 \times 10^{10}$ M$_\odot$ for J0423A and J0423C.

4.3.5 Star-Formation Rates

We determine the SFR of the CO-detected galaxy J0423B to test whether it is comparable with the identification of a LIRG based on the CO line flux ratios.

We estimate the SFR of J0423B based on the 1.2 mm flux. A set of template spectra for starburst galaxies from Polletta et al. (2007) are used which we scale to the observed 1.2 mm flux converted to the rest wavelength. The fitted spectrum is then integrated in the wavelength range from 8 - 1000 μm to obtain the total far-infrared luminosity $L_{\rm FIR}$. This is converted to the SFR using the Kennicutt (1998) relation:

$$SFR_{\rm FIR} = 4.5 \times 10^{-44} L_{\rm FIR} \tag{4.3.3}$$

based on this, we estimate a SFR of (50 ± 10) M$_\odot$ yr^{-1}. We note, however, that the uncertainty in this calculation is high since we use the median SFR from a set of template spectra which we scale to the flux at 1.2 mm. Additionally, the actual choice of the used SED templates is another factor of uncertainty. Using the template SEDs for spiral galaxies from Polletta et al. (2007) we estimate a SFR of (10.7 ± 2.5) M$_\odot$ yr^{-1}.

Furthermore, we derive the SFRs for the remaining three emission line galaxies based on the [OII] emission line using the relation given by Kennicutt (1998), which includes a dust correction:

$$SFR_{\rm [OII]} = (1.4 \pm 0.4) \times 10^{-41} L([\rm OII]) \times 10^{0.4 A_{\rm [OII]}}. \tag{4.3.4}$$

where $A_{\rm [OII]}$ is the extinction of the [OII] emission line. We determine the dust correction based on the stellar mass dependent $A_{\rm H\,\alpha}$ given by Garn & Best (2010) at $z \sim 0.1$, which is found to be valid up to $z \sim 1.5$ (Sobral et al., 2012). To convert the $A_{\rm H\,\alpha}$ to $A_{\rm [OII]}$ we use the prescription given by Calzetti (1997). The resulting dust-corrected SFRs are given in Table 4.6.

To test the identification of J0423B being a LIRG, we calculate the dust-uncorrected SFR based on the [OII] emission line for a comparison with the infrared based SFR. We

derive a SFR of 2.7 ± 0.3 $M_\odot$ yr^{-1} from the [OII] emission. This is 13–25 times lower than the SFR inferred from the far-infrared luminosity. It is in the lower envelope of the population of very luminous infrared galaxies studied by (Poggianti & Wu, 2000). This could be a further piece of evidence that J0423B is a LIRG. However, if we only use template SEDs for spiral galaxies to estimate the SFR, we find that the SFR determined based on the [OII] emission line is only four times lower.

We determine the limiting SFR for our MUSE observations based on the detection limit of the [OII] line to infer the maximum SFR of potential galaxy candidates below our detection limit. The mean rms noise in the MUSE cube around the [OII] emission line is measured from the cube with a velocity width of 865 km s^{-1}. We perform a 3σ clipping on this cube and another 3σ clipping on the clipped cube to remove any contribution from actual emission. The mean rms noise is then determined from this emission-free cube. Furthermore, we assume, that the minimum size of a galaxy is given by the seeing of $0.7''$, which corresponds to 4.8 kpc at the absorber redshift and the FWHM of the line is at least 3 Å. The resulting [OII] flux would be 0.3×10^{-17} erg s^{-1} cm $^{-2}$. This converts into a 3σ limiting SFR of 0.2 $M_\odot$ yr^{-1}. Additionally, we determine the limiting SFR at the quasar position. Therefore, we extract a $2'' \times 2''$ wide cube at the position of the quasar with a width of 865 km s^{-1} centred on the expected [OII] emission line covering all the observed [OII] emission. The emission from the quasar is determined by a linear fit and removed from the data cube. The limiting SFR at the position of the quasar is calculated from the noise in the continuum subtracted cube and assuming the same emission properties as described above. This yields a non-dust-corrected limiting SFR of 0.3 $M_\odot$ yr^{-1}.

4.3.6 Morphology and Kinematics

To study the kinematics of the molecular gas, we create a line-of-sight velocity map using the CASA task IMMOMENTS including pixels where the ^{12}CO line emission is detected at 3σ above the noise in each velocity channel of the cube. The resulting map is shown in Fig. 4.5. The velocity field is sampled with only three resolution elements across the major axis, but given this limitation, the velocity field is consistent with that of a rotating disk.

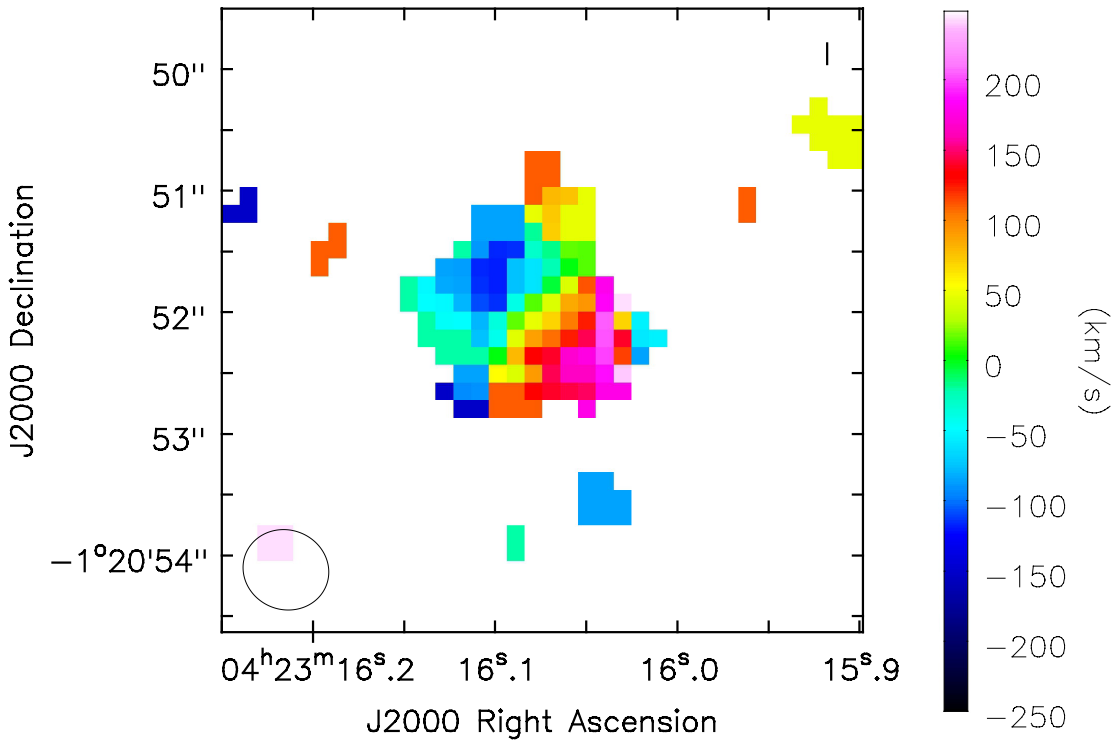

Figure 4.5: The intensity weighted line-of-sight velocity field of the ^{12}CO(2–1) emission from the ALMA observations for J0423B. The velocity map is consistent with a rotating disk and the orientation is consistent with the model velocity field based on [OIII] emission shown in Fig. 4.6.

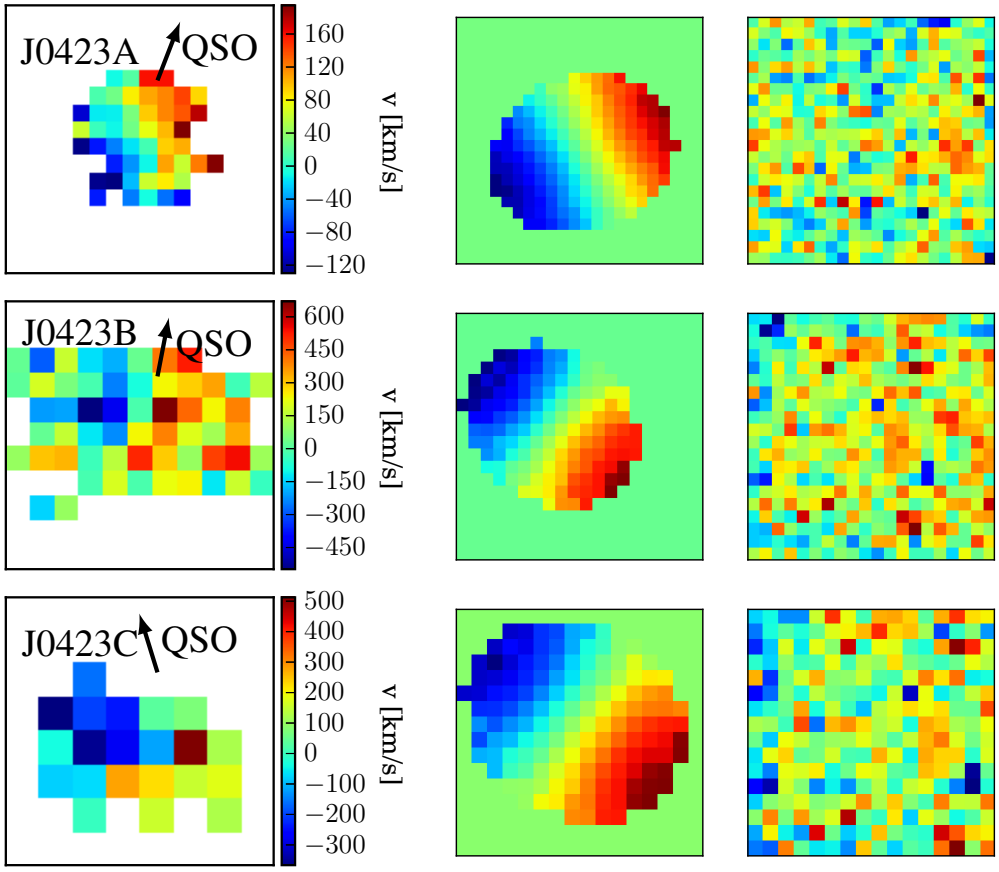

Figure 4.6: Results from the morpho-kinematic fitting to the [OIII] emission detected with MUSE, including the observed velocity field (left), the model velocity field from GalpaK^{3D} fitting (middle) and the residual map (right) for J0423A (top), J0423B (middle) and J0423C (bottom). The arrow indicated the direction towards the quasar sight-line. We find that all three galaxies have velocity fields consistent with rotating disks. We caution that the maximum velocity from the modelling is uncertain because all three galaxies are very compact and GalpaK^{3D} is known to overestimate the maximum velocity in the case of compact galaxies (Bouché et al., 2015). The observed velocity fields are spatially re-sampled for display purpose. The size of these images is 2" x 2" which translates to 13.6 x 13.6 kpc.

Table 4.6: Summary of the physical properties of the galaxies at the absorber redshift based on our MUSE data and the SED fitting.

Name	z	SFR $[M_\odot\ yr^{-1}]$	$\log M_\star$ $[M_\odot]$	12 + log(O/H)
J0423A	0.63317 ± 0.00048	7.5 ± 0.6	10.4 ± 0.2	8.80 ± 0.10^a
J0423B	0.63312 ± 0.00048	50 ± 10	11.2 ± 0.1	9.1 ± 0.9^b
J0423C	0.63376 ± 0.00032	4.6 ± 0.5	10.3 ± 0.2	8.94 ± 0.06^a
J0423D	0.63229 ± 0.00048	3.2 ± 0.5	10.2 ± 0.2	9.0 ± 0.9^b

Note: The SFRs of J0423A, J0423C, J0423D reported in this table are based on the [OII] emission line and are dust corrected. The SFR of J0423B is derived from $L_{\rm FIR}$. The metallicity ^{a} is determined from the emission lines and the metallicity ^{b} is derived from the mass-metallicity relation.

To determine the morphology and kinematics of the four [OIII]-detected galaxies in our MUSE cube, we perform a two-step analysis. First, we perform a Sersic-fit of the [OIII] pseudo-narrow-band image using GALFIT (Peng et al., 2002). Second, we use the GALPAK^{3D} algorithm (Bouché et al., 2015) to perform a 3D morpho-kinematic fit to the [OIII] emission line cube. We use the Sersic profile as input for the 3D morpho-kinematic fit. We infer from this fit whether the kinematics are compatible with that observed in a rotating disk and how the position angles of the galaxies are related to each other and how the quasar absorption is oriented with respect to the major and minor axes of the galaxies. However, given the data quality we will not be able to detect warps in the disks.

We determine the half-light radius, axis ratio, position angle (PA) and the Sersic index from the [OIII] pseudo-narrow-band image using GALFIT. This is a two-dimensional fitting algorithm extracting structural parameters from galaxy images. The algorithm models the light profile and is designed to fit multiple components. Here we perform a single component fit of the [OIII] pseudo-narrow band image. The fitting results are shown in Table 4.7. We find that for J0423D the PA and Sersic index are not very well constrained due to the low SNR of the detected line emission.

The GALPAK^{3D} algorithm is used to derive the kinematics of the galaxies based on the [OIII] emission line. We do not use the [OII] emission line, because it is an unresolved doublet and we do not know the exact line ratio.

The GALPAK^{3D} algorithm directly compares a number of parametric models, created from a Markov Chain Monte Carlo (MCMC) algorithm and mapped in x, y, λ coordinate

Table 4.7: Summary of the morphological parameters from 2D fitting and morpho-kinematic parameters from 3D fitting.

Name	$r_{1/2}^{\mathrm{Galfit}}$ [kpc]	$r_{1/2}^{\mathrm{GalpaK}}$ [kpc]	PA^{Galfit} [°]	PA^{GalpaK} [°]	i^{Galfit} [°]	i^{GalpaK} [°]	Sersic index	$v_{\mathrm{max}}^{\mathrm{GalpaK}}$ [km s^{-1}]	$\sigma_0^{\mathrm{GalpaK}}$ [km s^{-1}]
J0423A	1.5 ± 0.6	2.9 ± 0.3	106 ± 4	115 ± 4	33 ± 3	42 ± 6	3 ± 1	< 410	11 ± 7
J0423B	2.77 ± 0.08	$2.77^{\star}$	90 ± 2	54 ± 24	40.5 ± 0.8	51 ± 17	1.04 ± 0.03	< 170	84 ± 17
J0423C	1.54 ± 0.09	2.73 ± 0.03	67 ± 6	54 ± 21	47 ± 3	50 ± 16	0.71 ± 0.06	< 191	87 ± 17
J0423D	0.5 ± 0.1		-90 ± 90		60 ± 30		0.3 ± 0.4		

Note: * is fixed based on the 2D fitting from GALFIT. We find that for J0423A, J0423B and J0423C the morphological parameters from independent 2D and 3D fitting are comparable.

system, to the data. GALPAK^{3D} fits the model in three dimensions and offers even in poor seeing conditions a robust determination of the morpho-kinematics. It probes the posterior possibility density distribution via an MCMC chain of 15, 000 runs and fits 10 parameters simultaneously (position (x, y, λ), flux, half-light radius, inclination, PA, turnover radius, maximum velocity and intrinsic velocity dispersion).

The algorithm can only converge if the maximum SNR $>$ 3 per pixel, which is not fulfilled for J0423D. Furthermore, the maximum velocity is overestimated if the ratio of galaxy half-light radius to seeing radius is smaller than about 1.5.

We use the half-light radius from the 2D fitting as a fixed input parameter for J0423B. For J0423A it is necessary to fix the turnover radius to break the degeneracy with the maximum velocity. We set the turnover radius to 0.9 times the half-light radius based on the scaling relation found in local disc galaxies (Amorisco & Bertin, 2010). Since all the galaxies are found to be compact already from independent 2D profile fitting, we expect that the GalpaK^{3D} will overestimate the maximum velocity. The final fitting parameters are given in Table 4.7. We find that the velocity fields of the galaxies J0423A, J0423B, and J0423C are consistent with rotating disks. As can be seen in Table 4.7, the PAs from different objects are not aligned. Comparing the PA derived with Galpak^{3D} with the PA from the 2D fitting with GALFIT we find that they are comparable within the errors. We show the observed and model velocity fields from the MUSE observations in Fig. 4.6. It can be seen that in J0423B the velocity field of the ionized gas traced by the [OIII] emission line and of the molecular gas traced by the ^{12}CO(2–1) emission line shown in Fig. 4.5 are consistent. Furthermore, we find that the angular extent of $1.4'' \pm 0.1''$ for the [OIII] emission line matches the angular extent of $1.3'' \pm 0.2''$ found for the CO(2–1) emission line.

We explore the possibility that the absorption in the quasar spectrum is tracing the extended rotating gas disk of one of the two closest galaxies J0423A and J0423B. Therefore, we extrapolate the model velocity field derived above to the position of the absorber. The expected velocity is overplotted in the velocity space of the absorber on the MgII2796Å absorption line in the last panel of Fig. 4.7. It can be seen that the expected velocity from J0423A does not match the absorption profile. For J0423B on the other hand, we find that

Table 4.8: Fit parameters for the absorption line Voigt profile fitting using VPFIT.

Ion	No.	z	b	log N [atoms cm^{-2}]
FeII	1	0.633174 ± 0.000006	3.0 ± 2.4	12.21 ± 0.13
FeII	2	0.633080 ± 0.000005	8.9 ± 1.4	12.80 ± 0.05
MgI	1	0.633174 ± 0.000006	3.0 ± 2.4	11.04 ± 0.15
MgI	2	0.633080 ± 0.000005	8.9 ± 1.4	11.50 ± 0.07
MgII	1	0.631791 ± 0.000002	7.7 ± 0.5	12.49 ± 0.02
MgII	2	0.632558 ± 0.000005	5.7 ± 1.3	12.09 ± 0.06
MgII	3	0.632648 ± 0.000005	7.0 ± 1.8	12.16 ± 0.08
MgII	4	0.632788 ± 0.000003	2.9 ± 1.4	12.36 ± 0.09
MgII	5	0.632855 ± 0.000004	20.6 ± 0.9	13.17 ± 0.02
MgII	6	0.633108 ± 0.000003	11.5 ± 0.4	13.49 ± 0.04

Note: The top four rows above the dividing line show the parameters for the Voigt Profile fitting using only FeII and MgI. The bottom six lines below the dividing line show the fit parameters for the Voigt profile fit using only the MgII absorption lines. No. denotes the number of the component that is simultaneously fit in multiple absorption lines.

it agrees very well with one of the absorption components in the MgII2796Å absorption profile. Intriguingly, this galaxy is the one for which we measure a large cold gas content. We note, however, that projected separation between the quasar sight line and the gas-rich galaxy is 133 kpc, so the simple extrapolation of a rotating disk is a very naive assumption.

4.3.7 Neutral Gas Properties

In this section, we use the quasar spectrum presented by Churchill et al. (1996) to fit the absorption lines, determine the minimum number of components needed to reproduce the absorption profile and determine their redshift. We will use these fits in Section 4.3.8 to derive a lower limit on the total metallicity of the absorbing neutral gas. We use the kinematic information and the metallicity of the absorber to infer the alignment with the galaxies in velocity space as well as the possibility of probing an extended galactic disk with the absorption.

We model the metal absorption lines in the quasar spectrum associated with the Lyman Limit system with Voigt profiles using VPFIT[4]v.10.2. The VPFIT code is developed to fit multiple Voigt profiles to spectroscopic data by minimizing the χ^2. Here, we have performed a multicomponent fit assuming that for each absorption component all ions

[4]https://www.ast.cam.ac.uk/~rfc/vpfit.html

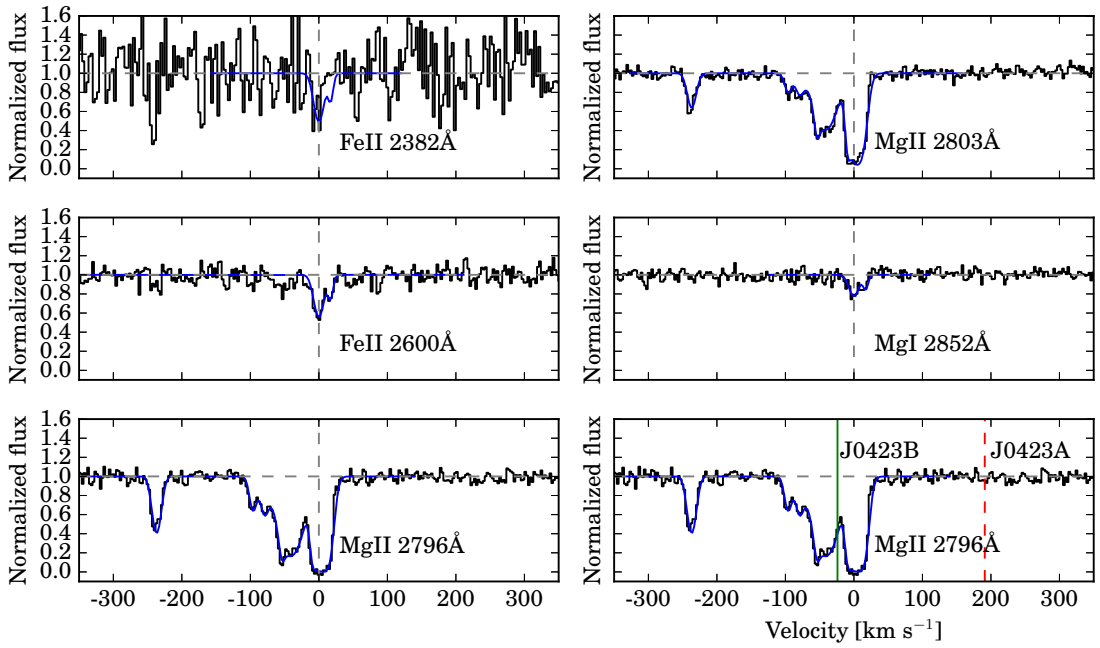

Figure 4.7: Fits to the FeII2382Å, FeII2600Å, MgII2796Å, MgII2803Å, MgI2852Å absorption lines in the QSO spectrum. In the fitting using vpfit we assumed two components for FeII and MgI and six components for the saturated MgII. Velocity zero corresponds to the redshift of the main component from the joint fits of FeII2600Å, FeII2382Å, MgI2852Å. The last panel shows a comparison of the MgII2796Å absorption line profile with the expected absorption caused by an extended rotating disk of J0423A and J0423B at the position of the quasar sight-line. We find that the absorption cannot be caused by an extended disk of J0423A, but the velocity extrapolated from the disk of J0423B matches the absorption profile. We note, however, that due to the large impact parameter of 133 kpc the absorption is unlikely tracing the disk of J0423B.

have the same redshift. We show the spectra and the Voigt profile fits in Fig. 4.7. It can be seen that the MgII2803Å, and MgII2796Å absorption lines are saturated and more complex than the FeII2600Å, FeII2382Å, and MgI2852Å absorption lines. Therefore, we fit the two sets of absorption lines separately. We find that the absorption lines are well fitted using two-components for the FeII and MgI lines. A separate fit is performed for the strong MgII lines using six components. We summarize the corresponding fit parameters in Table 4.8.

4.3.8 Metallicities

We study the metallicity of the ionised gas in the galaxies and of the neutral gas traced by the absorption. Using this information, we can compare the metallicities observed at different positions with each other and infer from this the connection between the galaxies and the absorbing gas.

HII Metallicities To determine the gas metallicities of the MUSE-detected galaxies from the emission lines, we use the R23 method as first introduced by Pagel et al. (1979), which is widely used to determine gas metallicities if the H β, [OII], and [OIII] fluxes are known. It uses the log R_{23} parameter, which is defined as follows:

$$\log(R_{23}) = \log\left(\frac{F([OII]\lambda3727,3729) + F([OIII]\lambda4959,5007)}{F(H\beta)}\right). \tag{4.3.5}$$

We derive the metallicities according to the formalism described as the "best" oxygen abundance determined by Kobulnicky & Kewley (2004). We use the O32 parameter ($f_{[\mathrm{OIII}]}/f_{[\mathrm{OII}]}$) as a branch indicator (Maiolino et al., 2008), where O32 $>$ 2 suggests the lower branch solution and O32 $<$ 1 suggests the upper branch solution. The four galaxies in this study have O32 values between 0.26 and 0.74 indicating that the upper branch solution is appropriate. The derived metallicities of our galaxies are listed in Table 4.6. Compared to the solar abundance of log(O/H) + 12 = 8.69 (Asplund et al., 2009) we find that galaxy J0423A and J0423C have metallicities of 0.1 ± 0.1 and 0.25 ± 0.06. However, since we are not applying a dust correction we could overestimate the metallicities.

Table 4.9: Metallicity of the galaxies and expected metallicity based on extrapolation using a constant slope at the absorber position assuming an extended gas disk.

Name	$Z_{\rm mean}$	$Z_{\rm central}$	θ[kpc]	$Z_{\rm exp}/Z_\odot$
J0423A	0.1 ± 0.1	0.2 ± 0.1	102	-2 ± 1
J0423B	0.4 ± 0.9	0.5 ± 0.9	133	-3 ± 1
J0423C	0.25 ± 0.06	0.32 ± 0.06	146	-3 ± 2
J0423D	0.3 ± 0.9	0.3 ± 0.9	216	-5 ± 2

Note: $Z = 0$ is equal to the solar abundance.

Since we do not detect the Hβ emission line from J0423B and J0423D, we use the stellar mass-metallicity relation to determine the gas phase metallicity of these two galaxies. We use the relation given by Zahid et al. (2014) who fits the following function to a sample from DEEP2 at $z \simeq 0.8$:

$$12 + \log(\mathrm{O/H}) = \mathrm{Z_0} + \log\left(1 - \exp\left(-\left[\frac{\mathrm{M_\star}}{\mathrm{M_0}}\right]^\gamma\right)\right), \tag{4.3.6}$$

where $Z_0 = 9.10$, $\log(M_0[\mathrm{M}_\odot]) = 9.80$ and $\gamma = 0.52$. This yields a metallicity of $12 + \log(\mathrm{O/H}) = 9.1 \pm 0.9$ and 9.0 ± 0.9 for J0423B and J0423D, respectively. The 1σ scatter in the DEEP2 data is quite large and therefore the derived metallicity has a large error bar.

Neutral Gas Metallicity We use the combined fits of FeII2600Å, and FeII2382Å and the HI column density derived by (Rao et al., 2006) to determine the metallicity of the absorbing gas without taking dust into account. A lower limit is reported to reflect possible ionisation correction. We find that $[\mathrm{Fe/H}] = \log(\mathrm{Fe/H})_{\rm abs} - \log(\mathrm{Fe/H})_\odot$ is higher than -1.16.

Comparison Large integral field surveys have shown that galaxies with $\log(M_\star) > 9.6$ have a uniform metallicity gradient within the disk of -0.026 dex kpc^{-1} Ho et al. (2015). However, at distances beyond $2R_{\rm e}$ first pieces of evidence for a flattening of the metallicity gradients are found (Belfiore et al., 2017). For absorption line systems a similar shallow negative metallicity gradient is observed out to 25 kpc (e.g. Péroux et al., 2014; Christensen et al., 2014; Rahmani et al., 2018). In the system presented in this work the impact parameter is > 100 kpc and therefore much larger than the ones probed in the aforementioned studies. We test whether we can connect the galaxies with the absorbing

gas using a uniform metallicity gradient. We extrapolate the metallicity observed in the four galaxies to the position of the intervening absorber using a constant gradient from the literature. First, we derive the central metallicity of the galaxies from the total metallicity reported in Table 4.9 and using the solar abundance of log(O/H) + 12 = 8.69 (Asplund et al., 2009). To derive the central metallicity we assume a linear distribution of the mean metallicity quoted in Table 4.9 over two $r_{1/2}$ where we use $r_{1/2}$ from the 3D fitting if available. We use the standard metallicity gradient determined within the disk quoted above. The same metallicity gradient is then used to extrapolate the derived central gas phase metallicity to the position of the absorber. The mean and central metallicity of the galaxies and the expected metallicity at the position of the absorber are given in Table 4.9 in dex offset from $Z_{\odot}$. We find that the extrapolated metallicity is above a simple extrapolation of the metallicity gradient. This shows that the metallicity gradient cannot be extended to such large distances.

However, here we are comparing the metallicity of the ionized gas in the galaxy with the metallicity of neutral gas probed by the absorption. Furthermore, the standard deviation in the observed gradients is ±0.010 dex kpc^{-1} in the study by Ho et al. (2015). The corresponding uncertainty in the extrapolation is shown in Table 4.9. Considering this and the additional caveat of using uniform gradients discussed above we regard this calculation only as an indication.

4.4 Discussion

4.4.1 The Nature of the Galaxy J0423B

Galaxy J0423B is detected in ^{12}CO(2–1) and the ^{12}CO(3–2) as well as our MUSE observations. Here we collect all this information and discuss the nature of this galaxy. In § 4.3.4 it is shown that the ratio of the ^{12}CO(2–1) and the ^{12}CO(3–2) emission line is consistent with J0423B being a LIRG. Deriving the SFR of J0423B based on $L_{\rm FIR}$ is strongly depending on the choice of template SEDs. We have conducted an analysis using different sets of templates, which yield yield $L_{\rm FIR}$ based SFR of 10 – 50 $M_{\odot}$ yr^{-1}. We conclude that J0423B could be identified as a LIRG, but to draw firm conclusions a better

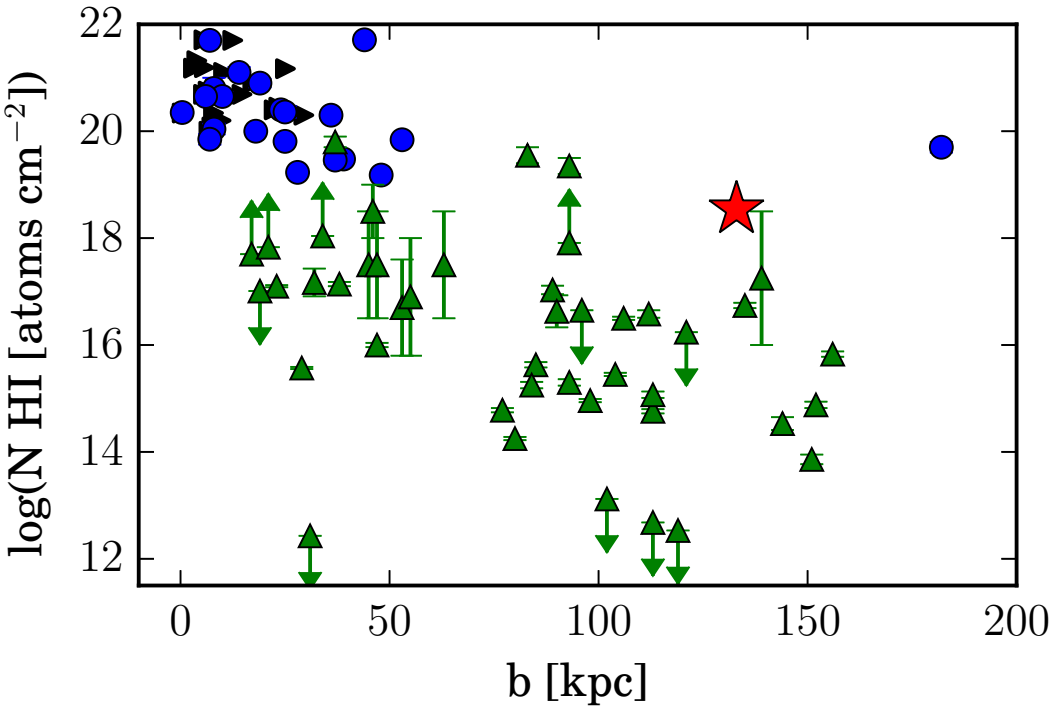

Figure 4.8: Column density of the intervening absorber as a function of impact parameter from J0423B (red star), DLAs from Zwaan et al. (2005) (black triangles) and Péroux et al. (2011) (blue circles) and subDLAs and LLS from the COS halos survey (Prochaska et al., 2017) (green triangles).

sampling of the SED is necessary.

4.4.2 Assessing the Possibility of a Misidentification

The fact that we only detect galaxies at large impact parameters from the quasar sight-line raises the question whether an undetected galaxy hiding in the bright quasar light could be responsible for the absorption. Interestingly, Churchill et al. (1996) report a galaxy at an impact parameter of 2.1″ or 14.6 kpc and Rao et al. (2011) report another galaxy at an impact parameter of 3.6″ or 25 kpc. We do not detect either of these galaxies in our data. In addition, these objects are not seen in quasar PSF-subtracted archival HST/NICMOS images (PID 7451). We determine the non-dust-corrected limiting SFR of 0.2 $M_\odot$ yr^{-1} over the full field of view and 0.3 $M_\odot$ yr^{-1} in a 2″ × 2″ wide field centred on the position of the quasar. We take this as the upper limit on the SFR of an undetected galaxy within

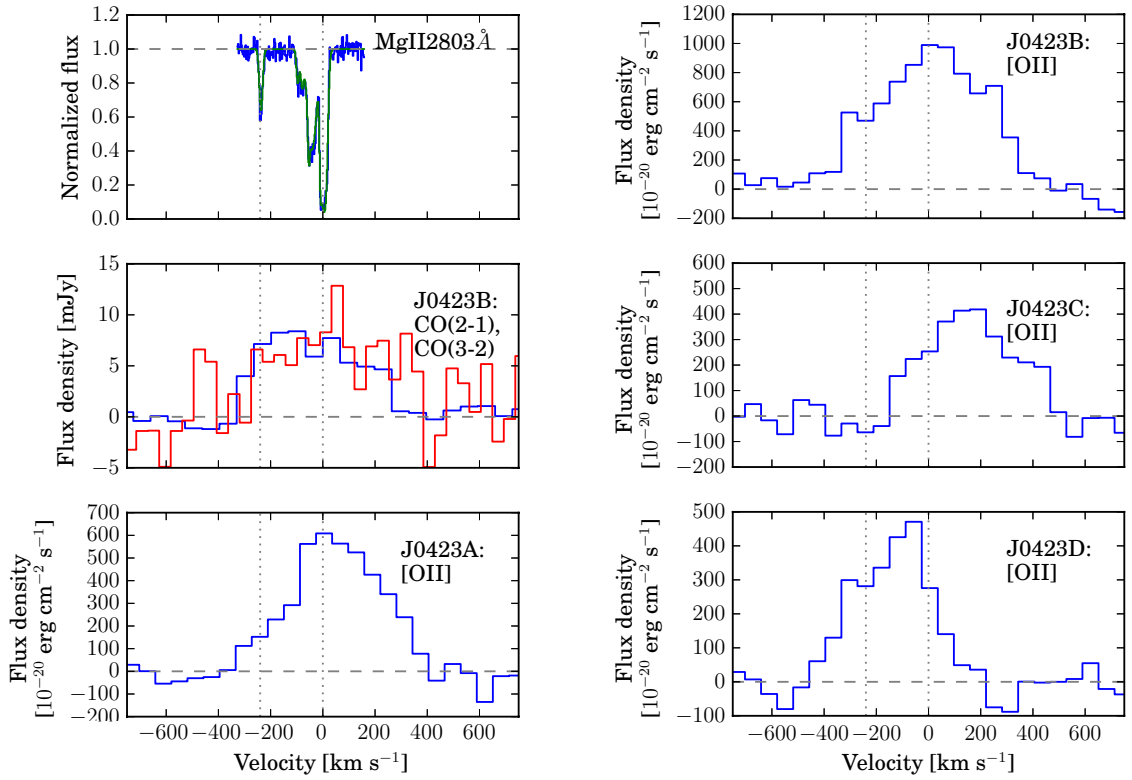

Figure 4.9: Comparison of all detected systems from top to bottom: MgII absorption in the quasar spectrum from the HIRES spectrum, ^{12}CO(2–1) (blue) and ^{12}CO(3–2) (red) from J0423B from ALMACAL, the continuum subtracted [OII] emission line spectra from J0423A, J0423B, J0423C and J0423D all plotted relative to the absorber redshift. We stress that the width of the ^{12}CO and [OII] emission lines cannot be directly compared in this plot since the [OII] emission line doublet is not resolved in the MUSE observations.

the quasar point spread function.

We compare the HI column density of the absorber and the impact parameter of the most massive group member with the column density - impact parameters observed for DLAs (Zwaan et al., 2005; Péroux et al., 2011) and subDLAs and LLS from the COS Halos survey (Prochaska et al., 2017) in Fig. 4.8. Assuming that J0423B can be uniquely associated with the Ly α absorption line, we see it is in the upper envelope of the relation between impact parameter and column density, but not atypical compared to other identified galaxy-absorption line pairs from the literature. This lessens the immediate need for another galaxy at a smaller impact parameter.

4.4.3 The Nature of the Absorbing Gas

Here, we discuss the possibility that the absorbing gas is tracing an outflow or intra group medium.

We consider whether the gas seen in absorption could be related to an outflow from one of the identified galaxies. In this galaxy group an outflow is most likely starburst-driven and would, therefore, originate from J0423B. This is further supported by the morpho-kinematic properties of the galaxies studied in § 4.3.6. If we assume that the outflow of gas from galaxies is most efficient along the minor axis theoretically predicted by Kereš et al. (2009); Stewart et al. (2011) and empirically motivated by recent studies (e.g. Bordoloi et al., 2011; Bouché et al., 2012b; Schroetter et al., 2015) the best candidate having an outflow that could be probed by the absorption is J0423B. Furthermore, we assume a constant typical velocity of a galactic wind in a star-forming galaxy of 300 km s^{-1} (Veilleux et al., 2005). This yields a travel time of $\sim$ 430 Myr from J0423B to the position where we see the absorption. Recently, first attempts in theoretical modelling were made to understand how a cool outflow can be produced (Richings & Faucher-Giguere, 2018).

Another explanation for the gas seen in absorption could be that it is tracing the intra-group medium. The MUSE observations revealed four galaxies at the absorber redshift, which is an over-density compared to the total redshift range. We expect based on the [OII] luminosity function given by Ly et al. (2007) 0.05 galaxies above the limiting SFR within the MUSE field of view in a redshift range covered by the galaxy group. Therefore,

we finally consider whether the gas seen in absorption against the background quasar is probing the CGM of the group of galaxies that we identify to be close in redshift space and in projected separation. We compare the alignment of the galaxies and the absorber in velocity space. In Fig. 4.9 we show the position of the absorber, the ^{12}CO detections from the ALMA observations and the ionized gas detected with MUSE in velocity space with respect to the absorber redshift. We find that all galaxies align well with the absorber, where J0423C is redshifted by 200 km s^{-1} and J0423D is blueshifted by -250 km s^{-1} with respect to the absorber systemic velocity. This could indicate that the quasar absorption line probes the intra-group gas rather than the CGM of a single galaxy. Intervening absorbers are often found to trace intra-group gas at low redshift (Whiting et al., 2006; Kacprzak et al., 2010; Gauthier, 2013; Bielby et al., 2017; Fumagalli et al., 2017; Péroux et al., 2017; Rahmani et al., 2018). In these cases the velocity width of the absorption ranges from less than 100 km s^{-1} to more than 600 km s^{-1}. At this stage, we cannot distinguish intra-group gas from CGM based on this property.

The spatial extent of the CGM in group galaxies is reported to be more than 140 kpc and the intra-group gas can be even more extended (Bordoloi et al., 2011).

As an illustration, we compute an estimate of the dynamical mass of the group and the radius of the zero-velocity surface. To calculate the dynamical mass, we use the 'projected mass estimator' (Heisler et al., 1985) defined by:

$$M_{\rm PM} = \frac{32/\pi}{\mathrm{G}(N_{\rm m} - 1.5)} \sum_i v_i^2 r_i, \tag{4.4.7}$$

where G is the gravitational constant, $N_{\rm m}$ is the number of observed group members, v_i is the velocity of the group member i with respect to the group mean velocity and r_i is the projected distance of the group member i from the group centre. Here we define the most massive galaxy as the group centre since we cannot be sure that all group members are observed. This yields a dynamical mass of the group of $10^{12.9}\mathrm{M}_\odot$. Furthermore, we compute the radius of the zero-velocity surface, R_0, defined as the surface beyond which galaxies participate in the Hubble expansion (Sandage, 1986). It is derived as follows:

$$R_0 = \left(\frac{8GT^2}{\pi^2} M_{\rm dyn}\right)^{1/3}, \tag{4.4.8}$$

where T is the age of the group. We assume that the age of the group is 7.5 Gyr, which is the age of the universe at the redshift of the group. This yields a radius of the zero-velocity surface of 1.2 Mpc. The gas that is probed by the Ly α absorption is well within this radius.

Furthermore, it is well-known from nearby interacting groups that the group galaxies can be embedded in a large-scale atomic gas reservoir (Yun et al., 1994).

4.5 Summary and Conclusion

In this case study of a Lyman Limit System at $z = 0.633$, we show the power of combining observations of the cool ionized gas with MUSE and ALMA observations of the ^{12}CO emission lines tracing the molecular gas in galaxies connected with a Ly α absorber. We measure two rotational transitions of the ^{12}CO line in emission, corresponding to a galaxy at the same redshift as the Ly α absorption line. This allows us to determine the molecular gas mass, as well as to put constraints on the ISM properties of this galaxy. We can efficiently identify star-forming galaxies at the absorber redshift using additional optical IFU observations. With these observations, we can probe the cool ionized gas in the galaxies and study their morpho-kinematics. In combination with the observations of the neutral gas probed in absorption, the observations of the cool ionized and molecular gas offer a complete census of the cool gas, which is needed to gain a better understanding of what types of galaxies are probed by Ly α absorbers.

In the particular system presented in this study we find a group of massive galaxies with masses of $M_\star = 10^{10.3-11.2}\,M_\odot$ connected to a LLS with $\log(N(\mathrm{HI})/\ \mathrm{atoms\ cm^{-2}}) = 18.54^{+0.07}_{-0.10}$ at a redshift of $z = 0.633$. The impact parameter between the quasar sight line and the closest galaxy is 102 kpc and 133 kpc for the most massive galaxy. No other galaxy is detected closer to the quasar down to a dust-uncorrected limiting SFR of 0.2 $M_\odot\ yr^{-1}$ in the field and 0.3 $M_\odot\ yr^{-1}$ at the quasar position. For the three lower mass galaxies, we find a dust corrected SFR of 3 $M_\odot\ yr^{-1}$ < SFR < 7.5 $M_\odot\ yr^{-1}$ and for the most massive galaxy we find a SFR based on the total far-infrared luminosity of $(10 - 50)\ M_\odot\ yr^{-1}$.

The most massive galaxy is also detected in our ALMA ^{12}CO(2–1) and ^{12}CO(3–2)

observations, from which we derive a molecular gas mass of $M_{H2} = 1 - 9 \times 10^{10}$ $M_\odot$. We infer that this galaxy is likely to be a LIRG based on the emission line ratios as well as the ratio of the far-infrared based SFR and the dust-uncorrected SFR based on the [OII] emission line flux. This is the first time that multiple ^{12}CO transitions are observed from one galaxy connected to a Ly α absorber. For the other galaxies in the field we determine an upper limit of $M_{H2} < 17 \times 10^9$ $M_\odot$.

We are able to model the morpho-kinematics of the three closest galaxies. As presented in Section 4.3.6, all three galaxies have velocity fields consistent with a rotating disk. Moreover, we construct a line of sight velocity map from the ^{12}CO(2–1) emission line for J0423B. It is found that the velocity field from the cool ionized gas and the molecular gas are comparable.

We explore different explanations for the neutral gas probed in absorption.

- Another galaxy could be closer to the line of sight towards the quasar, that is not seen in our observations. The limiting dust-uncorrected SFR in our MUSE data cubes is 0.2 $M_\odot$ yr^{-1} in the field and 0.3 $M_\odot$ yr^{-1} at the position of the quasar. At this low SFR, the galaxy is unlikely to have an outflow and therefore it must be close to the quasar line of sight and the absorption is actually probing the ISM of this galaxy. We note that we cannot rule out this possibility completely, but we emphasize that our MUSE observations reach a higher completeness compared to previous studies using broad-band imaging.

- The neutral gas could be tracing an outflow from the most massive galaxy J0423B since the quasar line of sight is aligned with the minor axis of the galaxy. We estimate, that for a constant outflow speed of 300 km s^{-1} it would take the gas 400 Myr to travel to the position of the absorber. However, the question remains how the gas can stay cool in the outflow or whether it can cool at larger distances. Furthermore, outflows of neutral gas are not yet observed at such large distances. Another caveat for this scenario is that a constant outflow in just one direction from a galaxy in a group environment over 400 Myr is unlikely.

- The impact parameter of 133 kpc for the most massive galaxy is comparable with the spatial extent of the intra-group gas quoted by Bordoloi et al. (2011). Moreover,

recent studies frequently find intervening absorbers probing the intra-group gas. We argue that this is, apart from an undetected galaxy closer to the quasar-line-of-sight, the most probable explanation for the gas traced by the absorption.

Finally, finding multiple galaxies at the absorber redshift adds further evidence to the findings by Whiting et al. (2006); Kacprzak et al. (2010); Gauthier (2013); Bielby et al. (2017); Fumagalli et al. (2017); Péroux et al. (2017); Rahmani et al. (2018) suggesting that the classical picture of a one-to-one correlation between a Ly α absorber and the host galaxy is incomplete and needs to be revised.

Chapter 5

Absorption-Selected Galaxies with Evidence for Excited ISMs

Abstract

Gas-rich galaxies are selected efficiently via quasar absorption lines, as outlined in Chapter 1. Recently, a new perspective on such absorption-selected systems has opened up by studying the molecular gas content of absorber host galaxies using ALMA CO emission line observations. Here, we present an analysis of the three absorber host galaxies presented in Chapter 3 that have multiple CO transitions. One of which was target of our multi-wavelength study reported in Chapter 4. Here we include in two additional absorption-selected galaxies at $z \sim 0.5$ associated with one Ly α absorber towards J0238+1636. The CO spectral line energy distribution (CO SLED) of these galaxies appear distinct from that of typical star-forming galaxies at similar redshifts and is comparable with that of luminous infrared galaxies or AGN. Indeed, these galaxies are associated with optically identified AGN activity. We infer that the CO line ratios and the $\alpha_{\rm CO}$ conversion factor differ from the Galactic values. Our findings suggest that at least a fraction of absorption-selected systems shows ISM conditions deviating from those of normal star-forming galaxies. For a robust molecular gas mass calculation, it is therefore important to construct the CO SLED. Absorption-line-selection identifies systems with widely distributed gas, which may preferentially select interacting galaxies, which in turn will have more excited CO SLEDs than isolated galaxies. Furthermore, we raise the

question whether quasar absorbers preferentially trace galaxy overdensities.

5.1 Introduction

The neutral phase of the gas traced by HI is thought to be the original reservoir for star formation (Wolfe et al., 1986). Quasar absorbers associated with foreground galaxies provide a unique tool to probe this neutral gas phase down to low gas densities and at any redshift. However, the physical processes that transform HI into molecular gas and hence stars remain unconstrained. A direct probe of the fuel for star formation has to come from measurements of molecular gas. Molecular Hydrogen (H_2) absorbers at UV wavelengths are only detected in $\approx 50\%$ of the HI-rich systems at low redshift (Muzahid et al., 2015b) and $\approx 15\%$ at high redshift (Noterdaeme et al., 2008). Furthermore, the median molecular fractions in absorbers with H_2 detections reported are low: $\log f(H_2)$ is -1.93 ± 0.63 at low redshift and -2.3 ± 0.8 at high redshift showing no significant evolution. These low detection rates in absorption are probably a consequence of the low sky cross section of molecular gas compared to HI neutral gas (Zwaan & Prochaska, 2006).

Progress in relating the properties of HI-rich systems to their star formation has to come from identifying the galaxy counterparts to quasar absorbers. Theoretical models suggest the true absorbers, at least those with large column density of neutral gas, are associated with galaxies (Fumagalli et al., 2011; van de Voort & Schaye, 2012; Bird et al., 2014). The observational challenge of identifying the absorber host galaxy in emission has been partly overcome using high-z absorbers to block the light from the background quasar in direct imaging (e.g. Fumagalli et al., 2010), using slit triangulation (e.g. Krogager et al., 2017), and thanks to integral field units (IFU) (e.g. Péroux et al., 2011; Fumagalli et al., 2017; Péroux et al., 2017; Rudie et al., 2017; Klitsch et al., 2018). Several studies report Lyα absorbers that are associated to galaxy groups instead of isolated galaxies similar to the study presented in Chapter 4 (e.g. Bielby et al., 2016; Fumagalli et al., 2017; Péroux et al., 2017; Rahmani et al., 2018). Furthermore, Lyα absorber host galaxies exhibiting strong winds are reported in the literature (e.g. Rudie et al., 2017; Fynbo et al., 2018b). Although the number of observations of quasar absorber host galaxies is rising, the impact of selection criteria (high metallicity, etc.) and different observation techniques is unclear.

Table 5.1: Summary of the ALMA observations of J0238+1636.

Band	ang. res. [″]	rms [mJy bm^{-1}]	vel. res [km s^{-1}]	$t_{\rm int}$ [ks]
4	0.43	0.18	36	0.6
6	0.96	0.24	25	5.0
7	0.67	0.14	20	1.5
7 cont.	0.32	0.04	–	5.1

Therefore, the question of exactly what population of galaxies is traced by the absorption remains.

Recently, a new perspective on relating baryons traced by cold gas and stars opened up with reports of CO rotational transitions emission in quasar absorber galaxy hosts observed with ALMA. To date ten molecular gas-rich absorption-selected galaxies with large inferred molecular gas masses of 10^{10} – 10^{11} $M_\odot$ have been analysed including the one presented in Chapter 4 (Neeleman et al., 2016, 2018; Kanekar et al., 2018; Møller et al., 2018; Klitsch et al., 2018; Fynbo et al., 2018b). The combination of low detection rates of H_2 absorption and the high molecular gas masses inferred from CO observations is a key question in this field. Here we report the detection of CO emission from two galaxies at the redshift of one Ly α absorber in our (sub-)millimetre survey ALMACAL. For each of these, we detect multiple CO transitions, which offers fresh clues on the molecular gas conditions of these galaxies.

5.2 Sample and Reduction

In this study we use ALMACAL version July 2017. The data retrieval and reduction are described in Chapter 2. The properties of the final data cubes are summarised in Table 5.1.The cross-matching and detection procedure are described in Chapter 3. Here we focus on absorber host galaxies with multiple CO emission line detections in order to study the CO excitation. We discover two new molecular gas-rich galaxies with multiple CO emission lines detected at the redshift of an HI absorber towards the quasar J0238+1636 at $z_{\rm abs} = 0.524$. Additionally, we include the molecular gas-rich galaxy detected in the field of J0423−0120 ($z_{\rm abs} = 0.633$) presented in Chapter 4 in this analysis.

The gas properties of the absorbers, CO detected host galaxies and impact parameters

Table 5.2: ALMA detections of multiple CO emission lines at the redshift of two absorbers towards J0238+1636 and J0423–0120.

Name	z	R.A. (J2000)	Dec. (J2000)	θ [kpc]	$S_{\rm int}^{\rm cont.}$ [mJy]	CO trans.	$S_{\rm peak}$ [mJy]	$S_{\rm int}$ [Jy km s^{-1}]	$\log(L'_{\rm CO})$ [K km s^{-1} pc^2]	FWHM [km s^{-1}]
J0238A	0.524	02 38 38.94	+16 36 57.3	12	$< 0.1^b$	2-1	1.5 ± 0.2	0.32 ± 0.06	9.07 ± 0.06	350 ± 20
						3-2	2.3 ± 0.2	0.70 ± 0.09	9.05 ± 0.09	380 ± 40
						4-3	4.1 ± 0.9	1.2 ± 0.4	9.0 ± 0.4	420 ± 30
J0238A1	0.524	02 38 39.01	+16 36 59.2	7	$< 0.1^b$	2-1	0.7 ± 0.2	0.2 ± 0.05	8.87 ± 0.05	350 ± 40
						3-2	1.4 ± 0.2	0.43 ± 0.04	8.8 ± 0.1	380 ± 40
						4-3	-	< 0.9	< 9	-
J0423B	0.633	04 23 16.07	−01 20 52.1	133	0.8 ± 0.2^a	2-1	8.4 ± 0.7	3.6 ± 0.2	10.28 ± 0.02	590 ± 30
						3-2	10 ± 1	5.2 ± 0.3	10.10 ± 0.02	610 ± 40

θ denotes the impact parameter between the galaxy and the background quasar. The properties of J0423B are taken from Chapter 4. ^{a} denotes the Band 6 and ^{b} denoted the Band 7 continuum flux. The upper limit on the continuum flux for J0238A and J0238A1 are based on the 3σ flux limit from the Band 7 map and assuming that they are unresolved. The upper limit of the CO(4-3) flux from J0238A1 is based on a 3σ flux limit assuming a FWHM of 350 km s^{-1}.

are given in Table 5.2 and 5.3, taken from Chapter 4 and Rao et al. (2006); Junkkarinen et al. (2004); Burbidge et al. (1996).

The absorption towards J0238+1636 (also known as AO 0235+164) is also seen at a restframe wavelength of 21 cm revealing a complex system of multiple absorbing clouds (Roberts et al., 1976). Two galaxies—J0238A and J0238A1—with small impact parameters (1.1″ = 7 kpc and 1.9″ = 12 kpc) between the galaxy position and the quasar sight line towards J0238+1636 were identified at the absorber redshift using [OII]-narrow-band imaging by Yanny et al. (1989). *HST* WFPC2 imaging suggests that these are two compact components embedded in an extended nebula (Chen et al., 2005). The CO detections from these galaxies are presented for the first time in this study. For consistency with previous publications we refer to these galaxies as J0238A and J0238A1.

For the absorber towards J04230–0120 we have identified a total of four galaxies at the absorber redshift using the MUSE IFU presented in Chapter 4. One of these four galaxies, J0423B, is also detected in CO(2–1) and CO(3–2) emission. It is proposed that the gas seen in absorption traces either intra-group gas, or an outflow from J0423B.

The properties of the ALMA-detected galaxies are given in Table 5.2. Flux maps and spectra are shown in Fig. 5.1. Flux maps are integrated over w_{20} which is also marked by the shaded area in the respective spectra. Spectra are measured using an aperture that encompasses the 3σ contours in the moment map. The line flux is determined by integrating over w_{20}. We use these multiple line detections to study the CO spectral line energy distribution (CO SLEDs) of these absorption-selected galaxies (see Fig. 5.2).

We cannot use the Band 6 observations to measure the continuum flux of J0238A and J0238A1, because of strong residuals from the quasar continuum. In Band 7 we do not see any residuals, however, we also do not detect the two galaxies. The 3σ upper limit assuming that the galaxies are not resolved is 0.1 mJy. As in Chapter 4, we use a set of template spectra for starburst galaxies from Polletta et al. (2007) which we scale to the observed 870 μm flux converted to the rest wavelength. Since the CO line ratios in J0238A and J0238A1 are more clearly destinct form those of normal star-forming galaxies, we have included more extreme SED templates in this analysis. The fitted spectrum is then integrated in the wavelength range from 8 - 1000 μm to obtain the total far-infrared luminosity $L_{\rm FIR}$. This is converted to the SFR using the Kennicutt (1998) relation. Based

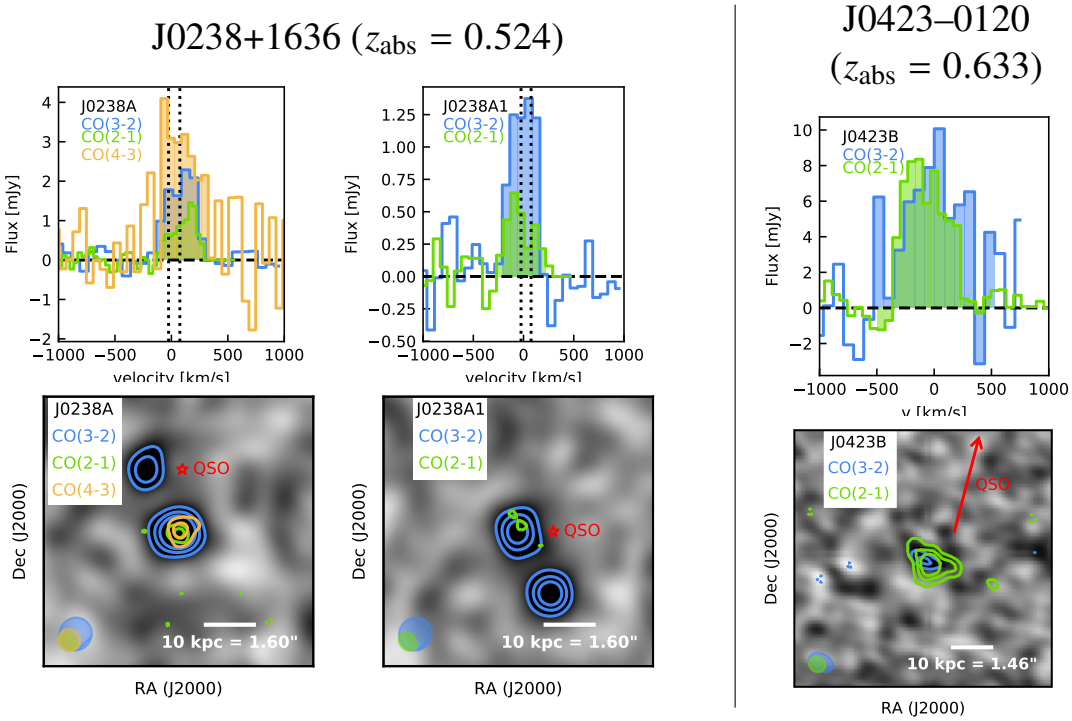

Figure 5.1: Spectra (*top*, primary beam corrected) and integrated flux maps (*bottom*, not primary beam corrected) of the absorption-selected galaxies with multiple ALMACAL CO lines detected from the same galaxy. *Top:* A velocity of 0 km s^{-1} corresponds to the redshift of the main absorption component. The dotted lines in the spectra of J0238A and J0238A1 represent the position of the second and third most prominent features in the 21 cm absorption spectrum. *Bottom:* The CO(3–2) emission line integrated flux maps are shown in grey-scale for all three galaxies, the contours mark the 3σ, 5σ and 7σ levels of the respective maps. For each map we integrate over the coloured region in the spectra shown above. The dotted contours mark the -3σ levels. The sight-line towards the quasar is marked by a red star. These are the first detections of multiple CO emission lines from absorption-selected galaxies enabling us to constrain the energetics of their ISM.

on this we derive the SFR limits reported in Table 5.3.

5.3 Analysis

At the redshift of the absorber towards J0238+1636, we find two CO-emitting galaxies. The absorption system is likely probing the joint gas distribution of both galaxies that was also seen in emission by Chen (2005). Roberts et al. (1976) reported a complex 21 cm absorption spectrum that might be due to several absorbing clouds. The main features are over-plotted in Fig. 5.1 and coincide with J0238A and J0238A1 in velocity space.

We use the CO SLEDs shown in Fig. 5.2 as a diagnostic plot to distinguish between

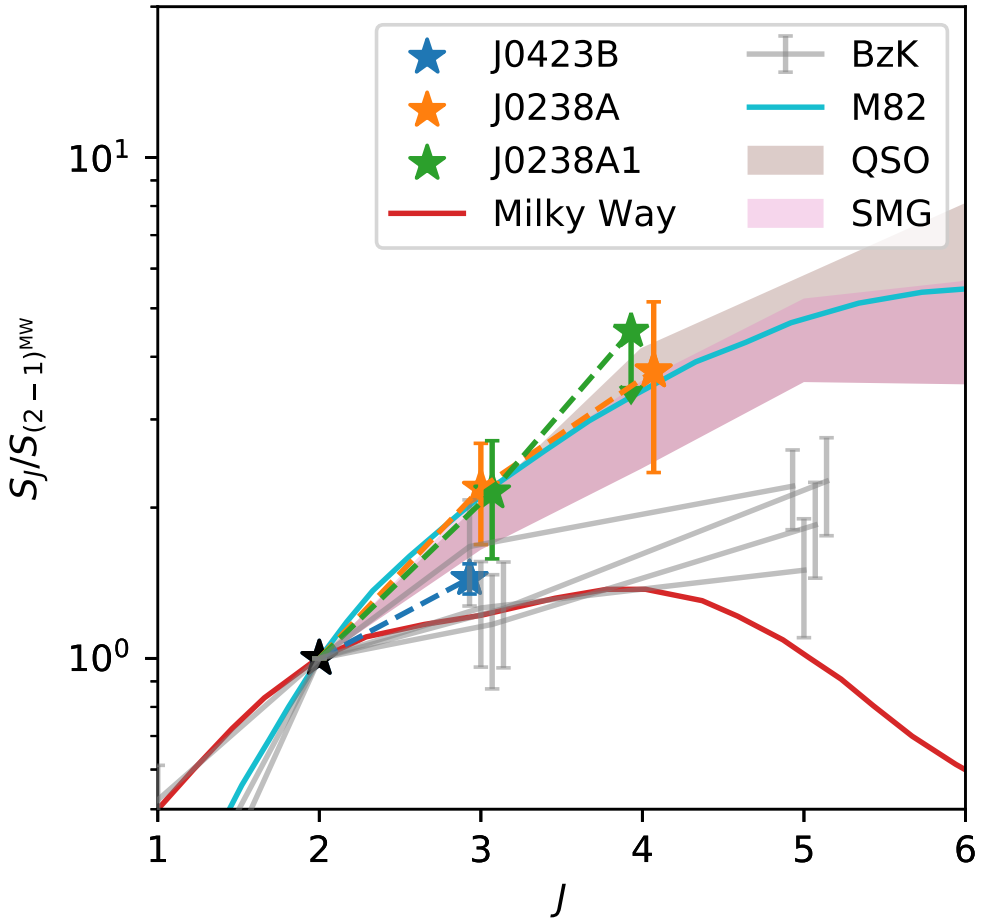

Figure 5.2: CO Spectral line energy distribution of the three absorption-selected galaxies with multiple CO emission lines detected in ALMACAL. We show the CO SLED for *BzK* galaxies (Daddi et al., 2015), the Milky Way, QSOs, SMGs and M82 (Ivison et al., 2011; Bothwell et al., 2013; Carilli & Walter, 2013) for comparison. The CO SLEDs of two absorption-selected galaxies differ from the CO SLED of normal star-forming galaxies at the low J transitions. This suggests that the temperature and density of the molecular gas in these galaxies is higher than in normal star-forming galaxies and is more similar to high redshift SMGs or AGN. We find hints that using the Galactic line luminosity conversion factors to derive molecular gas masses might overestimate the molecular gas masses for some absorption-selected galaxies.

Table 5.3: The derived physical properties of the CO-detected galaxies associated with two absorbers from our ALMA observations.

Name	log N(HI)	log $M_{\rm mol}$ [$M_\odot/\alpha_{\rm CO}$]	log $M_\star$ [$M_\odot$]	SFR[$M_\odot$ yr $^{-1}$]	$Z_{\rm abs}[Z_\odot]$	type
J0238A	$21.70^{+0.08}_{-0.10}$	9.12 ± 0.08	–	< 50	0.72 ± 0.24	BAL QSO[2]
J0238A1	$21.70^{+0.08}_{-0.10}$	8.9 ± 0.1	–	< 50	0.72 ± 0.24	AGN + starburst[3]
J0423B	$18.54^{+0.07}_{-0.10}$	10.33 ± 0.02	11.2 ± 0.1	50 ± 10	> 0.07	starburst[1]

References: [1] Chapter 4, [2] Burbidge et al. (1996), [3] Chen (2005)

gas conditions similar to normal star-forming galaxies and more active systems. We note that the CO SLEDs are normalized to the CO(2–1) flux because the CO(1–0) emission line was not observed towards the absorption-selected galaxies. Differences in the CO SLEDs at higher J transitions will appear smaller due to this normalization.

The shape of the CO SLED determines the conversion of higher J transition line fluxes to the CO(1–0) line flux, which is used to calculate the total molecular gas mass. The CO SLEDs of J0238A and J0238A1 are clearly distinct from the CO SLED of the Milky Way or BzK galaxies. This suggests that the temperature and density in these absorption-selected galaxies are higher than in "normal" star-forming galaxies. J0423B at $z = 0.633$ on the other hand shows a CO SLED only slightly steeper than that of the Milky Way and comparable with that of "normal" star-forming galaxies at higher redshift ($z \sim 1.5$). The SFR of this galaxy is 50 ± 10 $M_\odot$ yr^{-1} explaining the elevated CO SLED compared to the Milky Way (see Chapter 4). Hence, the Galactic conversion factor, $\alpha_{CO} \simeq 4.6$ $M_\odot$ $(K\,km\,s^{-1}pc^2)^{-1}$, and the Galactic CO line ratios might not be applicable. Instead, we argue that for the absorption-selected galaxies studied here, LIRG-like conversion factors are more appropriate. We convert the CO line flux to L'_{line} following the description from Solomon et al. (1992).

To derive the molecular gas mass we convert the luminosity of the CO(2–1) transition to the CO(1–0) line luminosity. We convert the line luminosities using the median conversion factor $r_{21} = L'_{CO(2-1)}/L'_{CO(1-0)} = 0.9$ for LIRGs (Papadopoulos et al., 2012a). The resulting molecular gas masses are reported in Table 5.3 and are $\sim 10^9 - 10^{10} M_\odot/\alpha_{CO}$.

Comparing the L'_{CO}–L_{FIR} relation we find that J0423B is consistent with local LIRGs and that J0238A and J0238A1 are in the lower envelope of local LIRGs (Greve et al., 2014).

5.4 Discussion and Conclusion

We report the detection of multiple CO emission lines from absorption-selected galaxies discovered in our ALMACAL survey. The CO SLEDs for two galaxies are more excited than those of "normal" star-forming galaxies indicating that the molecular gas temperature and density are higher in these galaxies. This confirms the optical identification as BAL

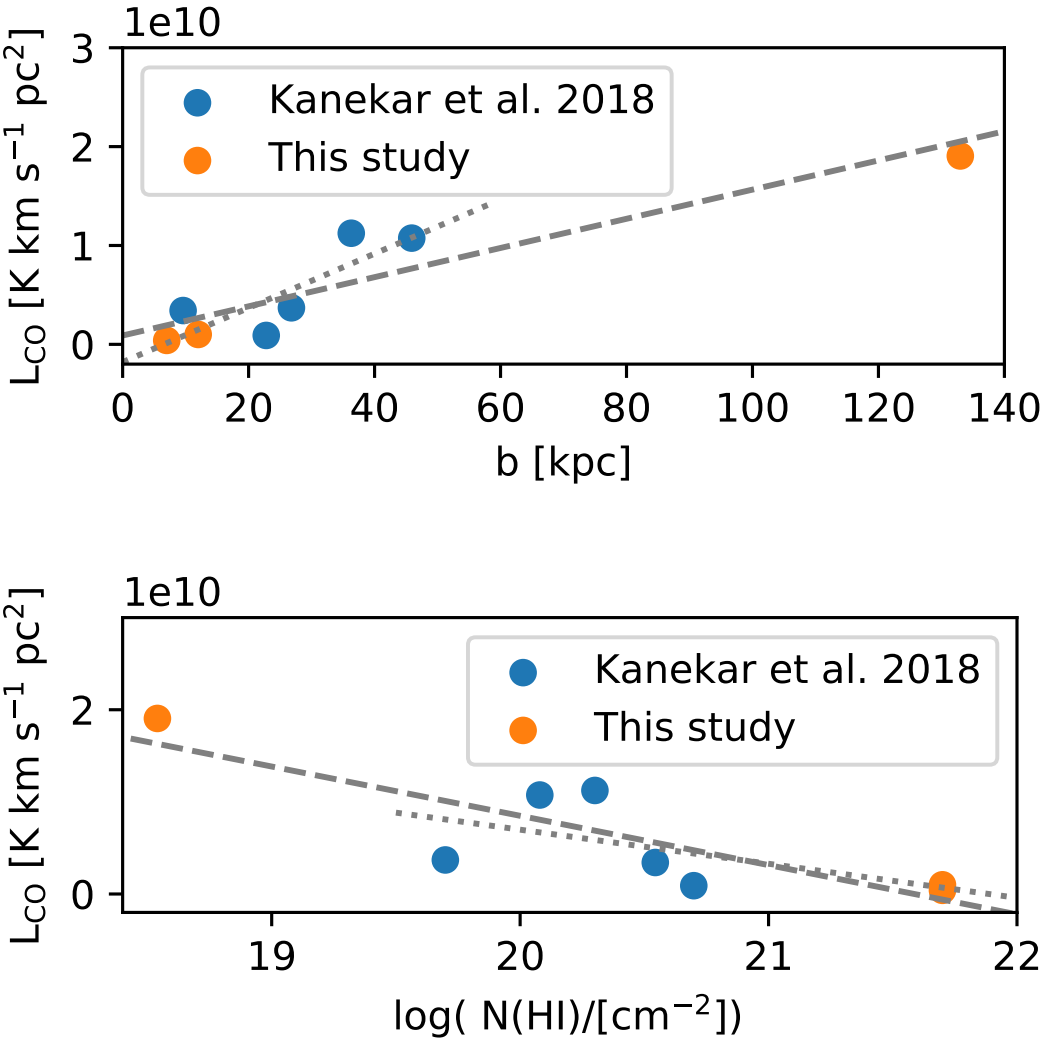

Figure 5.3: *Left:* CO(2-1) luminosity as a function of impact parameter. We show the absorption-selected galaxies presented by Kanekar et al. (2018), and the galaxies presented here. *Right:* CO(2-1) luminosity as a function of HI absorption column density. Errorbars are too small to be visible on these plots. We find correlation of L_{CO} with the impact parameter towards the QSO sight line and an anti-correlation of L_{CO} with the column density of the absorber. A fit of a linear function to the data is shown by the grey dashed line. We find the following best fits including J0423B: L_{CO}[K km s^{-1}pc^2] = $1.5\times10^8\,b$/[kpc]+9.0×10^8 and L_{CO}[K km s^{-1}pc^2] = -5.3×10^9 log(N(HI)/[cm^{-2}])+1.2×10^{11} and excluding J0423B: L_{CO}[K km s^{-1}pc^2] = $2.7\times10^8\ b$/[kpc] $-\ 1.8\times10^9$ and L_{CO}[K km s^{-1}pc^2] = -3.7×10^9 log(N(HI)/[cm^{-2}]) + 8.1×10^{10}.

QSO and mix of AGN and starburst, respectively. These findings suggest that the Galactic CO line ratios and $\alpha_{\rm CO}$ conversion factor might not be applicable to derive molecular gas masses of all damped Lyα galaxies.

We derive molecular gas masses of $10^{8.9}$ to $10^{10.33}$ $M_\odot/\alpha_{\rm CO}$ using a r_{21} conversion factor of 0.9. These derived molecular gas masses are smaller than those reported by Kanekar et al. (2018), who used a Galactic r_{21} ratio and a Galactic CO-to-H_2 conversion factor. Their resulting molecular gas masses are $10^{9.8-10.9} \times (\alpha_{\rm CO}/4.36) \times (0.63/r_{21})M_\odot$. As discussed above for a fraction of these galaxies a smaller CO-to-H_2 conversion factor could be more appropriate. Direct evidence for a more excited ISM from other wavelength regimes such as the detection of an AGN in J0238A and A1 should always be taken into account when choosing appropriate line ratios and $\alpha_{\rm CO}$. In fact, at least one galaxy in Kanekar et al. (2018) is reported to interact with another galaxy (Straka et al., 2016).

Comparing the line fluxes, we find that for J0423B the CO(2–1) flux is higher than in any of the galaxies presented by Kanekar et al. (2018) while for J0238A and A1 the fluxes are on the low end of the ones reported by Kanekar et al. (2018). This is also illustrated in Fig. 5.3, where we show the CO(2–1) luminosity of the absorber host galaxies as a function of impact parameters and column densities of the absorbers from this study and Kanekar et al. (2018). Using the Pearson correlation coefficient we find a correlation between $L_{\rm CO}$ and the impact parameter with a p-value of 0.01 and an anti-correlation between $L_{\rm CO}$ and log N(HI) with a p-value of 0.002. To test whether these relations are only driven by J0423B, we exclude it from the analysis resulting in p-values of 0.1 and 0.01. In these two samples low impact parameter absorbers probe the high density CGM close to low mass galaxies, while at high impact parameters the lower density diffuse gas around high mass galaxies is traced. Using a significance level of 0.05 we would only reject the null-hypothesis of a correlation between $L_{\rm CO}$ and the impact parameter. However, the results are based on a small dataset and more data is needed to further investigate these correlations.

The question remains whether the three galaxies presented here are special among absorption-selected systems? Verdes-Montenegro et al. (2001) proposed a scenario in which—depending on the evolutionary phase of the group—up to $\sim$ 60% of the HI gas is stripped from the galaxies by tidal interactions and resides in a diffuse intra-group

medium. This was tested in the Hickson groups. Borthakur et al. (2010) reported a diffuse gas fraction of $\sim 20-50\%$ increasing the cross-section of HI compared to isolated galaxies. This would result in a higher likelihood to probe interacting galaxies with Lyα absorbers. Such interacting systems are also more likely to contain galaxies with enhanced star formation and AGN activity. Hence, it could be expected that the CO SLEDs of some absorption-selected galaxies are more excited than typical gas rich field galaxies. To test further this hypothesis more data are needed to populate the CO SLEDs of absorption-selected galaxies. In general, it is important to study the CO SLED to properly derive molecular gas masses. Similarly, galactic winds can increase the cross-section of HI, where the most energetic events will produce the highest sky-coverage. Such galaxies will deviate from the Galactic CO SLED as well.

Since both interactions and winds are predicted to be enhanced at higher redshift this might have an important impact the types of galaxies identified through surveys of absorption-selected galaxies in the distant universe.

Chapter 6

Cosmic Molecular Gas Mass Density Constraints from a Blind Search for Intervening Molecular Absorbers

Abstract

The physical processes driving the dramatic change in star-formation rate between $z \sim 2$ and the present day are still to be identified convincingly. In order to address this issue we need to characterize the evolution of the molecular gas contents as fuel for star formation. Here we use intervening CO absorption lines against mm-bright background sources to provide a census of the molecular mass density of the Universe. The data used in this work are taken from the ALMACAL survey presented in Chapter 2. While we report multiple Galactic absorption lines and one intrinsic absorber, no extragalactic intervening molecular absorbers are detected. However, thanks to the large redshift path surveyed ($\Delta z = 181$), we provide constraints on the cosmic evolution of the molecular column density distribution function beyond $z \sim 0$. In addition, we probe column densities of $N(H_2) > 10^{16}$ atoms cm^{-2}, five orders of magnitude lower than in previous studies. We use the cosmological hydrodynamical simulation IllustrisTNG to show that our upper limits of $\rho(H_2) \lesssim 10^{8.3} M_\odot Mpc^{-3}$ at $0 < z \leq 1.7$ already provide new constraints on current theoretical predictions of the cold molecular phase of the gas. These results are in agreement with recent CO emission-line results and are complementary to those studies.

The combined constraints indicate that the present decrease of the cosmic star-formation rate history is consistent with an increasing depletion of molecular gas in galaxies compared to $z \sim 2$.

6.1 Introduction

Understanding the efficiency of converting baryons into stars is a challenge in studies of galaxy formation and evolution. The star-formation rate history (SFH) is well established from observations of star-forming galaxies across cosmic time at infrared, ultraviolet, submillimetre, and radio wavelengths. The star-formation rate (SFR) density increased at high redshift, reached a peak at around $z \sim 2$ and decreased until today (see Madau & Dickinson, 2014, for a review). Which physical processes are driving this dramatic change and their relative importance represent two of the main unanswered questions of modern astrophysics. Whether this is due to a lack of cold gas supply, or a lower efficiency in converting the gas into stars, or to the presence of strong outflows preventing the infall of new cold material, is still debated (e.g. Madau & Dickinson, 2014; Katsianis et al., 2017, and references therein). Simple expectations would have the SFH mirror the cold gas evolution, as gas is being consumed by star formation (e.g. Putman, 2017; Driver et al., 2018). The atomic gas density, $\Omega_{\rm HI}$, is the original reservoir of gas for star formation and is indeed well constrained locally and at $z > 2$. Most recent results, however, indicate a mild evolution in $\Omega_{\rm HI}$ with cosmic lookback time (e.g. Noterdaeme et al., 2009; Zafar et al., 2013; Rhee et al., 2018). Neutral hydrogen provides the essential reservoir, but it has to cool and transform to the molecular phase in order to provide the necessary conditions for star formation. Further studies using damped Ly α absorbers as well as H I 21 cm absorption traced with SKA path finder observations provide important clues on physical state of the atomic gas and the neutral ISM physics (Kanekar, 2014; Allison et al., 2016). However, a direct probe of the fuel for star formation has to come from measurements of the molecular phase of the gas.

In order to probe this essential phase of baryons over cosmic time, a number of deep cosmological surveys for CO emission lines have been conducted. The first study used the IRAM Plateau de Bure Interferometer to perform molecular line scans in the Hubble Deep

Field North and provided upper limits on Ω(CO) (Walter et al., 2014). More recently, the ALMA Spectroscopic Survey in the Hubble Ultra Deep Field (ASPECS), provided the first measurements of Ω(CO) at redshift $0 < z < 4.5$ (Decarli et al., 2016, 2019). The CO Luminosity Density at High Redshift (COLDz) survey (Riechers et al., 2018) undertaken with the VLA offers first indications of the molecular mass density at high redshift ($z \sim 2$–3 and $z \sim 5$–7). The fact that multiple transitions of CO at different redshifts can be searched in a given observed frequency setting greatly increases the redshift path, and hence the searched volume. These emission-line surveys are especially sensitive to the high-mass end of the molecular gas mass function. However, such observations require large investments in telescope time, and since typically only a small contiguous area is covered, the results are prone to cosmic variance effects.

Four intervening molecular absorbers have been detected in targeted surveys of strongly lensed systems that were known to show H I absorption (e.g. Wiklind & Combes, 1995; Kanekar et al., 2005; Wiklind et al., 2018; Combes et al., 2019). Only the molecular absorber towards PKS 1830-211 was detected before any other lines were known (Wiklind & Combes, 1996b). In addition, associated molecular absorption lines have been found in three intermediate-redshift AGN (Wiklind & Combes, 1994, 1996a; Allison et al., 2018). Similar, intrinsic absorption is observed more frequently in low redshift AGNs (e.g. Tremblay et al., 2018b; Maccagni et al., 2018; Rose et al., 2019) and in high-redshift SMGs (e.g. George et al., 2014; Falgarone et al., 2017; Indriolo et al., 2018). de Ugarte Postigo et al. (2018) also reported CO absorption lines against Gamma Ray Bursts (GRBs) observed with ALMA. However, to measure the cosmic molecular gas mass density in an unbiased way, blind detections of intervening molecular absorbers are required.

Here, we present a complementary approach to probing the molecular phase of the gas and its evolution with cosmic time free from cosmic variance issues. In analogy with studies at optical wavelengths (e.g. Péroux et al., 2003b; Zafar et al., 2013), we use mm-bright background sources to probe intervening molecular absorption lines. Moving from optical to mm wavelengths has the advantage that this study is not affected by dust attenuation in the quasar spectra which might be expected for molecular absorbers. Therefore, by choosing radio bright background sources we include potentially dusty absorbers. Furthermore, tracing molecular absorption offers a measurement of the cosmic

molecular gas density free from cosmic variance.

A similar "blind" study was performed at lower frequencies using the Green Bank Telescope (Kanekar et al., 2014). The authors surveyed a redshift path defined as $\Delta z = \sum_i (z_{\rm max} - z_{\rm min})$ of $\Delta z \sim 24$ at $0.81 < z < 1.91$ and did not detect any molecular absorbers with $N(H_2) \geq 3 \times 10^{21}$atoms cm^{-2}. In the present work, we perform a "blind" search for CO absorbers against a large sample of background sources. These sources are extracted from the ALMACAL survey, described in more detail in Oteo et al. (2016b). ALMACAL consists of observations of a large sample of bright, compact sources (generally blazars, see Bonato et al., 2018) which are used as calibrator sources for ALMA. These calibrators are ideal targets for an unbiased search for CO absorbers for two main reasons. First, as described in Chapter 2, the total integration time spent on ALMACAL sources is > 2000 hours, orders of magnitude more than what would be attainable in a targeted ALMA survey programme for intervening absorption lines. Secondly, since the calibrators are distributed all over the sky observable with ALMA, it is possible to quantify the effect of cosmic variance. In addition, the sensitivity of the absorption survey is independent of redshift and solely relies on the brightness of the unrelated background sources. Using absorption lines we are able to reach low gas column densities, providing us with a more complete and unbiased (with respect to excitation conditions) view of the molecular gas content of the Universe over cosmic time.

Caveats in this approach are similar to emission studies: Most significant is the uncertainty of the line identification resulting in an uncertainty of the redshift of the absorber as well as the derived column density. Our sample of quasars is flux limited at submm. wavelength and therefore susceptible to two effects of gravitational magnification. First the probability of finding quasars with absorbers is increased by the flux boosting from gravitational lensing by the absorber. Second the solid angle behind absorbers is gravitationally enlarged diluting the flux of the background quasar. Ménard & Péroux (2003) find indeed and excess of bright quasars with absorbers. Furthermore, ALMA calibrators are selected to be (sub)mm bright and have therefore all redshifts of $z \leq 3$.

The chapter is organised as follows: the data reduction is presented in Section 6.2, in Section 6.3 the detection method is described, in Section 6.3.2 the analysis is given, discussed in Section 6.4 and in Section 6.5 we summarize our conclusions. Throughout

this chapter we adopt a ΛCDM cosmological model with $H_0 = 70 \mathrm{kms}^{-1}\mathrm{Mpc}^{-1}$, $\Omega_\mathrm{m} = 0.3$ and $\Omega_\Lambda = 0.7$.

6.2 ALMACAL Observations and Data Reduction

We extract from the ALMACAL archive described in Chapter 2 all phase, amplitude and bandpass calibrator data from PI observations from Cycles 1 to 6, taken before the 4$^{\mathrm{th}}$ December 2018 (ALMACAL version December 2018). We only consider data taken with the ALMA 12-m array. This amounts to observations of 880 calibrators. To determine the redshift of the calibrators, we use the compilation of redshifts from the database presented by Bonato et al. (2018), combined with the updated redshift estimates of the AT20G sources (Mahony et al. (2011) and E. Mahony private comm.). For the remaining calibrators, we perform an additional query to the Simbad and NED databases. We note, however, that the accuracy of these redshifts might be limited. This results in redshift measurements of 622 calibrators presented in Figure 2.3. We test whether our sample of calibrators with and without redshift information are drawn from the same population of *WISE* colours and find that we have to reject the null-hypothesis based on a Kolmogorov-Smirnov test. However, we perform the line search on all quasar spectra irrespective of the availability of the redshift and therefore do not introduce a bias in out sample of calibrators.

We devise a new, optimised data processing strategy to handle the large data volume comprising several tens of thousands of spectra while maintaining the highest spectral resolution. A schematic view of the data reduction chain is illustrated by Fig. 6.1. To this end, the spectrum of the calibrator is extracted directly from the *uv* data, by fitting a point source model at the phase center. We extract the XX and YY polarisation data separately and add those in quadrature to obtain Stokes I spectra. We choose to only consider dual-polarization mode scans to keep the data retrieval simple and uniform, full polarisation data represents only a small fraction of the total ALMA archival data. For each calibrator observation, each spectral window is treated individually, resulting in a total of 28,644 spectra in our data base. To remove unwanted structures from the spectra, we apply a bandpass correction by taking ratios of the spectra of pairs of calibrators from

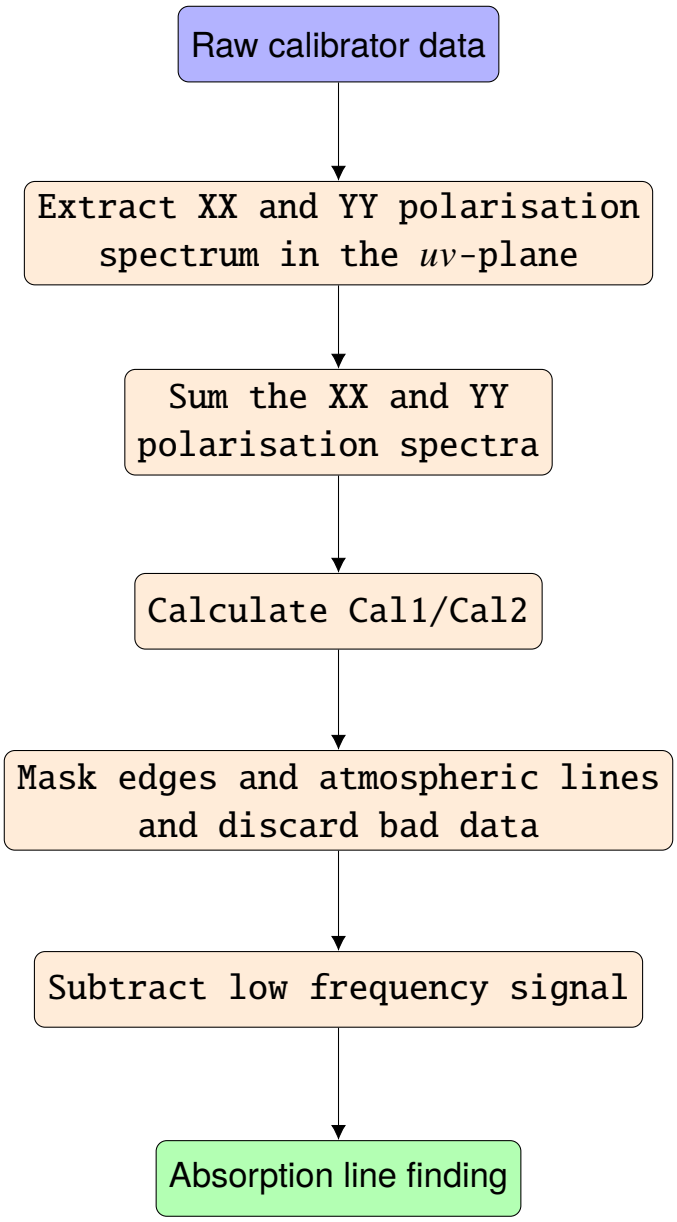

Figure 6.1: A flowchart describing our methodology to efficiently process the large data volume of ALMACAL while maintaining the highest spectral resolution.

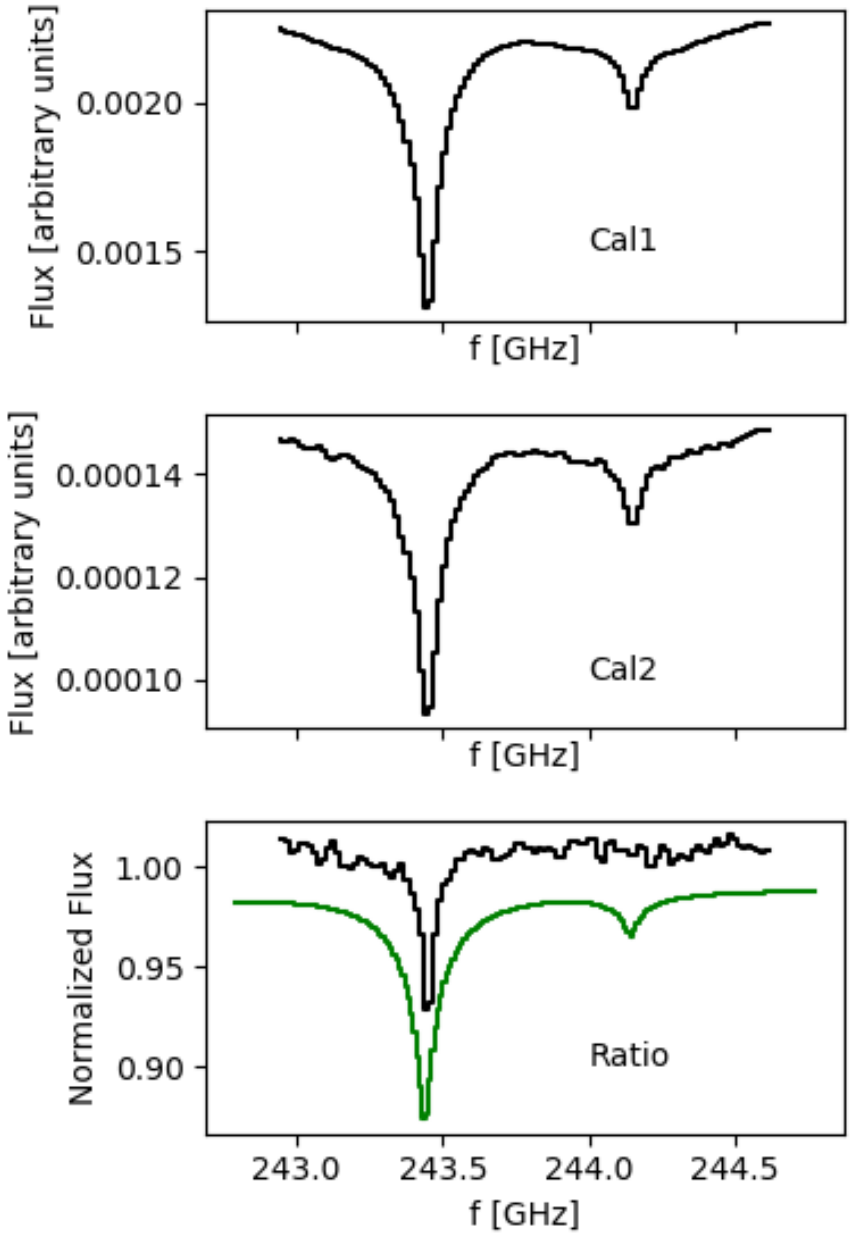

Figure 6.2: Example of the first data reduction step to construct the ratios of two calibrator spectra observed in the same ALMA execution block. Top/middle panels show the spectra of calibrator 1 and 2, respectively, with arbitrary flux units. The bottom panel shows the ratio of the spectra of calibrator 1 and calibrator 2. The green line represents the atmospheric model as described in Section 6.2. This data processing reduces atmospheric line signatures.

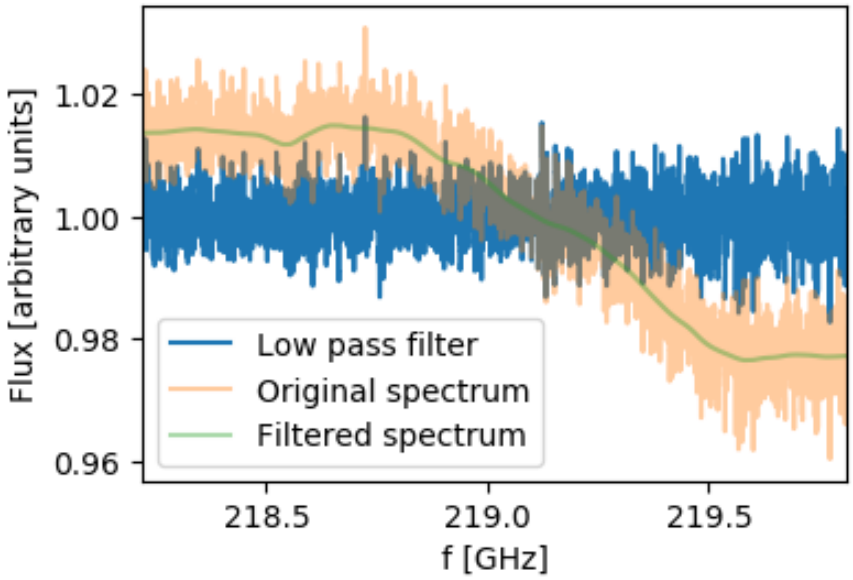

Figure 6.3: Illustration of the application of a low-pass filter in the data processing. The orange spectrum shows the processed data before filtering, the green curve represents the same data after applying a low-pass filter maintaining features that are on scales larger than 100 km s^{-1}. In blue, we show the resulting spectrum obtained by dividing the original spectrum by the low-pass curve. The resulting flat spectrum is then used as an input to the absorption line finder.

the same execution block. This procedure also removes some atmospheric absorption line signatures imprinted on the spectra. An example of this procedure is shown in Fig. 6.2. For the vast majority of the calibrator observations, this simple algorithm results in flat spectra, apart from those narrow spectral regions that correspond to strong atmospheric absorption. If more than two calibrators were used in one observation, all possible combinations of calibrator spectra pairs are used to produce bandpass-calibrated spectra. This approach allows us to confirm a potential detection identified in one ratio-ed spectrum using a second ratio.

For further processing of the spectra, we mask 5 per cent of the channels on each end of the spectrum to remove edge effects. These edge channels are often strongly affected by non-flat bandpass effects. Furthermore, we mask a 0.2 GHz wide window centred on the central frequencies of the strongest H_2O, O_2 and O_3 atmospheric absorption lines identified from the ALMA atmosphere model provided by Juan Pardo[1]. Spectra covering more than one atmospheric transition are not further considered. Finally, contiguous parts of the spectra narrower than 15 per cent of the total spectrum bandwidth are discarded to ensure a possible detection of the full absorption line and the continuum.

Despite the success of this simple algorithm, we observe that on several occasions, a second-order correction of the bandpass is required to remove all unwanted signal. To this end, we use a Butterworth low-pass filter developed as a maximally flat low-pass filter for signal processing. For each spectrum, we create a template of the spectrum including only structures wider than 100 km s^{-1}. The original spectrum is divided by this template of its low frequency shape. An example of this procedure is shown in Fig. 6.3. To test whether this filter is inadvertently masking real absorption features wider than 100 km s^{-1}, we run the filter a second time masking only structures wider than 200 km s^{-1} but the line search returns the same results as for the 100 km s^{-1} filter. We expect more molecular absorption features to be narrow (< 100 km s^{-1}) and moreover, the quality of the spectra do not allow us to search for wider spectral lines since they would be indistinguishable from instrumental artefacts and imperfect bandpass calibration.

[1] https://almascience.nrao.edu/about-alma/atmosphere-model

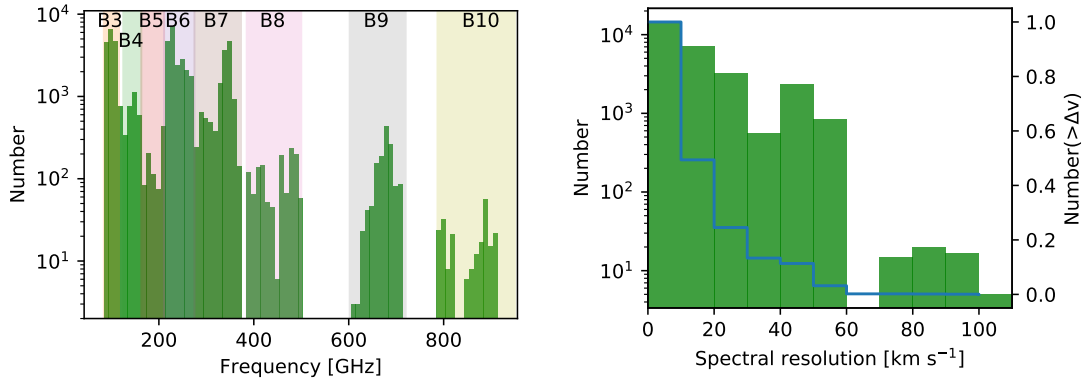

Figure 6.4: Key quantities of the ALMACAL spectra. *Top:* Histogram of the observed frequencies with the ALMA observing bands overlaid. Most of the observations are taken in ALMA band 3, 6, and 7. *Bottom:* Distribution of the velocity resolution of the ALMACAL spectra. Half of the spectra have a resolution higher than 10 km s^{-1}.

6.3 Analysis and Results

6.3.1 Blind Search for Intervening Absorbers

After the data processing described in the previous section and discarding spectra based on the criteria described above, we are left with 28,644 flattened spectra, cleaned from any unwanted atmospheric or instrumental effects, in which we search for absorption lines of astrophysical origin. The key properties of the data including observed frequencies and velocity resolution are shown in Fig. 6.4. We note that the spectra have varying bandwidth and spectral resolution, ranging from 0.03 MHz to 2 GHz, and from 256 to 3840 channels, respectively. We devise a search algorithm based on a signal-to-noise threshold of 5σ, and apply this algorithm to both the ratios and the inverted ratios to search for absorption in both calibrator spectra. Since the spectra show no significant bandpass variations based on manual inspection, we can apply a global σ-threshold for each individual spectrum. Before running the finder algorithm, we smooth each spectrum to increase the signal-to-noise ratio. We use a range of smoothing kernels between 10 and 190 km s^{-1} in steps of 10 km s^{-1}. Furthermore, we only record detections if the signal is significant in two consecutive channels.

From this initial list of candidates, we remove all detections which occur within the lowest or the highest 5 per cent of channels to remove lines absorption line candidates for which we do not see the continuum on both sides. Furthermore, we discard detections that

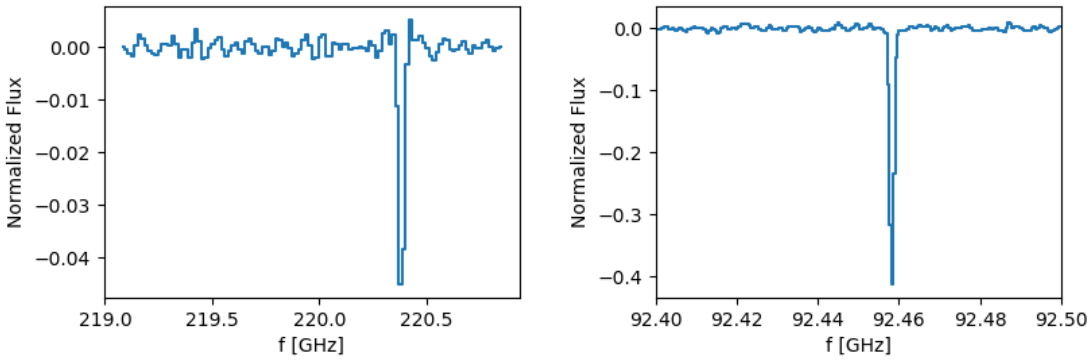

Figure 6.5: Examples of detected absorption lines. *Left:* A Galactic absorption line detection in the spectrum of J1744-3116. The absorption line is ^{13}CO(2-1) at 220.39 GHz that arises in the ISM of Milky Way Galaxy in the direction of J1744-3116. *Right:* Associated ^{12}CO(1-0) absorption in J1415+1322 at $z = 0.24671$. While we find multiple Galactic absorption lines, no extragalactic intervening molecular absorbers are detected.

lie within 200 km s^{-1} of the velocities of the centres of known Galactic CO lines. We apply an additional manual cleaning of candidate detections that can be identified as obvious electronic artefacts (such as strong periodic signals). For the remaining candidates, we identify atmospheric and Galactic transitions by cross-matching the detected frequencies observed in multiple sight lines. Finally, we match the candidate list with a list of frequencies corresponding to rare molecular species from SPLATALOGUE (Remijan et al., 2007) to filter out remaining absorption lines of Galactic origin. Examples of a detection of Galactic absorption and associated absorption are shown in Fig. 6.5. The Galactic absorption lines will be the subject of a forthcoming paper. Additionally, we compare the redshift of the lowest possible CO transition with the calibrator redshift and exclude implausible lines (i.e. the redshift of the absorber would be higher than the redshift of the background quasar). After performing these checks, we are left with one significant detection of an extragalactic molecular absorption line shown in Fig. 6.5, which we identify be intrinsic CO(1–0) absorption in the spectrum of the background calibrator J1415+1320 ($z = 0.2467$) (Wiklind & Combes, 1994). This detection validates the robustness of our finding algorithm.

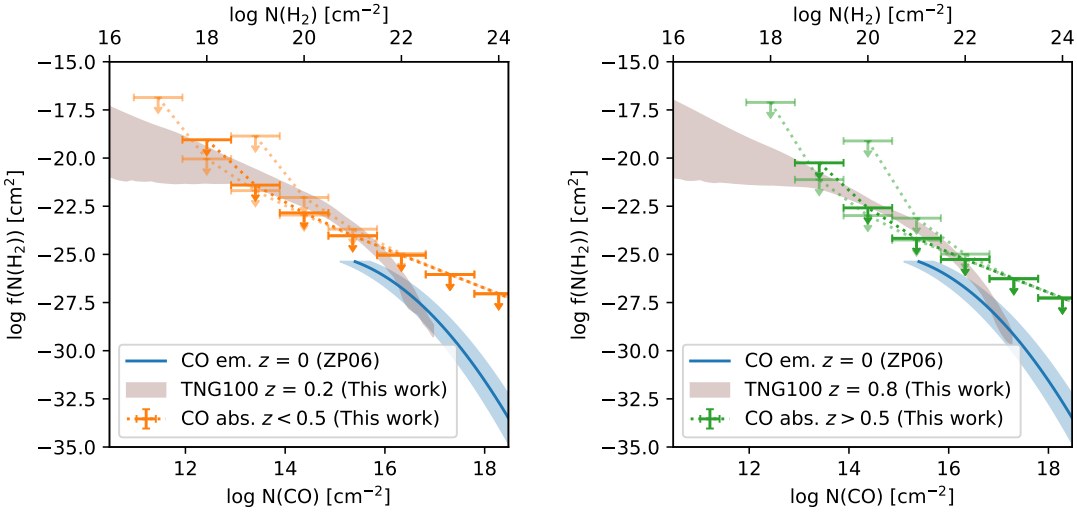

Figure 6.6: CO column density distribution functions in the two redshift bins. Column densities are expressed in molecules cm^{-2}. Arrows indicate the upper limits from our "blind" CO absorber survey within $\Delta N = 1$ dex. The left panel corresponds to $z < 0.5$ and the right panel to $z > 0.5$. Light coloured limits reflect the uncertainty introduced by the CO-to-H_2 column density factor. The H_2 column density distribution function at $z = 0$ based on CO emission line observations (Zwaan & Prochaska, 2006) is marked by the blue line. The brown shaded region marks the predictions based on IllustrisTNG100 results with a variation of post processing recipes to illustrate the uncertainties (see Section 6.3.3 for details). The top-axis shows the fiducial CO-to-H_2 conversion from Burgh et al. (2007).

6.3.2 The Column Density Distribution Function Based on Intervening Absorbers

We calculate the column density distribution function from the sensitivity limits we reach in the calibrator spectra. To illustrate the potential of this method we derive predictions of the column density distribution function from the IllustrisTNG100 cosmological hydrodynamical simulation (Pillepich et al., 2018; Naiman et al., 2018; Nelson et al., 2018a; Marinacci et al., 2018; Springel et al., 2018).

We first calculate the redshift path probed by the survey. For each spectrum, we compute the redshift path observed (see e.g. Zafar et al., 2013) given the observed frequencies and assuming CO transitions from $J = 1 - 0$ up to $J = 5 - 4$. The frequency coverage of the fully reduced and masked spectra is used for this calculation. The maximum probed redshift in each spectrum is set by the redshift of the calibrator. The cumulative redshift path surveyed, Δz, is 182.2 for CO transitions between $J = 1 - 0$ and $J = 5 - 4$.

Table 6.1: Redshift path surveyed, Δz, and comoving pathlength, ΔX, for each CO transition in two distinct redshift ranges, $z < 0.5$ and $z > 0.5$. The cumulative redshift path surveyed, Δz, is 182.2 for CO transitions between $J = 1 - 0$ and $J = 5 - 4$.

CO transition	Redshift range	Δz	ΔX
CO(1–0)	< 0.5	48.4	61.2
CO(2–1)	< 0.5	13.4	16.3
CO(3–2)	< 0.5	20.4	28.6
CO(4–3)	< 0.5	9.8	14.6
CO(5–4)	< 0.5	1.4	2.1
CO(1–0)	> 0.5	0.0	0.0
CO(2–1)	> 0.5	34.1	80.8
CO(3–2)	> 0.5	18.5	42.0
CO(4–3)	> 0.5	18.8	41.5
CO(5–4)	> 0.5	17.5	40.0

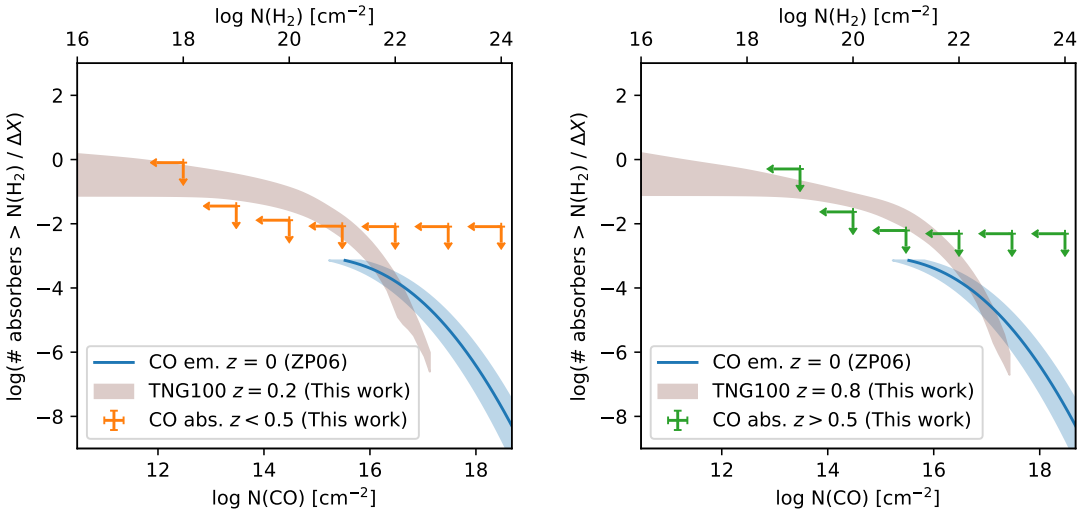

Figure 6.7: Cumulative number of molecular absorbers per comoving path length interval ΔX with a column density greater than N (notations same as in Fig. 6.6). This presentation of the column density distribution function is independent of the choice of a bin size, ΔN. We use this bin-free representation to calculate limits on the molecular gas densities with redefined redshift bins by scaling of the functional form from Zwaan & Prochaska (2006) to our upper limits (see Section 6.3.4 for details).

We further split the sample in two redshift ranges, at $z > 0.5$ and $0.5 < z < 1.7$ with mean redshifts of $z = 0.199$ and $z = 0.839$. Two subsamples are covering approximately the same path length of $\Delta z = 93.3$ at $z < 0.5$ and $\Delta z = 88.9$ at $z > 0.5$. Details of the redshift paths for each CO transition in the two sub-samples are listed in Table 6.1.

We then calculate the limiting CO column densities probed in our survey following Mangum & Shirley (2015).

$$N = \frac{8\pi\nu^3}{c^3 A_{ul} g_u} \frac{Q(T_{\rm ex}) \exp(E_J/T_{\rm ex})}{(1 - \exp(-h\nu/kT_{\rm ex}))} \int \tau dV, \tag{6.3.1}$$

where N is the column density, E_J is the energy of the lower level of the transition, $Q(T_{\rm ex})$ is the partition function, A_{ul} is the Einstein coefficient, and g_u is the degeneracy factor of the upper level. We assume an excitation temperature equal to the CMB temperature at the redshift probed with the spectrum, because this is the lowest possible temperature, which results in a lower limit of the column density. The physical conditions of the molecular absorbing gas in the galaxy lensing the quasar PKS1830–211 were investigated by Muller et al. (2013). They found that for polar molecules, the excitation temperature is close to that of the CMB at the corresponding redshift. A molecule like CO, on the other hand, is easier to excite due to its low electric dipole moment, and in general, we would not be able to constrain $T_{\rm ex}$ for CO to better than $T_{\rm cmb} < T_{\rm ex} < T_{\rm kin}$, without constraints from additional lines/species. Since we have no detections, we perform the calculation using the 5σ level from each spectrum as the detection threshold and an expected FWHM of the absorption line of 40 km s^{-1} (Wiklind et al., 2018). The CO column density limit is converted into a H_2 column density limit using a mean column density ratio of $N(\mathrm{CO})/N(\mathrm{H_2}) = 3 \times 10^{-6}$ (Burgh et al., 2007). In order to bound the large uncertainty on this conversion factor, we also present CO columns derived with upper and lower limits of 10^{-5} to 10^{-7}, respectively. The column density limits from non-detections are calculated for each observation using the corresponding frequency coverage and rms. We note that the column density ratio of $N(\mathrm{CO})/N(\mathrm{H_2})$ over a large range of H_2 column densities is not constant (Balashev et al. 2017). However, with the currently available data this is challenging to quantify.

Next, we estimate the 5σ limits on the column density distribution function following

the definition (Carswell et al., 1984):

$$f(N(\mathrm{H_2}), X)dN(\mathrm{H_2})\Delta X < \frac{1}{\Delta N(\mathrm{H_2})\Delta X} dN(\mathrm{H_2})\Delta X, \tag{6.3.2}$$

where the number of absorbers detected within the column density range $\Delta N(\mathrm{H_2})$ is less than one. ΔX is the comoving path length for the specific column density under consideration. The comoving path length ensures that for a constant physical size and comoving number density, the absorbers have a constant $f(N(\mathrm{H_2}), X)$ (Bahcall & Peebles, 1969). The comoving path length of a single sightline, ΔX_i, is defined as follows:

$$\Delta X = \frac{H_0}{H(z)}(1+z)^2 \mathrm{d}z \tag{6.3.3}$$

$$\Delta X_i = \int_{z_{\mathrm{min}}}^{z_{\mathrm{max}}} \mathrm{d}X = \int_{z_{\mathrm{min}}}^{z_{\mathrm{max}}} \frac{(1+z)^2}{\sqrt{\Omega_\Lambda + \Omega_\mathrm{M} \times (1+z)^3}} \mathrm{d}z. \tag{6.3.4}$$

The limiting column densities and covered path length are then combined for the whole survey.

The non-detections from our survey translate to upper limits on the column density distribution function. However, in the definition of $f(N(\mathrm{H_2}), X)$ the choice of the bin size influences the values of $f(N(\mathrm{H_2}), X)$ upper limits in the case of non-detections. Here, we use a bin width of $\Delta N = 1$ dex, as it is common practice in H I absorption line studies (e.g. Péroux et al., 2003b). The resulting upper limits on the column density distribution function are shown in Fig. 6.6 for the two redshift ranges.

To remedy the dependence on the bin size, we also calculate the cumulative number of absorbers per ΔX (Péroux et al., 2003b) as a function of column density, which is independent of the binning choice (see Fig. 6.7). We also calculate the cumulative number of absorbers expected based on the results from BIMA SONG observations of local star-forming galaxies (Zwaan & Prochaska, 2006) for comparison.

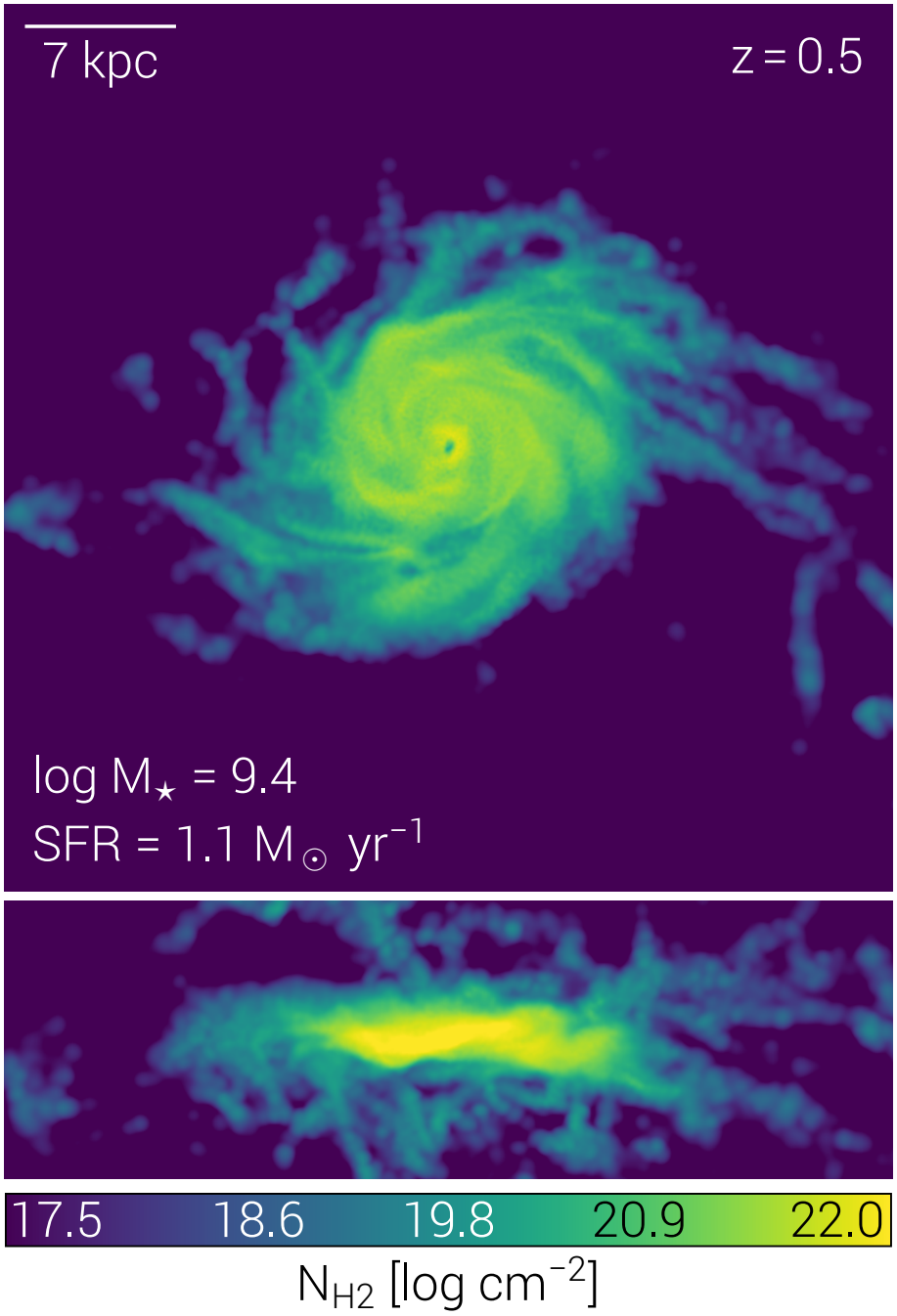

Figure 6.8: An example of a molecular gas disk in a z=0.5 galaxy (top panel: face-on, bottom panel: edge-on view) with $M_\star = 10^{9.4}\mathrm{M}_\odot$ and SFR = $1.1\mathrm{M}_\odot\mathrm{yr}^{-1}$ from post processing of the IllustrisTNG100 simulation. The highest column densities are only observed in edge-on disks, while intermediate column densities are predicted out to radii of ∼10 kpc in other viewing directions.

6.3.3 Predicting the Column Density Distribution Function from IllustrisTNG

From a modelling point of view, the molecular phase of the cold gas is challenging to assess because of the complexity of the physics involved and because it requires sub-grid modelling to capture the unresolved physics. Semi-analytical techniques of pressure-based models (Blitz & Rosolowsky, 2006; Gnedin & Kravtsov, 2011; Krumholz, 2013) are used to split the cold hydrogen from hydrodynamical simulations (such as the EAGLE or IllustrisTNG) into its atomic and molecular components (Obreschkow et al., 2009; Popping et al., 2014; Lagos et al., 2015; Chen et al., 2018).

Here we use the TNG100 volume of the IllustrisTNG simulations (Pillepich et al., 2018; Naiman et al., 2018; Nelson et al., 2018a; Marinacci et al., 2018; Springel et al., 2018) through its publicly available data (Nelson et al., 2018b) in order to compare our observations against the theoretical expectation for the H_2 column density distribution function. An example of the column density map in a typical galaxy from the simulations is shown in Fig. 6.8. We construct the column density distribution function at the mean redshift of the two subsamples ($z = 0.199, 0.839$) using the H_2 modelling methodology of Popping et al. (2019) (see also Stevens et al. (2019); Diemer et al. (2019) for assessments of the H I and H_2 outcomes of TNG) and the column density distribution function gridding procedure as described in Nelson et al. (2019). The column density is integrated over a path length of 10 cMpc h^{-1}. In order to assess the sensitivity of our result to various physical and numerical choices, we present a band which encompasses different column density distribution function calculations, which vary the H_2 model employed (three versions), the projection depth / effective path length (five values), different grid sizes for the computation of the column density (three values), and assumptions on the H_2 contents of star-forming versus non-star-forming gas cells. In Fig. 6.9, we show the expected evolution of the column density distribution function with redshift. We find that an increasing number of high column density absorbers at high redshift is expected. On the low column density end, on the other hand, the number of absorbers is almost constant from $z = 4 - 1$ and increases at $z = 1$. The prediction of the column density distribution function and the cumulative number of absorbers are shown in Fig. 6.6 and 6.7. We have conducted the

same analysis on the results from the EAGLE simulation (Schaye et al., 2015; Crain et al., 2015) and find that the qualitative expectations for the column density distribution function are in line with those from IllustrisTNG.

6.3.4 Cosmic Evolution of the Molecular Gas Mass Density

Finally, we calculate the molecular gas mass density $\rho(H_2)$ from the cumulative number of absorbers per ΔX. We use the functional form of the cumulative number of absorbers per ΔX from Zwaan & Prochaska (2006) at $z \sim 0$ as a proxy. We scale it to our upper limits and integrate over differential number of absorbers multiplied by the respective column density. Zwaan & Prochaska (2006) found that the contribution of low column density absorbers with $\log(N(H_2)) < 21$ to the total molecular gas mass at $z \sim 0$ is only 3 per cent. Therefore, we integrate only column densities $\log(N(H_2)) > 21$. Since we aim at a comparison with other surveys, we define similar redshift bins to those introduced by the ASPECS survey (Decarli et al., 2016, 2019) for this calculation. The resulting limits are shown in Fig. 6.10, where we also report measurements from the literature based on the same cosmology and CO-to-H_2 conversion factor.

6.4 Discussion

With our "blind" survey for intervening molecular absorbers we put significantly improved constraints on the column density distribution function of molecular gas beyond $z \sim 0$. We compare our upper limits with the measurements at $z \sim 0$ presented by Zwaan & Prochaska (2006) in Fig. 6.6 and find that our limits at $0 < z < 0.5$ and $0.5 < z < 1.7$ are consistent with the column density distribution function measurement at $z = 0$. The depth of our data translates to five orders of magnitude lower column densities than probed by Zwaan & Prochaska (2006). In addition, the absorption technique with a sensitivity independent of redshift in principle allows us to measure the redshift evolution of the column density distribution function.

We calculate limits on the limiting cross section of the molecular gas per galaxy based on the non-detection and the surveyed redshift path. A Schechter (1976) galaxy luminosity function and a uniform and spherically symmetric distribution of molecular gas

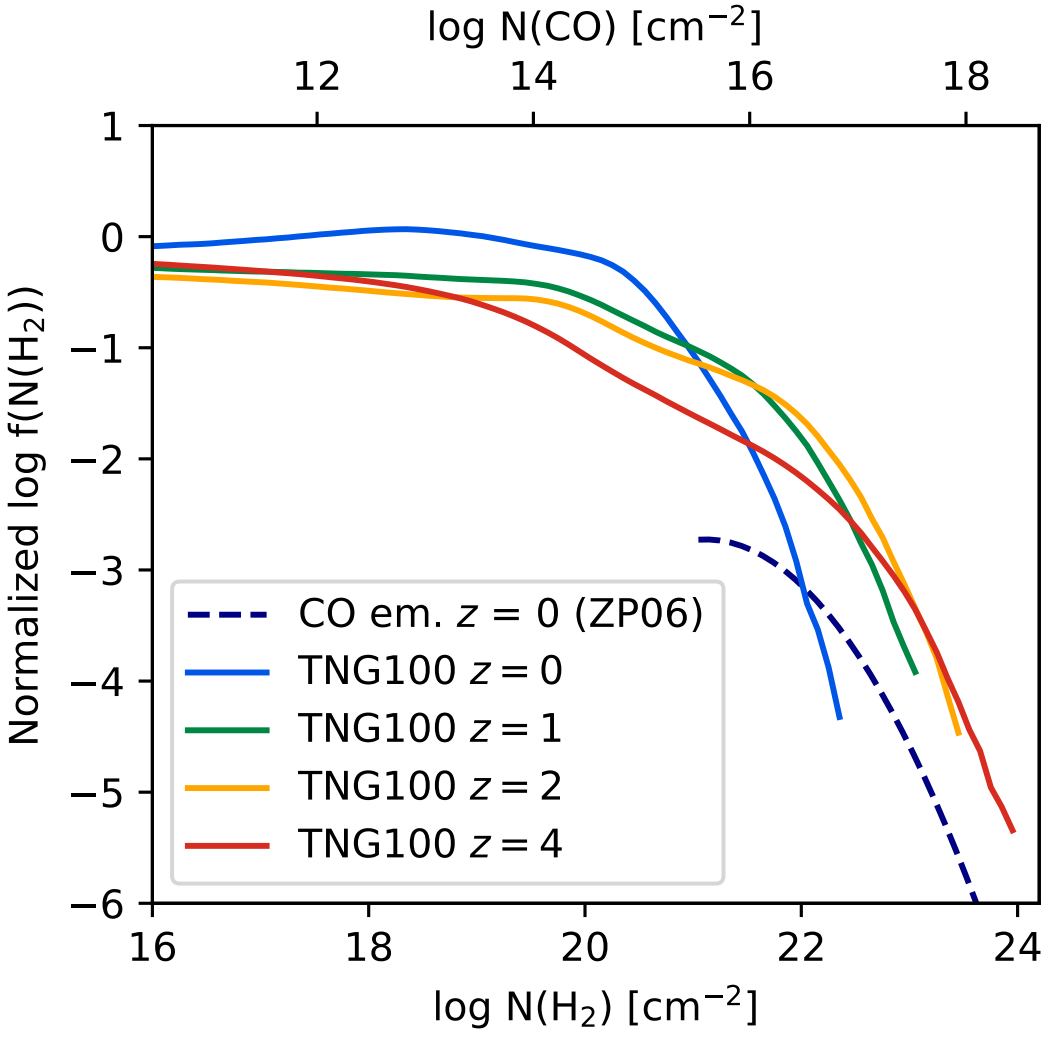

Figure 6.9: Redshift evolution of the H_2 column density distribution function as predicted from the IllustrisTNG simulation and from observations by Zwaan & Prochaska (2006) normalized by a power law function fitting the low column density end of the predictions. We find that the column density distribution functions determined from the post processing of IllustrisTNG results at different redshifts predict an increasing number of high column density absorbers at high redshift.

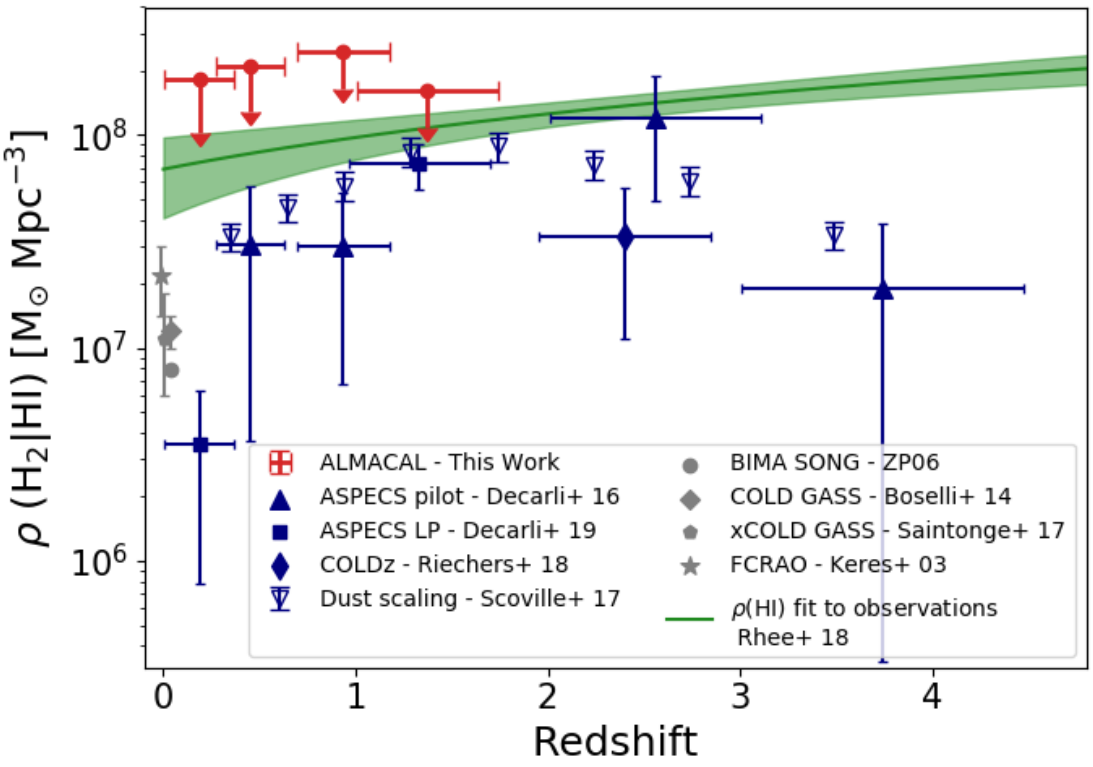

Figure 6.10: Cosmic evolution of the molecular and atomic gas densities. For $\rho(H_2)$, our limits are consistent with the measurements at $z = 0$ of Keres et al. (2003); Zwaan & Prochaska (2006); Boselli et al. (2014); Saintonge et al. (2017) and the results of Decarli et al. (2016, 2019) given the extended uncertainties (see text). This emphasizes the power of the absorption technique combined with ALMACAL to efficiently probe the cosmic evolution of the molecular gas density. A fit to ρ(HI) observations is shown as a solid line (Rhee et al., 2018).

are assumed and we follow the description in Péroux et al. (2005). We derive a maximum radius of 4.8 kpc at $z < 0.5$ and 4.6 kpc at $z > 0.5$. Zwaan & Prochaska (2006) find a median impact parameter of $N(H_2) > 10^{21}$ cm^{-2} of 2.5 kpc, consistent with our upper limits. Our results provide strong statistical evidence that molecular gas around galaxies have a limited extend, well below the typical size of CGM regions. It however does not exclude that the CGM contains more clumpy molecular gas.

Compared to the predictions from IllustrisTNG from Section 6.3.3 presented in Fig. 6.6 our limits are already close, within $\sim$ 1 dex, of the expected value of $f(N(H_2), X)$ at low column densities. This suggests that the first intervening molecular absorber in a "blind" survey will be detected soon or that we will in the near future be able to put stringent constraints on the simulations. The sensitivity reached in our survey is comparable to the column densities predicted by the simulations. However, uncertainties in this comparison are still large in both observations and simulations. The observations on the one hand involve a conversion from measured CO column densities to H_2 column densities. Cosmological simulations on the other hand are lacking the resolution and associated small-scale physics to follow molecular cloud formation and rely on sub-grid physics models. Improvements on both sides are necessary to further explore the molecular column density distribution.

Fig. 6.10 shows the cosmic evolution of the cold gas in the Universe. A fit to ρ(HI) observations is shown based on Rhee et al. (2018). These results show that the amount of cold gas in its atomic form is only a few times higher than that in its molecular phase from $z \sim 3$ to $z \sim 0$, implying that the decrease of H_2 density is faster than for H I towards late times. While the SFH evolves by a factor 20–30 from $z = 2$ to present day, $\rho(H_2)$ decreases by one order of magnitude in the same time-lapse and ρ(HI) by less than 15 per cent. These findings indicate that H_2 is being consumed faster than H I can replenish it unless it is constantly fed. The dramatic decrease of the cosmic star-formation rate density might therefore arise from a shortfall of molecular gas supply. On the contrary the MUFASA simulation predicts a shallower evolution of the molecular gas mass density than indicated by the observations (Davé et al., 2017). The uncertainty in the results from a dedicated effort to measure the cosmic evolution of $\rho(H_2)$, the ASPECS survey, can be considered larger than the fiducial values presented in Fig. 6.10. The authors discuss

the impact of uncertainty in the redshift, CO excitation, completeness and the choice of $\alpha_{\rm CO}$ (Decarli et al., 2019; Popping et al., 2019) which would all lead to non-negligible changes of $\rho(H_2)$. As we show in Fig. 6.10, our limits are therefore consistent with the measurements at $z = 0$ of Keres et al. (2003); Zwaan & Prochaska (2006); Boselli et al. (2014); Saintonge et al. (2017) and comparable with the results of Decarli et al. (2016, 2019) within the expected uncertainties.

Future blind absorption line surveys will offer more stringent constraints on the evolution of the cosmic molecular gas mass density by either moving to higher redshifts, where more high column density absorbers are predicted per dz, or by increasing the surveyed redshift path. To put this into perspective, it is important to realize that the ALMACAL results presented in this chapter are based on more observing time than the sum of all ALMA Large Programs from Cycles 4 to 7. ALMACAL is an ongoing survey, so more redshift path length is accumulated continuously. But even a modest increase of a factor of two will take several years of observing. Another significant improvement in the covered redshift path length would be achieved by increasing the instantaneous frequency coverage of ALMA observations from its current 8 GHz per polarisation to at least 16 GHz, as is recommended in the ALMA development roadmap (Carpenter et al., 2019). Apart from this technological improvement, an increase of the redshift path could be achieved by measuring more optical redshifts for ALMA calibrator sources, which is under way. However, the uncertainties introduced by lensing of the background quasar by the foreground absorber will remain a systematic issue.

6.5 Summary and Conclusions

We present constraints on the cosmic evolution of the molecular gas density of the Universe from a "blind" search for extragalactic intervening molecular absorbers using the ALMACAL survey. The novelty of the approach resides in *i)* its redshift-independent sensitivity, *ii)* its ability to reach low gas densities, and *iii)* the fact that it overcomes cosmic variance effects. Our survey is sensitive to column densities as low as N(CO)>10^{11} cm^{-2} (N(H_2) > 10^{16}cm^{-2}). This is five orders of magnitude lower than probed in previous surveys (Zwaan & Prochaska, 2006; Kanekar et al., 2014).

To keep the data reduction simple and uniform, we use a simple data processing method to handle the large data volume while maintaining the data at its highest spectral resolution. The resulting sample of 622 unique quasar spectra is searched "blindly" for CO absorption lines. At $z < 0.5$, we survey a total path length of $\Delta z = 92$ and a total comoving path length of $\Delta X = 123$. At $z > 0.5$, $\Delta z = 89$ and $\Delta X = 205$. The large path length surveyed allows us to put constraints on the CO column density distribution functions at $z < 0.5$ and $z > 0.5$. While we detect multiple Galactic absorption lines and one known extragalactic intrinsic absorber, no extragalactic intervening molecular absorbers have been found. Based on model predictions available at the beginning of the project (G. Popping private communication) we estimated to detect up to 30 extragalactic absorbers. In the meantime models have further developed and will take our findings into account for more accurate predictions of the molecular gas.

The upper limits on the molecular mass density reported in this survey are: $\rho(H_2) < 10^{8.26} M_\odot Mpc^{-3}$ at $0.003 < z \leq 0.369$, $\rho(H_2) < 10^{8.32} M_\odot Mpc^{-3}$ at $0.2713 < z \leq 0.6306$, $\rho(H_2) < 10^{8.39} M_\odot Mpc^{-3}$ at $0.695 < z \leq 1.1744$, and $\rho(H_2) < 10^{8.21} M_\odot Mpc^{-3}$ at $1.006 < z \leq 1.738$. These upper limits are consistent with previous surveys. Together, these findings indicate that the dramatic decrease of the star-formation rate history might arise from a shortfall of molecular gas supply. Our limits add a constraint on the contribution from low column density molecular hydrogen. In addition, the new absorption line technique offers a characterization of cosmic variance issues possibly affecting emission surveys (Popping et al., 2019).

We present the theoretical estimates of the molecular gas column density distribution from post-processing of the IllustrisTNG results. These estimates are consistent with our observational upper limits. However, both are subject to systematic uncertainties. Both a better understanding of the CO-to-H_2 conversion factor and advances in the modelling of molecular gas in cosmological simulations will decrease the uncertainties.

To put stronger constraints on the evolution of the molecular gas mass, a significant improvement on the redshift path covered per observation with ALMA is needed. This will occur naturally over time and will be accelerated by the proposed technological upgrades. Further improvement will result from the measurement of background quasar redshifts.

Chapter 7

First High-Frequency Number Counts Free of Blending

7.1 Introduction

An important technique to study galaxy formation and evolution in the submillimetre wavelength range is to determine the number of sources above a given flux density per unit area on the sky in deg^2: the so called cumulative number counts ($N(> S)$[deg^2]). What seems like a simple measurement turns out to be a challenging task in reality. One of the challenges are large beam sizes of $\sim 15'' - 30''$ for single dish observations at infrared and submillimetre wavelength, which result in bright confusion limits and can lead to blending of several sources into single detections (often referred to as *source confusion*). Despite the number counts being a challenging quantity to measure it can be used to shed light on galaxy formation theory (Baugh et al., 2005; Lacey et al., 2016).

Major efforts were undertaken to determine number counts at different wavelength. At 1.1 and 1.2 mm number counts were determined using the Bolocam at the Caltech Submillimeter Observatory (CSO) (Laurent et al., 2005), AzTEC bolometer camera on the JCMT and the Atacama Submillimeter Telescope Experiment (ASTE) (e.g. Scott et al., 2010; Hatsukade et al., 2011; Scott et al., 2012; Umehata et al., 2014) and ALMA (Aravena et al., 2016a; Oteo et al., 2016b; Umehata et al., 2017). High-frequency submillimetre number counts were derived from surveys at 850μm carried out with the SCUBA (e.g. Blain et al., 1999; Chapman et al., 2002; Coppin et al., 2006) and later SCUBA-2 bolometer

camera (e.g. Casey et al., 2013; Chen et al., 2013) on the single dish James Clerk Maxwell Telescope (JCMT), the Large APEX Bolometer Camera (LABOCA) on the Atacama Pathfinder Experiment (APEX) (Beelen et al., 2008; Weiß et al., 2009) and with ALMA (Karim et al., 2013). Number counts at 450μm and 500μm were derived based on surveys using SCUBA, *Herschel* and SCUBA-2. Surveys aiming to constrain the 450μm and 500μm number counts either used the aid of gravitational lensing to magnify the fluxes of faint galaxies (e.g. Smail et al., 2002; Chen et al., 2013), used a blind-source extraction above the confusion limit (Oliver et al., 2010; Geach et al., 2013; Casey et al., 2013; Valiante et al., 2016), used stacking to constrain the faint end of the number counts (Béthermin et al., 2012a) or used ancillary data to construct a de-blended source catalogue (Wang et al., 2019). Among those highest frequency studies, the number counts do not agree very well including early and more recent results from *Herschel*. This is most likely due to the effects of confusion and source blending or indicates, that most recent *Herschel* source catalogues are too strongly de-blended.

Sophisticated techniques were developed to characterize the flux boosting by confusion noise. One way is to perform a higher resolution follow-up survey using radio interferometric observations to detect and resolve the counterparts (e.g. Ivison et al., 1998; Chapman et al., 2003, 2005; Ivison et al., 2007). More recently, such studies were extended to submillimetre interferometric follow-up of single-dish surveys to remove the effect of blending on the source counts (e.g. Younger et al., 2009; Chen et al., 2013; Hodge et al., 2013; Simpson et al., 2015; Hill et al., 2018; Stach et al., 2018). However, the multiplicity (fraction of single-dish detections breaking up into multiple components at higher resolution) varies between 15 and > 90% depending on factors such as source flux, survey depth, and definition of multiplicity. Therefore, the resulting number counts at high frequencies are not conclusive.

Because of this uncertainty it is key to determine submillimetre number counts also at high frequencies directly from high resolution interferometric observations. The drawback of this approach, however, is the low survey speed of high resolution interferometers because of their small field of view. This becomes especially challenging at high frequencies where for example the FWHM of the primary beam of ALMA is 12″ at 440 GHz (corresponding to 680μm). This has limited early efforts to surveys at lower

frequencies. First single field number counts were presented by Hatsukade et al. (2013) and soon thereafter Ono et al. (2014); Carniani et al. (2015) presented the first deep, resolved, multi-field number counts. However, in these studies the contamination from cosmic variance is likely high. The first large surveys of submillimetre number counts were presented by Fujimoto et al. (2016); Oteo et al. (2016b). Later, dedicated observing programmes were carried out with ALMA targeting cosmological deep fields to study number counts at 1.1 and 1.2mm such as ASPECS (Aravena et al., 2016a), ALMA observations of the HUDF (Dunlop et al., 2017), the ASAGO survey in the GOODS-S field (Hatsukade et al., 2018) and the GOODS-ALMA survey (Franco et al., 2018).

Fujimoto et al. (2016) combined 66 fields observed in ALMA Band 6 and Band 7 from the ALMA archive. Using targeted observations of non-blind fields and lensed fields introduces a strong bias influencing the resulting the number counts. The authors of this study use a low detection threshold of $\sim 3.5\sigma$ possibly introducing a high number of spurious sources. Furthermore, the targeted fields were not blank fields introducing another bias. Oteo et al. (2016b) presented ALMA Band 6 and Band 7 number counts free of cosmic variance using our ALMACAL survey (see also Chapter 2.7.2). The authors used the 69 fields available at that time and applied a more conservative source detection threshold of 5σ. The number counts determined by Oteo et al. (2016b) are a factor of two lower than those determined by (Fujimoto et al., 2016) reflecting the differences in detection threshold and targeted fields.

Here we perform the first high-frequency blind survey free of blending expanding on the work of Oteo et al. (2016b). We use the ALMACAL observations in Band 8 (440GHz, 680μm) available in the ALMACAL version December 2018. This work is bridging the gap between high resolution number counts at lower frequencies and low resolution number counts available at higher frequencies from *Herschel* observations (e.g. Oliver et al., 2012; Valiante et al., 2016)

7.2 ALMACAL Data Reduction

We use all ALMACAL observations until 2018 December. The observed fields are distributed quasi-randomly on the sky visible from the Atacama desert since all ALMA

projects using Band 8 are contributing to this dataset. Therefore, the only biases we introduce are due to the observing latitude of ALMA, the annual weather patterns in the Atacama desert and the positions of sources of interest for studies in Band 8 by the astronomical community, e.g. the cosmological deep fields. The data retrieval is described in detail in Chapter 2. Since we are interested in high resolution number counts we select only observations with a spatial resolution higher than 1″. Furthermore, we use only fields for which we reach an rms of $\lesssim$ 1mJy beam^{-1} in the combined maps.

The calibrator-subtracted pseudo-continuum visibilities from every execution block are first imaged individually without combining data for a given calibrator. We visually inspect every map and discard those showing signs of poor calibration (e.g. stripes or significant halos and residuals around the quasar position). Since we use pseudo-continuum visibilities, we cannot recalculate the weights of the visibilities to have an equal representation of all observations in the combined image. Therefore, we also inspect the weights of the visibilities and include only those observations with weights similar to the average weights for a given calibrator. This leads to the loss of $\sim$ 26% of the data but for a homogeneous treatment and due to the overall size and complexity, flagging and recalibration is impracticable.

The data reduction is carried out using the Common Astronomy Software Application (CASA) (McMullin et al., 2007) version 5.5.0. We combine the data for each calibrator using the task CONCAT. The combined visibilities are imaged using the CASA task TCLEAN. We produce maps at ν = 440GHz (corresponding to 680μm). We define cleaning windows using the automatic masking procedure "auto-multithresh". A natural weighting is chosen to ensure optimal use of all base lines, resulting in high SNR detections. In order to not resolve the galaxies we set the outer taper to 0.3″. We produce a second set of images with an outer taper of 0.8″ to test if we are missing detections because they are resolved out in the higher resolution imaging. The maps without primary beam correction are used for the source finding and subsequent statistical analysis. However, for the final flux measurements, we correct for the primary beam attenuation using the task IMPBCOR.

We image ALMACAL observations of 81 calibrators observed in Band 8 covering a total of $\sim$ 5.5 arcmin^2 within 1.5 $\times$ FWMH of the primary beam. The exact survey area

is a function of the source flux density. The properties of the final images are listed in Table 7.3. We reach noise levels of $47-1022\mu$Jy beam^{-1} with a median of 187μJy beam^{-1} and resolutions of $0.34''-0.98''$ with a median of $0.52''$. The rms in the ALMACAL Band 8 maps is significantly higher than in Band 6 and 7 because of higher receiver and sky noise.

7.3 Analysis

7.3.1 Source Detection

Following the general practice in submillimetre number count studies Hatsukade et al. (e.g. 2013); Ono et al. (e.g. 2014); Oteo et al. (e.g. 2016b); Fujimoto et al. (e.g. 2016); Aravena et al. (e.g. 2016a) we perform the source detection using SExtractor (Bertin & Arnouts, 1996) on the clean maps before correcting for the primary beam attenuation to ensure uniform noise properties. The calibrators are very bright sources in the centres of the Band 8 maps. We detect strong residual signal from the calibrators more frequently than in the Band 6 and Band 7 maps presented by Oteo et al. (2016b). Therefore, we mask the central region of each map with a radius of $1''$ and exclude this region from the further analysis. Furthermore, we use a high detection threshold with a peak flux of at least $4.5\times$ the rms noise in the image. The threshold is comparable with those used in previous studies (Simpson et al., 2015; Oteo et al., 2016b; Stach et al., 2019). At this threshold we are able to detect galaxies down to ~ 0.7 mJy and at the same time introduce a minimal number of spurious detections $<< 2\%$.

The primary beam response function decreases steeply as a function of distance from the centre of the map. We choose a search region with a diameter of $1.5\times$ the FWHM of the primary beam. For each Band 8 detection we make maps from the ALMACAL Band 6 observations to confirm detections via multi-band observations and measure the slope of the SED. The FWHM of the primary beam in Band 6 is wider than in Band 8 ($\mathrm{FWHM_{B6}} = 27''$, $\mathrm{FWHM_{B8}} = 12''$). Therefore, any detection in Band 8 will be covered by the Band 6 observations if the calibrator is observed at both frequencies.

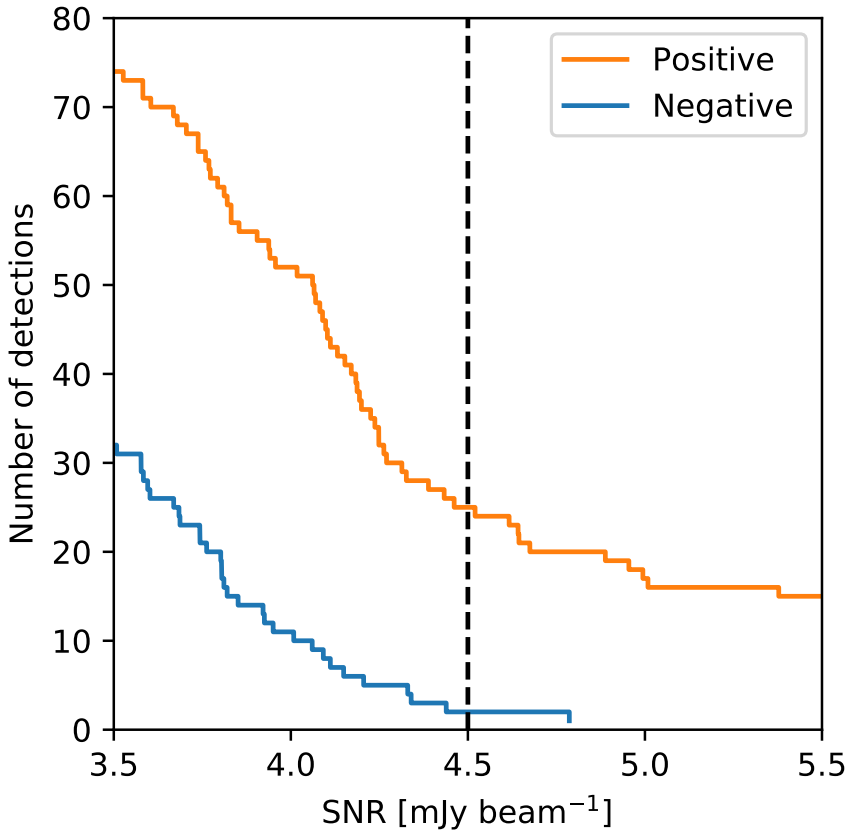

Figure 7.1: The cumulative number of spurious detections in the inverted maps as a function of the peak SNR. The highest significance spurious detection is at 4.7σ. Therefore, we choose a detection threshold of 4.5σ (black dashed line) corresponding to expecting one false detection. Combined with the multi-band detection this offers a high reliability of our detections.

7.3.2 Spurious Detections and Jets

Performing a source detection using a low detection threshold leads inevitably to the detection of spurious noise peaks. Since we are aiming at a reliable number counts measurement, we choose to include only high reliability detections. To test the reliability as a function of SNR we invert our maps and run the source finder with the same parameters as for the main search. Any detection in the inverted map is considered to be a spurious noise peak. The cumulative distribution of noise peaks as a function of SNR is shown in Fig. 7.1. We find that the highest SNR detection in the inverted map is at 4.7σ. Therefore, at our detection threshold of 4.5σ the contamination from spurious sources is negligible. Furthermore, we exclude detections with a $S_{680\mu\mathrm{m}}/S_{1.2\mathrm{mm}}$ flux density ratio indicative of

synchrotron radiation from a jet. After these checks we assume that the reliability of the DSFG detections is close to 100%.

7.3.3 Completeness

We use artificial sources to measure the completeness of our survey as a function of SNR. Thus, we inject artificial point sources with uniformly distributed random fluxes between 2 and 25 σ in the ALMACAL visibility data. The sources are put in random positions within the 1.5 $\times$ FWHM of the primary beam search radius. We inject 20 sources per map and repeat this procedure 50 times. To test the full data reduction and analysis chain, the visibilities with the injected artificial sources are imaged using the same settings for the CASA task TCLEAN as for the original visibilities. Then we use the same source finding procedure as for the real data to recover the artificial sources. In case a source was injected within a radius of 6$\times$ the beam width from another artificial source or within a radius of 1$''$ from the centre it is excluded from the further analysis. A source is considered to be recovered if it is detected with SExtractor at $\geq 2.5\sigma$ and within 1$\times$ the synthesized beam width from the position of the injection. To estimate the errors on the completeness, we perform a bootstrap resampling. We take the parent population of n artificial sources and replace those with n randomly selected sources. This process is repeated 200 times and the completeness is calculated for each realization. We determine the scatter of the different realizations of the completeness. The resulting completeness as a function of SNR is shown in Fig. 7.2.

Our survey is 100% complete at a SNR $\geq$ 9 and 50% complete at an SNR $\geq$ 5. Compared to the DSFG survey in Band 6 and 7 presented by Oteo et al. (2016b) our completeness function is slightly flatter reaching a high completeness only at higher SNR. This is due to the fact that the details of the analysis were chosen in a slightly different way. Furthermore, we have less observing time per field in Band 8, than in Band 6 and 7 (see Chapter 2), at higher frequencies, the uv coverage is not as high in Band 8 than in Band 6 and 7 and the noise in the ALMA maps becomes more non-Gaussian than at lower frequencies.

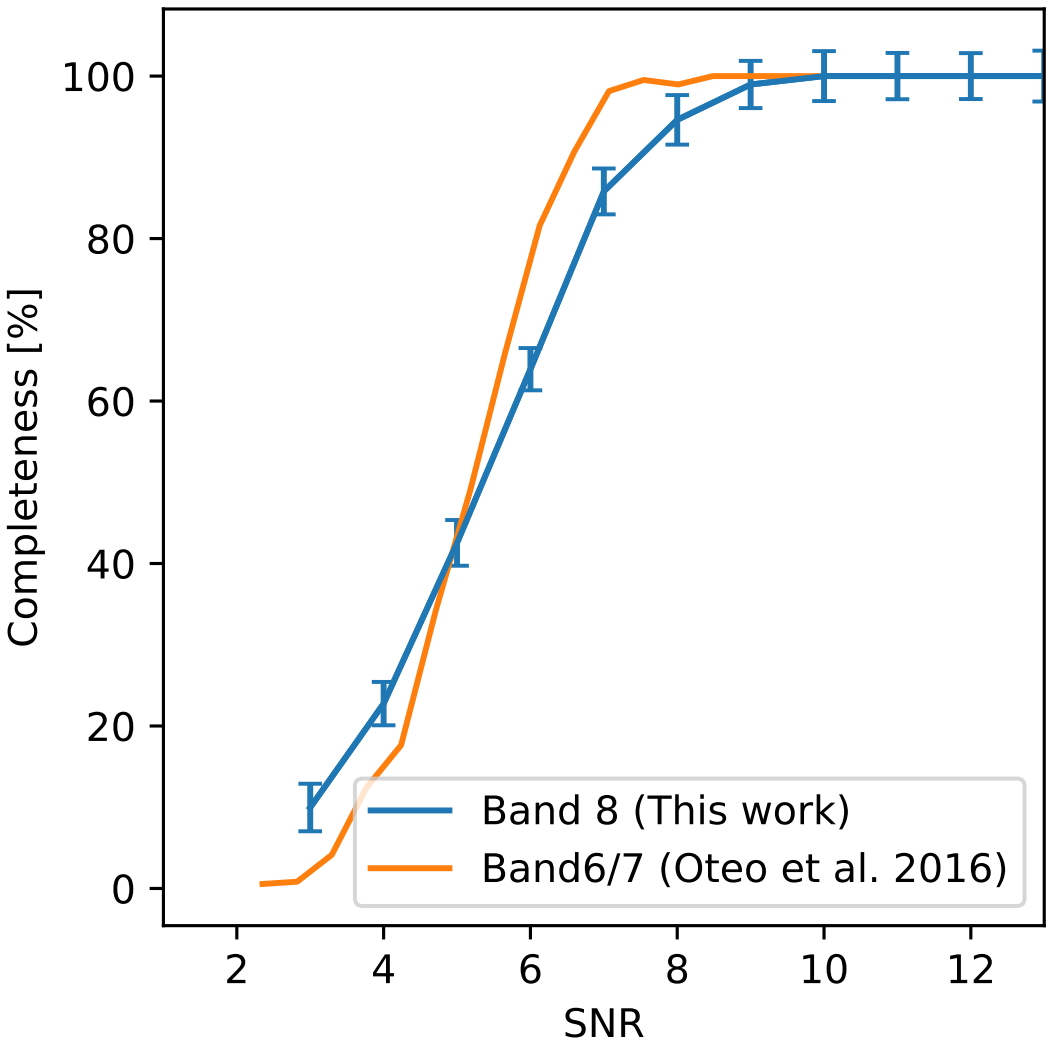

Figure 7.2: Completeness of ALMACAL Band 8 as a function of the SNR of the detected sources. We reach a completeness of 100% at 10σ and a completeness of 80% at a round 7σ. The detection threshold of 4.5σ the completeness is 33%.

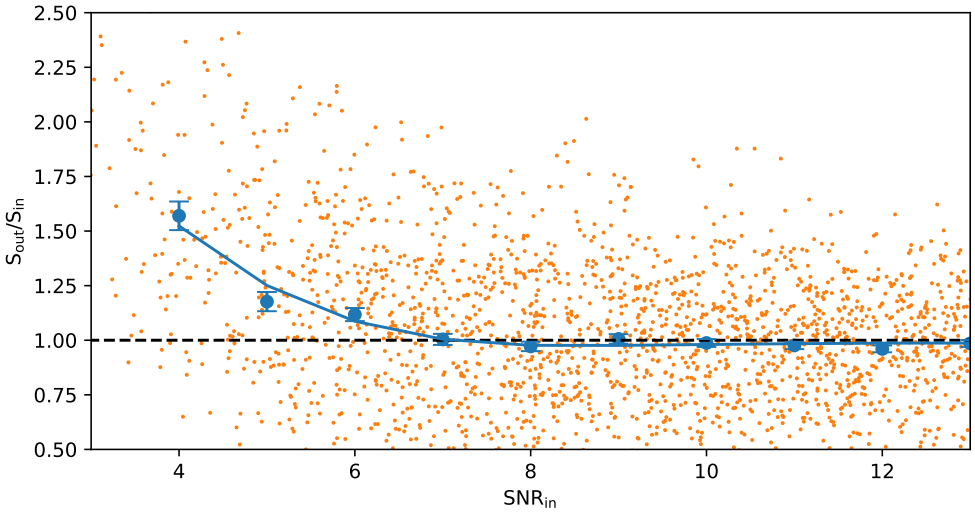

Figure 7.3: The ratio between the output and input flux densities of the simulated sources as a function of the input SNR (defined as the ratio between the input flux density and the rms at the centre of the map). The output flux densities tend to be increasingly overestimated at an SNR $< 7\sigma$. At 4.5σ the flux boosting is 38%.

7.3.4 Flux Deboosting

A known issue of measuring flux densities of continuum sources detected at low SNR is the fact that their flux densities can be boosted due to the presence of noise fluctuations. To measure this effect we use the same set of artificial point sources described in Section 7.3.3. We measure the flux density of the detected sources relative to the input flux density prior to PB correction. The flux measurement is performed in the same way as for the real detections. The results are shown in Fig. 7.3. We find that the flux density for sources detected at 4.5σ is boosted by $\sim$ 38%. At a SNR of $\geq$ 7 the effect of flux boosting is negligible. Half of our DSFG detections fall in this regime below 7σ where flux boosting needs to be corrected. To correct for the flux boosting we resample the flux boosting in bins of 0.25 and fit a cubic spline to the mean in each bin. We correct the flux densities of our catalogue based on the SNR of each source and using the spline fit.

7.3.5 Source Catalogue

Figure 7.4: Band 8 and Band 6 maps of the 0.3″ resolution detections part 1. Band 8 detections are marked with squares on both maps (Band 8 and Band 6 detection: orange, Band 8 only detection: blue, identified jets: black), the solid black circle indicates the area over which we search for continuum emission (1.5× the expected primary beam FWHM in Band 8) corresponding to 18″, the dashed black circle indicates the central 1″ region excluded from the survey due to possible contamination from quasar residuals. The same areas are also marked on the Band 6 images for reference. The blue ellipse marks the synthesized beam. For J1058+0133 we reproduce the Band 7 map presented by Oteo et al. (2017).

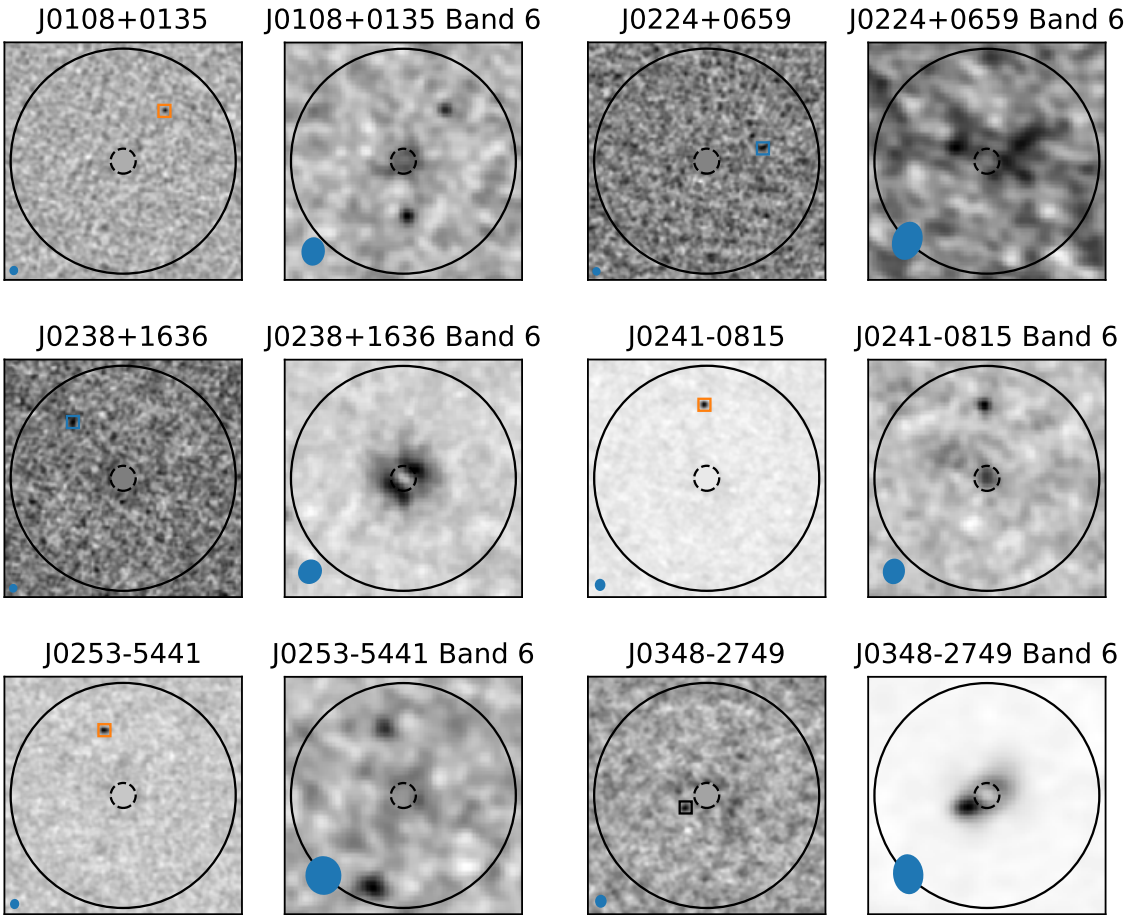

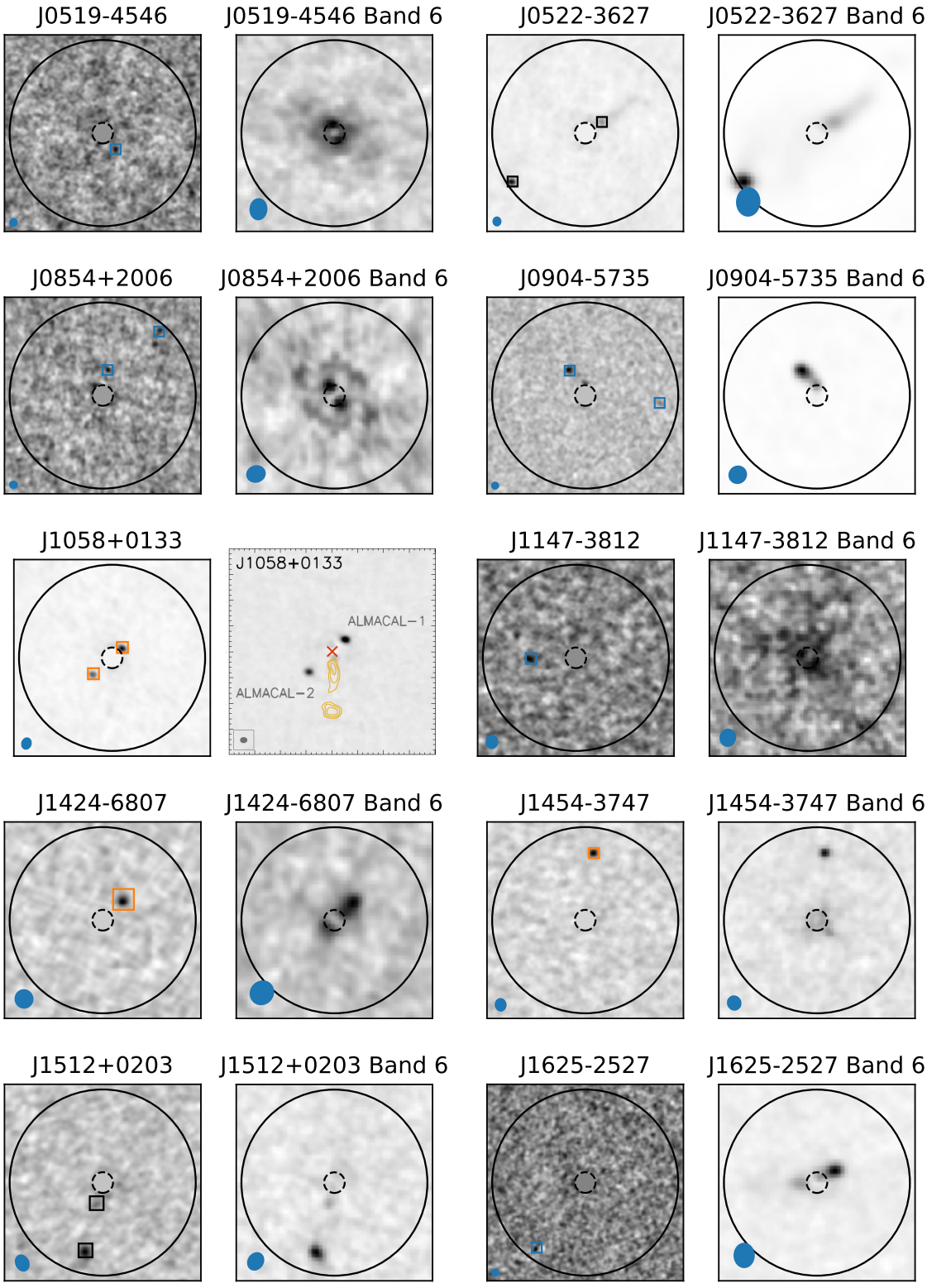
J0519-4546
J0519-4546 Band 6
J0522-3627
J0522-3627 Band 6
J0854+2006
J0854+2006 Band 6
J0904-5735
J0904-5735 Band 6
J1058+0133
J1058+0133
ALMACAL−1
ALMACAL−2
J1147-3812
J1147-3812 Band 6
J1424-6807
J1424-6807 Band 6
J1454-3747
J1454-3747 Band 6
J1512+0203
J1512+0203 Band 6
J1625-2527
J1625-2527 Band 6

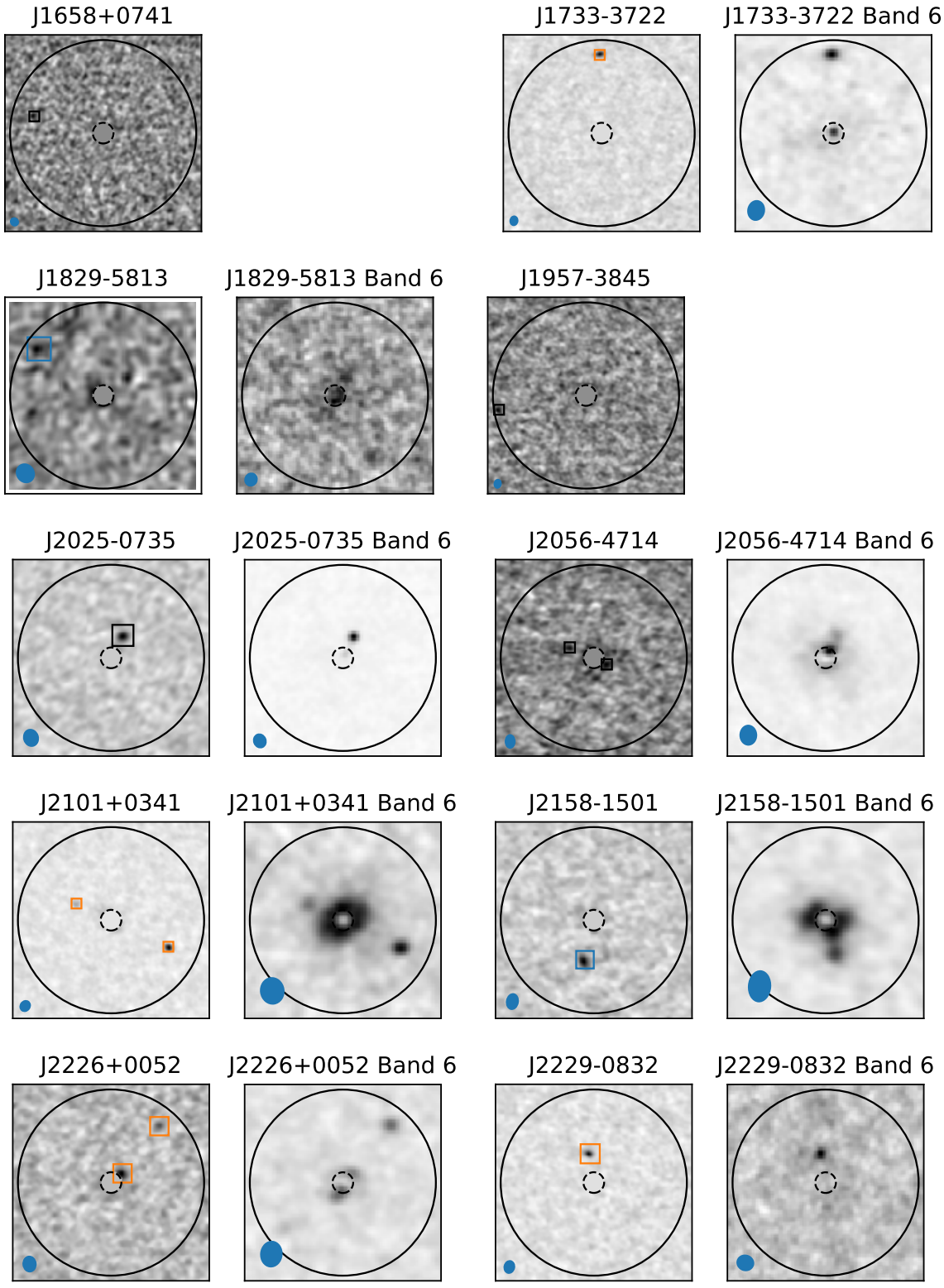
J1658+0741
J1733-3722
J1733-3722 Band 6
J1829-5813
J1829-5813 Band 6
J1957-3845
J2025-0735
J2025-0735 Band 6
J2056-4714
J2056-4714 Band 6
J2101+0341
J2101+0341 Band 6
J2158-1501
J2158-1501 Band 6
J2226+0052
J2226+0052 Band 6
J2229-0832
J2229-0832 Band 6

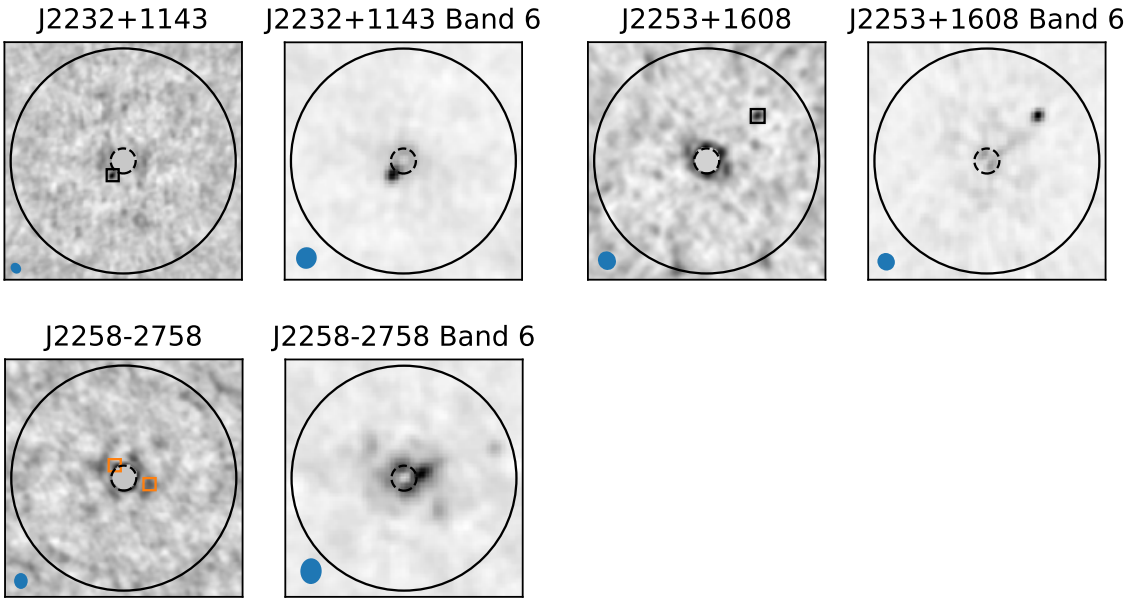
J2232+1143
J2232+1143 Band 6
J2253+1608
J2253+1608 Band 6
J2258-2758
J2258-2758 Band 6

Table 7.1: DSFGs detected at 680μm up to December 2019 in our ALMACAL survey.

Name	$z_{\rm cal}$	$S_{680\mu{\rm m}}$ [mJy]	$S_{1.2{\rm mm}}$ [mJy]
ALMACAL 010838.56+013504.3	2.099	3.6 ± 0.6	0.6 ± 0.2
ALMACAL 022428.13+065924.3	0.511	1.7 ± 0.3	<0.7
ALMACAL 023839.21+163703.7	0.94	2.7 ± 0.2	<0.3
ALMACAL 024104.81–081514.9	0.00512	3.0 ± 0.1	0.5 ± 0.1
ALMACAL 025329.36–544146.3	0.539	2.1 ± 0.1	0.3 ± 0.1
ALMACAL 034838.28–274914.6	0.176	0.7 ± 0.2	4.0 ± 0.2
ALMACAL 051949.61–454645.5	0.035	0.7 ± 0.2	<0.1
ALMACAL 052257.86–362729.8	0.05629	8.7 ± 0.5	24.8 ± 2.9
ALMACAL 052258.57–362735.6	0.05629	45.8 ± 0.4	61.0 ± 2.3
ALMACAL 085448.49+200636.8	0.306	6.8 ± 0.5	<0.4
ALMACAL 085448.85+200633.0	0.306	2.3 ± 0.6	0.7 ± 0.1
ALMACAL 090453.37–573503.4	0.695	16.1 ± 1.0	37.1 ± 1.4
ALMACAL 090452.29–573506.6	0.695	5.9 ± 0.9	<5.2
ALMACAL 105829.73+013357.2	0.888	7.2 ± 0.6	2.0 ± 0.1
ALMACAL 105829.54+013359.8	0.888	13.4 ± 0.6	1.5 ± 0.1
ALMACAL 114701.74–381211.2	1.048	2.7 ± 0.6	<0.3
ALMACAL 142455.22–680756.2	...	3.8 ± 0.5	1.1 ± 0.1
ALMACAL 145427.34–374726.7	0.31421	9.4 ± 0.4	2.3 ± 0.1
ALMACAL 151215.86+020310.3	0.219	4.0 ± 0.2	5.9 ± 0.2
ALMACAL 151215.79+020314.9	0.219	0.9 ± 0.2	0.8 ± 0.3
ALMACAL 162547.24–252744.7	0.786	1.2 ± 0.3	<0.3
ALMACAL 165809.46+074129.1	0.621	9.9 ± 1.6	...
ALMACAL 173315.21–372224.9	...	11.0 ± 0.2	2.2 ± 0.1
ALMACAL 182913.20–581350.8	1.531	3.4 ± 0.4	<0.7
ALMACAL 195800.54–384507.8	0.63	2.8 ± 0.2	...
ALMACAL 202540.59–073550.6	1.388	2.2 ± 0.3	4.0 ± 0.1
ALMACAL 205616.59–471446.7	1.489	1.4 ± 0.4	0.6 ± 0.1

. . . Table 7.1 continued.

Name	$z_{\rm cal}$	$S_{680\mu{\rm m}}$ [mJy]	$S_{1.2{\rm mm}}$ [mJy]
ALMACAL 205616.24–471448.3	1.489	1.8 ± 0.4	1.2 ± 0.1
ALMACAL 210139.06+034132.9	1.013	1.4 ± 0.2	0.7 ± 0.1
ALMACAL 210138.47+034128.7	1.013	5.8 ± 0.2	0.8 ± 0.1
ALMACAL 215806.35–150113.3	0.67183	2.9 ± 0.2	<1.2
ALMACAL 222646.23+005216.7	2.25	0.7 ± 0.2	0.3 ± 0.0
ALMACAL 222646.47+005212.1	2.25	1.3 ± 0.2	0.4 ± 0.1
ALMACAL 222940.12–083251.8	1.5595	4.9 ± 0.4	1.6 ± 0.2
ALMACAL 223236.47+114349.7	1.037	2.2 ± 0.2	4.8 ± 0.2
ALMACAL 225357.47+160857.1	0.859	1.3 ± 0.4	6.0 ± 0.3
ALMACAL 225806.02–275820.3	0.92562	2.1 ± 0.2	1.6 ± 0.1
ALMACAL 225805.81–275821.8	0.92562	1.4 ± 0.2	1.9 ± 0.1

Notes:

[a] Flux densities reported in this Table are corrected for primary beam attenuation.

[b] Naming scheme: ALMACAL hhmmss.ss±ddmmss.s

In the 81 ALMACAL Band 8 maps, we found 38 continuum detections in Band 8 out of which 13 are identified as jets. Of the remaining 25 detections 16 are detected at 1.2mm. All 25 detections have flux density ratios $S_{680\mu{\rm m}}/S_{1.2{\rm mm}}$ compatible with DSFGs based on the most recent ALMACAL data (Version June 2019). Four of the new Band 8 detections were already detected in a previous ALMACAL Band 6 source detection (Version July2015 Oteo et al., 2016b). The Band 8 and Band 6 maps of the calibrator fields with a peak flux detection at $> 4.5\sigma$ are shown in Fig. 7.4. Since all Band 8 detections not detected in Band 6 are low SNR detections we exclude these detections from the further analysis.

We measure the flux from the primary beam corrected maps by integrating the signal in a circular aperture with a radius of 1.5× synthesized beam width around the position of the peak flux determined by SExtractor. We measure Band 6 flux densities at the position of the Band 8 detections using an aperture with a radius of 1.5× beam width in Band 6.

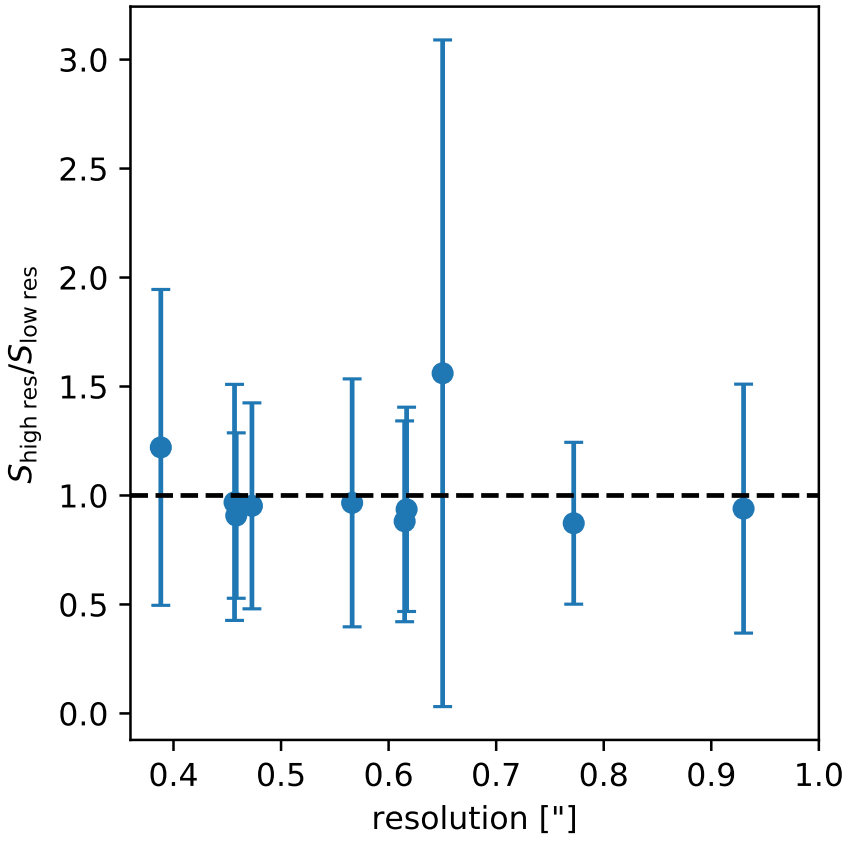

Figure 7.5: Ratio of the fluxes measured in the low and high resolution maps as a function of resolution in the high resolution maps. We find that within the errors the two flux measurements are consistent with a median flux ratio of 0.94. No flux correction needs to be applied to the higher resolution maps.

The multi-band flux densities of the detections are given in Table 7.1.

We use the low resolution maps to test if we are missing flux in the high resolution maps because the sources have more extended emission. Therefore, we measure the flux in bright detections in the 0.8″ maps and compare it with the flux measured in the high resolution maps. The flux ratios are shown in Fig. 7.5. We find that within the errors the two flux measurements are consistent and no correction factor needs to be applied.

7.3.6 Band 6 Counterparts and Redshift Distribution

Our aim is to build reliable 680μm number counts. To identify spurious detections we measure the Band 6 flux densities at the position of Band 8 detections. Since observations in Band 6 are more frequent than Band 8 the ALMACAL maps of the same calibrator

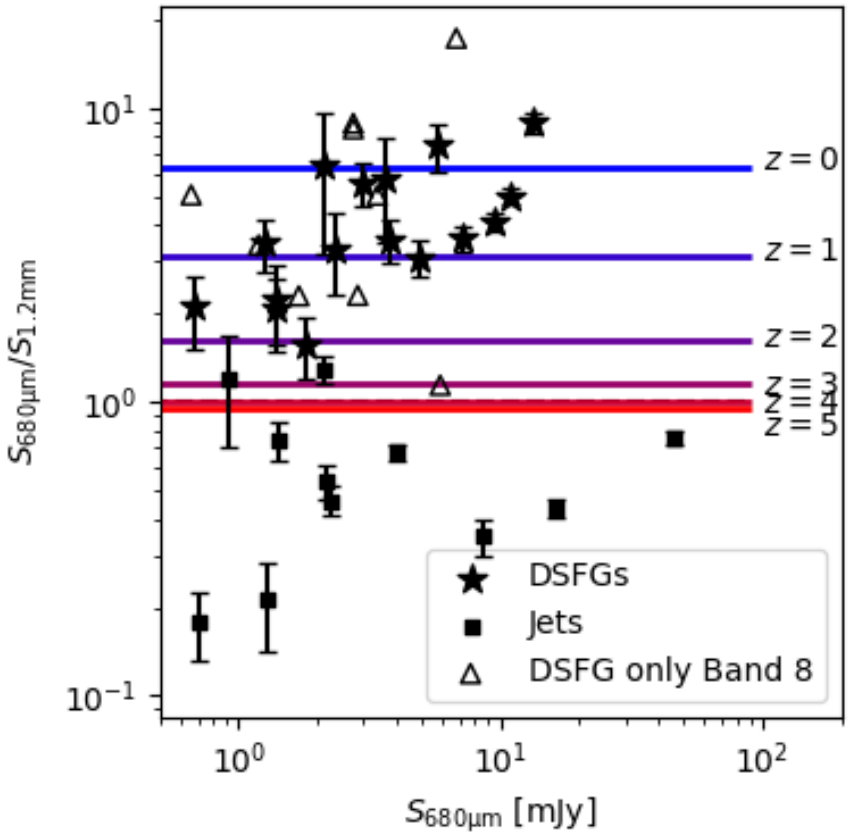

Figure 7.6: The ratio between the primary beam corrected flux densities at 680μm and 1.2mm for the DSFGs with a detection in our ALMACAL Band 8 and Band 6 data as a function of Band 8 flux density. The horizontal lines mark the expected average flux density ratio at different redshifts (blue - red: $z = 0 - 6$) based on the SEDs of SMGs from the ALESS survey (Swinbank et al., 2014). Detections with a flux density ratio $\lesssim 1$ are identified to be jets based on the difference between the dust and synchrotron emission in the SED and excluded from the number count calculation. Trangles marking Band 8 detections with out Band 6 counterparts are lower limits for the flux density ratio.

are deeper in Band 6 than in Band 8, securing a detection at a second frequency. We use the Band 6 observations to discriminate between DSFGs and jets related to the calibrator. Therefore, we measure the flux densities in Band 6 as described in Section 7.3.5 and calculate the ratio between the Band 8 and Band 6 flux densities (see Fig. 7.6). The emission from jets is synchrotron radiation, which is increasing with increasing wavelength at the ALMA observing frequencies. The emission from dust on the other hand is black body radiation which is decreasing with increasing wavelength at the ALMA observing frequencies. Therefore, we identify jet emission with flux density ratios $S_{680\mu\mathrm{m}}/S_{1.2\mathrm{mm}}$ of $\lesssim 1$ as jets and discarded from the further analysis.

We compare the colours of our DSFGs with the expected colours based on SEDs from the ALESS survey (Swinbank et al., 2014). We calculate the expected average flux density ratio from the ALESS SEDs if shifted to different redshifts. The corresponding expected flux density ratios are marked as horizontal lines in Fig. 7.6. We find that most DSFGs are consistent with an SMG population at $z < 2$. This is lower than the DSFG population detected at 850μm at $z = 1 - 3$ (e.g. Chapman et al., 2005; Simpson et al., 2014) and comparable to the DSFG population detected at 450μm at $z = 0 - 3$ with an average redshfit of $z = 1.3$ (Geach et al., 2013). We test whether the DSFG redshifts are correlated with the redshifts of the calibrators for which a redshift is known. The redshifts are estimated based on the average flux density ratios of the ALESS SEDs. The errors are calculated based on the spread in the ALESS SEDs. As shown in Fig. 7.8 we do not find a significant correlation between the redshift of the DSFGs based on the SED and the redshift of the calibrator in the respective field. We conclude that the presence of the calibrator in the field does not introduce a bias in our detection rate of DSFGs.

Nine galaxies detected in Band 8 are not detected in Band 6. This can be explained by the increased CMB temperature at higher redshift. As outlined by Zhang et al. (2016) the higher CMB temperatures at high redshift can result in a dimming of the low frequency flux densities compared to high frequency flux densities. The Band 6 non-detections could therefore partly trace a high redshift population of DSFGs.

In addition to the Band 6 detections that are also detected in Band 8, we find in Fig. 7.4 also sources that are detected in Band 6, but not seen in Band 8. We will run a full search of continuum detection in Band 6 and construct SEDs to study the properties of the galaxies

detected at this wavelength. This will be subject of a future project.

7.3.7 Challenges

The submillimetre-bright quasars used as ALMA calibrators might launch jets which can be confused with DSFGs. We do find clear signatures of jets in the Band 6 and Band 8 maps. Jets are systematically aligned with the calibrator, have a more extended shape and have sometimes even curved tails connecting to the calibrator. It is therefore easy to visually distinguish detections of jets and DSFGs based on their morphology. Additionally, we measure the spectral slope of the Band 8 detections by measuring the flux density in the Band 6 maps at the position of the Band 8 detection. We find that in some fields with two Band 8 detections the DSFGs and the calibrator are connected by a straight line indicating the possible identification as a jet. However, using the slope of the SED we can exclude this possibility.

The ALMA calibrators are dominated by blazars Bonato et al. (2018). These galaxies are radio bright, because the line of sight coincides with the direction of the jet and not because they are particularly massive. However, searching for DSFGs around submillimetre bright galaxies might introduce a low level bias depending on the redshifts of the calibrators. Most DSFGs are at $z \gtrsim 1$ while the calibrators are mostly below $z \sim 1$ with a tail to $z \sim 3$. Therefore, it is less likely that the calibrator and the DSFGs are associated. Since previous attempts to measure submillimetre number counts targeted fields with infrared bright or otherwise extreme objects the bias introduced in our fields is expected to be smaller than in previous cases.

Calculating number counts at high frequencies is also challenging due to the decreasing FOV with increasing observing frequency which can make a survey susceptible to cosmic variance effects. We follow the description by Driver & Robotham (2010) to estimate to cosmic variance of the ALMACAL survey at 440 GHz. We assume a median redshift of the sources of 1, based on the photometric redshifts determined in this chapter. The radial depth is assumed to be $z = 0 - 2$, which corresponds to 15537 Mpc. We calculate the cosmic variance for the full survey volume as well as only for the deepest maps. For the deep maps, we include only sight lines with a central rms of $< 300\mu$Jy and take only half of the nominal search radius into account. This results in only 62 sight-lines. In both

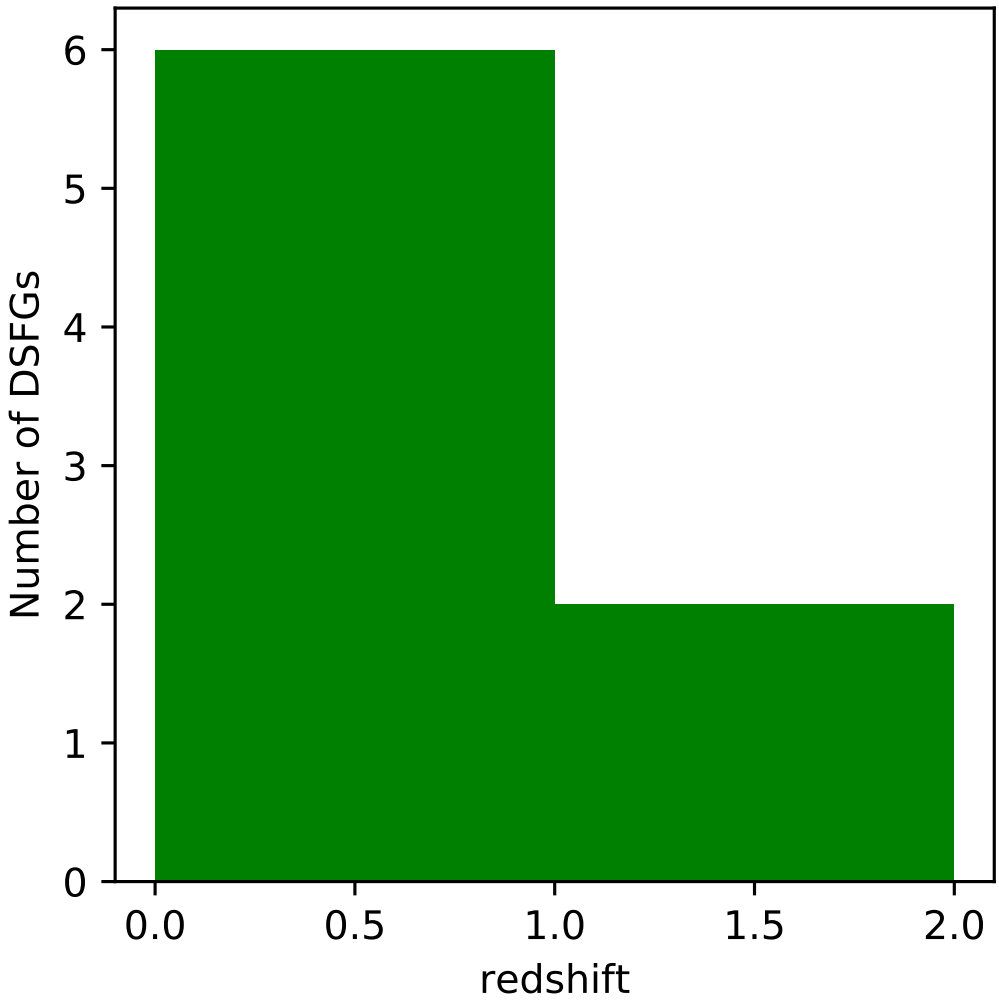

Figure 7.7: The redshift distribution of the DSFGs detected at 680μm based on the average SED from ALESS. Most of the DSFGs are at $z = 0 - 1.5$.

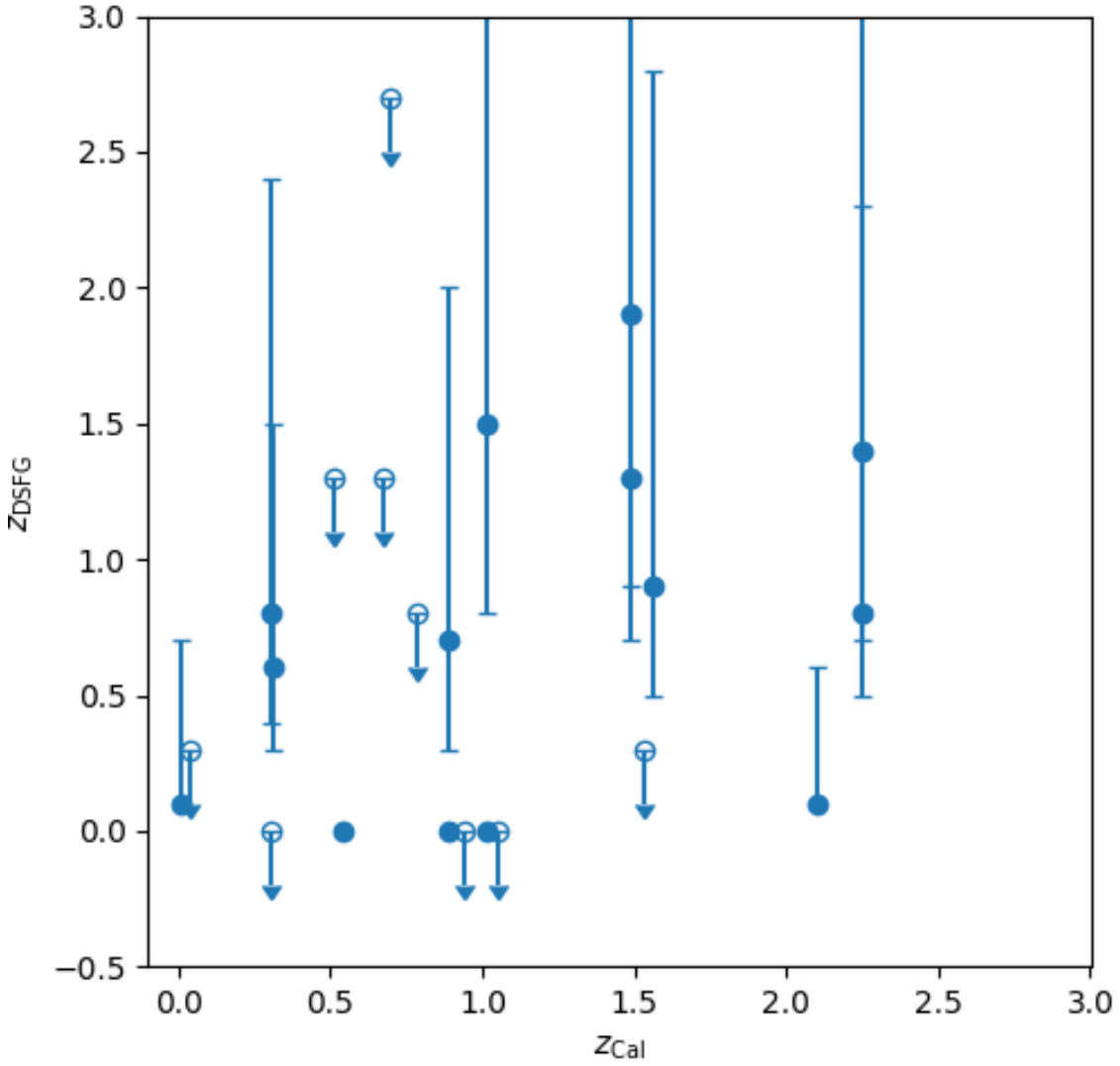

Figure 7.8: The redshift of the DSFGs based on the SED as a function of the redshift of the calibrator in the field. We find no correlation between the redshift of the DSFG and the calibrator in the respective field.

cases the cosmic variance is below 5%.

7.3.8 Effective Area

The sensitivity in an interferometric observation (like our ALMA observations) is not uniform within the field of view, but decreases with increasing distance from the centre due to the primary beam response. The effective area over which a galaxy can be detected is therefore a function of the flux density. We define the maximum extent of a map to be 1.5× the FWHM of the primary beam expected at Band 8.

We measure the effective area as a function of SNR for our survey (shown in Fig. 7.9). Here we exclude the central region that is potentially contaminated by residuals from the calibrators. We reach an effective area of $\sim$ 5.5 arcmin^2 for a flux density of $\geqslant$ 5 mJy (4.5σ). In the earlier work using ALMACAL Version June 2015 Oteo et al. (2016b) achieved effective areas of $\sim$ 6 and $\sim$ 16 arcmin^2 for a flux density of 1 mJy at Band 7 and Band 6, respectively. This study benefited from the on average deeper maps in Band 6 and 7 due to lower receiver and sky noise as well as the much wider field of view at lower frequencies (FOV $\propto \lambda^2$).

This pioneering work using multi-field observations from ALMACAL is a unique opportunity to derive statistically meaningful number counts at high frequencies from high resolution observations and therefore free of source blending.

7.4 Results and Discussion

7.4.1 Number Counts

Finally, we present the cumulative number counts derived from our ALMACAL Band 8 detections. These are the highest frequency number counts derived from interferometric observations.

A galaxy i contributes to the cumulative number counts as follows:

$$N_i(S_i) = \frac{1 - f_{\mathrm{SP}(S_i)}}{C(S_i) \times A(S_i)}, \tag{7.4.1}$$

where S_i is the flux density of the source i, $f_{\mathrm{SP}(S_i)}$ is the fraction of spurious sources

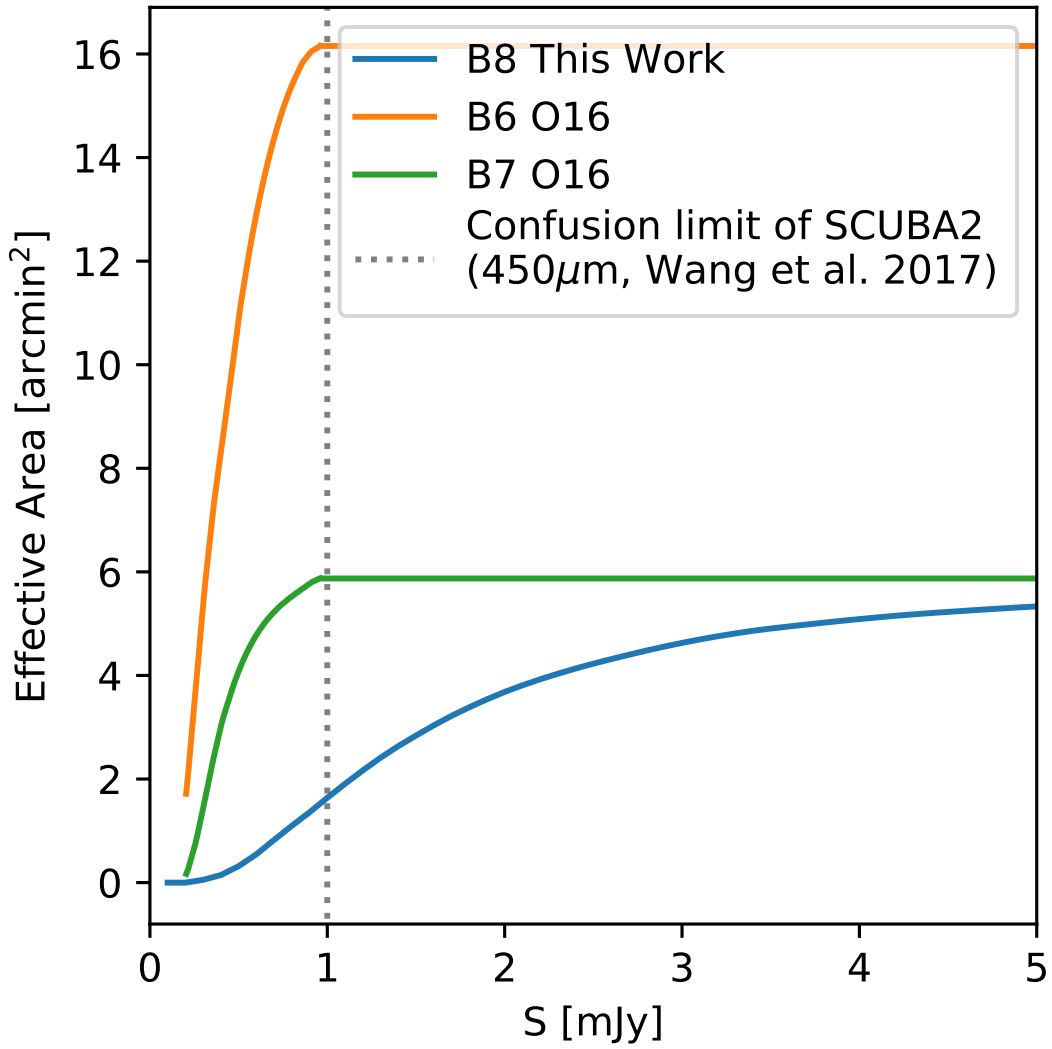

Figure 7.9: The effective are covered by the current ALMACAL Band 8 observations as a function of the flux density of detected sources. The sensitivity of an ALMA map is a function of the distance from the centre of the map. The effective area covered by the ALMACAL survey is therefore a function of the detected flux density. We calculate the area over which a galaxy could be detected at a peak SNR of 4.5σ. For comparison, we show the effective area probed in the Band 6 and Band 7 study by Oteo et al. (2016b) which benefits from the much larger primary beam in Band 6 and 7. Only with the multi field observations offered by ALMACAL we can derive statistically meaningful number counts at high frequencies.

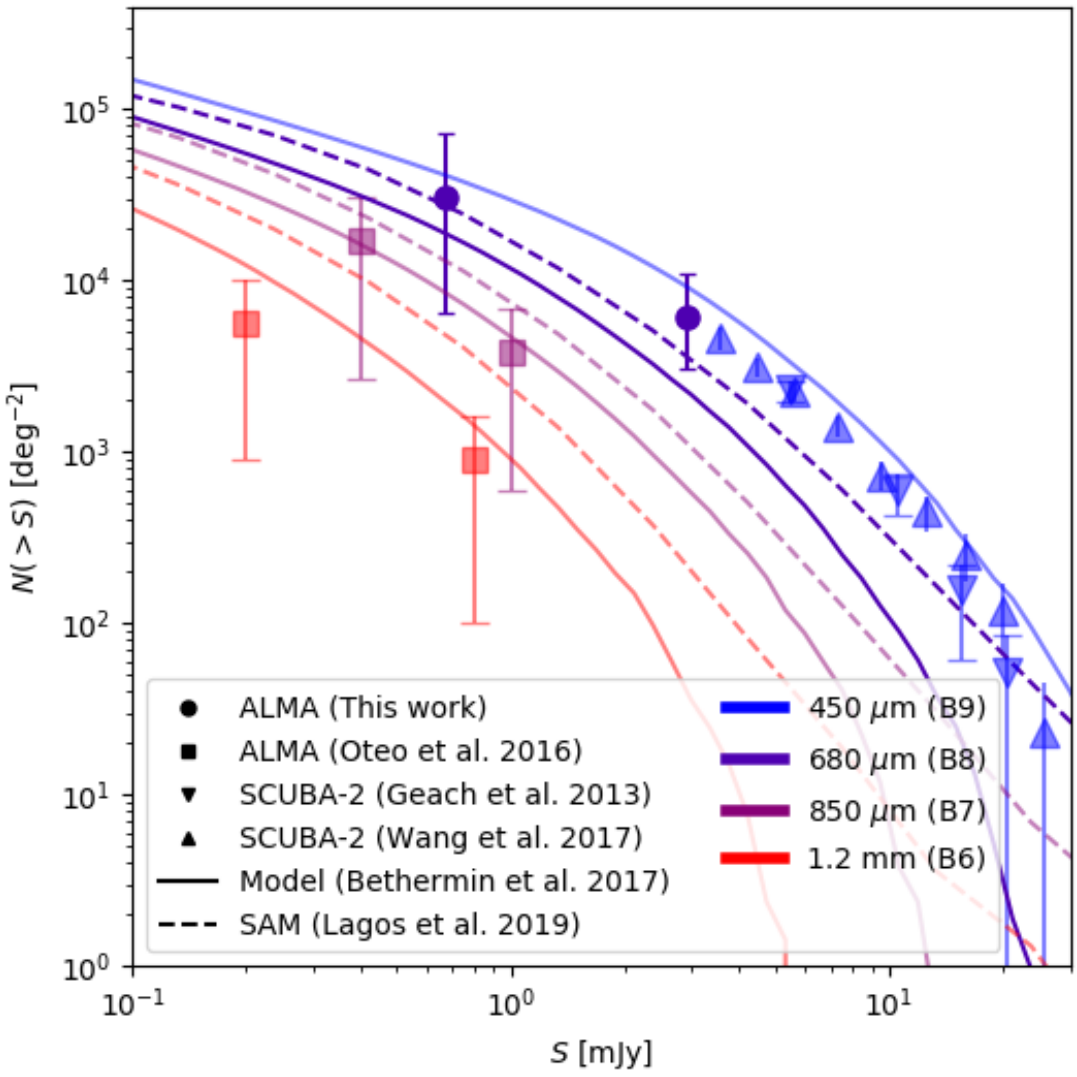

Figure 7.10: Cumulative number counts of DSFGs at 680μm (in ALMA Band 8, at 440 GHz). For comparison we show number counts from observations at different wavelengths as well as preditions from an empirical and semi-analytical model (Béthermin et al., 2017; Lagos et al., 2019). We use those models to calculate a model prediction for the number counts at 680μm by linearly interpolating between the 500μm and 850μm number count models. The number counts reported by Geach et al. (2013) are shifted by −2.5mJy to the low flux end of the bin.

Table 7.2: Cumulative 680μm number counts.

S [mJy]	$\log N(>S)$ [deg^{-2}]
0.67	$3.1^{4.2}_{-2.4}$
2.50	$0.61^{+0.48}_{-0.31}$

at S_i, $C(S_i)$ is the survey completeness at S_i and $A(S_i)$ is the effective area covered by the survey at S_i. Using our multi-band data we exclude all sources that are not detected in Band 6 and all Band 8 detections with Band 8 to Band 6 flux density ratios indicative of jets. Therefore, we expect the number of spurious sources at any flux density to be zero. The effective area and completeness are taken from Sections 7.3.3 and 7.3.8, respectively. To calculate the cumulative number counts we sum over all galaxies with flux densities higher than a given value:

$$N(>S) = \sum_{S_i>S} \frac{1 - f_{\mathrm{SP}(S_i)}}{C(S_i) \times A(S_i)}. \tag{7.4.2}$$

To calculate the errors on the cumulative number counts we combine bootstrapping errors with Poissonian errors. First we assign random fluxes to all detections within the uncertainties quoted in Table 7.1. This is done 1000 times to derive alternative realizations of the number counts. The bootstrapping error is the standard deviation in the 1000 realizations of the number counts. Second we determine the Poissonian errors given the number of high and low flux sources using the tables provided by Gehrels (1986). The total error is the quadratic sum of the bootstrap and Poissonian error. Results are shown in Fig. 7.10 and listed in Table 7.2. The derived number counts follow the expected trend of increasing number counts with increasing observing frequency. The Band 8 number counts are also consistent the emirical ans semi-analytical models presented by Béthermin et al. (2017); Lagos et al. (2019).

We note that the definition of the binning for cumulative number counts in the literature is not unique. Geach et al. (2013) for example quote $N(>S')$ at the center of the flux bin S while Oteo et al. (2016b); Wang et al. (2017) report $N(>S)$ at the lower edge of the flux bin. Since the latter is consistent with the results from semi-analytic models, we also report $N(>S)$ at the lower edge of the flux bin and shift the data points from Geach et al. (2013) accordingly.

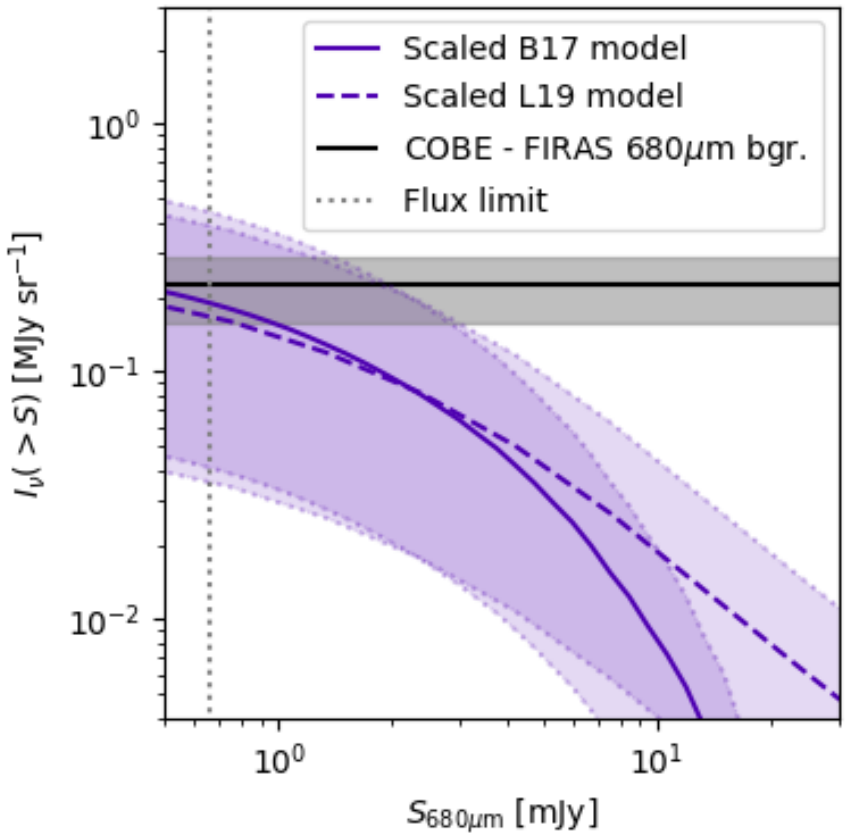

Figure 7.11: The integrated surface brightness of the 680μm emitters relative to the CIB measured by COBE-FIRAS at 680μm (Fixsen et al., 1998). The scaled model from Béthermin et al. (2017) and Lagos et al. (2019) amount to $\sim$ 87% of the cosmic infrared background at the lowest flux density observed in this study (indicated by the dotted vertical line).

7.4.2 Resolving the 680μm Background Light

We test what fraction of the cosmic infrared background (CIB) is resolved by our observations. Due to the limited amount of data we do not constrain the shape of the number counts. Therefore, we scale the semi-analytical model prediction from Béthermin et al. (2012b) to our observations. By integrating this scaled model we calculate the integrated surface brightness of the 680μm emitters (see Fig. 7.11) and compare this with the cosmic infrared background at the same wavelength as measured by the COBE-Far Infrared Absolute Spectrophotometer (FIRAS) (Fixsen et al., 1998). The authors find a CIB flux density of $I_\nu(680\mu\text{m}) = 0.22\text{MJy sr}^{-1}$. At the lowest observed flux density we find an integrated flux density of point sources detected at 680μm of

$I_\nu(680\mu\text{m}) = 0.19^{+0.27}_{-0.15}\text{MJy sr}^{-1}$. Therefore, we are resolving $\sim$ 87% of the cosmic infrared background consistently between the two different models. We conclude that the 680μm ALMACAL observations are deep enough to resolve the majority of the cosmic infrared background at 680μm. However, a wider effective area would be beneficial to increase the number of detections and therefore enable a measurement of the shape of the number counts at 680μm.

7.5 Summary and Conclusion

In this chapter we present the first high-frequency number counts at 680μm free of blending. We use observations from the ALMACAL survey version December 2018. In 81 fields 25 DSFGs were detected at a detection threshold of 4.5σ reaching flux densities as low as 0.66mJy. We combine the detections in Band 8 with observations of the same fields in Band 6 from ALMACAL to remove jets. We report 25 DSFGs detected at 680μm out of which 16 are also detected at 1.2mm. We calculate submillimetre colours and compare them with the expected colours of SMGs at different redshifts using the SMG SEDs from the ALESS survey (Swinbank et al., 2014). The DSFGs in our sample are consistent with SMGs at $z = 0 - 2$ consistent with samples of DSFGs detected at 450μm (e.g. Geach et al., 2013). We calculate number counts from our Band 8 detections. We do not find a correlation between the DSFG redshifts and the redshifts of the calibrators in the respective fields. The presence of the calibrator does therefore not introduce a bias in the derived number counts. The cumulative number counts follow the expected trend of increasing number counts with increasing observing frequency. They are also consistent empirical and semi-analytical models presented by Béthermin et al. (2017) and Lagos et al. (2019). Furthermore, we reach flux densities sensitive enough to resolve $\sim$ 87% of the cosmic infrared background at 680μm. This is a large improvement over the 24 – 33% previously reached at 450μm with SCUBA-2 (Wang et al., 2017). A larger survey area would be beneficial to pin down the shape of the number counts at this wavelength.

7.6 Appendix

7.6.1 Details of the Observations

In Table 7.3 we list the properties of our ALMACAL Band 8 and Band6 observations.

Table 7.3: Summary of the ALMACAL Band 8 (680μm) and Band 6 (1.2mm) observations used in this analysis (ALMACAL Version December 2018). The quoted σ is measured in the center of the field.

Name	R.A. [ICRS]	dec [ICRS]	detect.	σ_{B8} [μJy beam^{-1}]	θ_{B8} [$'' \times ''$]	σ_{B6} [μJy beam^{-1}]	θ_{B6} [$'' \times ''$]
J0006–0623	00h06m13.89s	–06d23m35.3s	N	124	0.50×0.44	...	...
J0013–0423	00h13m54.13s	–04d23m52.3s	N	189	0.46×0.40	...	...
J0038–2459	00h38m14.74s	–24d59m02.2s	N	115	0.67×0.57	...	...
J0108+0135	01h08m38.77s	+01d35m00.3s	Y	278	0.38×0.35	99	1.14×0.93
J0137–2430	01h37m38.35s	-2-4d30m53.9s	N	262	0.42×0.36	...	...
J0141–0928	01h41m25.83s	–09d28m43.7s	N	76	0.76×0.63	...	...
J0204–1701	02h04m57.67s	-1-7d01m19.8s	N	601	0.41×0.36	...	...
J0214–6149	02h14m16.20s	–61d49m33.7s	N	195	0.50×0.41	...	...
J0217+0144	02h17m48.95s	+01d44m49.7s	N	79	0.57×0.49	...	...
J0224+0659	02h24m28.43s	+06d59m23.3s	Y	129	0.34×0.33	99	1.56×1.18
J0238+1636	02h38m38.93s	+16d36m59.3s	Y	123	0.35×0.34	40	1.01×0.92
J0239–0234	02h39m45.47s	–02d34m40.9s	N	1022	0.69×0.66	...	...

* The rms of the Band 6 image of J1256–0547 is given in nJy beam^{-1}

... Table 7.3 continued.

Name	R.A. [ICRS]	dec [ICRS]	detect.	σ_{B8} [μJy beam^{-1}]	θ_{B8} [$'' \times ''$]	σ_{B6} [μJy beam^{-1}]	θ_{B6} [$'' \times ''$]
J0241–0815	02h41m04.80s	–08d15m20.8s	Y	47	0.49×0.43	40	1.03×0.88
J0253–5441	02h53m29.18s	–54d41m51.4s	Y	50	0.41×0.37	73	1.55×1.44
J0303–6211	03h03m50.63s	–62d11m25.5s	N	104	0.54×0.46	...	...
J0334–4008	03h34m13.65s	–40d08m25.4s	N	137	0.42×0.38	...	...
J0348–2749	03h48m38.14s	–27d49m13.6s	Y	80	0.52×0.46	109	1.60×1.21
J0407–1211	04h07m48.43s	–12d11m36.7s	N	189	0.49×0.38	...	...
J0423–0120	04h23m15.80s	–01d20m33.1s	N	130	0.76×0.60	...	...
J0440–4333	04h40m17.18s	–43d33m08.6s	N	354	0.43×0.37	...	...
J0505+0459	05h05m23.18s	+04d59m42.7s	N	453	0.78×0.70	...	...
J0510+1800	05h10m02.37s	+18d00m41.6s	N	257	0.46×0.36	...	...
J0519–4546	05h19m49.72s	–45d46m43.9s	Y	88	0.43×0.40	19	1.07×0.87
J0522–3627	05h22m57.98s	–36d27m30.9s	Y	238	0.48×0.44	1314	1.42×1.18
J0538–4405	05h38m50.36s	–44d05m08.9s	N	145	0.41×0.38	...	...
J0854+2006	08h54m48.87s	+20d06m30.6s	Y	289	0.43×0.39	45	0.96×0.84
J0904–5735	09h04m53.18s	–57d35m05.8s	Y	462	0.39×0.38	628	0.92×0.88
J0909+0121	09h09m10.09s	+01d21m35.6s	N	198	0.43×0.38	...	...

* The rms of the Band 6 image of J1256–0547 is given in nJy beam^{-1}

... Table 7.3 continued.

Name	R.A. [ICRS]	dec [ICRS]	detect.	σ_{B8} [μJy beam^{-1}]	θ_{B8} [$'' \times ''$]	σ_{B6} [μJy beam^{-1}]	θ_{B6} [$'' \times ''$]
J0948+0022	09h48m57.32s	+00d22m25.6s	N	52	0.54×0.48	...	...
J1028–0236	10h28m34.04s	–02d36m59.7s	N	109	0.74×0.55	...	...
J1037–2934	10h37m16.08s	–29d34m02.8s	N	152	0.89×0.68	...	...
J1058+0133	10h58m29.60s	+01d33m58.8s	Y	254	0.61×0.51	...	...
J1146–2859	11h46m26.19s	–28d59m18.5s	N	337	0.39×0.37	...	...
J1147–3812	11h47m01.37s	–38d12m11.0s	Y	309	0.69×0.61	44	0.89×0.80
J1218–0119	12h18m34.93s	–01d19m54.3s	N	511	0.81×0.65	...	...
J1222+0413	12h22m22.55s	+04d13m15.8s	N	207	1.12×0.85	...	...
J1224+2122	12h24m54.46s	+21d22m46.4s	N	74	0.53×0.46	...	...
J1229+0203	12h29m06.70s	+02d03m08.6s	N	205	0.58×0.54	264	1.30×1.16
J1256–0547	12h56m11.17s	-05d47m21.5s	N	399	0.58×0.53	154*	1.00×0.92
J1312–0424	13h12m50.90s	–04d24m49.9s	N	121	0.46×0.40	...	...
J1316–3338	13h16m07.99s	–33d38m59.2s	N	212	0.56×0.50	...	...
J1321–4342	13h21m12.84s	–43d42m16.8s	N	139	0.70×0.59	...	...
J1327+2210	13h27m00.86s	+22d10m50.2s	N	167	0.84×0.74	...	...
J1332+0200	13h32m53.27s	+02d00m45.7s	N	173	0.90×0.67	...	...

* The rms of the Band 6 image of J1256–0547 is given in nJy beam^{-1}

... Table 7.3 continued.

Name	R.A. [ICRS]	dec [ICRS]	detect.	σ_{B8} [μJy beam^{-1}]	θ_{B8} [$'' \times ''$]	σ_{B6} [μJy beam^{-1}]	θ_{B6} [$'' \times ''$]
J1347+1217	13h47m33.36s	+12d17m24.2s	N	157	0.79×0.57	...	...
J1408–0752	14h08m56.48s	–07d52m26.7s	N	122	0.82×0.67	...	...
J1424–6807	14h24m55.56s	–68d07m58.1s	Y	235	0.94×0.92	43	1.24×1.15
J1427–4206	14h27m56.30s	–42d06m19.4s	N	184	0.79×0.65	71	0.95×0.84
J1454–3747	14h54m27.41s	–37d47m33.1s	Y	212	0.66×0.57	60	0.75×0.70
J1512+0203	15h12m15.74s	+02d03m17.0s	Y	89	0.86×0.68	116	0.94×0.79
J1516+1932	15h16m56.80s	+19d32m13.0s	N	207	0.38×0.34	...	...
J1517–2422	15h17m41.81s	–24d22m19.5s	N	142	0.76×0.63	...	...
J1549+0237	15h49m29.44s	+02d37m01.2s	N	269	1.05×0.74	...	...
J1604–4441	16h04m31.02s	–44d41m32.0s	N	577	0.96×0.81	...	...
J1610–3958	16h10m21.88s	–39d58m58.3s	N	147	0.45×0.41	...	...
J1617–5848	16h17m17.89s	–58d48m07.9s	N	331	0.93×0.70	...	...
J1625–2527	16h25m46.89s	–25d27m38.3s	Y	192	0.40×0.37	40	1.23×1.03
J1658+0741	16h58m09.01s	+07d41m27.5s	N	846	0.46×0.43	...	...
J1733–1304	17h33m02.71s	–13d04m49.5s	N	303	0.57×0.46	...	...
J1733–3722	17h33m15.19s	–37d22m32.4s	Y	132	0.51×0.43	57	1.01×0.86

* The rms of the Band 6 image of J1256–0547 is given in nJy beam^{-1}

... Table 7.3 continued.

Name	R.A. [ICRS]	dec [ICRS]	detect.	σ_{B8} [μJy beam^{-1}]	θ_{B8} [$'' \times ''$]	σ_{B6} [μJy beam^{-1}]	θ_{B6} [$'' \times ''$]
J1751+0939	17h51m32.82s	+09d39m00.7s	N	260	0.41×0.38	...	...
J1802–3940	18h02m42.68s	–39d40m07.9s	N	422	0.55×0.44	...	...
J1826–2924	18h26m20.60s	–29d24m25.0s	N	529	1.12×0.61	...	...
J1829–5813	18h29m12.40s	–58d13m55.2s	Y	218	0.99×0.89	79	0.69×0.64
J1924–2914	19h24m51.06s	–29d14m30.1s	N	98	0.61×0.51	...	...
J1957–3845	19h57m59.82s	–38d45m06.4s	N	119	0.48×0.39	...	...
J2025–0735	20h25m40.66s	–07d35m52.7s	Y	122	0.88×0.76	65	0.73×0.65
J2056–4714	20h56m16.36s	–47d14m47.6s	Y	174	0.71×0.53	33	1.01×0.86
J2101+-0341	21h01m38.83s	+03d41m31.3s	Y	115	0.60×0.53	64	1.34×1.19
J2141–6411	21h41m46.44s	–64d11m14.5s	N	623	0.55×0.41	...	...
J2148+0657	21h48m05.46s	+06d57m38.6s	N	348	0.44×0.41	...	...
J2158–1501	21h58m06.28s	–15d01m09.3s	Y	94	0.82×0.62	168	1.56×1.13
J2226+0052	22h26m46.54s	+00d52m11.3s	Y	81	0.81×0.69	22	1.29×1.09
J2229–0832	22h29m40.08s	–08d32m54.4s	Y	172	0.67×0.56	79	0.87×0.80
J2230–4416	22h30m56.44s	–44d16m29.9s	N	209	0.41×0.40	...	...
J2232+1143	22h32m36.41s	+11d43m50.9s	Y	104	0.46×0.39	100	0.87×0.82

* The rms of the Band 6 image of J1256–0547 is given in nJy beam^{-1}

... Table 7.3 continued.

Name	R.A. [ICRS]	dec [ICRS]	detect.	σ_{B8} [μJy beam^{-1}]	θ_{B8} [$'' \times ''$]	σ_{B6} [μJy beam^{-1}]	θ_{B6} [$'' \times ''$]
J2235–4835	22h35m13.24s	–48d35m58.8s	N	335	0.74×0.58	...	...
J2253+1608	22h53m57.75s	+16d08m53.6s	Y	206	0.76×0.70	137	0.72×0.68
J2258–2758	22h58m05.96s	–27d58m21.3s	Y	89	0.63×0.54	74	0.92×0.80
J2357–5311	23h57m53.27s	–53d11m13.7s	N	127	0.44×0.41	...	...

* The rms of the Band 6 image of J1256–0547 is given in nJy beam^{-1}

Chapter 8

Conclusions and Future Work

A key ingredient to galaxy formation and evolution is the baryon cycle. It describes the accretion of gas onto galaxies, its transformation into stars and the exchange of gas with the galaxy surroundings via outflows. At $z = 0$ the majority ($> 90\%$) of the baryons exist in the form of molecular, neutral and ionized gas, which together form the essential component in the evolution of galaxies. A very small fraction ($\sim 2\%$) of this gas is condensed into galaxies (Fukugita et al., 1998), while most of the gas is in the diffuse reservoir of the circum-galactic, intra-group or intra-cluster medium or unbound to any halo.

In addition to conventional studies of emission-selected galaxies probing mainly galaxies with high stellar masses, the population of gas-rich galaxies is an important ingredient for a better understanding of galaxy evolution. Absorption lines imprinted in the spectra of otherwise unrelated background quasars can be used as an optimized tool to probe the circum-galactic medium of gas-rich galaxies with current instrumentation. For a better comprehension of the baryon cycle, we need to connect the neutral gas seen in absorption and the molecular gas traced by the CO emission on the one hand with the physical properties of the galaxies (star formation rate, stellar mass ($M_\star$), metallicity, kinematics, etc.) on the other hand. This allows us to probe the relation between accretion, outflows, tidal streams and the efficiency of the conversion of cold gas into stars. A good understanding of physical properties as well as the environment of the underlying gas-rich galaxy population is crucial to draw any firm conclusions on the baryon cycle using absorption-selected galaxies.

The aim of this thesis has been to explore some of the physical processes driving galaxy evolution. Key to the success of this work was the use and combination of state-of-the-art observing facilities such as ALMA and VLT/MUSE as well as the unconventional idea to make use of archival calibration data. In this final chapter, we summarize the key findings and highlight ongoing and future projects.

8.1 Summary of the Presented Work

8.1.1 The Baryon Cycle in an Absorption-Selected System

The flow of baryons into and out of galaxies is a crucial ingredient to galaxy evolution. For a full understanding of the galactic baryon cycle it is important to combine observations of the molecular, neutral and ionized gas of a galaxy and its environment.

In a case study, we have combined observations of the cool ionized gas from MUSE observations (PI Klitsch) with observations of the cold molecular gas from ALMACAL for a gas-rich system selected by Ly α absorption at $z = 0.633$ towards an ALMA calibrator. We find in total four massive ($M_\star = 10^{10.3-11.2}\mathrm{M}_\odot$) galaxies at the absorber redshift out of which one is also molecular gas-rich ($M_{\mathrm{mol}} = 10^{10}\mathrm{M}_\odot$). The CO line ratios as well as the dust-based SFR of $50\mathrm{M}_\odot\mathrm{yr}^{-1}$ suggest that this galaxy is a LIRG. We have studied the kinematics of the ionized and molecular gas and find that the gas seen in absorption is either tracing an outflow from the most massive galaxy or the intra-group medium. This study adds further evidence to the fact that absorbers cannot always simply be related to a single galaxy, but in many cases are rather related to a more complex environment.

8.1.2 Evidence for More Excited ISMs in Absorption-Selected Galaxies

The population of gas-rich galaxies selected by absorption towards background objects remains elusive. We have used ALMACAL multi-frequency detections of absorption-selected galaxies to study for the first time their CO spectral line energy distribution. The CO line ratios and the CO-to-H_2 conversion factor differ from those of the Milky Way. Thus, we have found evidence for more excited ISMs than normal star-forming galaxies

have. As a consequence, assuming Milky Way-type conversion factors to absorption-selected galaxies can potentially overestimate the total molecular gas mass. The results also suggest that quasar absorbers might preferentially trace galaxy overdensities.

8.1.3 Estimating the Molecular Gas Mass Density Over Cosmic Time from Intervening Molecular Absorbers

The physical processes shaping the dramatic change in the SFR between $z \sim 2$ and the present day are still a subject of ongoing research. We used the spectra of ALMA calibrators from our ALMACAL survey to search blindly for intervening molecular absorbers that could be detected against the emission from the background calibrator sources. In this survey adding up all redshift search ranges in all calibrator fields, we cover a redshift path of $\Delta z = 181$. We detect a multitude of Galactic absorbers and one absorber associated with the background AGN, but we do not detect any intervening molecular absorbers down to column densities as low as $N(\mathrm{CO}) \sim 10^{11}\mathrm{cm}^{-2}$. Based on these statistics, we calculate upper limits on the cosmic CO column density distribution function beyond $z = 0$, which is found to be consistent with predictions from hydrodynamical simulations from IllustrisTNG. Integrating our column density distribution function, we derive upper limits on the cosmic molecular gas mass density as a function of redshift free from cosmic variance. Combined with literature results our measurement suggests a strong evolution of the molecular gas mass density following that of the star formation rate density. The maximum radius of the molecular gas derived from our non-detection is ~ 5 kpc. To put stronger constraints on the molecular gas mass a significant increase of the redshift path covered per observation with ALMA is needed.

8.1.4 High-Frequency Submillimetre Number Counts Free of Source Confusion

Twenty years ago Fixsen et al. (1998) measured the cosmic far-infrared background (CIB) with the COBE-Far Infrared Absolute Spectrometer (FIRAS) indicating that half of the star formation activity in the Universe is obscured by dust. Resolving the CIB to study the population of galaxies in which this star formation takes place is a major research goal

in submillimetre astronomy. Furthermore, models of galaxy formation and evolution aim to reproduce submillimetre number counts at different wavelengths. We have presented the first high-frequency, high-resolution submillimetre number counts free from source blending and cosmic variance. We have used all ALMACAL Band 8 (680μm) observations up until December 2018. The number counts at 680μm consistently follow the trend of increasing number counts towards higher frequencies seen in previous surveys and theoretical models. Furthermore, they are consistent with a simple interpolation between the models for the 500μm and 850μm number counts from Béthermin et al. (2012b). With our deep and high spatial resolution 680μm number counts form ALMACAL we resolve the majority of the cosmic infrared background at that wavelength, which is a significant improvement over previous shallower studies using single-dish observations (Wang et al., 2019). Using the multi-wavelength observations from ALMACAL we will be able to study the spectral energy distribution of this galaxy population. We will also search for line emission from these galaxies to derive their redshifts. Combined with observations at lower frequencies our results will help us to better understand the population of galaxies in which half of the star formation activity in the Universe takes place.

8.2 Ongoing and Future Work

We have used absorption-selected galaxies as a tool to study gas-rich as opposed to massive galaxies traced in emission-selected samples. Focussing on the molecular gas content we started to establish the missing link between the cold neutral gas and the star formation in the baryon cycle. Furthermore, we studied the evolution of dust-rich galaxies in which half of the star formation in the Universe is taking place. Gaining a better understanding of the local and global baryon cycle from multiple angles, we have identified three areas that are central to further progress. Details on how these goals can be achieved in the near future are discussed in the remainder of this section.

Goal 1: Understand the gas flows in the population of gas-rich galaxies:

Tool 1: Increase the sample of CO detections in absorber host galaxies.

Tool 2: Study the following properties of molecular gas-rich absorption-selected galaxies.

* Constrain the ISM conditions by measuring the CO spectral line energy distribution.
* Analyse the environment and physical properties such as $M_\star$, SFR, metallicity and kinematics.

Goal 2: Trace the evolution of the molecular gas mass density over cosmic time to uncover the processes driving the strong evolution of the cosmic star formation history.

Tool 1: Continue searches for intervening molecular absorbers increasing the covered redshift path

Tool 2: Expand blind CO emission line surveys to studies free of cosmic variance.

Goal 3: Study the population of submillimetre galaxies in which half of the star formation activity in the Universe takes place.

Tool 1: Increase the sample of dusty star-forming galaxies at all wavelength.

Tool 2: Use multi-wavelength coverage to study physical properties of the underlying population including redshift, star formation rate, dust mass and stellar mass.

8.2.1 Understand the Gas Flows in the Population of Gas-Rich Galaxies

To improve our understanding of the population of gas-rich galaxies traced by absorption-selected systems we plan to increase the sample of absorber host galaxies with molecular gas mass measurements at low and high redshift. Furthermore, we will study the ISM conditions in these galaxies improving the measurement of molecular gas masses. This information combined with studies of the galaxy environments and other physical properties of gas-rich galaxies such as $M_\star$, star formation rate, metallicity and kinematics will offer vital clues on the baryon cycle.

Towards a Statistically Significant Sample of Gas-Rich Galaxies We have been awarded ALMA observing time (PI: A. Klitsch) to test a new approach to efficiently select molecular gas-rich absorption-selected galaxies. With these observations, we targeted six quasar fields with H_2 absorption previously identified in the UV ($0.2 < z_{\rm abs} < 1$). In total, seven galaxies at the absorber redshift have been optically identified in these fields. We have already obtained a first detection from this program. We will not only increase the number of molecular gas measurements in absorption-selected galaxies, but also test if, based on the impact parameter, the H_2 absorption arises from the molecular gas disk of a galaxy or the diffuse CGM. Additionally, we will establish a first relation between the HI and H_2 column density of the absorbing gas and the molecular gas mass of the host galaxy traced by CO. This ALMA Cycle 6 program serves as a pilot study which we will expand to a larger number of targets at the same redshift as well as higher redshift H_2 absorbers. In the northern hemisphere at low-redshift five H_2 absorbers are known that we will include in a similar program with NOEMA. Furthermore, thirteen H_2 absorbers and seven CO absorbers are detected at high redshift of $1.7 < z < 4.2$ (Noterdaeme et al., 2008, 2018). Once the relation between the H_2 column density and the H_2 mass of the host galaxy has been derived from the low-redshift pilot study, we will efficiently probe the CO emission of absorption-selected galaxies out to higher redshifts. Even assuming a detection rate of 50%, this study will at least double the number of CO detections in absorber host galaxies offering the largest sample of gas-rich galaxies with a complete census of the cold baryons.

Physical Properties and Environment of Gas-Rich Galaxies Most molecular gas mass measurements currently rely on observations of single higher order CO rotational transitions. For calculating gas masses from the CO fluxes, line ratios and the $\alpha_{\rm CO}$ conversion factor are assumed to be similar to those in the Milky Way. As we have shown in Chapter 5, at least a fraction of absorption-selected galaxies have more excited ISMs.

It is important to extend this analysis to a larger sample of galaxies to quantify the range of ISM properties and measure reliable molecular gas masses. We have applied for follow-up observations with ALMA to cover a second CO line for the CO detections presented in Chapter 3. Furthermore, our group has applied for observations of multiple

CO lines in molecular gas-rich absorber host galaxies (PI: L. Christensen). We will continue to apply for observation time with NOEMA, VLA and ALMA to follow-up the CO detections presented so far, and measure the CO SLEDs of a larger sample of absorber host galaxies. This will allow us to determine the correct conversion factors and shed light on the ISM temperature and density in absorption-selected systems.

It is important to study the physical properties of the absorber host systems to disentangle the relationship between the gas seen in absorption and the host galaxy. By measuring physical properties of the galaxies such as SFR, metallicity, and kinematics, we will pin down the origin of the absorbing gas. By comparing the positions in velocity space and absorption and emission metallicities, we will determine whether it is tracing inflow, outflow, an extended rotating gas disk, or intra-group medium. Therefore, we are planning to follow up all CO detections of absorption-selected galaxies with MUSE. As showcased in Chapter 4, we will be able to detect galaxies down to low SFR (SFR $\sim 0.1 M_{\odot}$/yr) within modest observing times (2h per field at $z \sim 0.5$). With such observations we will also test if the molecular gas-rich galaxies are actually not isolated, but exist in a group environment.

8.2.2 Evolution of the Molecular Gas Mass Density

Studying the evolution of the molecular gas mass density with cosmic time is a promising avenue to understand the evolution of the cosmic star formation rate history. Two complementary approaches were used so far to measure the cosmic molecular gas mass density: blind absorption line studies presented in Chapter 6 and blind emission line studies (Decarli et al., 2016, 2019; Riechers et al., 2018). Blind absorption line studies still suffer from short redshift paths while blind emission line studies are susceptible to cosmic variance effects. The two approaches are complementary since blind absorption line studies are sensitive to the low column densities tracing the low mass end of the distribution function, while blind emission line studies are mostly sensitive to the high mass end of the distribution function.

The Future of Blind Absorption Line Studies As long as ALMA is operational we will continue to increase our ALMACAL database ever-increasing the frequency coverage and

number of calibrator spectra. This will be supported by the technological improvements of ALMA recommended in the ALMA development roadmap, such as an increased frequency coverage per observation (Carpenter et al., 2019). Furthermore, new telescopes will provide further possibilities to increase the observed redshift path. Large single dish telescopes complementing ALMA such as AtLAST (Klaassen et al., 2019) promise high sensitivity and a higher efficiency for spectral scans. Pathfinder experiments for the Square Kilometre Array (SKA) MeerKAT and the Australian Square Kilometre Array Pathfinder (ASKAP) are already complementing this research by carrying out blind HI 21-cm absorption line surveys (Allison et al., 2016). This highlights the potential of future combined surveys of blind atomic and molecular absorption once the full SKA will be available.

The Future of Blind Emission Line Studies Large surveys of CO emission in cosmological deep fields such as COLDz (Riechers et al., 2018) and ASPECS (Decarli et al., 2016, 2019) have demonstrated the potential of blind emission line surveys. However, due to the limited field of view in interferometric observations these surveys are affected by cosmic variance effects. Our group is currently working on a comparable blind emission line survey in the ALMACAL fields. For a first pilot study our group has compiled a sample of 37 fields for which the total integration time at a given frequency is longer than 40 minutes. The area on sky of the pilot sample is 7.5 arcmin^2 and the total volume is 10 times that of the ASPECS survey. A challenge of our survey will be the confirmation and identification of single line detections since we do not yet have ancillary data at other wavelength regimes for the ALMACAL fields.

8.2.3 Deciphering the Population of Galaxies in which Half of the Star formation Activity in the Universe Takes Place

We will continue to use the growing ALMACAL database to search for dusty star-forming galaxies at different wavelengths. We will derive submillimetre number counts as shown in Chapter 7. We will expand the work to ALMA Bands 3, 6 and 7. At the different wavelength we will see different populations of DSFGs at different redshifts. In addition to the number counts, we will study the population of DSFGs by constructing SEDs

for multi-band detections and search for emission lines to pin down their redshift and molecular gas content. We will include also lower frequency Band 3 observations for which the expected population of DSFGs is tracing the highest redshifts and will help to constrain the high redshift slope of the star formation history.

8.3 Concluding Remarks

Within the next decade astronomy is entering the era of 40m-class telescopes. The increase in collecting area by more than one order of magnitude will allow us to detect ever fainter emission. With the integral field spectrograph HARMONI available for the first light of the Extremely Large Telescope (ELT) it will be possible to detect the CGM of normal star-forming galaxies in emission. We will be able to detect the Ly α emission line at $z > 3$ or Hα and other metal lines at redshifts $z < 2$ (Augustin et al. subm.). This will allow us to spatially resolve the distribution of neutral gas in the CGM in a small number of objects. As a second step the multi-object spectrograph MOSAIC planned for the second generation of instruments on the ELT will allow us to study the CGM and IGM in a larger sample.

The observations with the ELT will be complementary to the ongoing efforts of understanding absorption-selected systems. With a statistical sample of absorber host galaxies with a complete census of the cold baryons it will be possible to disentangle the physical processes driving galaxy formation and evolution. We will learn how gas is accreting onto galaxies, how it is expelled in outflows, what physical mechanisms drive the outflows and how the pristine inter-galactic material and the pre-enriched gas mix.

In addition, technological advances of existing instruments such as the BlueMUSE project (Richard et al., 2019) will be vital to progress in the field of galaxy formation and evolution. The authors are proposing to increase the wavelength coverage of MUSE to shorter wavelength. The upgraded instrument will be complementary to other new facilities such as the ELT and the James Webb Space Telescope (JWST) that are optimized to observations in the infrared. With BlueMUSE we will be able to detect Ly α emission down to $z \sim 2$ probing the peak of the cosmic star formation rate history. The instrument will be capable to detect the CGM directly in emission at lower redshifts making it an

important complementary tool to HARMONI and MOSAIC on the ELT.

The next advance in submillimetre astronomy will be a large single dish telescope complementing ALMA. Projects such as AtLAST (Klaassen et al., 2019) promise high sensitivity and large fields of view and therefore much higher survey speeds compared to interferometric telescopes suffering form small fields of view. Complementing follow-up with ALMA will enable large surveys of submillimetre galaxies with a well understood source blending. Furthermore, increases in the total observed bandwidth in both ALMA and future large single dish telescopes will allow for efficient spectral scans to determine redshifts or blind searches for intervening absorption.

At lower frequencies the SKA will provide measurements of the atomic gas mass density from blind 21 cm absorption surveys. The capabilities are already highlighted by the first results from the pathfinder experiments MeerKAT and ASKAP (Allison et al., 2016).

Blind emission line surveys for molecular gas will benefit from the planned advances of the Very Large Array (VLA): the next generation Very Large Array (ngVLA McKinnon & Selina, 2019). Planned advances are an increased sensitivity and frequency coverage. It will enable observations of molecular gas in normal star-forming galaxies out to high redshifts including low J transitions that are necessary to derive reliable molecular gas masses.

Combined with the advances in telescopes and instrumentation, high resolution hydrodynamical simulations will include a better treatment of the physical processes acting on the different gas phases. This will help us to uncover the mechanisms driving gas flows into and out of galaxies.

We are looking into a bright future for extra-galactic astronomy. The technological advances foreseen in the near future on both telescopes and instrumentation as well as numerical recipes and computing power will enable the scientific community to make the next big leap forward in understanding the physical processes that shape our Universe.

Bibliography

Al-Biruni, R., & Wright, R. 2004, The Book Of Instruction In The Elements Of The Art Of Astrology (Kessinger Publishing)

Allison, J. R., Zwaan, M. A., Duchesne, S. W., & Curran, S. J. 2016, Monthly Notices of the Royal Astronomical Society, 462, 1341

Allison, J. R., Mahony, E. K., Moss, V. A., et al. 2018, Monthly Notices of the Royal Astronomical Society

Amorisco, N. C., & Bertin, G. 2010, A&A, 519, A47

Andrews, S. M., Huang, J., Pérez, L. M., et al. 2018, The Astrophysical Journal, 869, L41

Anglés-Alcázar, D., Davé, R., Özel, F., & Oppenheimer, B. D. 2014, The Astrophysical Journal, 782, 84

Anglés-Alcázar, D., Faucher-Giguère, C.-A., Kereš, D., et al. 2017, Mon Not R Astron Soc, 470, 4698

Aravena, M., Decarli, R., Walter, F., et al. 2016a, The Astrophysical Journal, 833, 68

—. 2016b, The Astrophysical Journal, 833, 71

Arnouts, S., Cristiani, S., Moscardini, L., et al. 1999, Mon Not R Astron Soc, 310, 540

Arrigoni Battaia, F., Hennawi, J. F., Cantalupo, S., & Prochaska, J. X. 2016, The Astrophysical Journal, 829, 3

Arrigoni Battaia, F., Hennawi, J. F., Prochaska, J. X., et al. 2019, Monthly Notices of the Royal Astronomical Society, 482, 3162

Asplund, M., Grevesse, N., Sauval, A. J., & Scott, P. 2009, Annu. Rev. Astron. Astrophys., 47, 481

Bachiller, R., & Quintanilla, J. C., eds. 2008, Science with the Atacama Large Millimeter Array:: A New Era for Astrophysics (Springer Netherlands)

Bahcall, J. N., & Peebles, P. J. E. 1969, The Astrophysical Journal, 156, L7

Bahcall, J. N., Bergeron, J., Boksenberg, A., et al. 1996, The Astrophysical Journal, 457, 19

Baldry, I. K., Glazebrook, K., & Driver, S. P. 2008, Monthly Notices of the Royal Astronomical Society, 388, 945

Baldry, I. K., Driver, S. P., Loveday, J., et al. 2012, Monthly Notices of the Royal Astronomical Society, 421, 621

Barger, A. J., Cowie, L. L., Sanders, D. B., et al. 1998, Nature, 394, 248

Barger, A. J., Wang, W.-H., Cowie, L. L., et al. 2012, The Astrophysical Journal, 761, 89

Barnes, L. A., & Haehnelt, M. G. 2009, Monthly Notices of the Royal Astronomical Society, 397, 511

Baugh, C. M., Lacey, C. G., Frenk, C. S., et al. 2005, Monthly Notices of the Royal Astronomical Society, 356, 1191

Beaver, E. A., Burbidge, E. M., McIlwain, C. E., Epps, H. W., & Strittmatter, P. A. 1972, The Astrophysical Journal, 178, 95

Beelen, A., Omont, A., Bavouzet, N., et al. 2008, Astronomy and Astrophysics, 485, 645

Behroozi, P. S., Conroy, C., & Wechsler, R. H. 2010, The Astrophysical Journal, 717, 379

Belfiore, F., Maiolino, R., Tremonti, C., et al. 2017, Mon Not R Astron Soc, 469, 151

Bertin, E., & Arnouts, S. 1996, Astron. Astrophys. Suppl. Ser., 117, 393

Béthermin, M., Le Floc'h, E., Ilbert, O., et al. 2012a, Astronomy and Astrophysics, 542, A58

Béthermin, M., Daddi, E., Magdis, G., et al. 2012b, The Astrophysical Journal, 757, L23

Béthermin, M., Wu, H.-Y., Lagache, G., et al. 2017, Astronomy and Astrophysics, 607, A89

Bielby, R., Crighton, N. H. M., Fumagalli, M., et al. 2017, Monthly Notices of the Royal Astronomical Society, 468, 1373

Bielby, R. M., Tummuangpak, P., Shanks, T., et al. 2016, Mon Not R Astron Soc, 456, 4061

Bird, S., Vogelsberger, M., Haehnelt, M., et al. 2014, Mon Not R Astron Soc, 445, 2313

Bisbas, T. G., van Dishoeck, E. F., Papadopoulos, P. P., et al. 2017, The Astrophysical Journal, 839, 90

Blades, J. C., Hunstead, R. W., Murdoch, H. S., & Pettini, M. 1985, The Astrophysical Journal, 288, 580

Blain, A. W., Kneib, J.-P., Ivison, R. J., & Smail, I. 1999, The Astrophysical Journal, 512, L87

Blain, A. W., Smail, I., Ivison, R. J., Kneib, J.-P., & Frayer, D. T. 2002, Physics Reports, 369, 111

Blitz, L., & Rosolowsky, E. 2006, The Astrophysical Journal, 650, 933

Blumenthal, G. R., Faber, S. M., Primack, J. R., & Rees, M. J. 1984, Nature, 311, 517

Bock, D. 2007, From Planets to Dark Energy: the Modern Radio Universe, 13

Bolatto, A. D., Wolfire, M., & Leroy, A. K. 2013, Annual Review of Astronomy and Astrophysics, 51, 207

Bonato, M., Liuzzo, E., Giannetti, A., et al. 2018, Mon Not R Astron Soc, 478, 1512

Bordoloi, R., Lilly, S. J., Knobel, C., et al. 2011, The Astrophysical Journal, 743, 10

Bordoloi, R., Lilly, S. J., Hardmeier, E., et al. 2014, The Astrophysical Journal, 794, 130

Borisova, E., Cantalupo, S., Lilly, S. J., et al. 2016, The Astrophysical Journal, 831, 39

Borthakur, S., Yun, M. S., & Verdes-Montenegro, L. 2010, The Astrophysical Journal, 710, 385

Boselli, A., Cortese, L., Boquien, M., et al. 2014, Astronomy and Astrophysics, 564, A66

Bothwell, M. S., Smail, I., Chapman, S. C., et al. 2013, Monthly Notices of the Royal Astronomical Society, 429, 3047

Bouché, N., Carfantan, H., Schroetter, I., Michel-Dansac, L., & Contini, T. 2015, The Astronomical Journal, 150, 92

Bouché, N., Hohensee, W., Vargas, R., et al. 2012a, Monthly Notices of the Royal Astronomical Society, 426, 801

Bouché, N., Murphy, M. T., Kacprzak, G. G., et al. 2013, Science, 341, 50

Bouché, N., Murphy, M. T., Péroux, C., et al. 2007, ApJ, 669, L5

—. 2012b, Mon Not R Astron Soc, 419, 2

Bouché, N., Finley, H., Schroetter, I., et al. 2016, The Astrophysical Journal, 820, 121

Bowen, D. V., Chelouche, D., Jenkins, E. B., et al. 2016, The Astrophysical Journal, 826, 50

Brook, C. B., Stinson, G., Gibson, B. K., et al. 2014, Mon Not R Astron Soc, 443, 3809

Brooks, A. M., Governato, F., Quinn, T., Brook, C. B., & Wadsley, J. 2009, The Astrophysical Journal, 694, 396

Burbidge, E. M., Beaver, E. A., Cohen, R. D., Junkkarinen, V. T., & Lyons, R. W. 1996, The Astronomical Journal, 112, 2533

Burgh, E. B., France, K., & McCandliss, S. R. 2007, The Astrophysical Journal, 658, 446

Calzetti, D. 1997, The Astronomical Journal, 113, 162

Cantalupo, S., Arrigoni-Battaia, F., Prochaska, J. X., Hennawi, J. F., & Madau, P. 2014, Nature, 506, 63

Cantalupo, S., Porciani, C., Lilly, S. J., & Miniati, F. 2005, The Astrophysical Journal, 628, 61

Carilli, C., & Walter, F. 2013, Annual Review of Astronomy and Astrophysics, 51, 105

Carniani, S., Maiolino, R., De Zotti, G., et al. 2015, Astronomy and Astrophysics, 584, A78

Carpenter, J., Iono, D., Testi, L., et al. 2019, arXiv:1902.02856 [astro-ph]

Carroll, S. M., Press, W. H., & Turner, E. L. 1992, Annual Review of Astronomy and Astrophysics, 30, 499

Carswell, R. F., Hilliard, R. L., Strittmatter, P. A., Taylor, D. J., & Weymann, R. J. 1975, The Astrophysical Journal, 196, 351

Carswell, R. F., Morton, D. C., Smith, M. G., et al. 1984, The Astrophysical Journal, 278, 486

Casey, C. M., Hodge, J., Zavala, J. A., et al. 2018, The Astrophysical Journal, 862, 78

Casey, C. M., Chen, C.-C., Cowie, L. L., et al. 2013, Monthly Notices of the Royal Astronomical Society, 436, 1919

Chapman, S. C., Blain, A. W., Smail, I., & Ivison, R. J. 2005, The Astrophysical Journal, 622, 772

Chapman, S. C., Scott, D., Borys, C., & Fahlman, G. G. 2002, Monthly Notices of the Royal Astronomical Society, 330, 92

Chapman, S. C., Barger, A. J., Cowie, L. L., et al. 2003, ApJ, 585, 57

Chen, C.-C., Cowie, L. L., Barger, A. J., et al. 2013, The Astrophysical Journal, 776, 131

Chen, C.-C., Smail, I., Ivison, R. J., et al. 2016, The Astrophysical Journal, 820, 82

Chen, H.-W. 2005, in Extra-Planar Gas, Vol. 331, eprint: arXiv:astro-ph/0410558, 371

Chen, H.-W., Boettcher, E., Johnson, S. D., et al. 2019, arXiv:1906.00005 [astro-ph]

Chen, H.-W., Kennicutt, R. C., & Rauch, M. 2005, The Astrophysical Journal, 620, 703

Chen, L.-H., Hirashita, H., Hou, K.-C., et al. 2018, Monthly Notices of the Royal Astronomical Society, 474, 1545

Chisholm, J., Tremonti, C. A., Leitherer, C., Chen, Y., & Wofford, A. 2016, Monthly Notices of the Royal Astronomical Society, 457, 3133

Chisholm, J., Tremonti, C. A., Leitherer, C., et al. 2015, The Astrophysical Journal, 811, 149

Christensen, C. R., Davé, R., Governato, F., et al. 2016, The Astrophysical Journal, 824, 57

Christensen, L., Møller, P., Fynbo, J. P. U., & Zafar, T. 2014, Mon Not R Astron Soc, 445, 225

Churchill, C. W., Steidel, C. C., & Vogt, S. S. 1996, ApJ, 471, 164

Combes, F., Gupta, N., Jozsa, G. I. G., & Momjian, E. 2019, arXiv:1901.04683 [astro-ph]

Coppin, K., Chapin, E. L., Mortier, A. M. J., et al. 2006, Monthly Notices of the Royal Astronomical Society, 372, 1621

Cowley, W. I., Lacey, C. G., Baugh, C. M., & Cole, S. 2015, Monthly Notices of the Royal Astronomical Society, 446, 1784

Crain, R. A., Schaye, J., Bower, R. G., et al. 2015, Monthly Notices of the Royal Astronomical Society, 450, 1937

Dabrowski, I. 1984, Canadian Journal of Physics, 62, 1639

Daddi, E., Dannerbauer, H., Liu, D., et al. 2015, Astronomy and Astrophysics, 577, A46

Davé, R., Finlator, K., & Oppenheimer, B. D. 2012, Monthly Notices of the Royal Astronomical Society, 421, 98

Davé, R., Rafieferantsoa, M. H., Thompson, R. J., & Hopkins, P. F. 2017, Monthly Notices of the Royal Astronomical Society, 467, 115

de Blok, W. J. G., Walter, F., Ferguson, A. M. N., et al. 2018, The Astrophysical Journal, 865, 26

de Ugarte Postigo, A., Thöne, C. C., Bolmer, J., et al. 2018, Astronomy and Astrophysics, 620, A119

Decarli, R., Walter, F., Aravena, M., et al. 2016, The Astrophysical Journal, 833, 69

Decarli, R., Walter, F., Gónzalez-López, J., et al. 2019, arXiv:1903.09164 [astro-ph]

Dekel, A., Birnboim, Y., Engel, G., et al. 2009, Nature, 457, 451

Diemer, B., Stevens, A. R. H., Lagos, C. d. P., et al. 2019, arXiv:1902.10714 [astro-ph]

Driver, S. P., & Robotham, A. S. G. 2010, Monthly Notices of the Royal Astronomical Society, 407, 2131

Driver, S. P., Andrews, S. K., Davies, L. J., et al. 2016, The Astrophysical Journal, 827, 108

Driver, S. P., Andrews, S. K., da Cunha, E., et al. 2018, Monthly Notices of the Royal Astronomical Society, 475, 2891

Drory, N., Bundy, K., Leauthaud, A., et al. 2009, The Astrophysical Journal, 707, 1595

Dunlop, J. S., McLure, R. J., Biggs, A. D., et al. 2017, Monthly Notices of the Royal Astronomical Society, 466, 861

Ekers, R. D., Massardi, M., & Sadler, E. M. 2007, in From Planets to Dark Energy: The Modern Radio Universe, 47

Emonts, B. H. C., De Breuck, C., Lehnert, M. D., et al. 2015, Astronomy and Astrophysics, 584, A99

Erb, D. K. 2008, The Astrophysical Journal, 674, 151

Falgarone, E., Zwaan, M. A., Godard, B., et al. 2017, Nature, 548, 430

Faucher-Giguère, C.-A., Kereš, D., & Ma, C.-P. 2011, Monthly Notices of the Royal Astronomical Society, 417, 2982

Fixsen, D. J., Dwek, E., Mather, J. C., Bennett, C. L., & Shafer, R. A. 1998, The Astrophysical Journal, 508, 123

Fluetsch, A., Maiolino, R., Carniani, S., et al. 2019, Mon Not R Astron Soc, 483, 4586

Ford, A. B., Davé, R., Oppenheimer, B. D., et al. 2014, Monthly Notices of the Royal Astronomical Society, 444, 1260

Fox, A., & Davé, R., eds. 2017, Gas Accretion onto Galaxies, Astrophysics and Space Science Library (Springer International Publishing)

Fox, A. J., Wakker, B. P., Barger, K. A., et al. 2014, The Astrophysical Journal, 787, 147

Franco, M., Elbaz, D., Béthermin, M., et al. 2018, Astronomy and Astrophysics, 620, A152

Fu, H., Cooray, A., Feruglio, C., et al. 2013, Nature, 498, 338

Fujimoto, S., Ouchi, M., Ono, Y., et al. 2016, The Astrophysical Journal Supplement Series, 222, 1

Fukugita, M., Hogan, C. J., & Peebles, P. J. E. 1998, The Astrophysical Journal, 503, 518

Fumagalli, M., O'Meara, J. M., Prochaska, J. X., & Kanekar, N. 2010, Mon Not R Astron Soc, 408, 362

Fumagalli, M., O'Meara, J. M., Prochaska, J. X., & Worseck, G. 2013, The Astrophysical Journal, 775, 78

Fumagalli, M., Prochaska, J. X., Kasen, D., et al. 2011, Mon Not R Astron Soc, 418, 1796

Fumagalli, M., Mackenzie, R., Trayford, J., et al. 2017, Monthly Notices of the Royal Astronomical Society, 471, 3686

Fynbo, J. P. U., Laursen, P., Ledoux, C., et al. 2010, Monthly Notices of the Royal Astronomical Society, 408, 2128

Fynbo, J. P. U., Geier, S. J., Christensen, L., et al. 2013, Monthly Notices of the Royal Astronomical Society, 436, 361

Fynbo, J. P. U., Heintz, K. E., Neeleman, M., et al. 2018a, Mon Not R Astron Soc, 479, 2126

—. 2018b, ArXiv e-prints, 1806, arXiv:1806.01715

Fynbo, J. U., Møller, P., & Warren, S. J. 1999, Monthly Notices of the Royal Astronomical Society, 305, 849

Galilei, G. 1610, Sidereus Nuncius: Atque Medicea Sidera : Magna, Longeque Admirabilia Spectacula Pandens... (Culture et Civilisation)

Gallego, S. G., Cantalupo, S., Lilly, S., et al. 2018, Monthly Notices of the Royal Astronomical Society, 475, 3854

Garn, T., & Best, P. N. 2010, Mon Not R Astron Soc, 409, 421

Gauthier, J.-R. 2013, Mon Not R Astron Soc, 432, 1444

Geach, J. E., Chapin, E. L., Coppin, K. E. K., et al. 2013, Monthly Notices of the Royal Astronomical Society, 432, 53

Gehrels, N. 1986, The Astrophysical Journal, 303, 336

George, R. D., Ivison, R. J., Smail, I., et al. 2014, Monthly Notices of the Royal Astronomical Society, 442, 1877

Gnedin, N. Y., & Kravtsov, A. V. 2011, The Astrophysical Journal, 728, 88

Greve, T. R., Leonidaki, I., Xilouris, E. M., et al. 2014, The Astrophysical Journal, 794, 142

Guimarães, R., Petitjean, P., de Carvalho, R. R., et al. 2009, Astronomy and Astrophysics, 508, 133

Haehnelt, M. G., Steinmetz, M., & Rauch, M. 1998, The Astrophysical Journal, 495, 647

Hatsukade, B., Ohta, K., Seko, A., Yabe, K., & Akiyama, M. 2013, ApJ, 769, L27

Hatsukade, B., Kohno, K., Aretxaga, I., et al. 2011, Monthly Notices of the Royal Astronomical Society, 411, 102

Hatsukade, B., Kohno, K., Yamaguchi, Y., et al. 2018, Publications of the Astronomical Society of Japan, 70

Hayatsu, N. H., Ivison, R. J., Andreani, P., et al. 2019, arXiv:1907.05742 [astro-ph]

Heckman, T. M., Alexandroff, R. M., Borthakur, S., Overzier, R., & Leitherer, C. 2015, The Astrophysical Journal, 809, 147

Heisler, J., Tremaine, S., & Bahcall, J. N. 1985, The Astrophysical Journal, 298, 8

Herschel, W. 1786, Philosophical Transactions of the Royal Society of London Series I, 76, 457

Herschel William. 1785, Philosophical Transactions of the Royal Society of London, 75, 213

Hill, R., Chapman, S. C., Scott, D., et al. 2018, Monthly Notices of the Royal Astronomical Society, 477, 2042

Ho, I.-T., Kudritzki, R.-P., Kewley, L. J., et al. 2015, Mon Not R Astron Soc, 448, 2030

Ho, P. T. P., Moran, J. M., & Lo, K. Y. 2004, The Astrophysical Journal, 616, L1

Ho, S. H., Martin, C. L., Kacprzak, G. G., & Churchill, C. W. 2017, The Astrophysical Journal, 835, 267

Hobbs, A., Read, J., & Nicola, A. 2015, Monthly Notices of the Royal Astronomical Society, 452, 3593

Hodge, J. A., Karim, A., Smail, I., et al. 2013, The Astrophysical Journal, 768, 91

Holland, W. S., Robson, E. I., Gear, W. K., et al. 1999, Monthly Notices of the Royal Astronomical Society, 303, 659

Hubble, E. P. 1929, The Astrophysical Journal, 69

Hughes, D. H., Serjeant, S., Dunlop, J., et al. 1998, Nature, 394, 241

Ilbert, O., Arnouts, S., McCracken, H. J., et al. 2006, Astronomy and Astrophysics, 457, 841

Indriolo, N., Bergin, E. A., Falgarone, E., et al. 2018, The Astrophysical Journal, 865, 127

Ivison, R. J., Papadopoulos, P. P., Smail, I., et al. 2011, Monthly Notices of the Royal Astronomical Society, 412, 1913

Ivison, R. J., Smail, I., Le Borgne, J.-F., et al. 1998, Monthly Notices of the Royal Astronomical Society, 298, 583

Ivison, R. J., Greve, T. R., Dunlop, J. S., et al. 2007, Monthly Notices of the Royal Astronomical Society, 380, 199

Jannuzi, B. T., Bahcall, J. N., Bergeron, J., et al. 1998, The Astrophysical Journal Supplement Series, 118, 1

Jorgenson, R. A., & Wolfe, A. M. 2014, The Astrophysical Journal, 785, 16

Junkkarinen, V. T., Cohen, R. D., Beaver, E. A., et al. 2004, ApJ, 614, 658

Kacprzak, G. G., Murphy, M. T., & Churchill, C. W. 2010, Monthly Notices of the Royal Astronomical Society, 406, 445

Kanekar, N. 2014, The Astrophysical Journal, 797, L20

Kanekar, N., Athreya, R. M., & Chengalur, J. N. 2002, Astronomy and Astrophysics, 382, 838

Kanekar, N., Gupta, A., Carilli, C. L., Stocke, J. T., & Willett, K. W. 2014, ApJ, 782, 56

Kanekar, N., Carilli, C. L., Langston, G. I., et al. 2005, Phys. Rev. Lett., 95, 261301

Kanekar, N., Prochaska, J. X., Christensen, L., et al. 2018, ApJL, 856, L23

Kant, I. 1755, Zeitz

Karim, A., Swinbank, A. M., Hodge, J. A., et al. 2013, Monthly Notices of the Royal Astronomical Society, 432, 2

Katsianis, A., Tescari, E., Blanc, G., & Sargent, M. 2017, Monthly Notices of the Royal Astronomical Society, 464, 4977

Kennicutt, Jr., R. C. 1998, The Astrophysical Journal, 498, 541

Kereš, D., Katz, N., Fardal, M., Davé, R., & Weinberg, D. H. 2009, Mon Not R Astron Soc, 395, 160

Kereš, D., Katz, N., Weinberg, D. H., & Davé, R. 2005, Monthly Notices of the Royal Astronomical Society, 363, 2

Keres, D., Yun, M. S., & Young, J. S. 2003, The Astrophysical Journal, 582, 659

Klaassen, P., Mroczkowski, T., Bryan, S., et al. 2019, arXiv:1907.04756 [astro-ph]

Klitsch, A., Péroux, C., Zwaan, M. A., et al. 2018, Monthly Notices of the Royal Astronomical Society, 475, 492

Klitsch, A., Zwaan, M. A., Péroux, C., et al. 2019, Mon Not R Astron Soc Lett, 482, L65

Kobulnicky, H. A., & Kewley, L. J. 2004, ApJ, 617, 240

Krogager, J.-K., Møller, P., Fynbo, J. P. U., & Noterdaeme, P. 2017, Mon Not R Astron Soc, 469, 2959

Krogager, J.-K., Noterdaeme, P., O'Meara, J. M., et al. 2018, arXiv:1809.01053 [astro-ph]

Krumholz, M. R. 2013, Monthly Notices of the Royal Astronomical Society, 436, 2747

Lacey, C. G., Baugh, C. M., Frenk, C. S., et al. 2016, Monthly Notices of the Royal Astronomical Society, 462, 3854

Lagos, C. d. P., Crain, R. A., Schaye, J., et al. 2015, Monthly Notices of the Royal Astronomical Society, 452, 3815

Lagos, C. d. P., Robotham, A. S. G., Trayford, J. W., et al. 2019, arXiv:1908.03423 [astro-ph]

Lanyi, G. E., Boboltz, D. A., Charlot, P., et al. 2010, AJ, 139, 1695

Lanzetta, K. M., Wolfe, A. M., & Turnshek, D. A. 1995, The Astrophysical Journal, 440, 435

Lanzetta, K. M., Wolfe, A. M., Turnshek, D. A., et al. 1991, The Astrophysical Journal Supplement Series, 77, 1

Laurent, G. T., Aguirre, J. E., Glenn, J., et al. 2005, The Astrophysical Journal, 623, 742

Leavitt, H. S. 1908, Annals of Harvard College Observatory, 60, 87

Lehner, N., Howk, J. C., Tripp, T. M., et al. 2013, The Astrophysical Journal, 770, 138

Lilly, S. J., Carollo, C. M., Pipino, A., Renzini, A., & Peng, Y. 2013, The Astrophysical Journal, 772, 119

Lilly, S. J., Eales, S. A., Gear, W. K. P., et al. 1999, The Astrophysical Journal, 518, 641

Loukitcheva, M. 2019, Advances in Space Research, 63, 1396

Ly, C., Malkan, M. A., Kashikawa, N., et al. 2007, ApJ, 657, 738

Maccagni, F. M., Morganti, R., Oosterloo, T. A., Oonk, J. B. R., & Emonts, B. H. C. 2018, Astronomy and Astrophysics, 614, A42

Madau, P., & Dickinson, M. 2014, Annual Review of Astronomy and Astrophysics, 52, 415

Magnelli, B., Lutz, D., Santini, P., et al. 2012, Astronomy and Astrophysics, 539, A155

Mahony, E. K., Sadler, E. M., Croom, S. M., et al. 2011, Monthly Notices of the Royal Astronomical Society, 417, 2651

Maiolino, R., Nagao, T., Grazian, A., et al. 2008, A&A, 488, 463

Mangum, J. G., & Shirley, Y. L. 2015, Publications of the Astronomical Society of the Pacific, 127, 266

Marinacci, F., Vogelsberger, M., Pakmor, R., et al. 2018, Monthly Notices of the Royal Astronomical Society

Martin, C. L. 2005, The Astrophysical Journal, 621, 227

Martin, C. L., Shapley, A. E., Coil, A. L., et al. 2012, ApJ, 760, 127

Mathes, N. L., Churchill, C. W., Kacprzak, G. G., et al. 2014, The Astrophysical Journal, 792, 128

McKee, C. F., & Ostriker, E. C. 2007, Annual Review of Astronomy and Astrophysics, 45, 565

McKinnon, M., & Selina, R. 2019, American Astronomical Society Meeting Abstracts #233, 233, 361.02

McMullin, J. P., Waters, B., Schiebel, D., Young, W., & Golap, K. 2007, Astronomical Data Analysis Software and Systems XVI, 376, 127

Ménard, B., & Péroux, C. 2003, Astronomy and Astrophysics, 410, 33

Messier, C. 1781, Catalogue Des Nébuleuses et Des Amas d'Étoiles (Catalog of Nebulae and Star Clusters), Tech. rep.

Meyer, E. T., Petropoulou, M., Georganopoulos, M., et al. 2018, The Astrophysical Journal, 860, 9

Mitra, S., Davé, R., & Finlator, K. 2015, Mon Not R Astron Soc, 452, 1184

Moffett, A. J., Lange, R., Driver, S. P., et al. 2016, Monthly Notices of the Royal Astronomical Society, 462, 4336

Møller, P., Fynbo, J. P. U., & Fall, S. M. 2004, Astronomy and Astrophysics, 422, L33

Møller, P., Christensen, L., Zwaan, M. A., et al. 2018, Mon Not R Astron Soc, 474, 4039

Momose, R., Ouchi, M., Nakajima, K., et al. 2014, Monthly Notices of the Royal Astronomical Society, 442, 110

Morris, S. L., & van den Bergh, S. 1994, The Astrophysical Journal, 427, 696

Muller, S., Beelen, A., Black, J. H., et al. 2013, A&A, 551, A109

Muratov, A. L., Kereš, D., Faucher-Giguère, C.-A., et al. 2015, Monthly Notices of the Royal Astronomical Society, 454, 2691

—. 2017, Monthly Notices of the Royal Astronomical Society, 468, 4170

Muzahid, S., Kacprzak, G. G., Churchill, C. W., et al. 2015a, The Astrophysical Journal, 811, 132

Muzahid, S., Srianand, R., & Charlton, J. 2015b, Mon Not R Astron Soc, 448, 2840

Naiman, J. P., Pillepich, A., Springel, V., et al. 2018, Monthly Notices of the Royal Astronomical Society, 477, 1206

Neeleman, M., Kanekar, N., Prochaska, J. X., et al. 2017, Science, 355, 1285

Neeleman, M., Kanekar, N., Prochaska, J. X., Rafelski, M. A., & Carilli, C. L. 2018, arXiv:1812.06113 [astro-ph]

—. 2019, The Astrophysical Journal, 870, L19

Neeleman, M., Prochaska, J. X., Zwaan, M. A., et al. 2016, ApJL, 820, L39

Nelson, D., Pillepich, A., Springel, V., et al. 2018a, Monthly Notices of the Royal Astronomical Society, 475, 624

Nelson, D., Springel, V., Pillepich, A., et al. 2018b, arXiv:1812.05609 [astro-ph]

—. 2019, Computational Astrophysics and Cosmology, 6, 2

Newman, S. F., Genzel, R., Förster-Schreiber, N. M., et al. 2012, The Astrophysical Journal, 761, 43

Noterdaeme, P., Ledoux, C., Petitjean, P., & Srianand, R. 2008, A&A, 481, 327

Noterdaeme, P., Ledoux, C., Srianand, R., Petitjean, P., & Lopez, S. 2009, A&A, 503, 765

Noterdaeme, P., Ledoux, C., Zou, S., et al. 2018, Astronomy and Astrophysics, 612, A58

Noterdaeme, P., Petitjean, P., Pâris, I., et al. 2014, Astronomy and Astrophysics, 566, A24

Noterdaeme, P., Petitjean, P., Carithers, W. C., et al. 2012, Astronomy and Astrophysics, 547, L1

Obreschkow, D., Croton, D., De Lucia, G., Khochfar, S., & Rawlings, S. 2009, The Astrophysical Journal, 698, 1467

Oliver, S. J., Wang, L., Smith, A. J., et al. 2010, Astronomy and Astrophysics, 518, L21

Oliver, S. J., Bock, J., Altieri, B., et al. 2012, Monthly Notices of the Royal Astronomical Society, 424, 1614

O'Meara, J. M., Prochaska, J. X., Chen, H.-W., & Madau, P. 2011, The Astrophysical Journal Supplement Series, 195, 16

Ono, Y., Ouchi, M., Kurono, Y., & Momose, R. 2014, ApJ, 795, 5

Oppenheimer, B. D., & Davé, R. 2008, Monthly Notices of the Royal Astronomical Society, 387, 577

Oppenheimer, B. D., Davé, R., Kereš, D., et al. 2010, Monthly Notices of the Royal Astronomical Society, 406, 2325

Oteo, I., Zwaan, M., Ivison, R., Smail, I., & Biggs, A. 2016a, The Messenger, 164, 41

Oteo, I., Zwaan, M. A., Ivison, R. J., Smail, I., & Biggs, A. D. 2016b, The Astrophysical Journal, 822, 36

—. 2017, The Astrophysical Journal, 837, 182

Pagel, B. E. J., Edmunds, M. G., Blackwell, D. E., Chun, M. S., & Smith, G. 1979, Mon Not R Astron Soc, 189, 95

Pagel, B. E. J., & Patchett, B. E. 1975, Monthly Notices of the Royal Astronomical Society, 172, 13

Papadopoulos, P. P., van der Werf, P., Xilouris, E., Isaak, K. G., & Gao, Y. 2012a, The Astrophysical Journal, 751, 10

Papadopoulos, P. P., van der Werf, P. P., Xilouris, E. M., et al. 2012b, Monthly Notices of the Royal Astronomical Society, 426, 2601

Pavesi, R., Sharon, C. E., Riechers, D. A., et al. 2018

Peeples, M. S., Werk, J. K., Tumlinson, J., et al. 2014, ApJ, 786, 54

Peng, C. Y., Ho, L. C., Impey, C. D., & Rix, H.-W. 2002, AJ, 124, 266

Peng, Y.-j., Lilly, S. J., Kovač, K., et al. 2010, The Astrophysical Journal, 721, 193

Pereira-Santaella, M., Colina, L., García-Burillo, S., et al. 2016, Astronomy and Astrophysics, 594, A81

—. 2018, A&A, 616, A171

Péroux, C., Bouché, N., Kulkarni, V. P., York, D. G., & Vladilo, G. 2011, Mon Not R Astron Soc, 410, 2237

Péroux, C., Dessauges-Zavadsky, M., D'Odorico, S., Kim, T.-S., & McMahon, R. G. 2003a, Monthly Notices of the Royal Astronomical Society, 345, 480

Péroux, C., Dessauges-Zavadsky, M., D'Odorico, S., Sun Kim, T., & McMahon, R. G. 2005, Monthly Notices of the Royal Astronomical Society, 363, 479

Péroux, C., Dessauges-Zavadsky, M., Kim, T., McMahon, R. G., & D'Odorico, S. 2002, Astrophysics and Space Science, 281, 543

Péroux, C., Kulkarni, V. P., & York, D. G. 2014, Mon Not R Astron Soc, 437, 3144

Péroux, C., McMahon, R. G., Storrie-Lombardi, L. J., & Irwin, M. J. 2003b, Monthly Notices of the Royal Astronomical Society, 346, 1103

Péroux, C., Quiret, S., Rahmani, H., et al. 2016, Monthly Notices of the Royal Astronomical Society, 457, 903

Péroux, C., Rahmani, H., Quiret, S., et al. 2017, Mon Not R Astron Soc, 464, 2053

Peroux, C., Zwaan, M., Klitsch, A., et al. 2019, arXiv:1901.05217 [astro-ph]

Pillepich, A., Nelson, D., Hernquist, L., et al. 2018, Monthly Notices of the Royal Astronomical Society, 475, 648

Plutarch. 2006, The Complete Works Volume 3: Essays and Miscellanies (Echo Library)

Poggianti, B. M., & Wu, H. 2000, ApJ, 529, 157

Polletta, M., Tajer, M., Maraschi, L., et al. 2007, ApJ, 663, 81

Pontzen, A., Governato, F., Pettini, M., et al. 2008, Monthly Notices of the Royal Astronomical Society, 390, 1349

Popping, A., Jurek, R., Westmeier, T., et al. 2012, Publications of the Astronomical Society of Australia, 29, 318

Popping, G., Somerville, R. S., & Trager, S. C. 2014, Monthly Notices of the Royal Astronomical Society, 442, 2398

Popping, G., Pillepich, A., Somerville, R. S., et al. 2019, arXiv:1903.09158 [astro-ph]

Prochaska, J. X., Hennawi, J. F., & Herbert-Fort, S. 2008, The Astrophysical Journal, 675, 1002

Prochaska, J. X., Herbert-Fort, S., & Wolfe, A. M. 2005, The Astrophysical Journal, 635, 123

Prochaska, J. X., O'Meara, J. M., & Worseck, G. 2010, The Astrophysical Journal, 718, 392

Prochaska, J. X., Werk, J. K., Worseck, G., et al. 2017, ApJ, 837, 169

Putman, M. E. 2017, in Gas Accretion onto Galaxies, Vol. 430, eprint: arXiv:1612.00461, 1

Putman, M. E., Peek, J. E. G., & Joung, M. R. 2012, Annual Review of Astronomy and Astrophysics, 50, 491

Rahmani, H., Péroux, C., Augustin, R., et al. 2018, Mon Not R Astron Soc, 474, 254

Rao, S. M., Belfort-Mihalyi, M., Turnshek, D. A., et al. 2011, Mon Not R Astron Soc, 416, 1215

Rao, S. M., Nestor, D. B., Turnshek, D. A., et al. 2003, The Astrophysical Journal, 595, 94

Rao, S. M., Turnshek, D. A., & Nestor, D. B. 2006, ApJ, 636, 610

Remijan, A. J., Markwick-Kemper, A., & ALMA Working Group on Spectral Line Frequencies. 2007, in Bulletin of the American Astronomical Society, Vol. 211, 132.11

Rhee, J., Lah, P., Briggs, F. H., et al. 2018, Monthly Notices of the Royal Astronomical Society, 473, 1879

Richard, J., Bacon, R., Blaizot, J., et al. 2019, arXiv e-prints, arXiv:1906.01657

Richings, A. J., & Faucher-Giguere, C.-A. 2018, Monthly Notices of the Royal Astronomical Society, 474, 3673

Riechers, D. A., Pavesi, R., Sharon, C. E., et al. 2018, arXiv:1808.04371 [astro-ph]

Roberts, M. S., Brown, R. L., Brundage, W. D., et al. 1976, The Astronomical Journal, 81, 293

Romano-Díaz, E., Shlosman, I., Choi, J.-H., & Sadoun, R. 2014, The Astrophysical Journal, 790, L32

Rose, T., Edge, A. C., Combes, F., et al. 2019, arXiv:1902.01863 [astro-ph]

Rubin, K. H. R., Prochaska, J. X., Koo, D. C., & Phillips, A. C. 2012, The Astrophysical Journal, 747, L26

Rudie, G. C., Newman, A. B., & Murphy, M. T. 2017, ApJ, 843, 98

Rudie, G. C., Steidel, C. C., Pettini, M., et al. 2019, arXiv e-prints, arXiv:1903.00004

Rupke, D. S., Veilleux, S., & Sanders, D. B. 2005, ApJS, 160, 115

Sadoun, R., Shlosman, I., Choi, J.-H., & Romano-Díaz, E. 2016, The Astrophysical Journal, 829, 71

Saintonge, A., Catinella, B., Tacconi, L. J., et al. 2017, ApJS, 233, 22

Sánchez Almeida, J., Elmegreen, B. G., Muñoz-Tuñón, C., & Elmegreen, D. M. 2014, Astronomy and Astrophysics Review, 22, 71

Sandage, A. 1986, The Astrophysical Journal, 307, 1

Sargent, W. L. W., Boksenberg, A., & Steidel, C. C. 1988, The Astrophysical Journal Supplement Series, 68, 539

Schaye, J., Crain, R. A., Bower, R. G., et al. 2015, Monthly Notices of the Royal Astronomical Society, 446, 521

Schechter, P. 1976, The Astrophysical Journal, 203, 297

Schmidt, M. 1963, The Astrophysical Journal, 137, 758

Schroetter, I., Bouché, N., Péroux, C., et al. 2015, ApJ, 804, 83

Schroetter, I., Bouché, N., Wendt, M., et al. 2016, ApJ, 833, 39

Schruba, A., Leroy, A. K., Walter, F., et al. 2012, The Astronomical Journal, 143, 138

Scott, K. S., Yun, M. S., Wilson, G. W., et al. 2010, Monthly Notices of the Royal Astronomical Society, 405, 2260

Scott, K. S., Wilson, G. W., Aretxaga, I., et al. 2012, Monthly Notices of the Royal Astronomical Society, 423, 575

Sembach, K. R., Howk, J. C., Savage, B. D., Shull, J. M., & Oegerle, W. R. 2001, The Astrophysical Journal, 561, 573

Serra, P., Oosterloo, T., Morganti, R., et al. 2012, Mon Not R Astron Soc, 422, 1835

Serra, P., Westmeier, T., Giese, N., et al. 2015, Mon Not R Astron Soc, 448, 1922

Shapley, H., & Curtis, H. D. 1921, Bulletin of the National Research Council, 2, 171

Shen, S., Madau, P., Aguirre, A., et al. 2012, The Astrophysical Journal, 760, 50

Shen, S., Madau, P., Conroy, C., Governato, F., & Mayer, L. 2014, ApJ, 792, 99

Shull, J. M., Smith, B. D., & Danforth, C. W. 2012, The Astrophysical Journal, 759, 23

Simpson, J. M., Swinbank, A. M., Smail, I., et al. 2014, The Astrophysical Journal, 788, 125

Simpson, J. M., Smail, I., Swinbank, A. M., et al. 2015, The Astrophysical Journal, 807, 128

Smail, I., Ivison, R. J., & Blain, A. W. 1997, The Astrophysical Journal, 490, L5

Smail, I., Ivison, R. J., Blain, A. W., & Kneib, J.-P. 2002, Monthly Notices of the Royal Astronomical Society, 331, 495

Smolčić, V., Aravena, M., Navarrete, F., et al. 2012, Astronomy and Astrophysics, 548, A4

Sobral, D., Best, P. N., Matsuda, Y., et al. 2012, Mon Not R Astron Soc, 420, 1926

Solomon, P. M., Downes, D., & Radford, S. J. E. 1992, The Astrophysical Journal, 387, L55

Sommer-Larsen, J. 1991, Monthly Notices of the Royal Astronomical Society, 249, 368

Soto, K. T., Lilly, S. J., Bacon, R., Richard, J., & Conseil, S. 2016, Mon Not R Astron Soc, 458, 3210

Springel, V., Pakmor, R., Pillepich, A., et al. 2018, Monthly Notices of the Royal Astronomical Society, 475, 676

Stach, S. M., Smail, I., Swinbank, A. M., et al. 2018, The Astrophysical Journal, 860, 161

Stach, S. M., Dudzevičiūtė, U., Smail, I., et al. 2019, arXiv:1903.02602 [astro-ph]

Steidel, C. C., Bogosavljević, M., Shapley, A. E., et al. 2011, The Astrophysical Journal, 736, 160

Steidel, C. C., Erb, D. K., Shapley, A. E., et al. 2010, The Astrophysical Journal, 717, 289

Stevens, A. R. H., Diemer, B., Lagos, C. d. P., et al. 2019, Monthly Notices of the Royal Astronomical Society, 483, 5334

Stewart, K. R., Kaufmann, T., Bullock, J. S., et al. 2011, ApJ, 738, 39

Stocke, J. T., Keeney, B. A., Danforth, C. W., et al. 2013, The Astrophysical Journal, 763, 148

Storey, P. J., & Zeippen, C. J. 2000, Mon Not R Astron Soc, 312, 813

Straka, L. A., Johnson, S., York, D. G., et al. 2016, Monthly Notices of the Royal Astronomical Society, 458, 3760

Swinbank, A. M., Simpson, J. M., Smail, I., et al. 2014, Monthly Notices of the Royal Astronomical Society, 438, 1267

Tacconi, L. J., Genzel, R., Neri, R., et al. 2010, Nature, 463, 781

Talbot, R. J., & Arnett, W. D. 1971, The Astrophysical Journal, 170, 409

Tappe, A., & Black, J. H. 2004, Astronomy and Astrophysics, 423, 943

Tollet, É., Cattaneo, A., Macciò, A. V., Dutton, A. A., & Kang, X. 2019, Monthly Notices of the Royal Astronomical Society, 485, 2511

Tremblay, G. R., Combes, F., Oonk, J. B. R., et al. 2018a, ApJ, 865, 13

—. 2018b, ApJ, 865, 13

Tremonti, C. A., Moustakas, J., & Diamond-Stanic, A. M. 2007, ApJ, 663, L77

Tremonti, C. A., Heckman, T. M., Kauffmann, G., et al. 2004, The Astrophysical Journal, 613, 898

Tumlinson, J., Peeples, M. S., & Werk, J. K. 2017, Annual Review of Astronomy and Astrophysics, 55, 389

Tumlinson, J., Thom, C., Werk, J. K., et al. 2011a, Science, 334, 948

—. 2011b, Science, 334, 948

—. 2013, ApJ, 777, 59

Turner, M. L., Schaye, J., Steidel, C. C., Rudie, G. C., & Strom, A. L. 2014, Monthly Notices of the Royal Astronomical Society, 445, 794

Turnshek, D. A., Monier, E. M., Rao, S. M., et al. 2015, Monthly Notices of the Royal Astronomical Society, 449, 1536

Übler, H., Naab, T., Oser, L., et al. 2014, Monthly Notices of the Royal Astronomical Society, 443, 2092

Umehata, H., Tamura, Y., Kohno, K., et al. 2014, Monthly Notices of the Royal Astronomical Society, 440, 3462

—. 2017, ApJ, 835, 98

Valiante, E., Smith, M. W. L., Eales, S., et al. 2016, Monthly Notices of the Royal Astronomical Society, 462, 3146

van de Voort, F. 2017, Gas Accretion onto Galaxies, 430, 301

van de Voort, F., & Schaye, J. 2012, Mon Not R Astron Soc, 423, 2991

van de Voort, F., Schaye, J., Booth, C. M., Haas, M. R., & Dalla Vecchia, C. 2011, Monthly Notices of the Royal Astronomical Society, 414, 2458

van den Bergh, S. 1962, The Astronomical Journal, 67, 486

Veilleux, S., Cecil, G., & Bland-Hawthorn, J. 2005, Annu. Rev. Astron. Astrophys., 43, 769

Verdes-Montenegro, L., Yun, M. S., Williams, B. A., et al. 2001, Astronomy & Astrophysics, 377, 812

Vestergaard, M. 2003, The Astrophysical Journal, 599, 116

Villanueva, V., Ibar, E., Hughes, T. M., et al. 2017, Mon Not R Astron Soc, 470, 3775

Vogt, S. S., Allen, S. L., Bigelow, B. C., et al. 1994, in Instrumentation in Astronomy VIII, Vol. 2198 (International Society for Optics and Photonics), 362–376

Walter, F., Decarli, R., Sargent, M., et al. 2014, The Astrophysical Journal, 782, 79

Walter, F., Decarli, R., Aravena, M., et al. 2016, The Astrophysical Journal, 833, 67

Wang, L., Pearson, W. J., Cowley, W., et al. 2019, A&A, 624, A98

Wang, W.-H., Cowie, L. L., Barger, A. J., & Williams, J. P. 2011, The Astrophysical Journal, 726, L18

Wang, W.-H., Lin, W.-C., Lim, C.-F., et al. 2017, The Astrophysical Journal, 850, 37

Wardlow, J. L., Smail, I., Coppin, K. E. K., et al. 2011, Monthly Notices of the Royal Astronomical Society, 415, 1479

Warren, S. J., Møller, P., Fall, S. M., & Jakobsen, P. 2001, Monthly Notices of the Royal Astronomical Society, 326, 759

Weiner, B. J., Coil, A. L., Prochaska, J. X., et al. 2009, ApJ, 692, 187

Weiß, A., Kovács, A., Coppin, K., et al. 2009, The Astrophysical Journal, 707, 1201

Weiß, A., De Breuck, C., Marrone, D. P., et al. 2013, The Astrophysical Journal, 767, 88

Werk, J. K., Prochaska, J. X., Tumlinson, J., et al. 2014, The Astrophysical Journal, 792, 8

Werk, J. K., Prochaska, J. X., Cantalupo, S., et al. 2016, The Astrophysical Journal, 833, 54

Whitaker, K. E., van Dokkum, P. G., Brammer, G., & Franx, M. 2012, The Astrophysical Journal, 754, L29

Whiting, M. T. 2012, Monthly Notices of the Royal Astronomical Society, 421, 3242

Whiting, M. T., Webster, R. L., & Francis, P. J. 2006, Mon Not R Astron Soc, 368, 341

Wiklind, T., & Combes, F. 1994, Astronomy and Astrophysics, 286, L9

—. 1995, Astronomy and Astrophysics, 299, 382

—. 1996a, Astronomy and Astrophysics, 315, 86

—. 1996b, Nature, 379, 139

Wiklind, T., Combes, F., & Kanekar, N. 2018, ApJ, 864, 73

Wills, B. J., Netzer, H., Uomoto, A. K., & Wills, D. 1980, The Astrophysical Journal, 237, 319

Wisotzki, L., Bacon, R., Blaizot, J., et al. 2016, Astronomy and Astrophysics, 587, A98

Wisotzki, L., Bacon, R., Brinchmann, J., et al. 2018, Nature, 562, 229

Wolfe, A. M., Gawiser, E., & Prochaska, J. X. 2005, Annual Review of Astronomy and Astrophysics, 43, 861

Wolfe, A. M., Turnshek, D. A., Smith, H. E., & Cohen, R. D. 1986, The Astrophysical Journal Supplement Series, 61, 249

Wootten, A. 2001, in Science with the Atacama Large Millimeter Array, Vol. 235

Wootten, A., & Thompson, A. R. 2009, IEEE Proceedings, 97, 1463

Worthey, G., Dorman, B., & Jones, L. A. 1996, The Astronomical Journal, 112, 948

Wright, A. H., Robotham, A. S. G., Driver, S. P., et al. 2017, Monthly Notices of the Royal Astronomical Society, 470, 283

Wright, T. 1750, An original theory or new hypothesis of the universe : founded upon the laws of nature

Yanny, B., & York, D. G. 1992, The Astrophysical Journal, 391, 569

Yanny, B., York, D. G., & Gallagher, J. S. 1989, The Astrophysical Journal, 338, 735

Yanny, B., York, D. G., & Williams, T. B. 1990, The Astrophysical Journal, 351, 377

Younger, J. D., Fazio, G. G., Huang, J.-S., et al. 2009, ApJ, 704, 803

Yun, M. S., Ho, P. T. P., & Lo, K. Y. 1994, Nature, 372, 530

Zafar, T., Péroux, C., Popping, A., et al. 2013, Astronomy & Astrophysics, 556, A141

Zahid, H. J., Dima, G. I., Kudritzki, R.-P., et al. 2014, ApJ, 791, 130

Zhang, Z.-Y., Papadopoulos, P. P., Ivison, R. J., et al. 2016, Royal Society Open Science, 3, 160025

Zheng, Y., Peek, J. E. G., Werk, J. K., & Putman, M. E. 2017, The Astrophysical Journal, 834, 179

Zheng, Y., Putman, M. E., Peek, J. E. G., & Joung, M. R. 2015, The Astrophysical Journal, 807, 103

Zhu, G., & Ménard, B. 2013, The Astrophysical Journal, 770, 130

Zwaan, M. A., & Prochaska, J. X. 2006, The Astrophysical Journal, 643, 675

Zwaan, M. A., Van Der Hulst, J. M., Briggs, F. H., Verheijen, M. A. W., & Ryan-Weber, E. V. 2005, Monthly Notices of the Royal Astronomical Society, 364, 1467

Appendix A

Appendix

A.1 ALMACAL

In the following we give an overview of the observed frequencies per calibrator field in ALMACAL. For each calibrator a blue box indicates if a frequency was observed. ALMA receiver bands are also marked for reference.

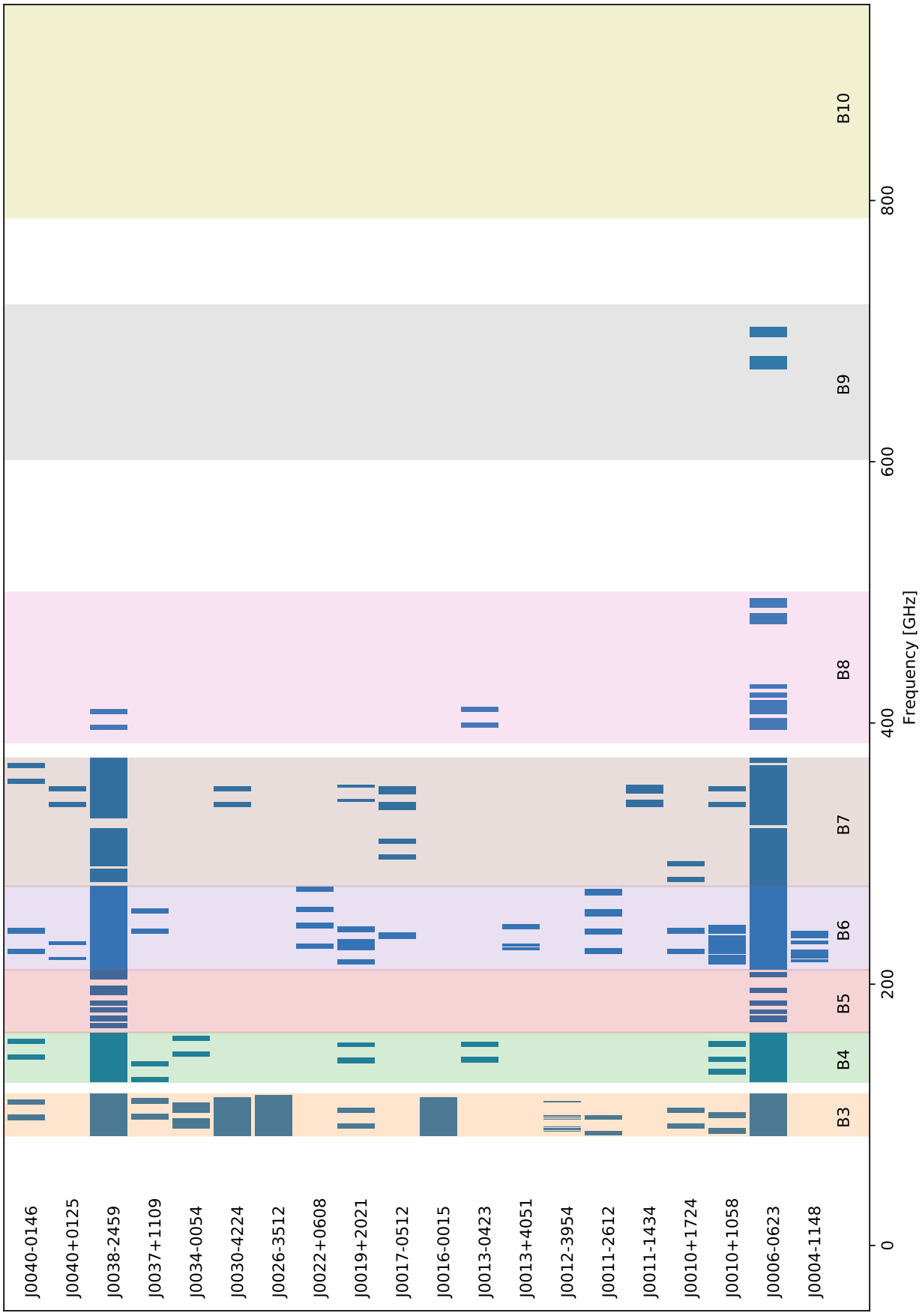
J0040-0146
J0040+0125
J0038-2459
J0037+1109
J0034-0054
J0030-4224
J0026-3512
J0022+0608
J0019+2021
J0017-0512
J0016-0015
J0013-0423
J0013+4051
J0012-3954
J0011-2612
J0011-1434
J0010+1724
J0010+1058
J0006-0623
J0004-1148
B3
B4
B5
B6
B7
B8
B9
B10
0
200
400
600
800
Frequency [GHz]

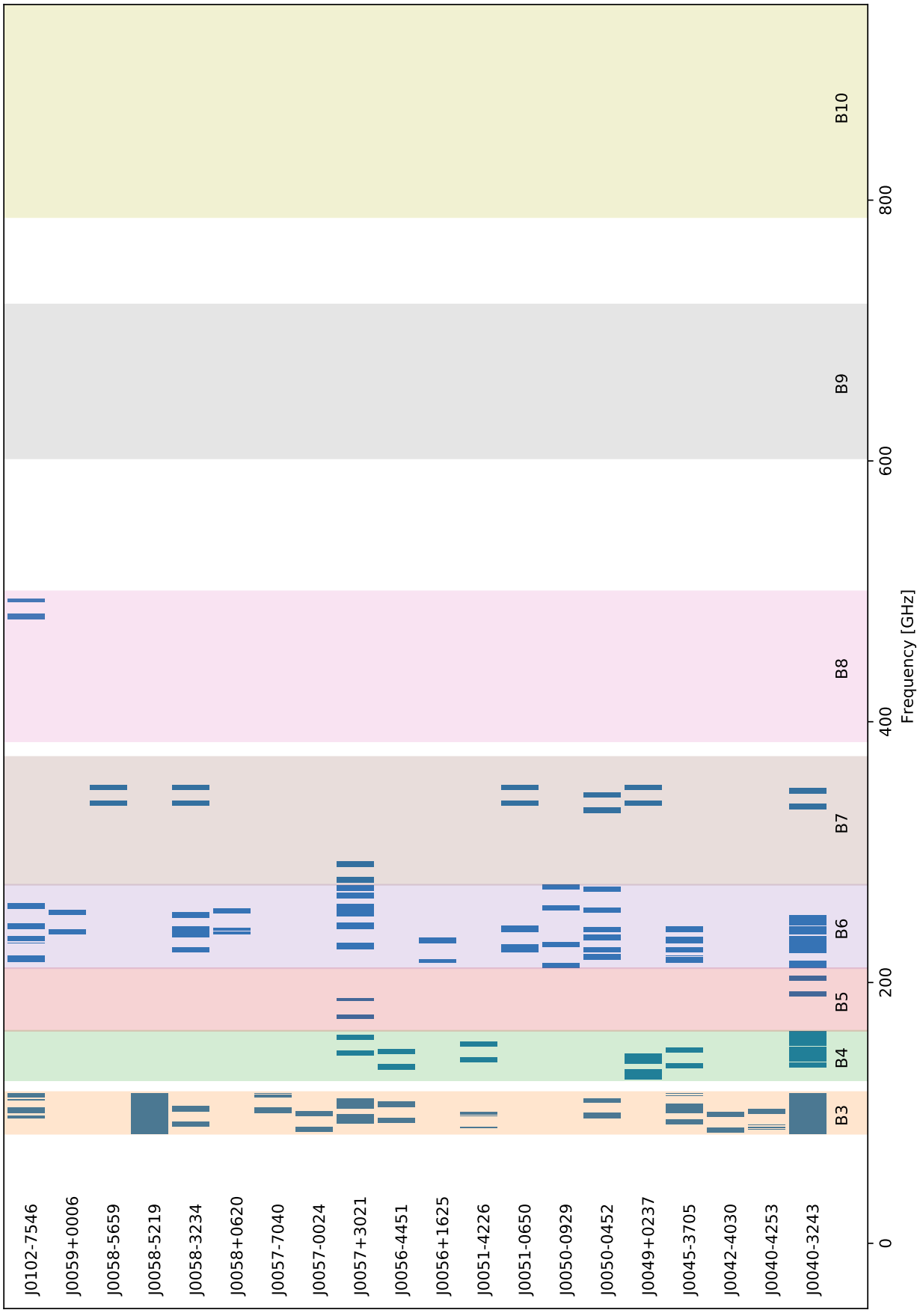
J0102-7546
J0059+0006
J0058-5659
J0058-5219
J0058-3234
J0058+0620
J0057-7040
J0057-0024
J0057+3021
J0056-4451
J0056+1625
J0051-4226
J0051-0650
J0050-0929
J0050-0452
J0049+0237
J0045-3705
J0042-4030
J0040-4253
J0040-3243
B3
B4
B5
B6
B7
B8
B9
B10
0
200
400
600
800
Frequency [GHz]

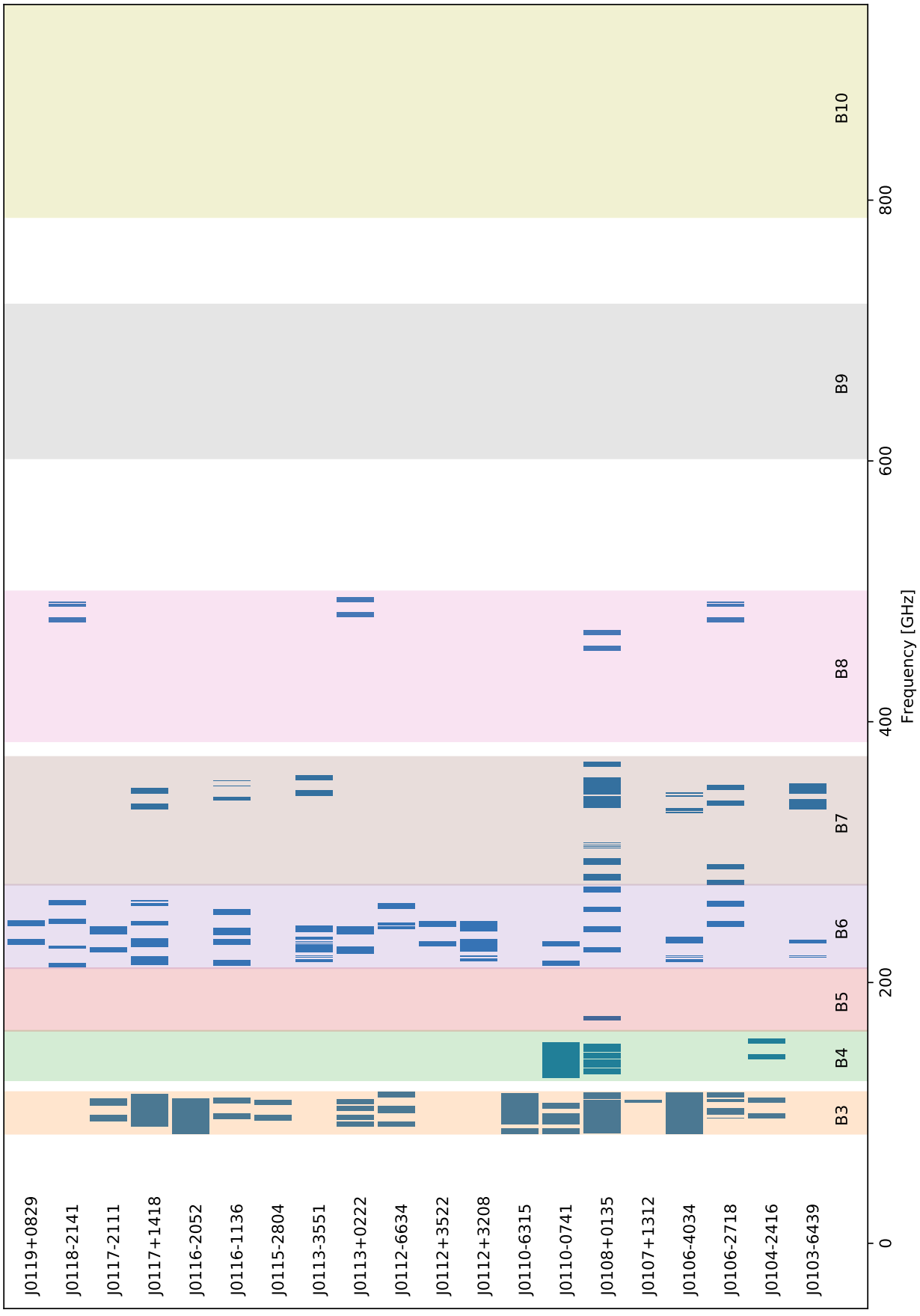
J0119+0829
J0118-2141
J0117-2111
J0117+1418
J0116-2052
J0116-1136
J0115-2804
J0113-3551
J0113+0222
J0112-6634
J0112+3522
J0112+3208
J0110-6315
J0110-0741
J0108+0135
J0107+1312
J0106-4034
J0106-2718
J0104-2416
J0103-6439
B3
B4
B5
B6
B7
B8
B9
B10
0
200
400
600
800
Frequency [GHz]

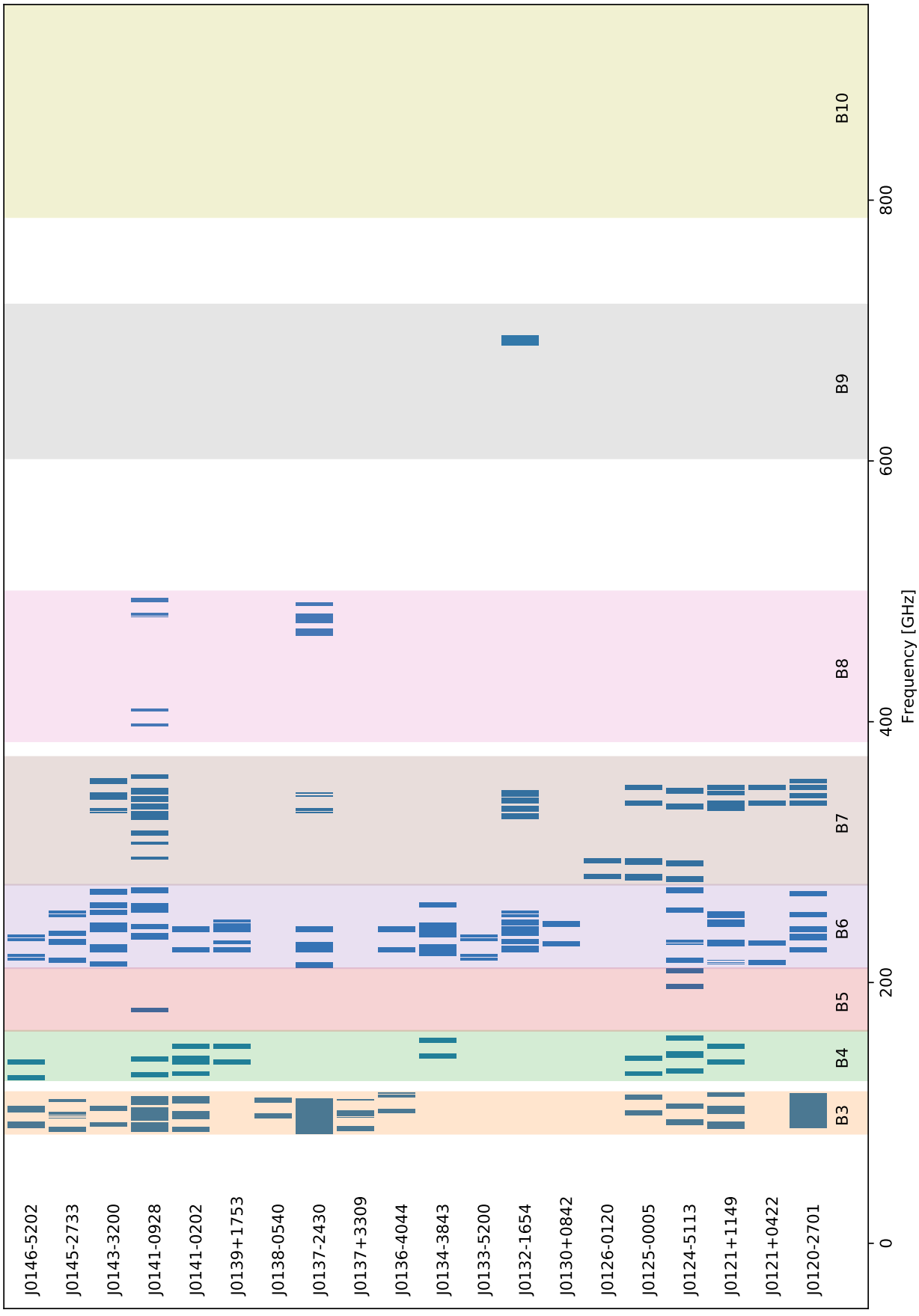
J0146-5202
J0145-2733
J0143-3200
J0141-0928
J0141-0202
J0139+1753
J0138-0540
J0137-2430
J0137+3309
J0136-4044
J0134-3843
J0133-5200
J0132-1654
J0130+0842
J0126-0120
J0125-0005
J0124-5113
J0121+1149
J0121+0422
J0120-2701
B3
B4
B5
B6
B7
B8
B9
B10
0
200
400
600
800
Frequency [GHz]

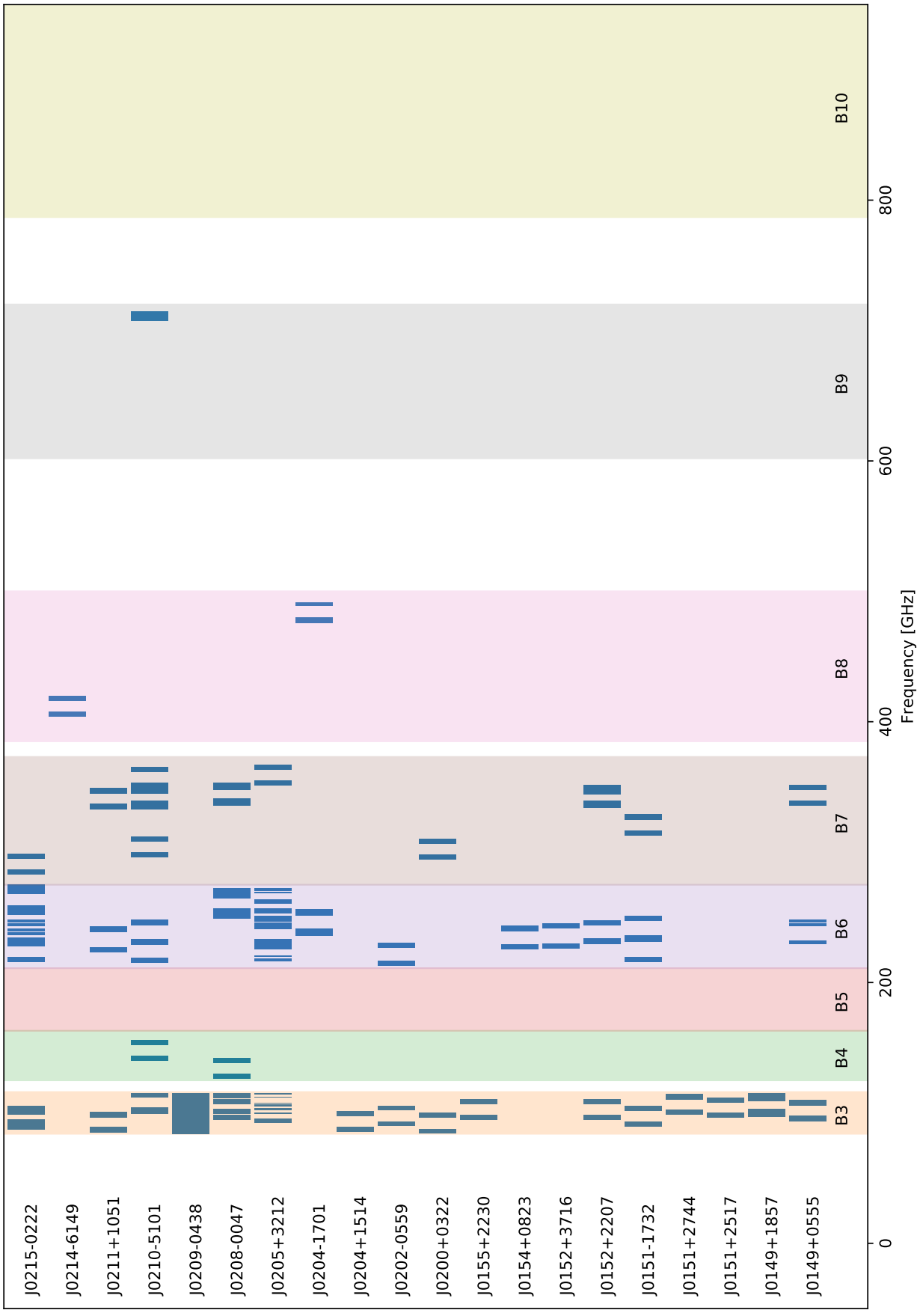
J0215-0222
J0214-6149
J0211+1051
J0210-5101
J0209-0438
J0208-0047
J0205+3212
J0204-1701
J0204+1514
J0202-0559
J0200+0322
J0155+2230
J0154+0823
J0152+3716
J0152+2207
J0151-1732
J0151+2744
J0151+2517
J0149+1857
J0149+0555
B3
B4
B5
B6
B7
B8
B9
B10
0
200
400
600
800
Frequency [GHz]

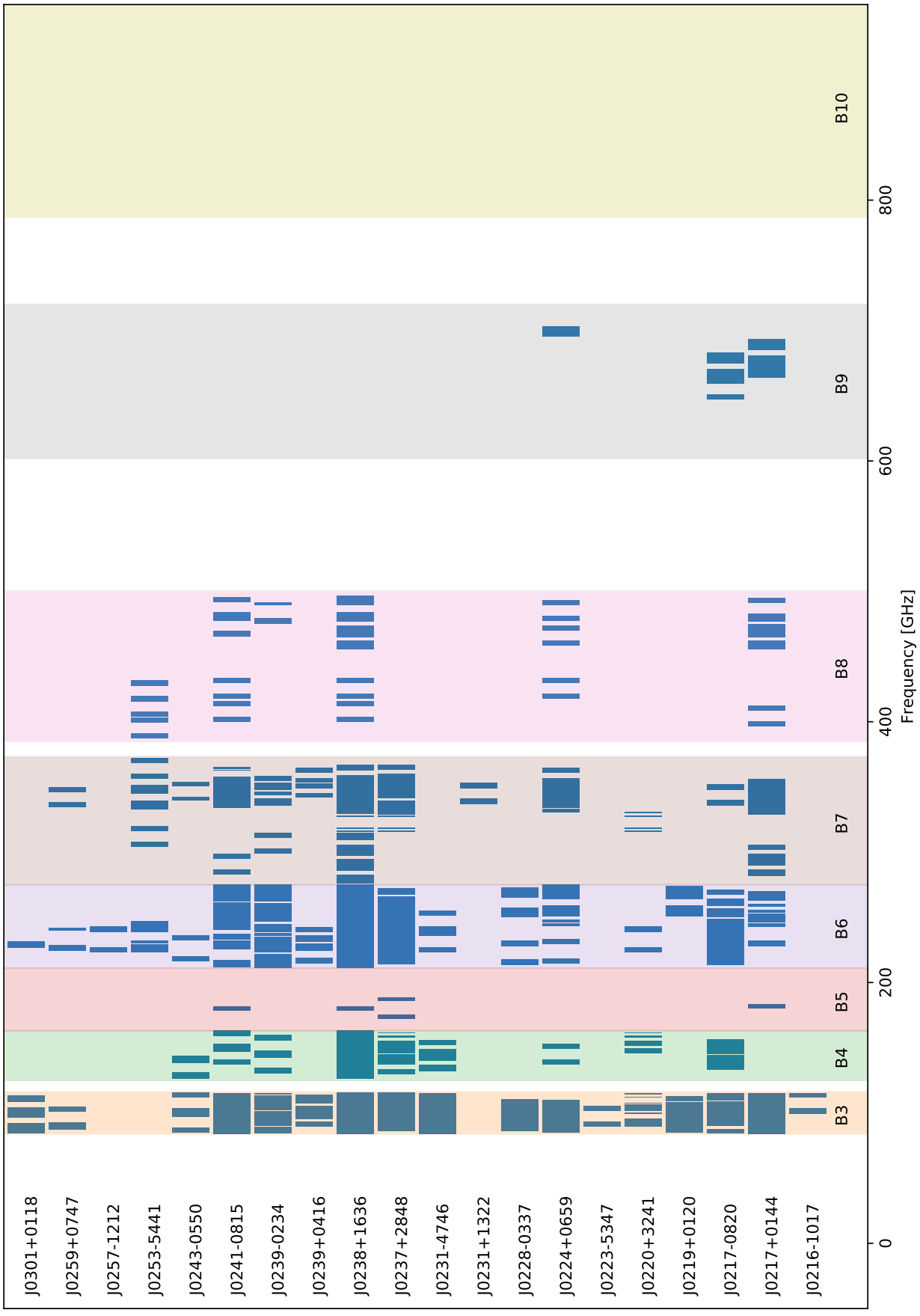
J0301+0118
J0259+0747
J0257-1212
J0253-5441
J0243-0550
J0241-0815
J0239-0234
J0239+0416
J0238+1636
J0237+2848
J0231-4746
J0231+1322
J0228-0337
J0224+0659
J0223-5347
J0220+3241
J0219+0120
J0217-0820
J0217+0144
J0216-1017
B3
B4
B5
B6
B7
B8
B9
B10
0
200
400
600
800
Frequency [GHz]

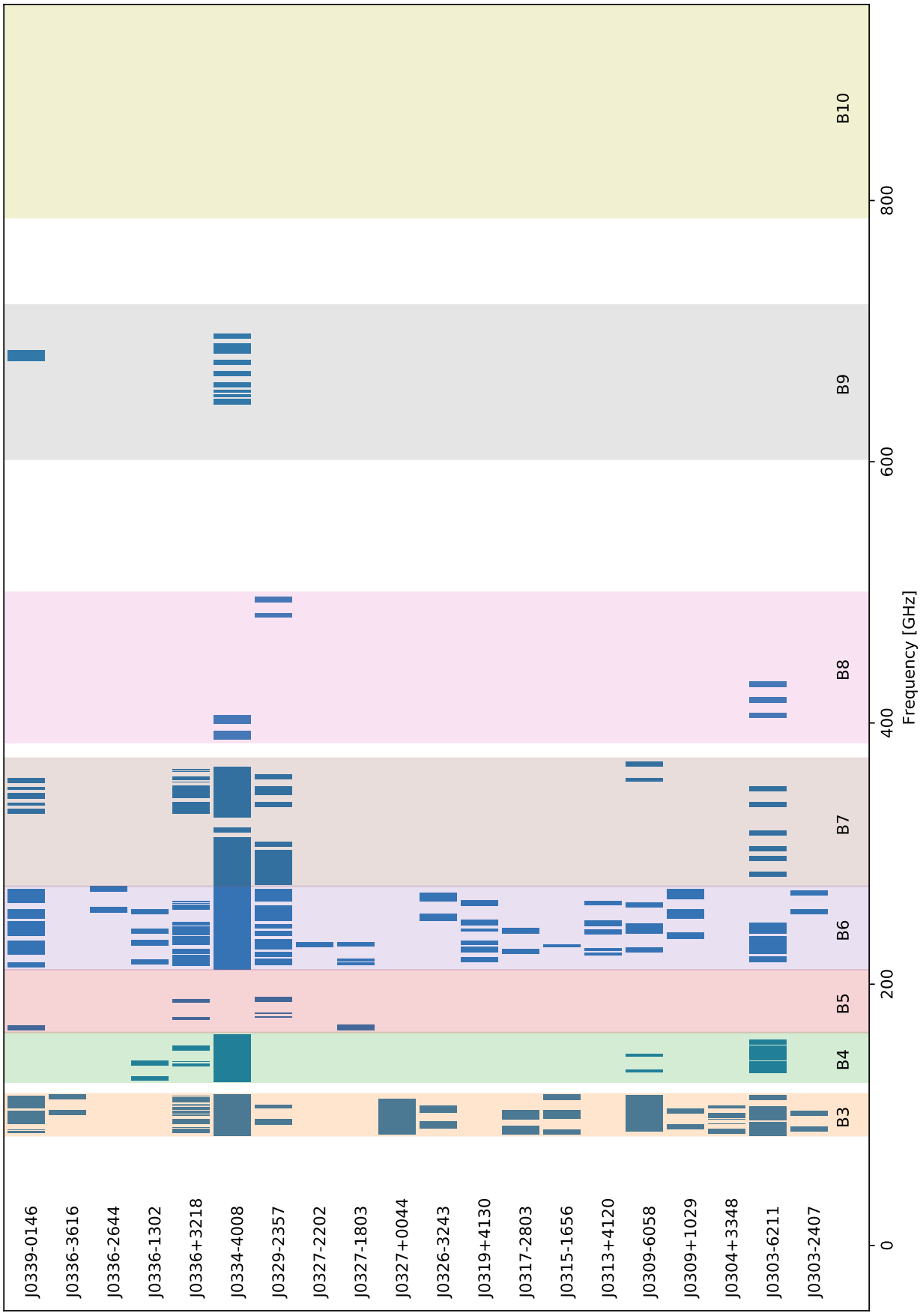
J0339-0146
J0336-3616
J0336-2644
J0336-1302
J0336+3218
J0334-4008
J0329-2357
J0327-2202
J0327-1803
J0327+0044
J0326-3243
J0319+4130
J0317-2803
J0315-1656
J0313+4120
J0309-6058
J0309+1029
J0304+3348
J0303-6211
J0303-2407
B3
B4
B5
B6
B7
B8
B9
B10
0
200
400
600
800
Frequency [GHz]

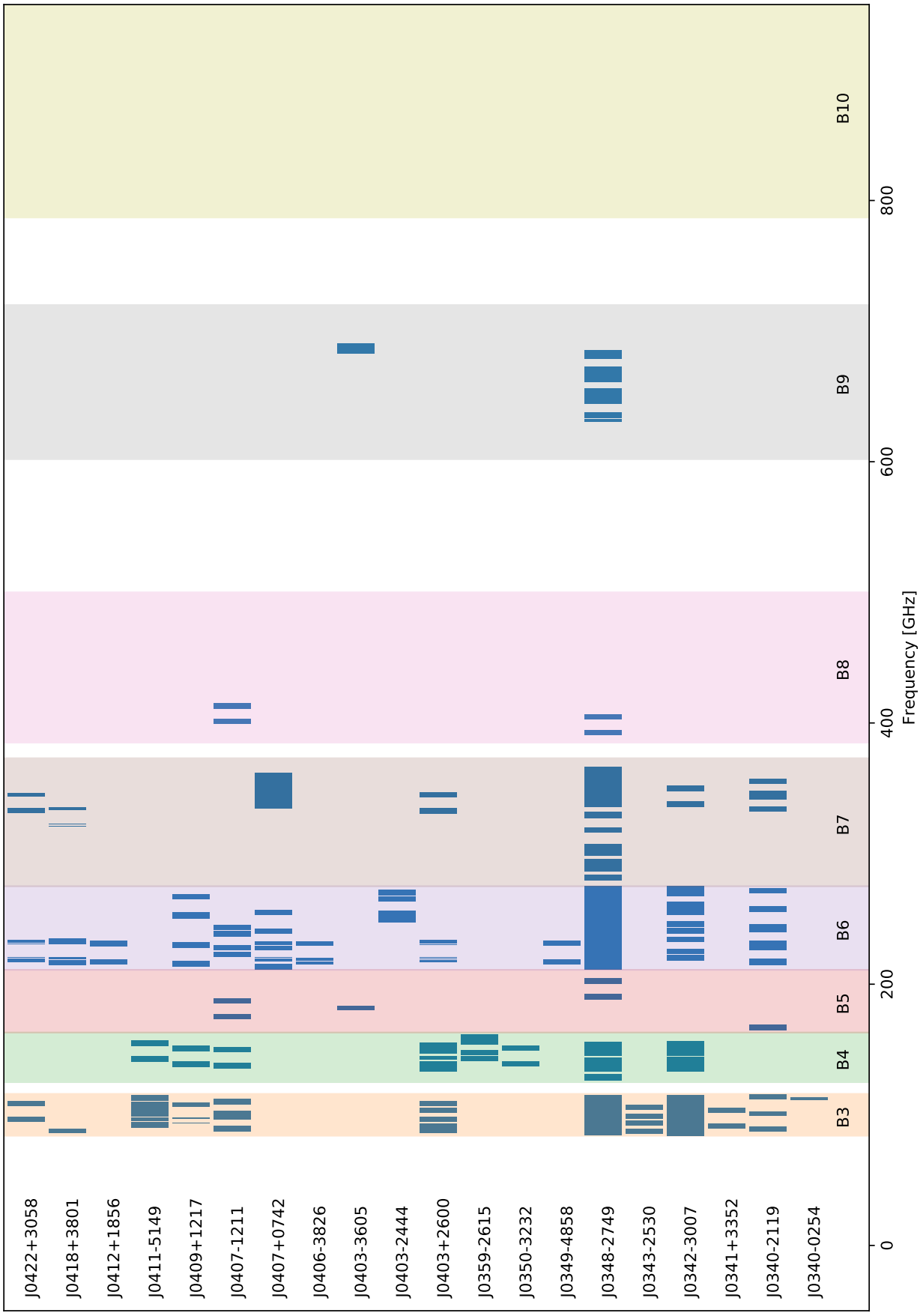
J0422+3058
J0418+3801
J0412+1856
J0411-5149
J0409+1217
J0407-1211
J0407+0742
J0406-3826
J0403-3605
J0403-2444
J0403+2600
J0359-2615
J0350-3232
J0349-4858
J0348-2749
J0343-2530
J0342-3007
J0341+3352
J0340-2119
J0340-0254
B3
B4
B5
B6
B7
B8
B9
B10
0
200
400
600
800
Frequency [GHz]

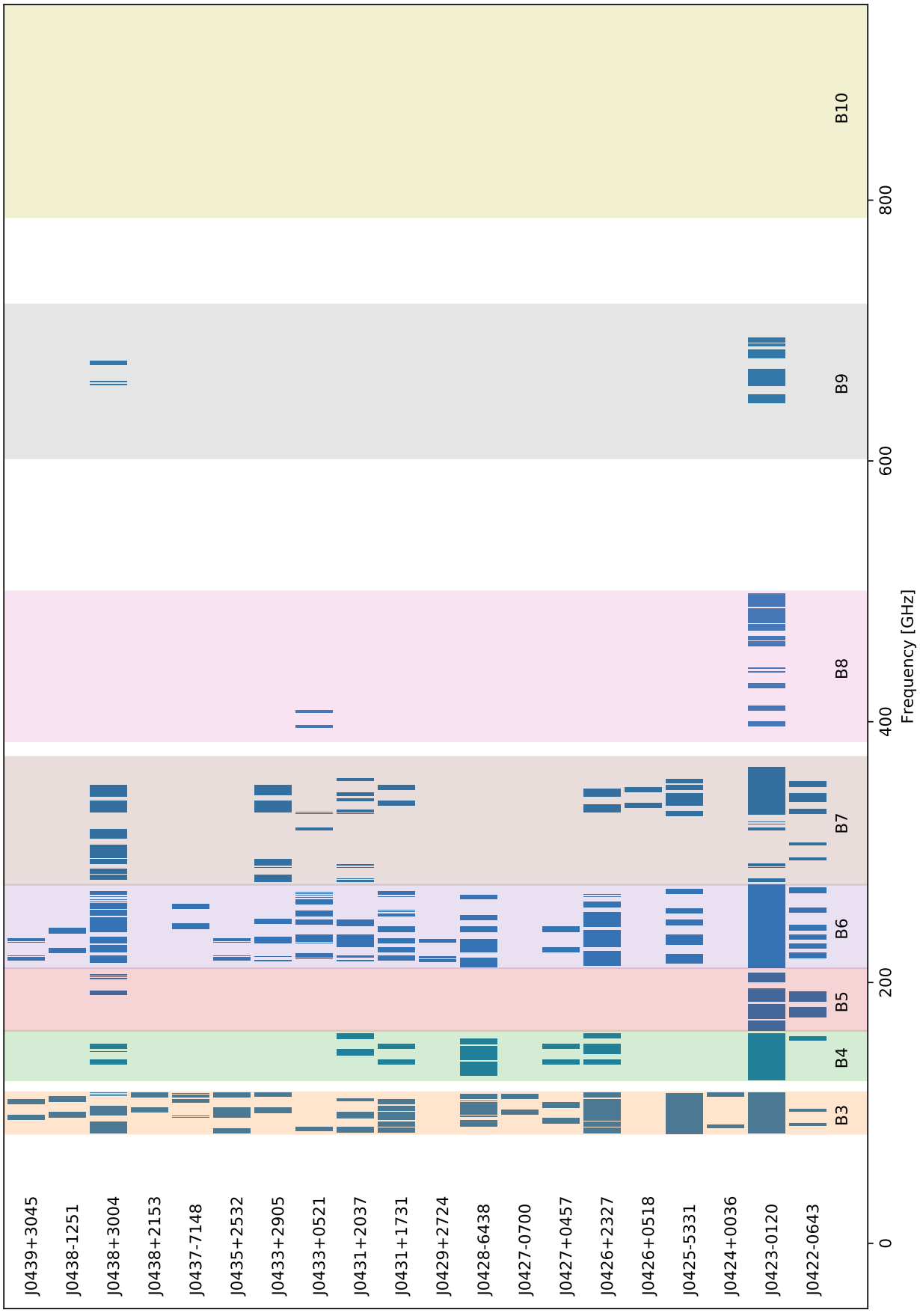
J0439+3045
J0438-1251
J0438+3004
J0438+2153
J0437-7148
J0435+2532
J0433+2905
J0433+0521
J0431+2037
J0431+1731
J0429+2724
J0428-6438
J0427-0700
J0427+0457
J0426+2327
J0426+0518
J0425-5331
J0424+0036
J0423-0120
J0422-0643
B3
B4
B5
B6
B7
B8
B9
B10
0
200
400
600
800
Frequency [GHz]

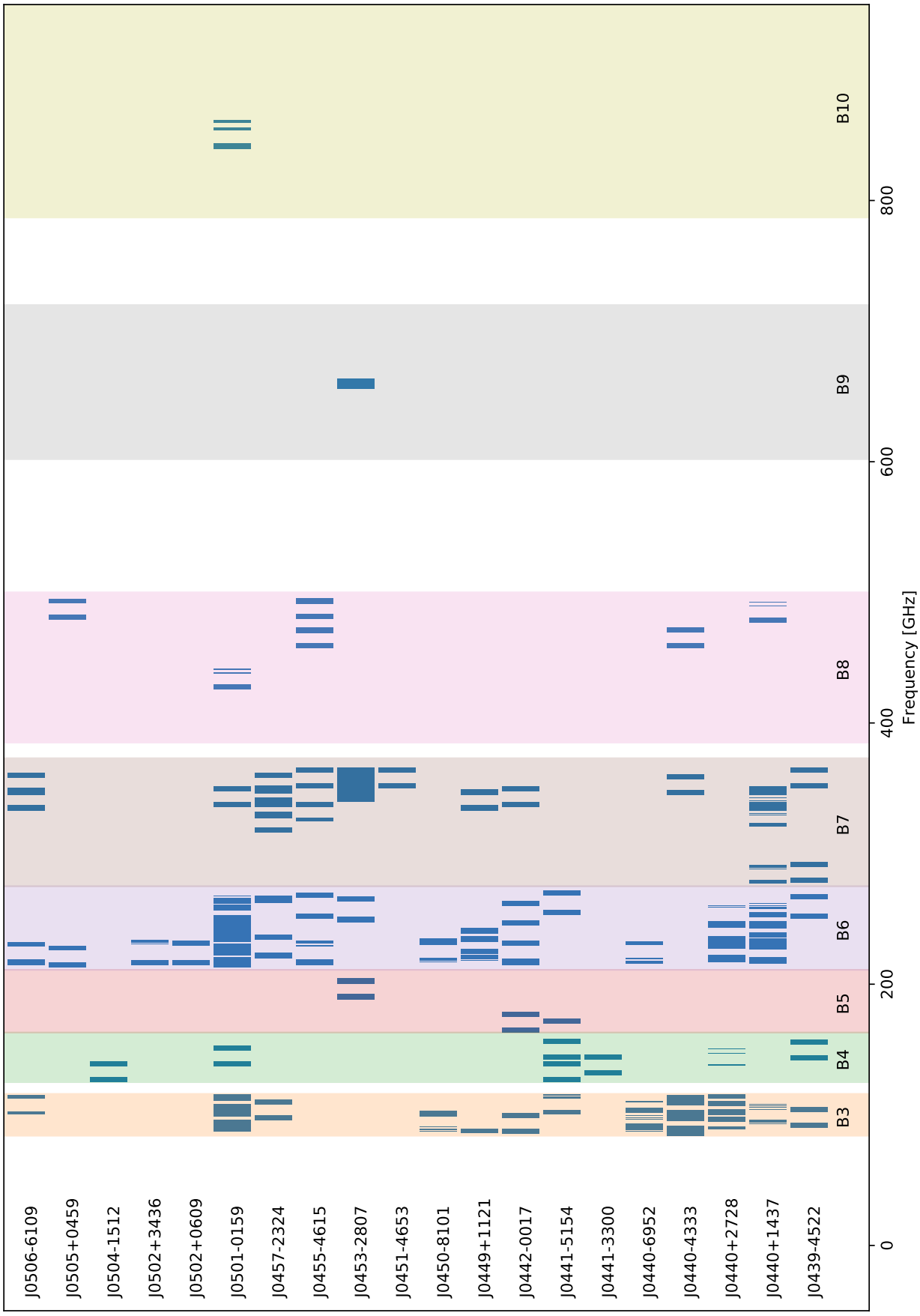
J0506-6109
J0505+0459
J0504-1512
J0502+3436
J0502+0609
J0501-0159
J0457-2324
J0455-4615
J0453-2807
J0451-4653
J0450-8101
J0449+1121
J0442-0017
J0441-5154
J0441-3300
J0440-6952
J0440-4333
J0440+2728
J0440+1437
J0439-4522
B3
B4
B5
B6
B7
B8
B9
B10
0
200
400
600
800
Frequency [GHz]

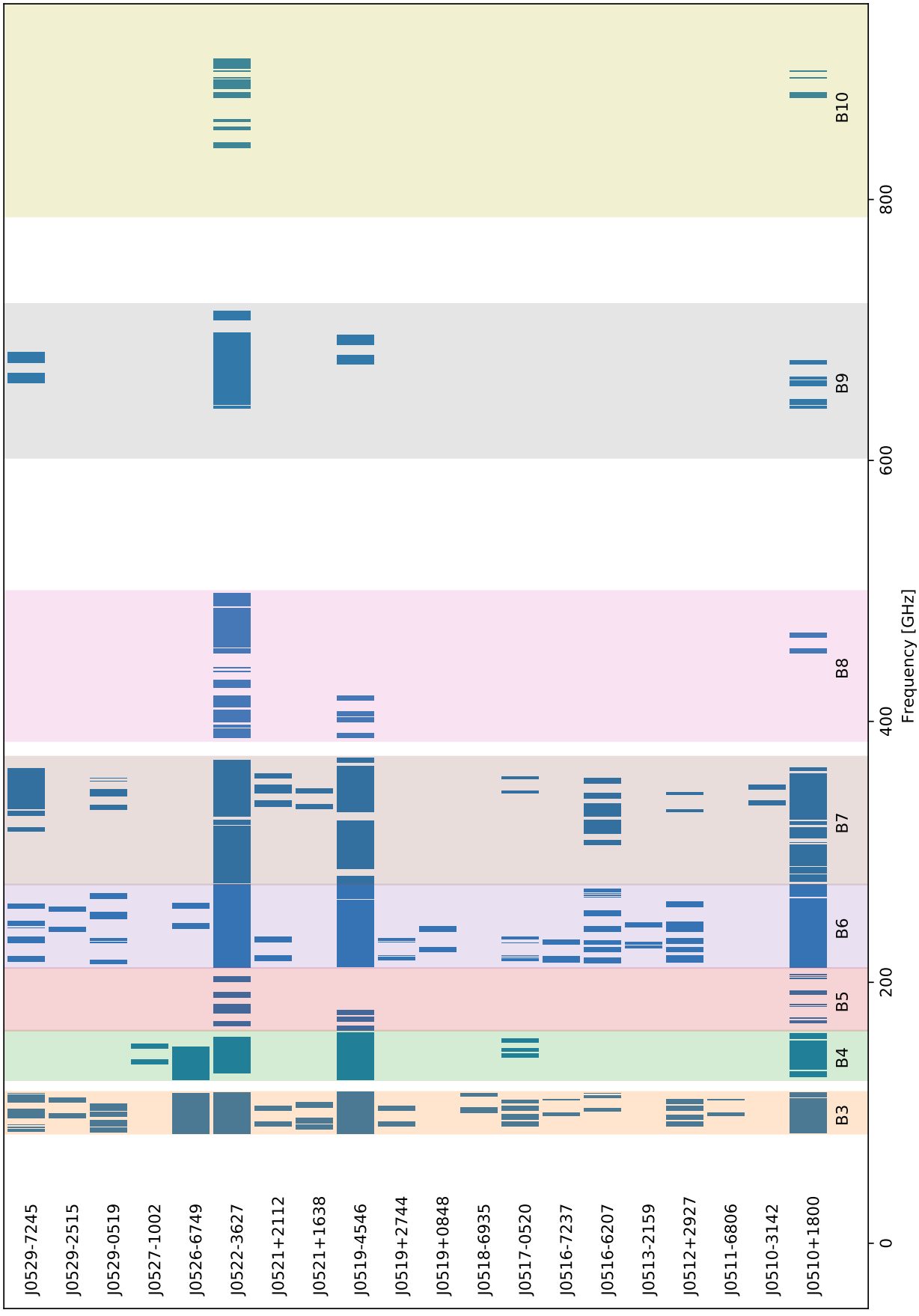
J0529-7245
J0529-2515
J0529-0519
J0527-1002
J0526-6749
J0522-3627
J0521+2112
J0521+1638
J0519-4546
J0519+2744
J0519+0848
J0518-6935
J0517-0520
J0516-7237
J0516-6207
J0513-2159
J0512+2927
J0511-6806
J0510-3142
J0510+1800
B3
B4
B5
B6
B7
B8
B9
B10
0
200
400
600
800
Frequency [GHz]

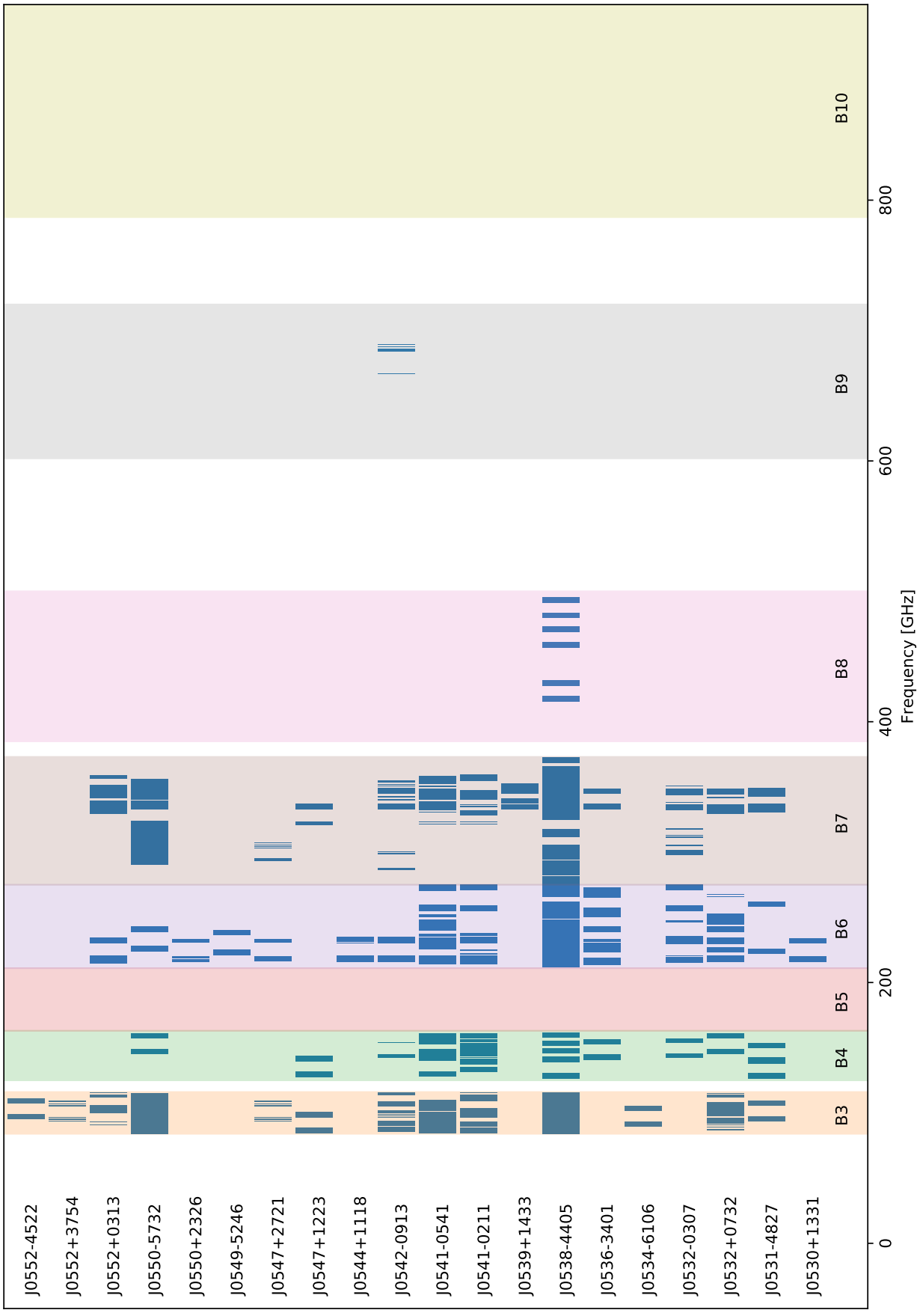
J0552-4522
J0552+3754
J0552+0313
J0550-5732
J0550+2326
J0549-5246
J0547+2721
J0547+1223
J0544+1118
J0542-0913
J0541-0541
J0541-0211
J0539+1433
J0538-4405
J0536-3401
J0534-6106
J0532-0307
J0532+0732
J0531-4827
J0530+1331
B3
B4
B5
B6
B7
B8
B9
B10
0
200
400
600
800
Frequency [GHz]

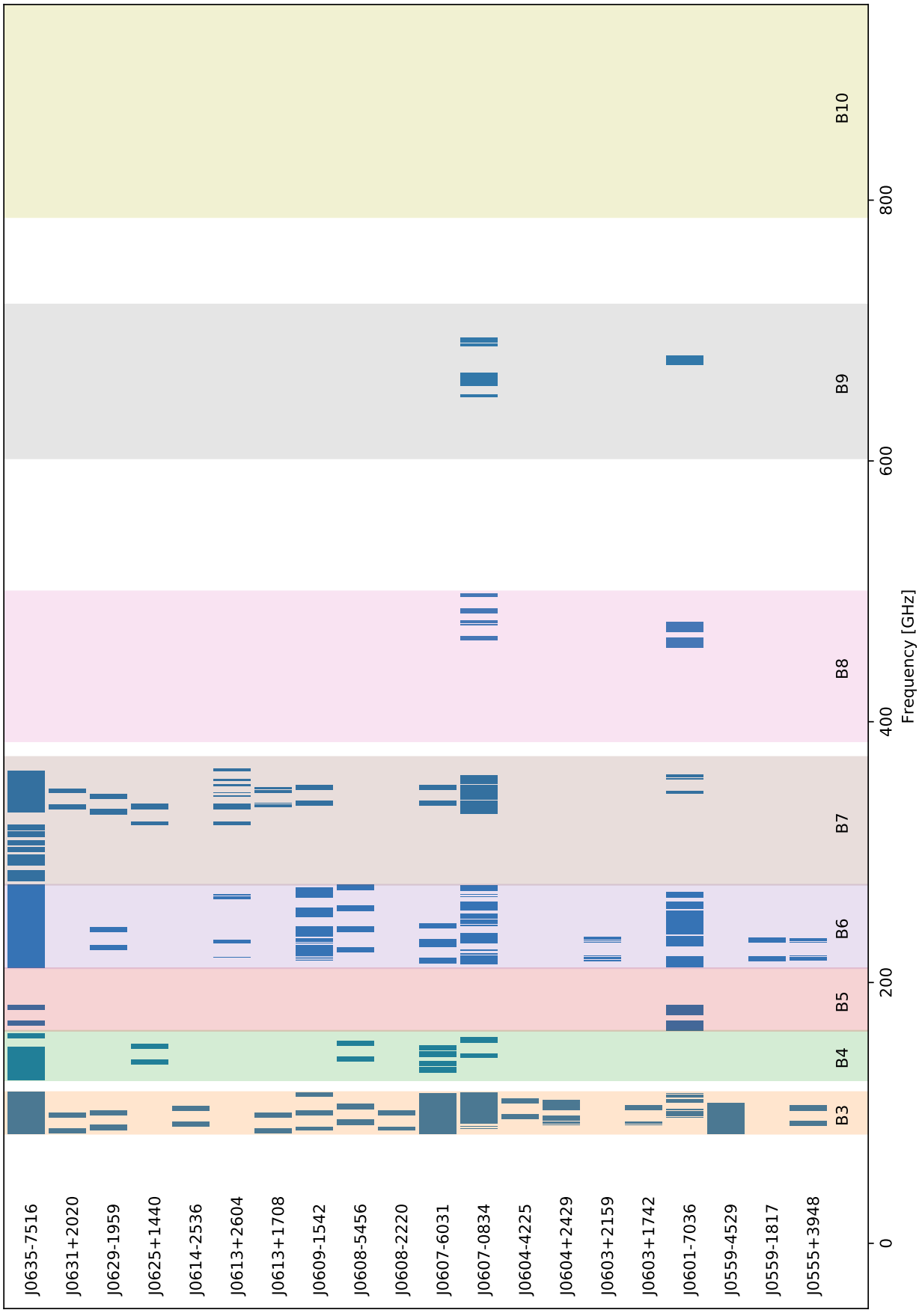
J0635-7516
J0631+2020
J0629-1959
J0625+1440
J0614-2536
J0613+2604
J0613+1708
J0609-1542
J0608-5456
J0608-2220
J0607-6031
J0607-0834
J0604-4225
J0604+2429
J0603+2159
J0603+1742
J0601-7036
J0559-4529
J0559-1817
J0555+3948
B3
B4
B5
B6
B7
B8
B9
B10
0
200
400
600
800
Frequency [GHz]

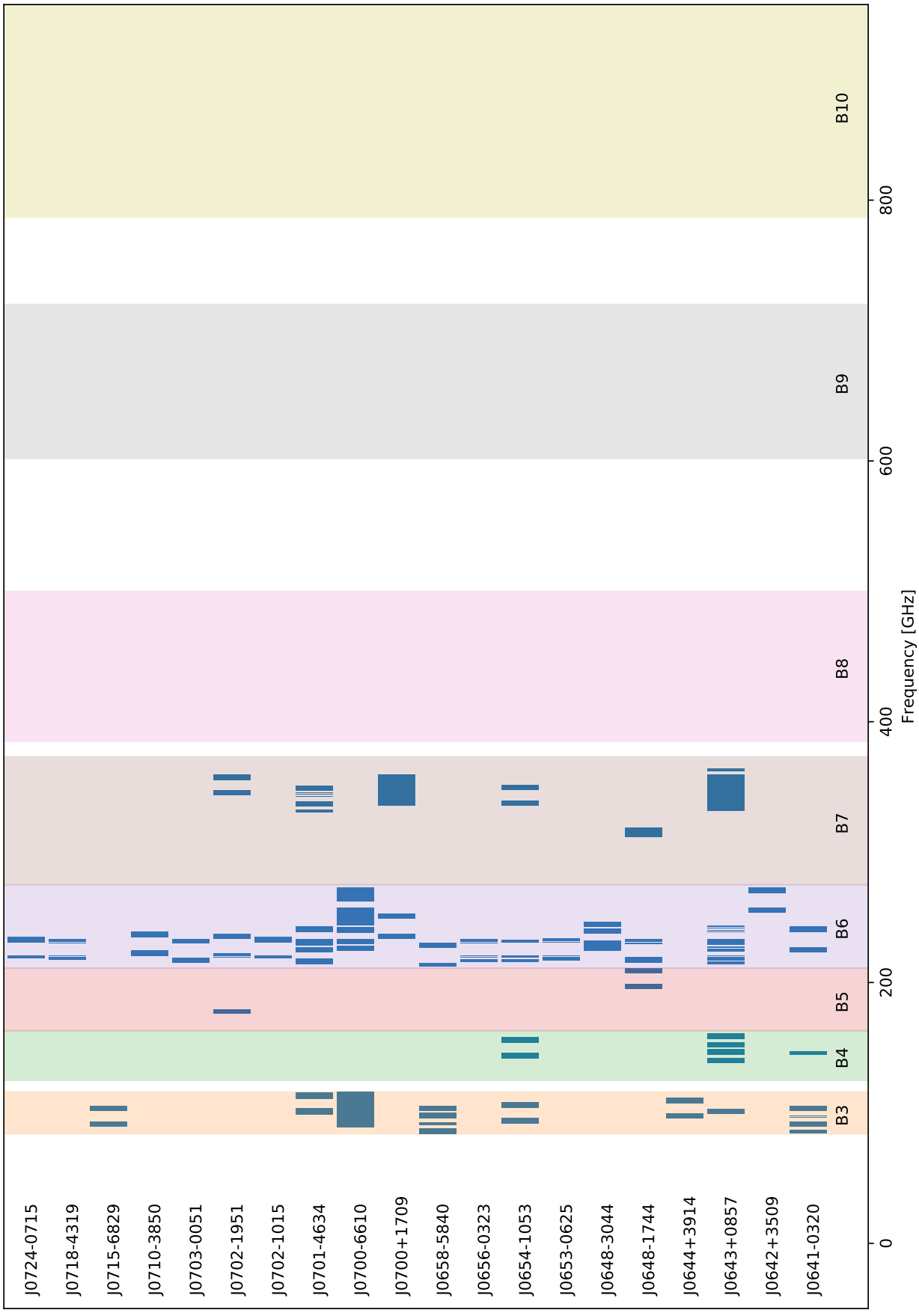
J0724-0715
J0718-4319
J0715-6829
J0710-3850
J0703-0051
J0702-1951
J0702-1015
J0701-4634
J0700-6610
J0700+1709
J0658-5840
J0656-0323
J0654-1053
J0653-0625
J0648-3044
J0648-1744
J0644+3914
J0643+0857
J0642+3509
J0641-0320
B3
B4
B5
B6
B7
B8
B9
B10
0
200
400
600
800
Frequency [GHz]

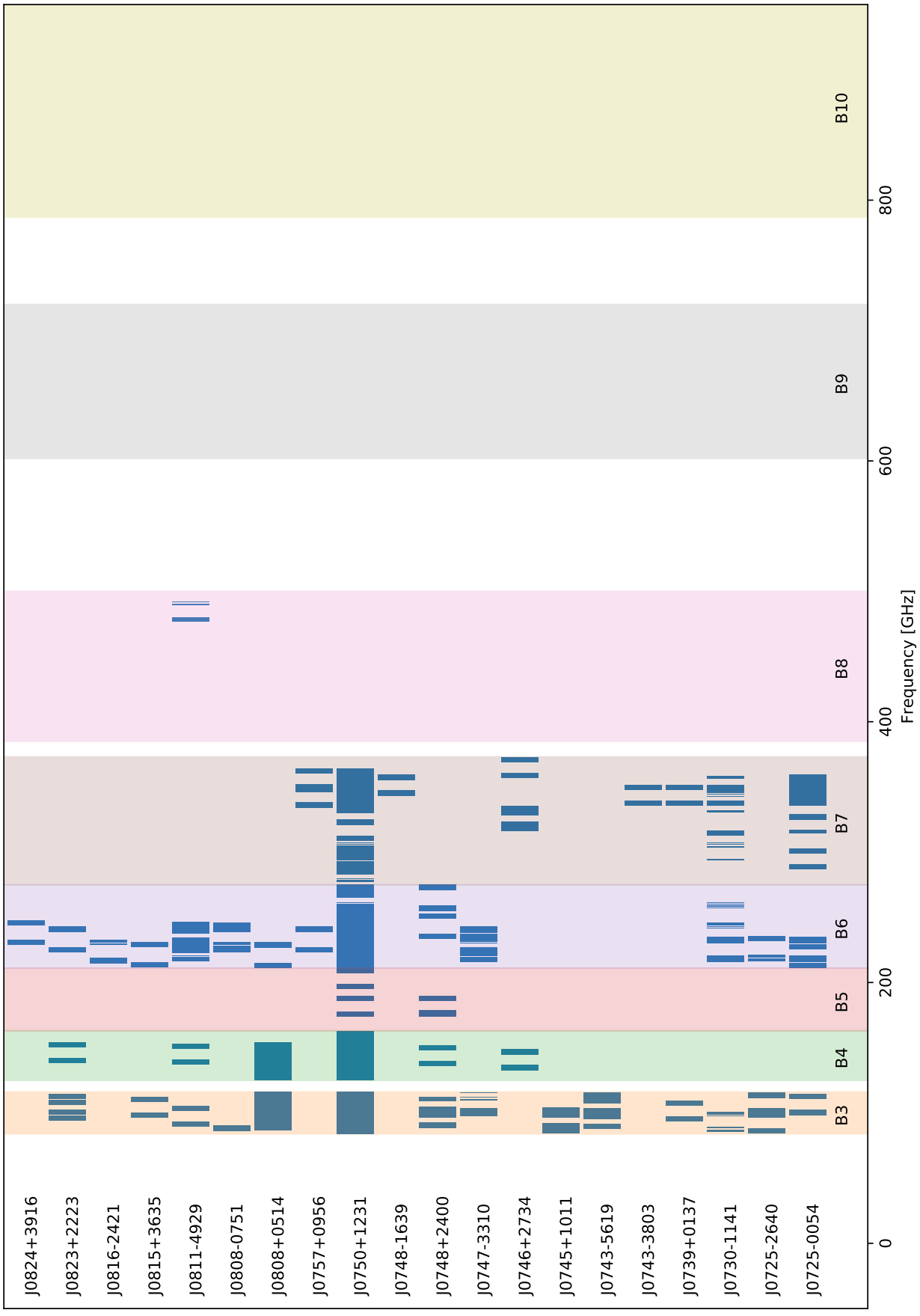
J0824+3916
J0823+2223
J0816-2421
J0815+3635
J0811-4929
J0808-0751
J0808+0514
J0757+0956
J0750+1231
J0748-1639
J0748+2400
J0747-3310
J0746+2734
J0745+1011
J0743-5619
J0743-3803
J0739+0137
J0730-1141
J0725-2640
J0725-0054
B3
B4
B5
B6
B7
B8
B9
B10
0
200
400
600
800
Frequency [GHz]

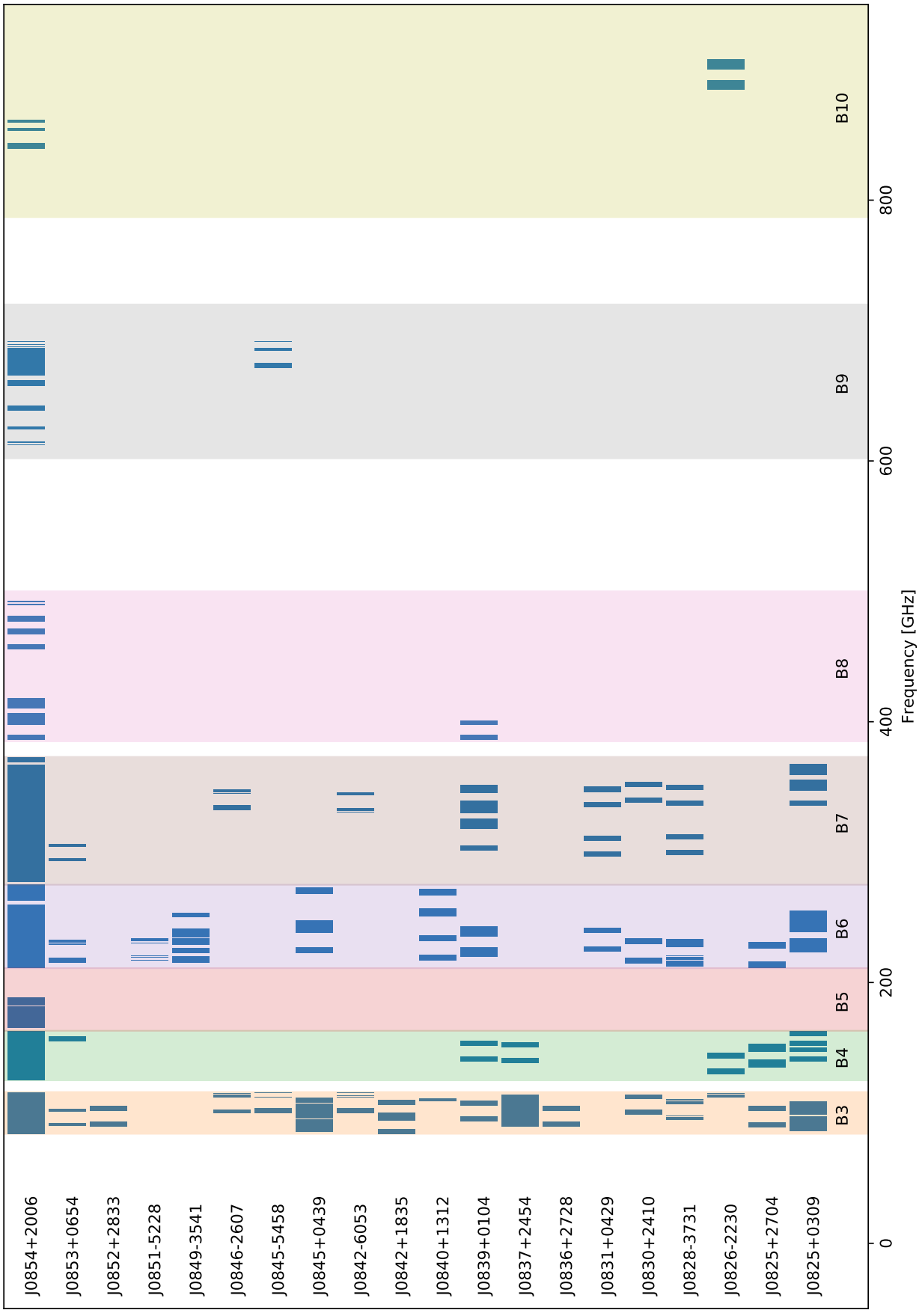
J0854+2006
J0853+0654
J0852+2833
J0851-5228
J0849-3541
J0846-2607
J0845-5458
J0845+0439
J0842-6053
J0842+1835
J0840+1312
J0839+0104
J0837+2454
J0836+2728
J0831+0429
J0830+2410
J0828-3731
J0826-2230
J0825+2704
J0825+0309
B3
B4
B5
B6
B7
B8
B9
B10
0
200
400
600
800
Frequency [GHz]

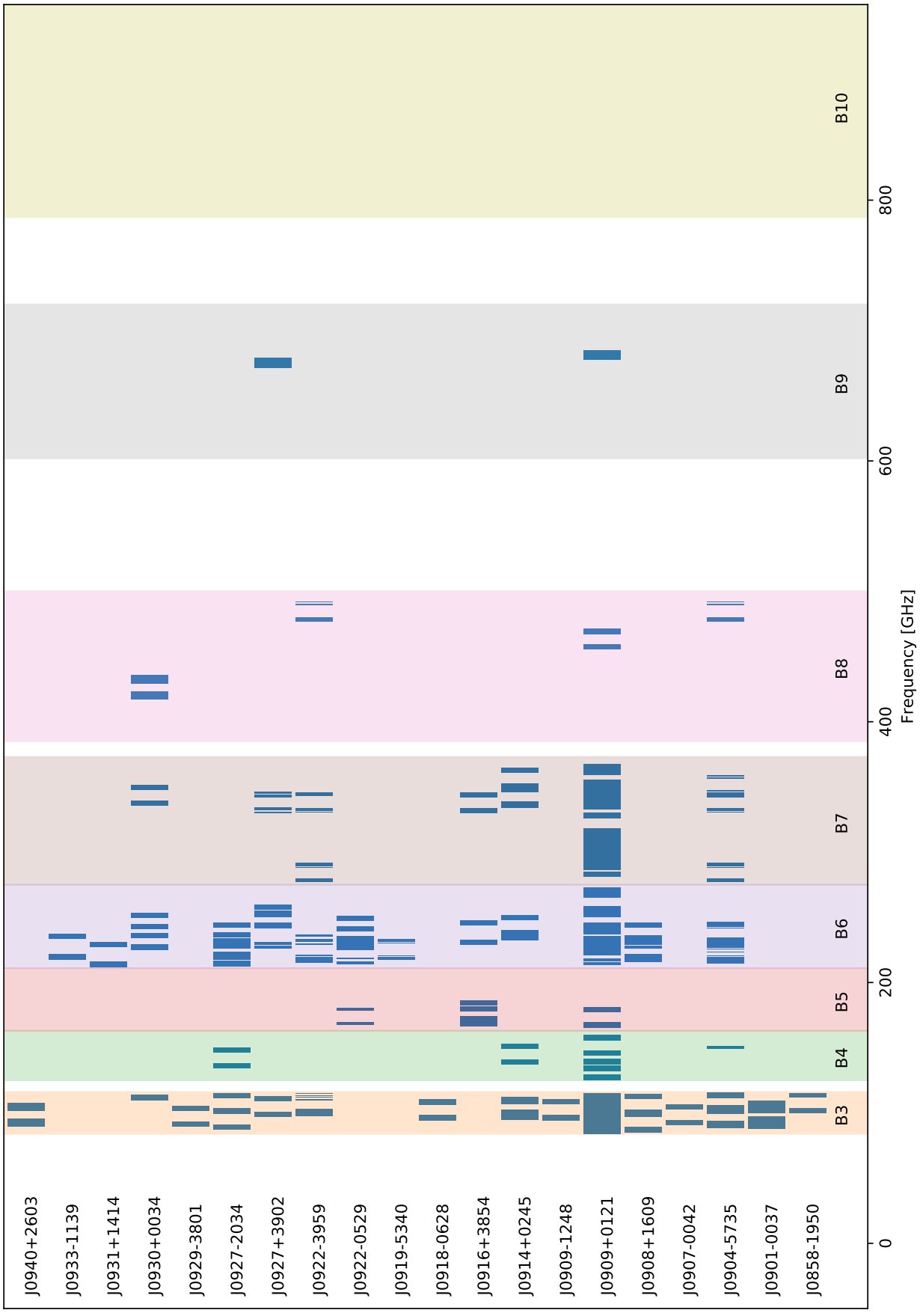
J0940+2603
J0933-1139
J0931+1414
J0930+0034
J0929-3801
J0927-2034
J0927+3902
J0922-3959
J0922-0529
J0919-5340
J0918-0628
J0916+3854
J0914+0245
J0909-1248
J0909+0121
J0908+1609
J0907-0042
J0904-5735
J0901-0037
J0858-1950
B3
B4
B5
B6
B7
B8
B9
B10
0
200
400
600
800
Frequency [GHz]

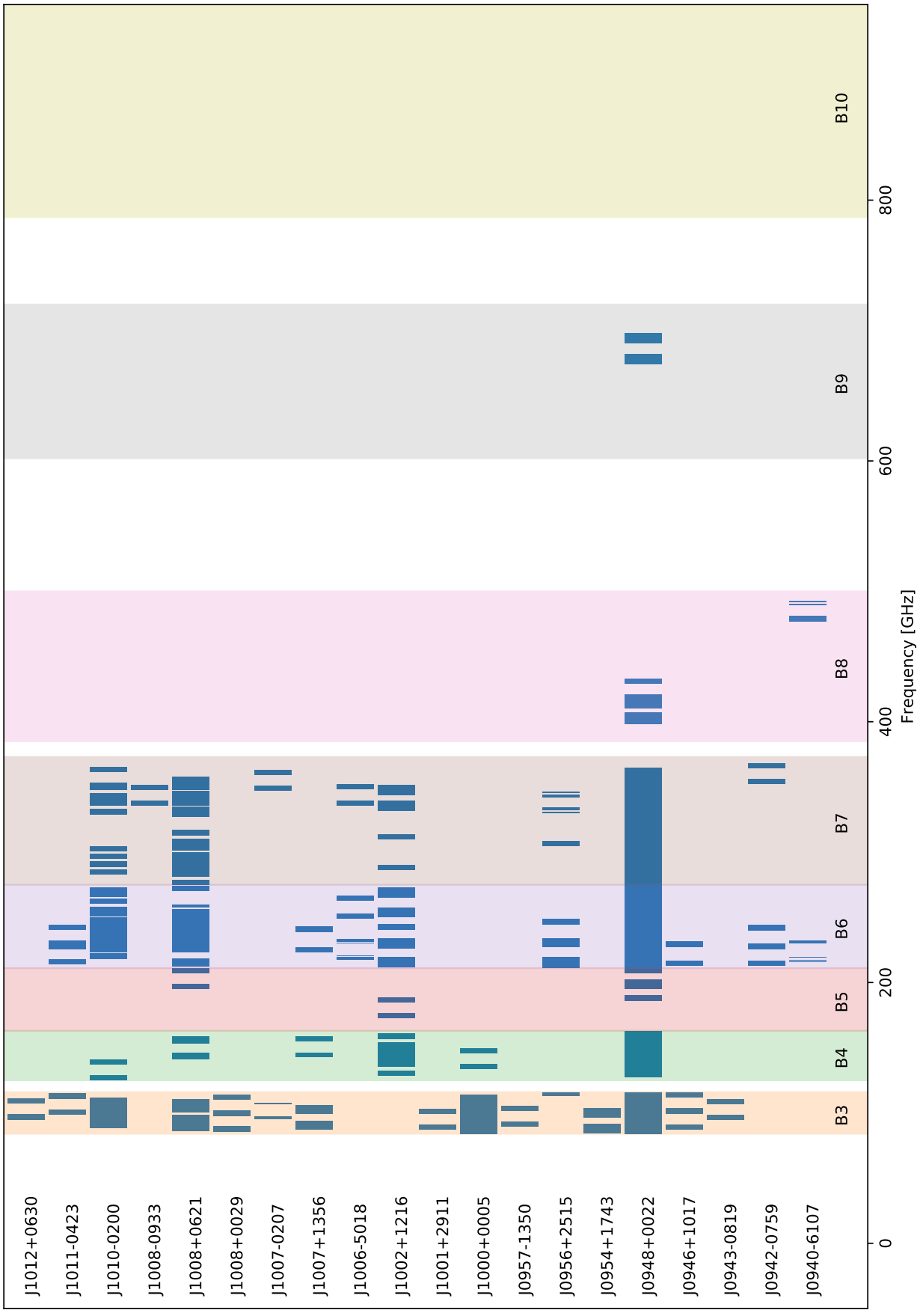
J1012+0630
J1011-0423
J1010-0200
J1008-0933
J1008+0621
J1008+0029
J1007-0207
J1007+1356
J1006-5018
J1002+1216
J1001+2911
J1000+0005
J0957-1350
J0956+2515
J0954+1743
J0948+0022
J0946+1017
J0943-0819
J0942-0759
J0940-6107
B3
B4
B5
B6
B7
B8
B9
B10
0
200
400
600
800
Frequency [GHz]

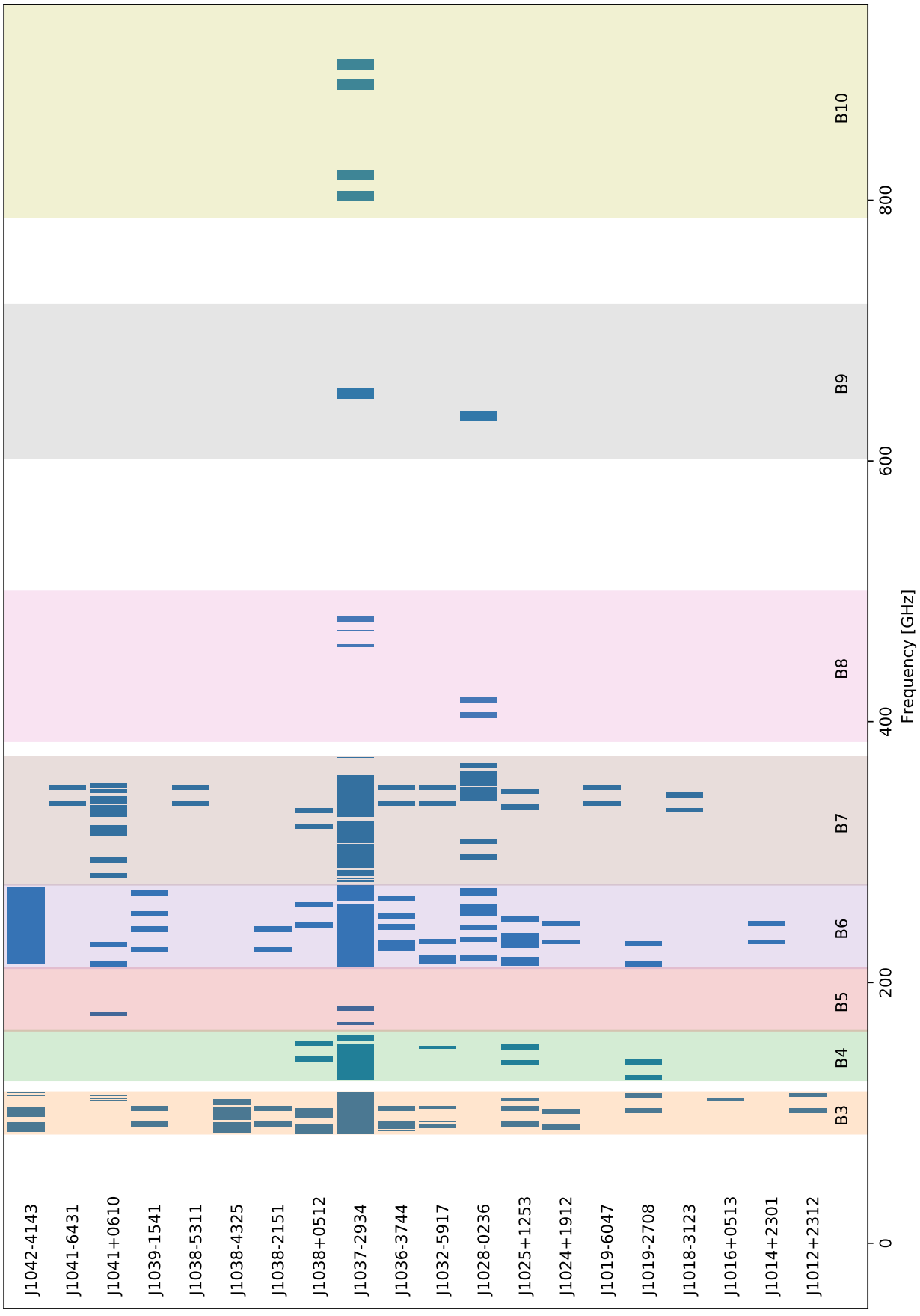
J1042-4143
J1041-6431
J1041+0610
J1039-1541
J1038-5311
J1038-4325
J1038-2151
J1038+0512
J1037-2934
J1036-3744
J1032-5917
J1028-0236
J1025+1253
J1024+1912
J1019-6047
J1019-2708
J1018-3123
J1016+0513
J1014+2301
J1012+2312
B3
B4
B5
B6
B7
B8
B9
B10
0
200
400
600
800
Frequency [GHz]

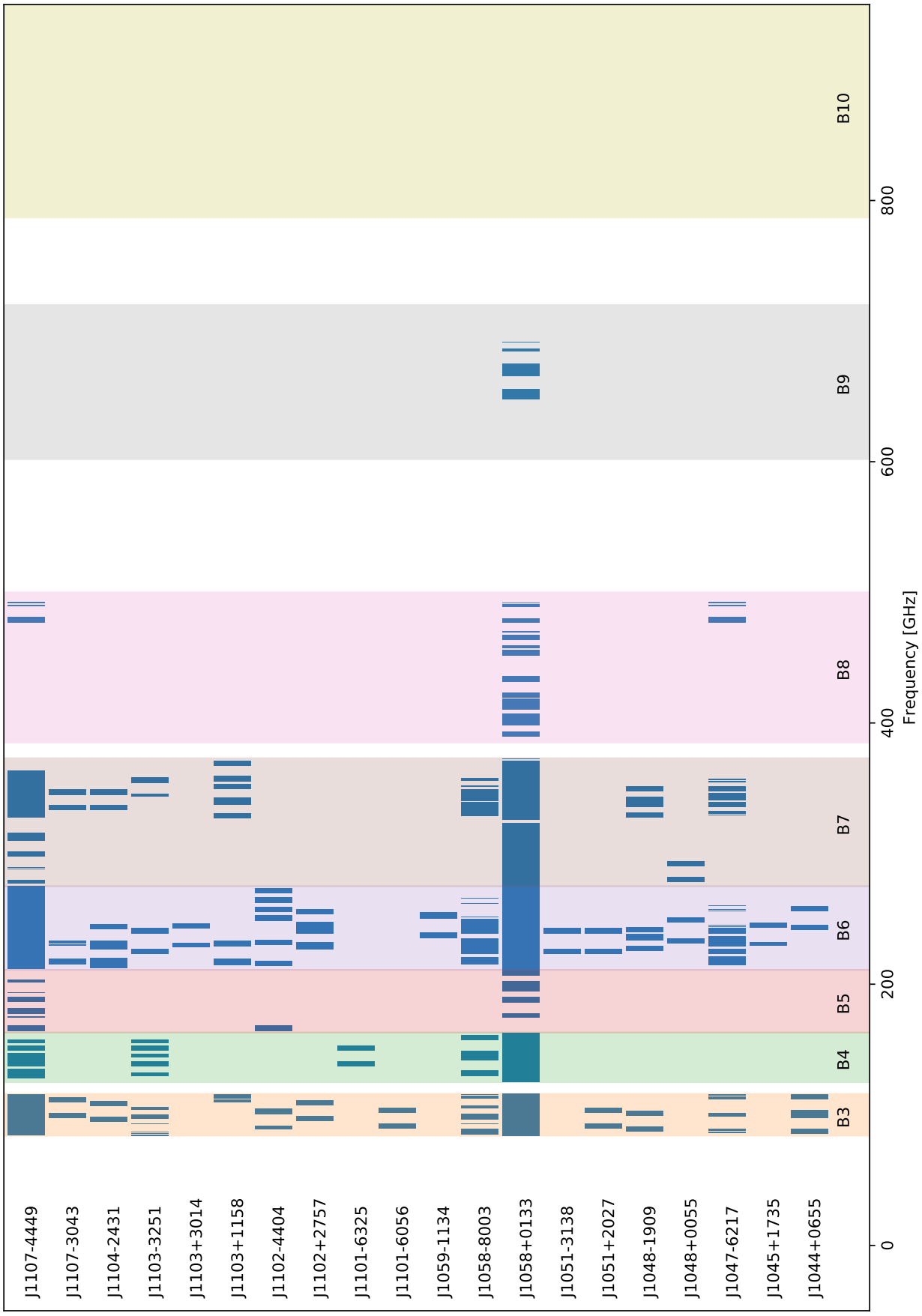
J1107-4449
J1107-3043
J1104-2431
J1103-3251
J1103+3014
J1103+1158
J1102-4404
J1102+2757
J1101-6325
J1101-6056
J1059-1134
J1058-8003
J1058+0133
J1051-3138
J1051+2027
J1048-1909
J1048+0055
J1047-6217
J1045+1735
J1044+0655
B3
B4
B5
B6
B7
B8
B9
B10
0
200
400
600
800
Frequency [GHz]

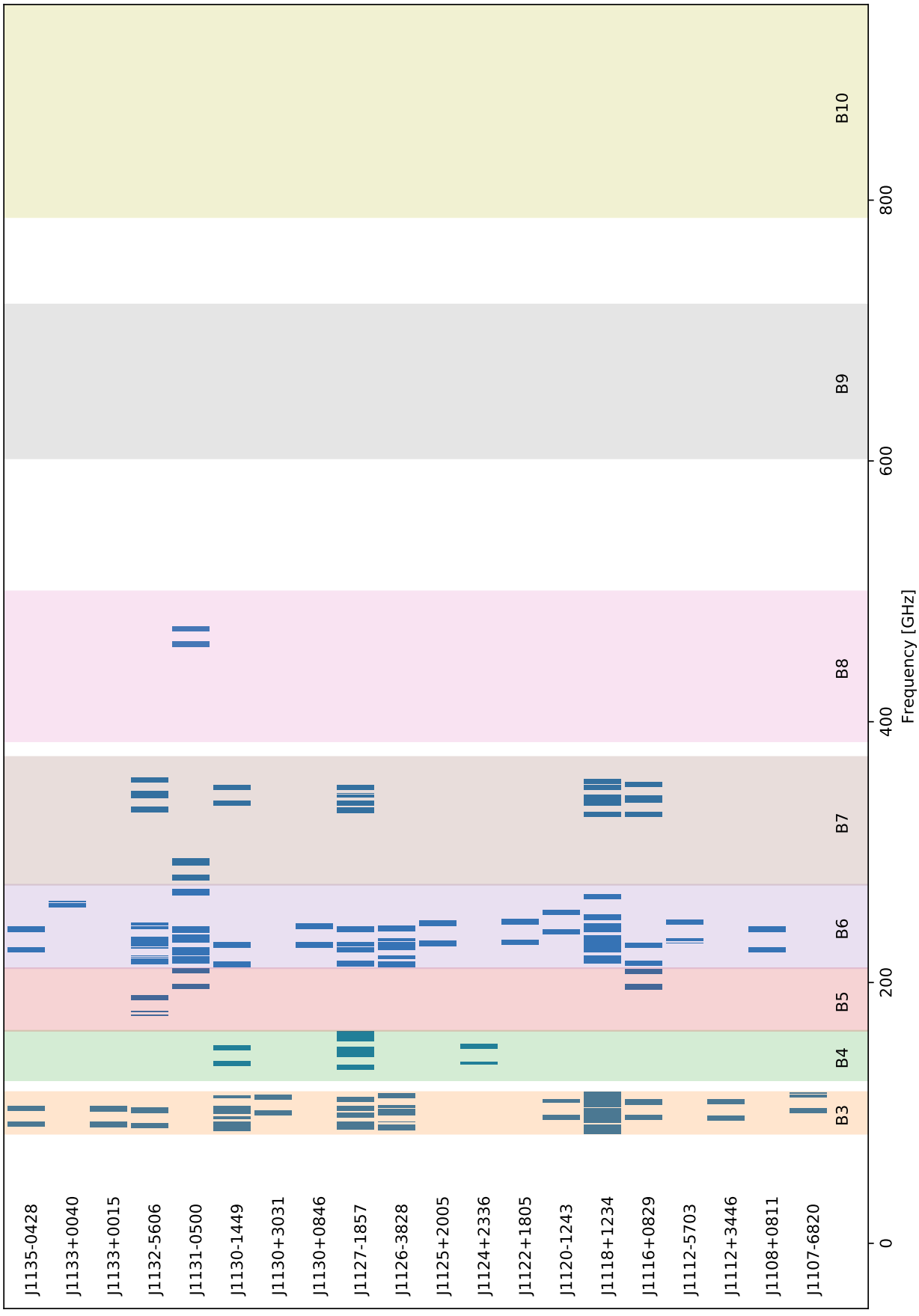
J1135-0428
J1133+0040
J1133+0015
J1132-5606
J1131-0500
J1130-1449
J1130+3031
J1130+0846
J1127-1857
J1126-3828
J1125+2005
J1124+2336
J1122+1805
J1120-1243
J1118+1234
J1116+0829
J1112-5703
J1112+3446
J1108+0811
J1107-6820
B3
B4
B5
B6
B7
B8
B9
B10
0
200
400
600
800
Frequency [GHz]

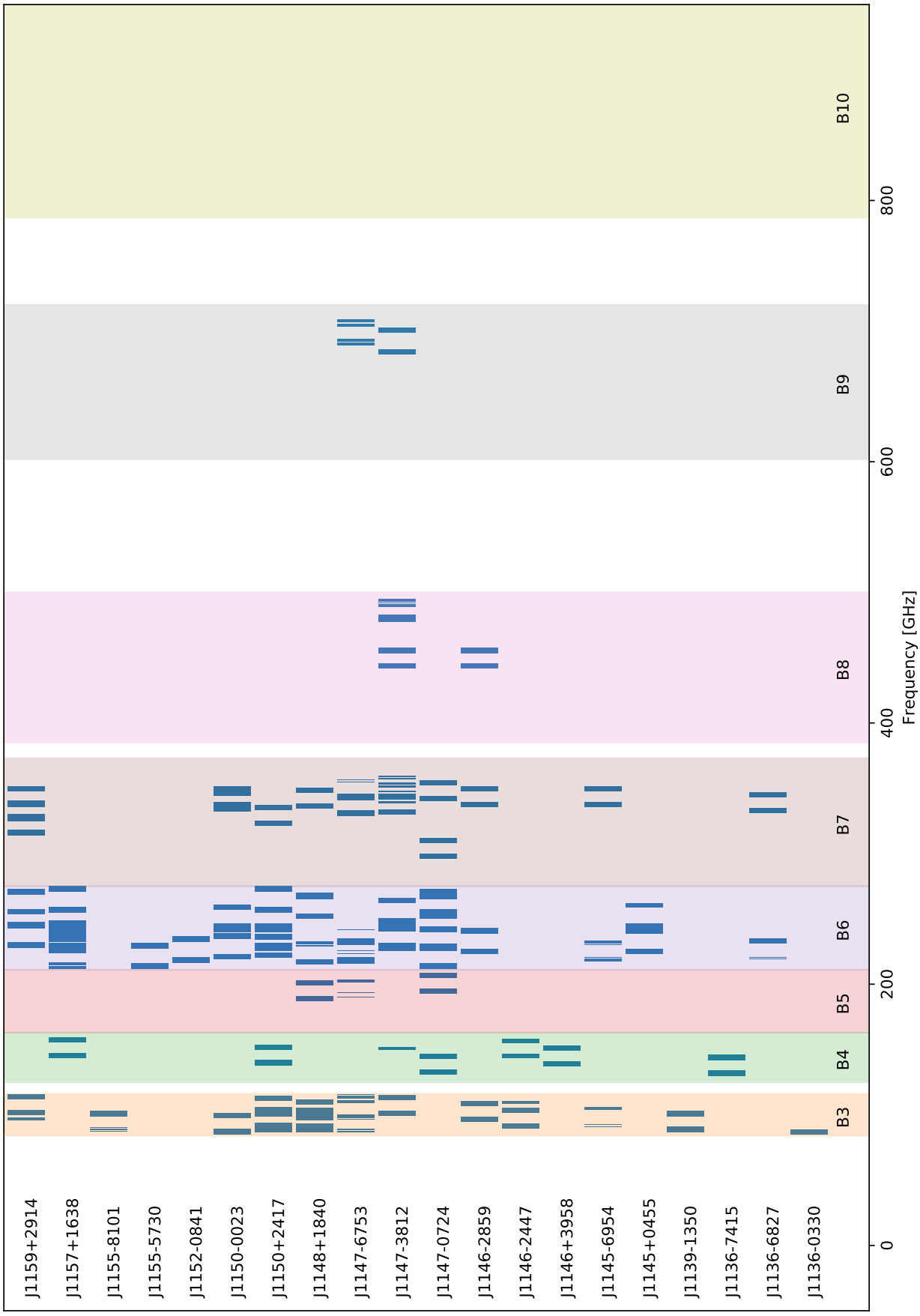
J1159+2914
J1157+1638
J1155-8101
J1155-5730
J1152-0841
J1150-0023
J1150+2417
J1148+1840
J1147-6753
J1147-3812
J1147-0724
J1146-2859
J1146-2447
J1146+3958
J1145-6954
J1145+0455
J1139-1350
J1136-7415
J1136-6827
J1136-0330
B3
B4
B5
B6
B7
B8
B9
B10
0
200
400
600
800
Frequency [GHz]

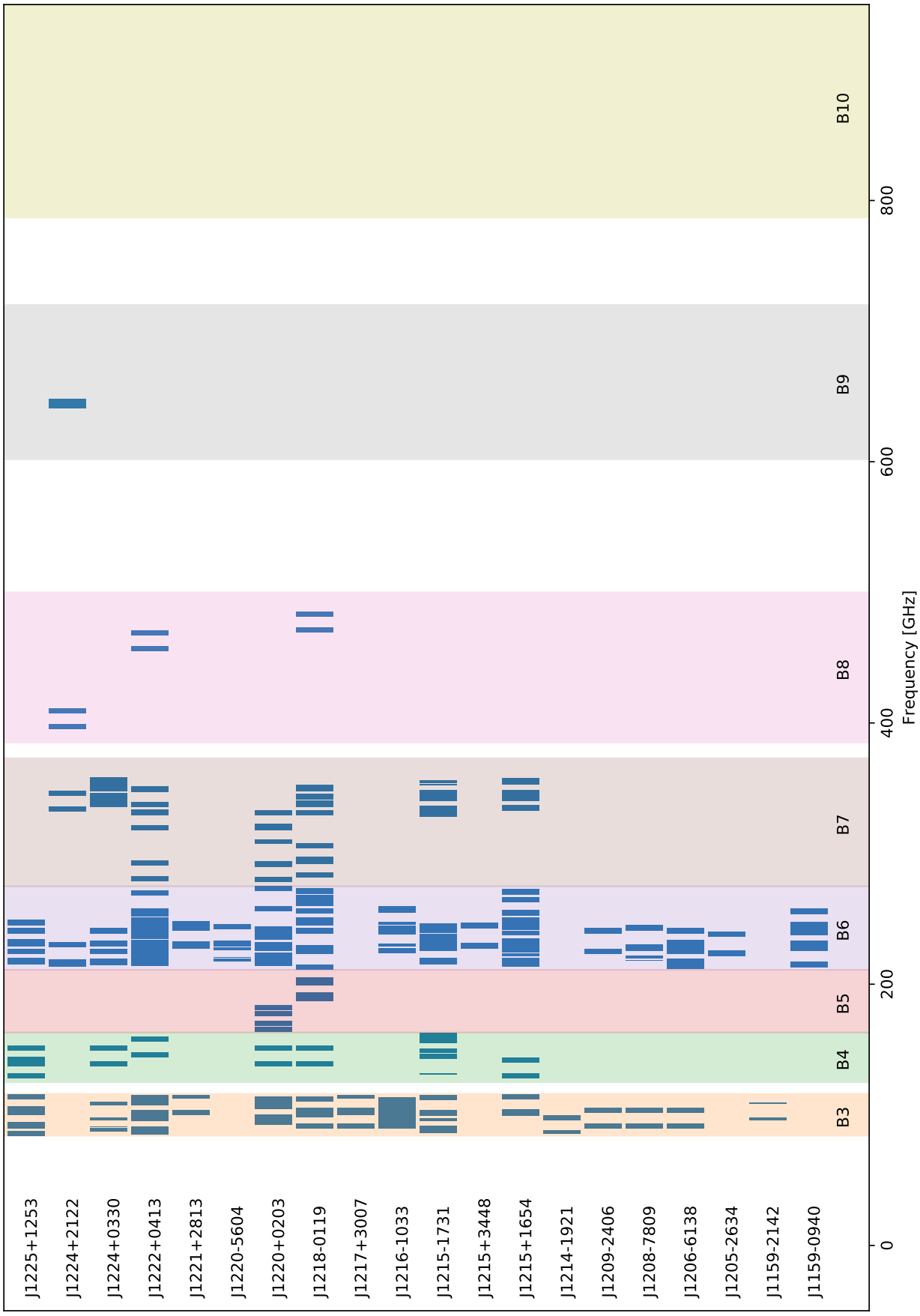
J1225+1253
J1224+2122
J1224+0330
J1222+0413
J1221+2813
J1220-5604
J1220+0203
J1218-0119
J1217+3007
J1216-1033
J1215-1731
J1215+3448
J1215+1654
J1214-1921
J1209-2406
J1208-7809
J1206-6138
J1205-2634
J1159-2142
J1159-0940
B3
B4
B5
B6
B7
B8
B9
B10
0
200
400
600
800
Frequency [GHz]

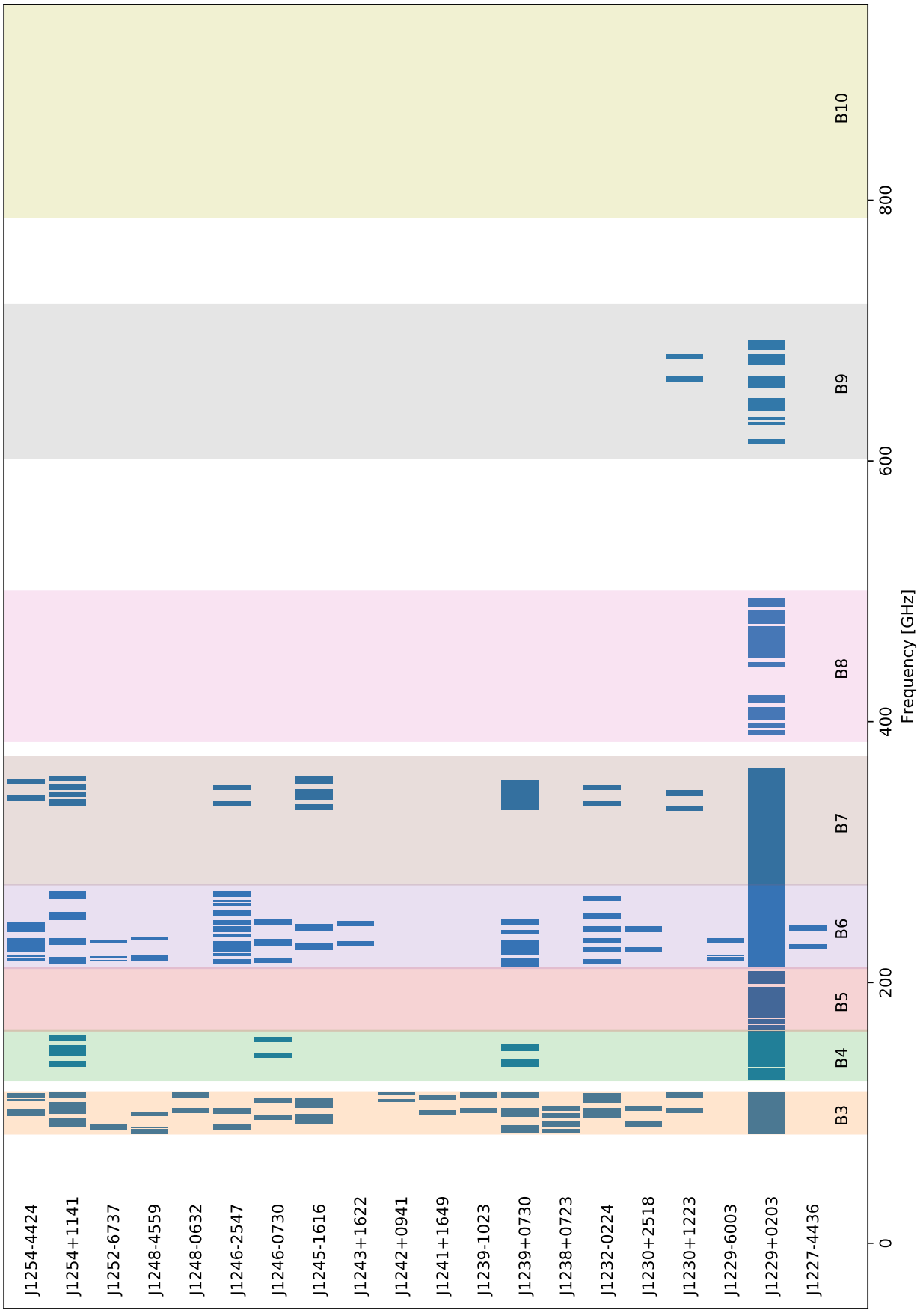
J1254-4424
J1254+1141
J1252-6737
J1248-4559
J1248-0632
J1246-2547
J1246-0730
J1245-1616
J1243+1622
J1242+0941
J1241+1649
J1239-1023
J1239+0730
J1238+0723
J1232-0224
J1230+2518
J1230+1223
J1229-6003
J1229+0203
J1227-4436
B3
B4
B5
B6
B7
B8
B9
B10
0
200
400
600
800
Frequency [GHz]

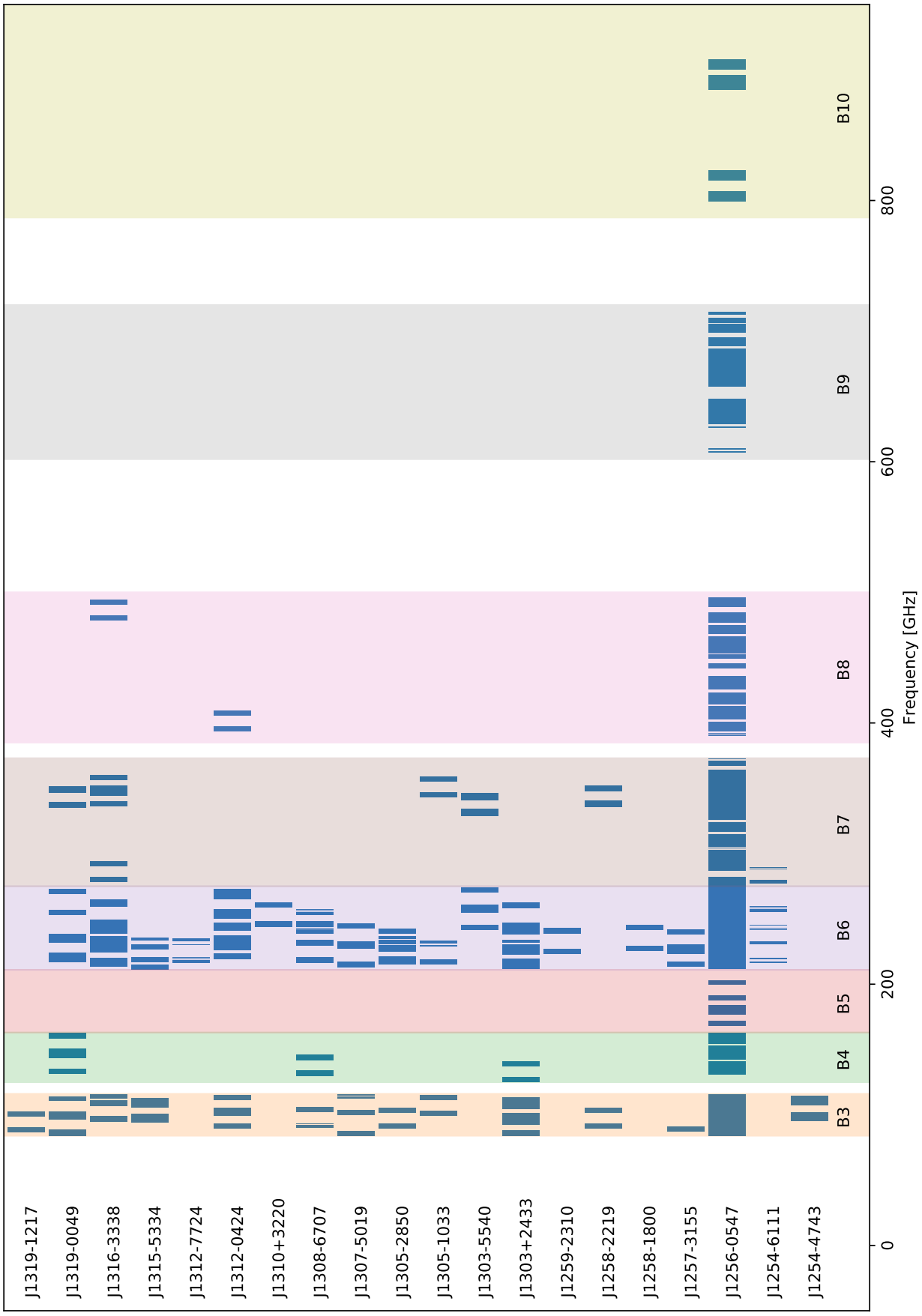
J1319-1217
J1319-0049
J1316-3338
J1315-5334
J1312-7724
J1312-0424
J1310+3220
J1308-6707
J1307-5019
J1305-2850
J1305-1033
J1303-5540
J1303+2433
J1259-2310
J1258-2219
J1258-1800
J1257-3155
J1256-0547
J1254-6111
J1254-4743
B3
B4
B5
B6
B7
B8
B9
B10
0
200
400
600
800
Frequency [GHz]

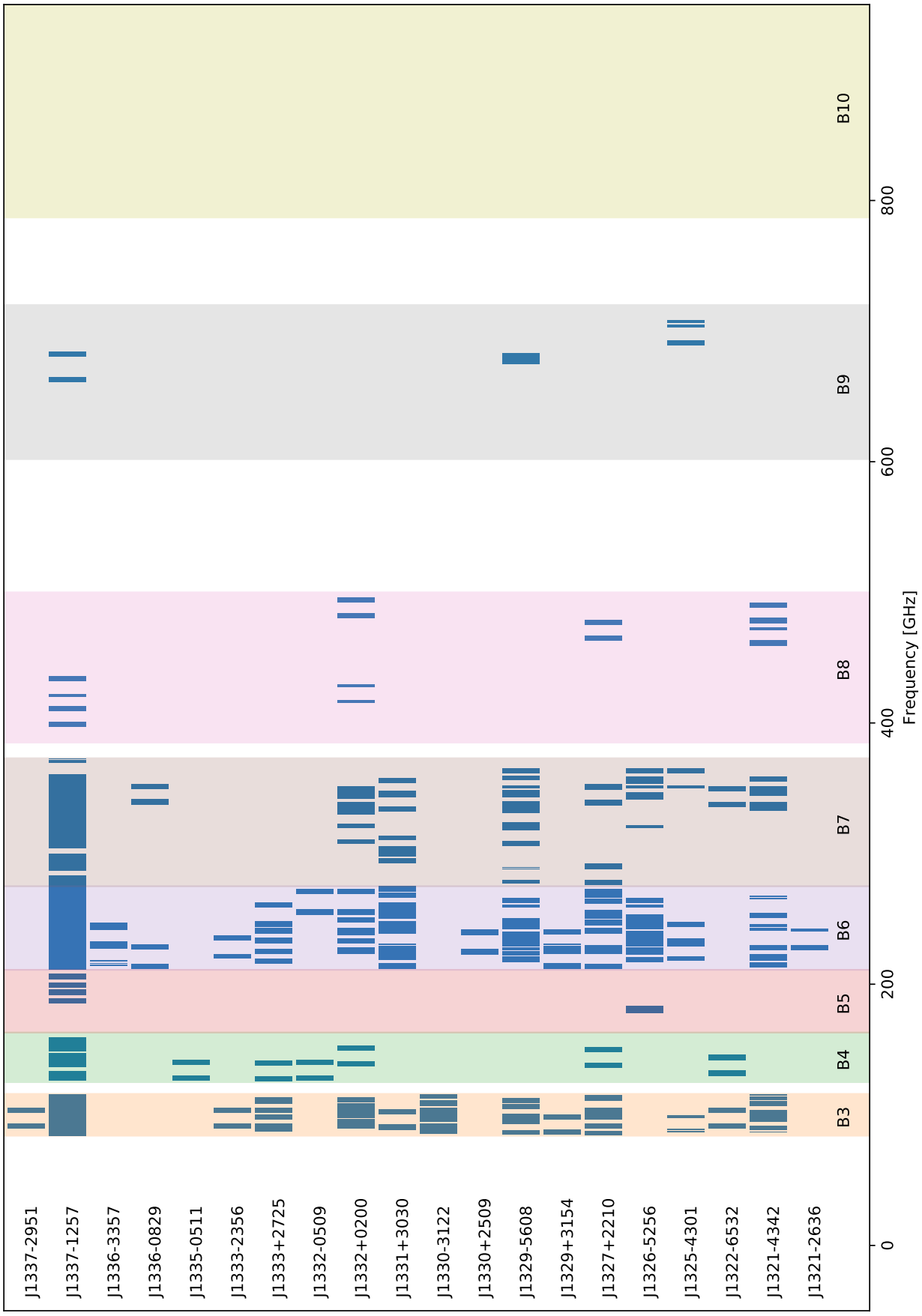
J1337-2951
J1337-1257
J1336-3357
J1336-0829
J1335-0511
J1333-2356
J1333+2725
J1332-0509
J1332+0200
J1331+3030
J1330-3122
J1330+2509
J1329-5608
J1329+3154
J1327+2210
J1326-5256
J1325-4301
J1322-6532
J1321-4342
J1321-2636
B3
B4
B5
B6
B7
B8
B9
B10
0
200
400
600
800
Frequency [GHz]

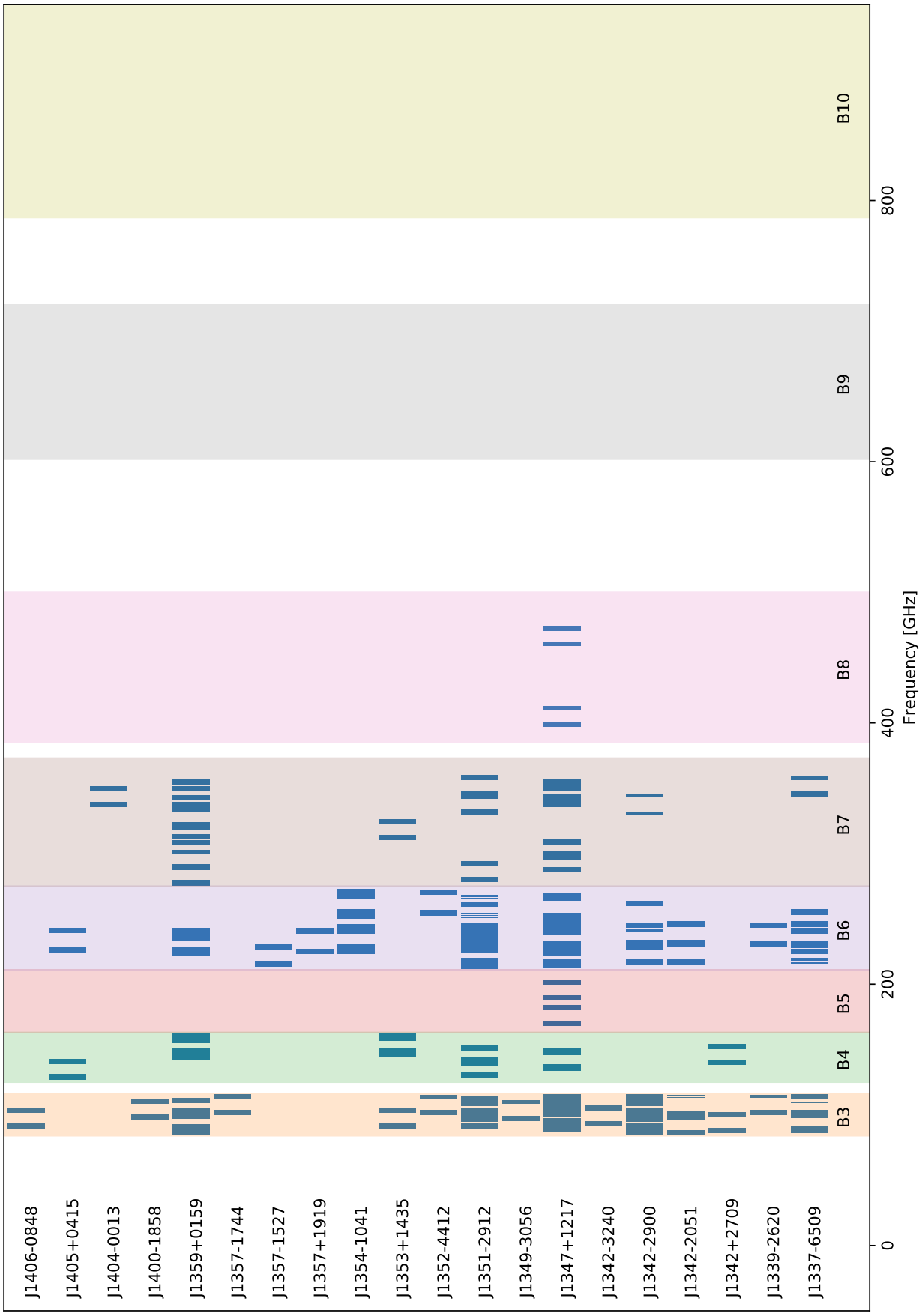
J1406-0848
J1405+0415
J1404-0013
J1400-1858
J1359+0159
J1357-1744
J1357-1527
J1357+1919
J1354-1041
J1353+1435
J1352-4412
J1351-2912
J1349-3056
J1347+1217
J1342-3240
J1342-2900
J1342-2051
J1342+2709
J1339-2620
J1337-6509
B3
B4
B5
B6
B7
B8
B9
B10
0
200
400
600
800
Frequency [GHz]

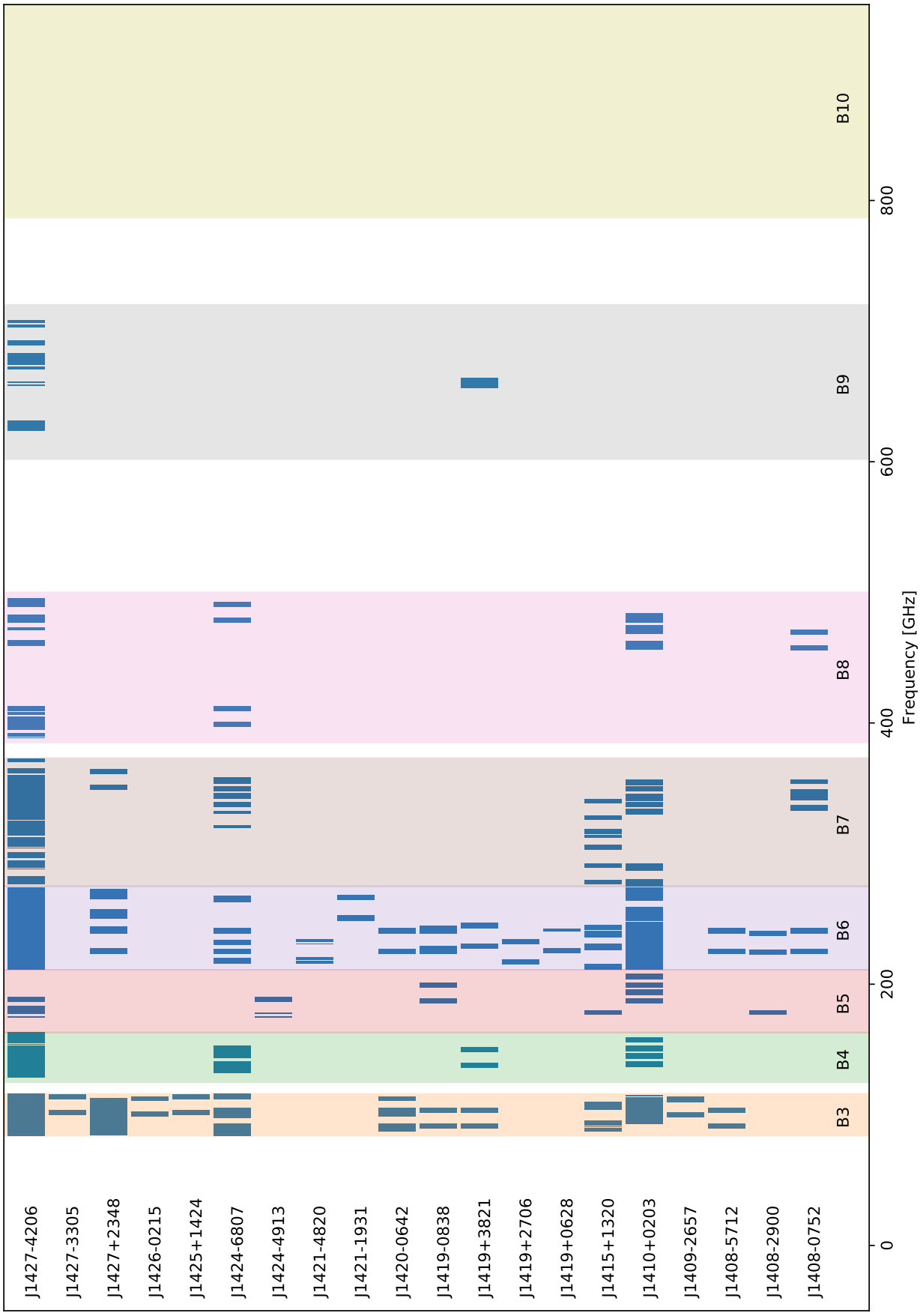
J1427-4206
J1427-3305
J1427+2348
J1426-0215
J1425+1424
J1424-6807
J1424-4913
J1421-4820
J1421-1931
J1420-0642
J1419-0838
J1419+3821
J1419+2706
J1419+0628
J1415+1320
J1410+0203
J1409-2657
J1408-5712
J1408-2900
J1408-0752
B3
B4
B5
B6
B7
B8
B9
B10
0
200
400
600
800
Frequency [GHz]

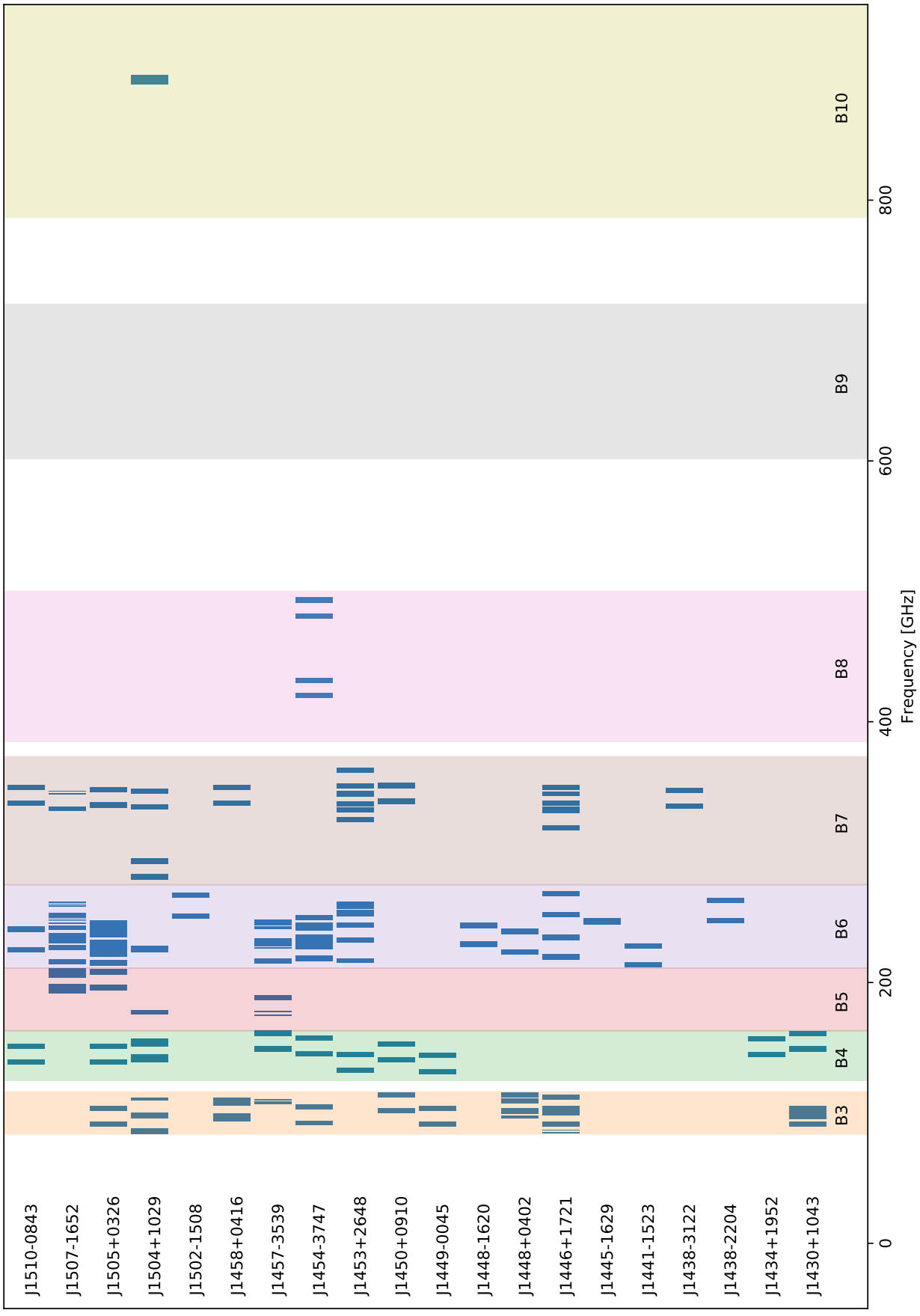
J1510-0843
J1507-1652
J1505+0326
J1504+1029
J1502-1508
J1458+0416
J1457-3539
J1454-3747
J1453+2648
J1450+0910
J1449-0045
J1448-1620
J1448+0402
J1446+1721
J1445-1629
J1441-1523
J1438-3122
J1438-2204
J1434+1952
J1430+1043
B3
B4
B5
B6
B7
B8
B9
B10
0
200
400
600
800
Frequency [GHz]

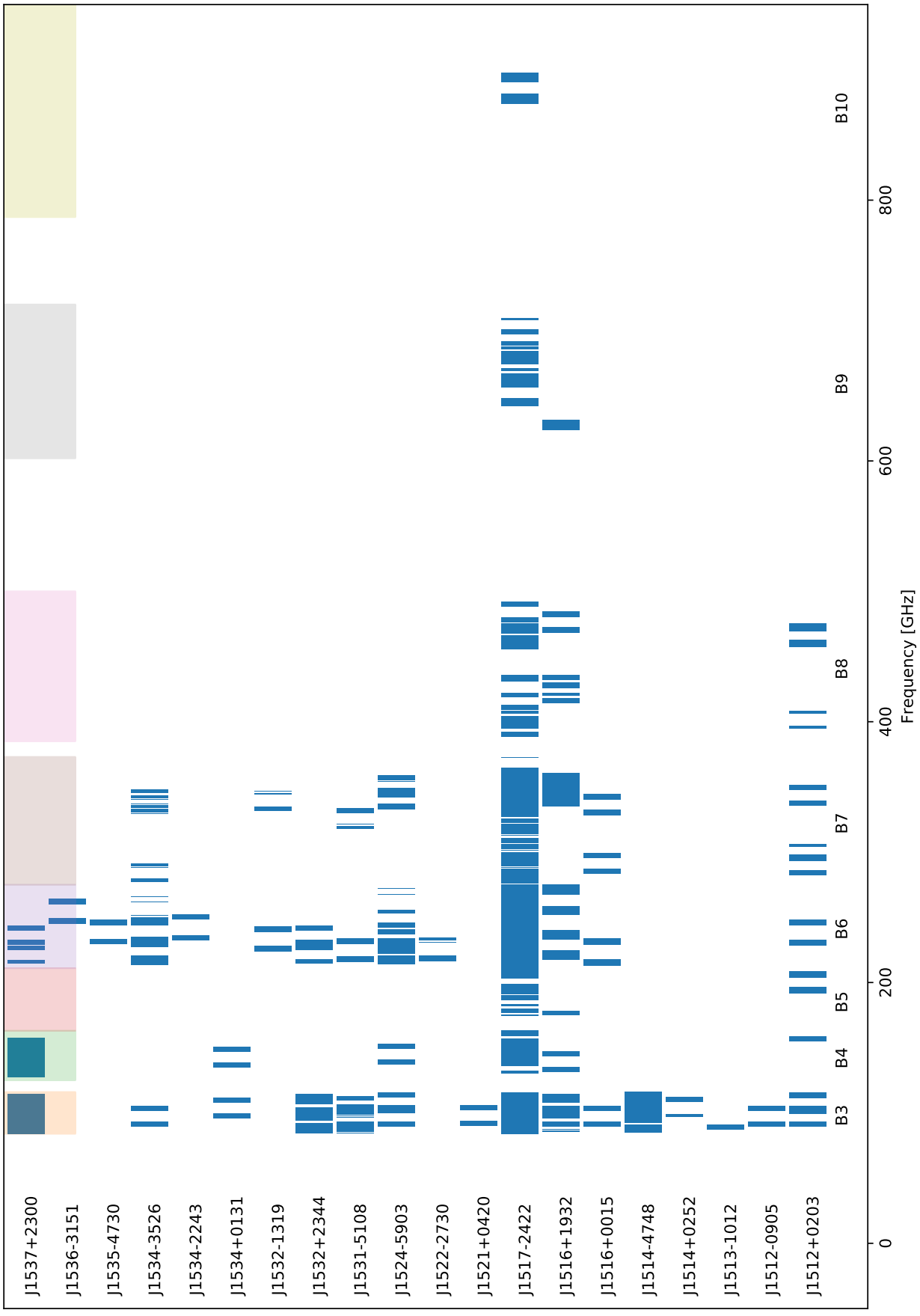
J1537+2300
J1536-3151
J1535-4730
J1534-3526
J1534-2243
J1534+0131
J1532-1319
J1532+2344
J1531-5108
J1524-5903
J1522-2730
J1521+0420
J1517-2422
J1516+1932
J1516+0015
J1514-4748
J1514+0252
J1513-1012
J1512-0905
J1512+0203
B3
B4
B5
B6
B7
B8
B9
B10
0
200
400
600
800
Frequency [GHz]

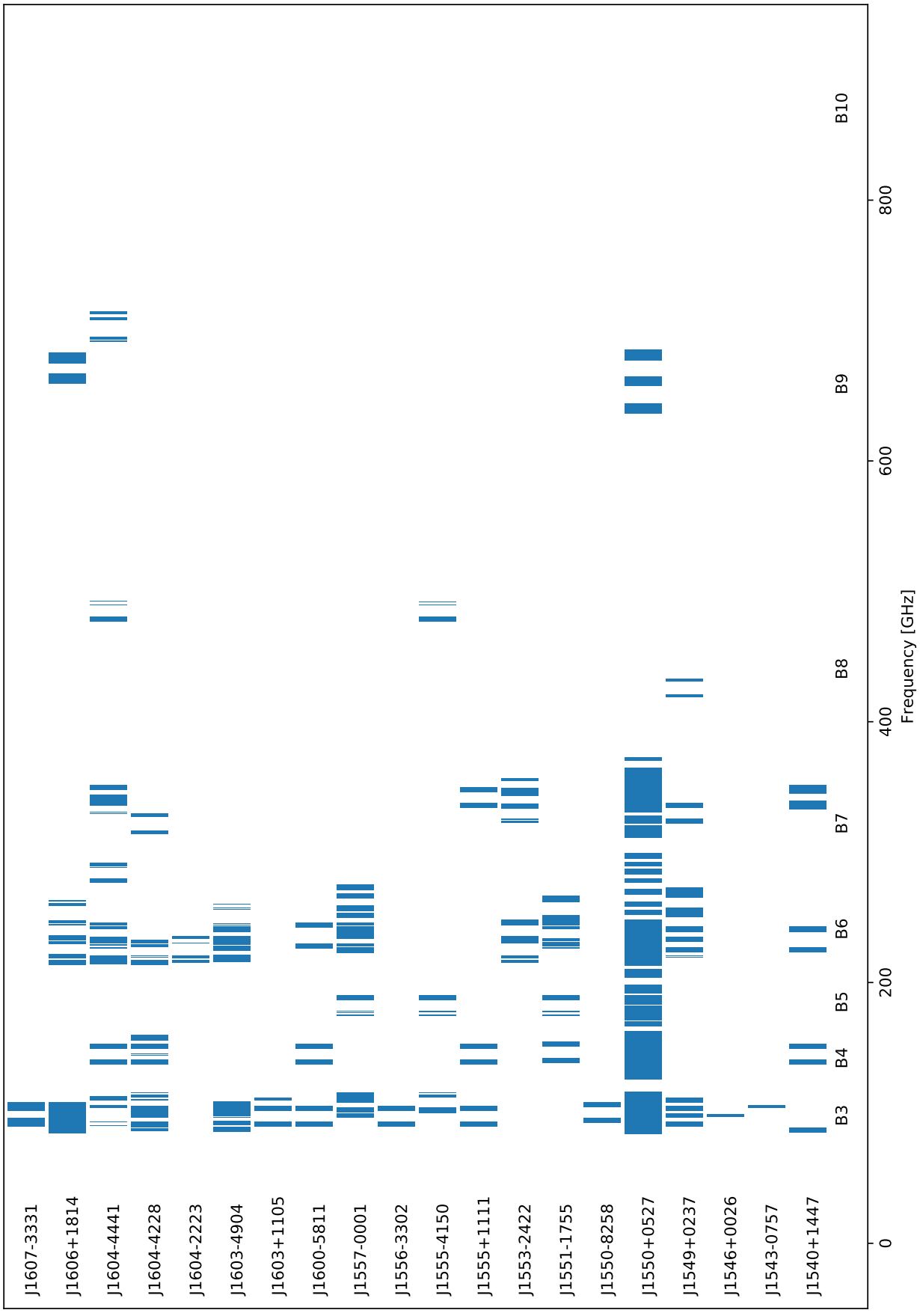
J1607-3331
J1606+1814
J1604-4441
J1604-4228
J1604-2223
J1603-4904
J1603+1105
J1600-5811
J1557-0001
J1556-3302
J1555-4150
J1555+1111
J1553-2422
J1551-1755
J1550-8258
J1550+0527
J1549+0237
J1546+0026
J1543-0757
J1540+1447
B3
B4
B5
B6
B7
B8
B9
B10
0
200
400
600
800
Frequency [GHz]

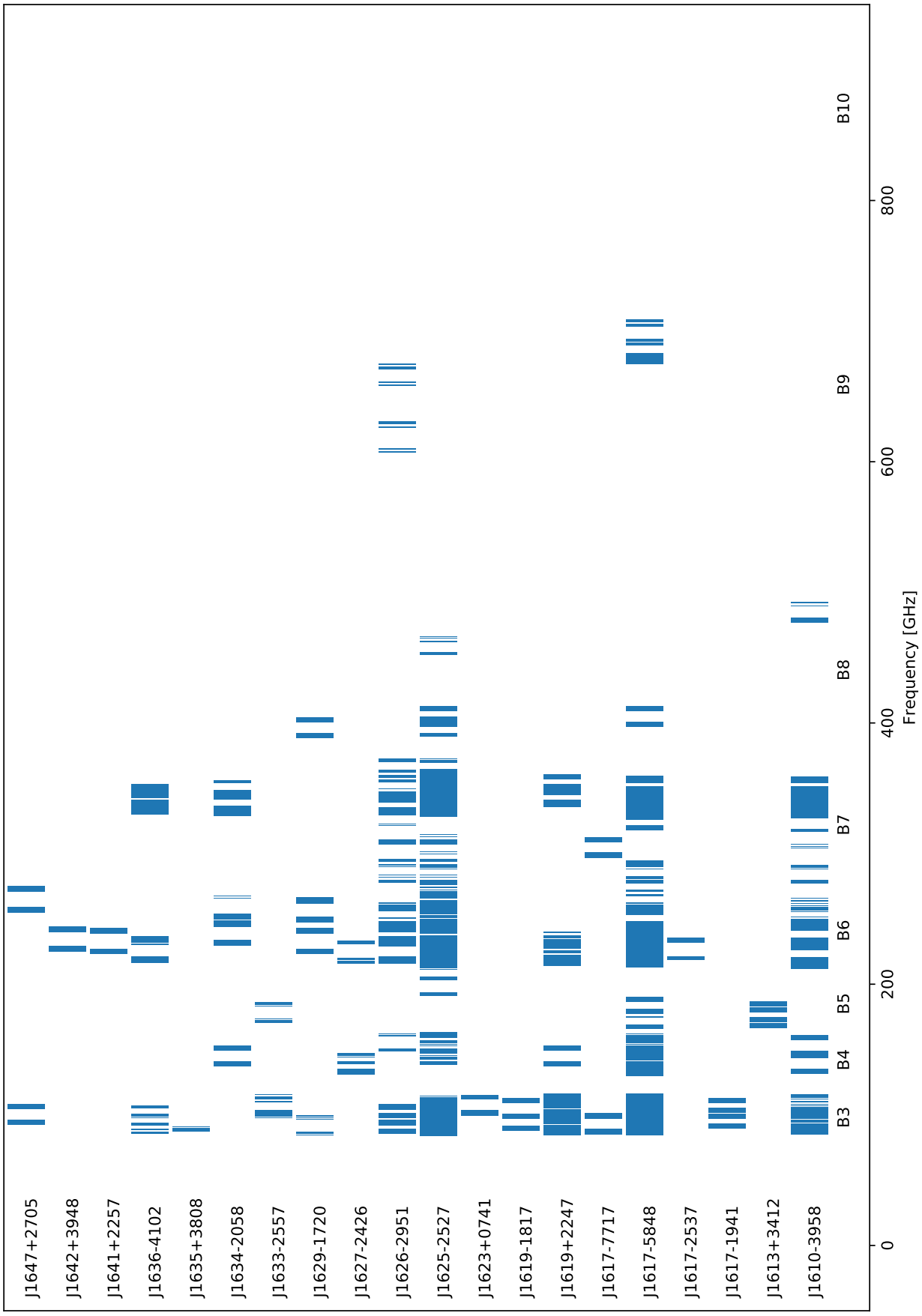
J1647+2705
J1642+3948
J1641+2257
J1636-4102
J1635+3808
J1634-2058
J1633-2557
J1629-1720
J1627-2426
J1626-2951
J1625-2527
J1623+0741
J1619-1817
J1619+2247
J1617-7717
J1617-5848
J1617-2537
J1617-1941
J1613+3412
J1610-3958
B3
B4
B5
B6
B7
B8
B9
B10
0
200
400
600
800
Frequency [GHz]

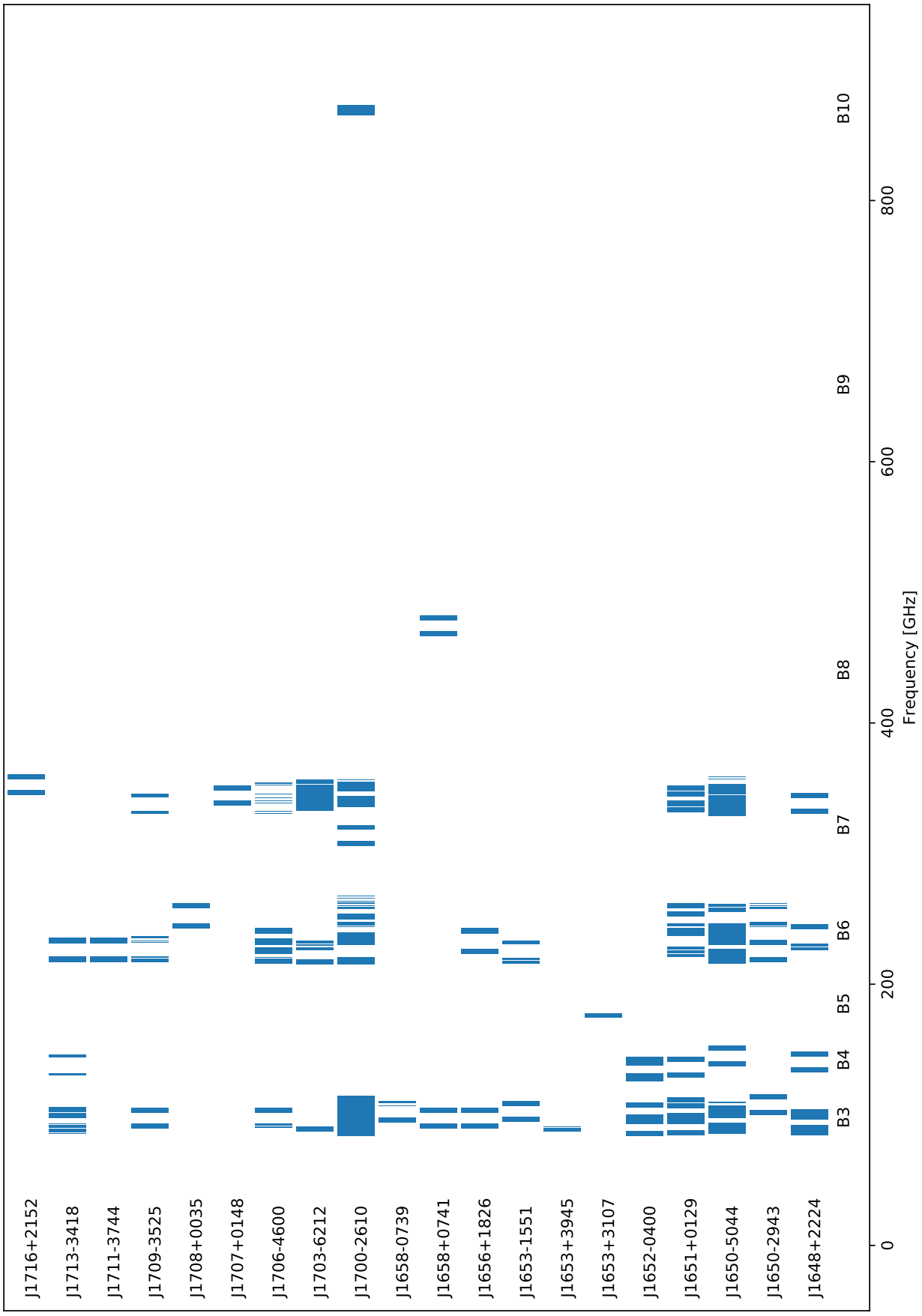
J1716+2152
J1713-3418
J1711-3744
J1709-3525
J1708+0035
J1707+0148
J1706-4600
J1703-6212
J1700-2610
J1658-0739
J1658+0741
J1656+1826
J1653-1551
J1653+3945
J1653+3107
J1652-0400
J1651+0129
J1650-5044
J1650-2943
J1648+2224
B3
B4
B5
B6
B7
B8
B9
B10
0
200
400
600
800
Frequency [GHz]

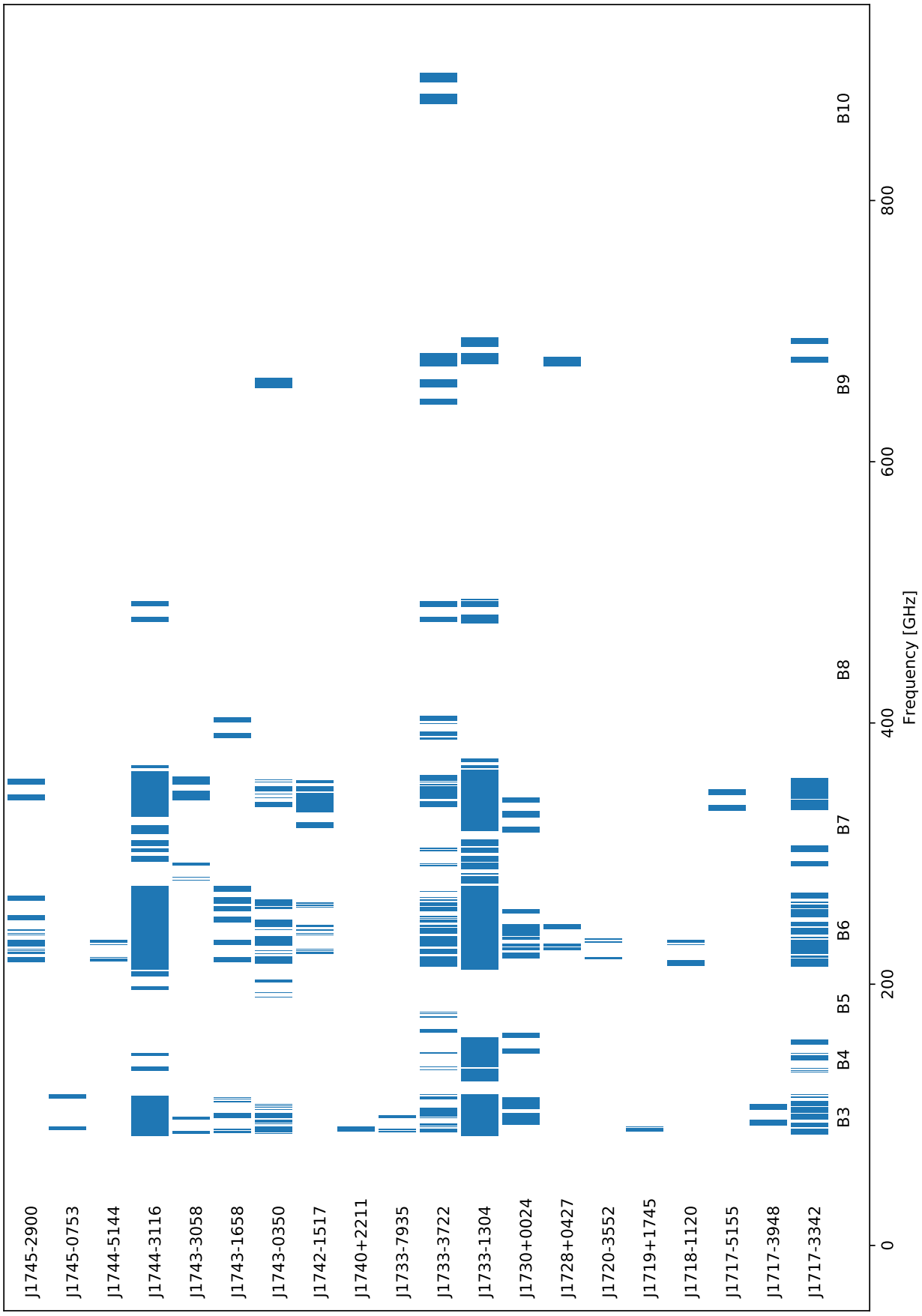
J1745-2900
J1745-0753
J1744-5144
J1744-3116
J1743-3058
J1743-1658
J1743-0350
J1742-1517
J1740+2211
J1733-7935
J1733-3722
J1733-1304
J1730+0024
J1728+0427
J1720-3552
J1719+1745
J1718-1120
J1717-5155
J1717-3948
J1717-3342
B3
B4
B5
B6
B7
B8
B9
B10
0
200
400
600
800
Frequency [GHz]

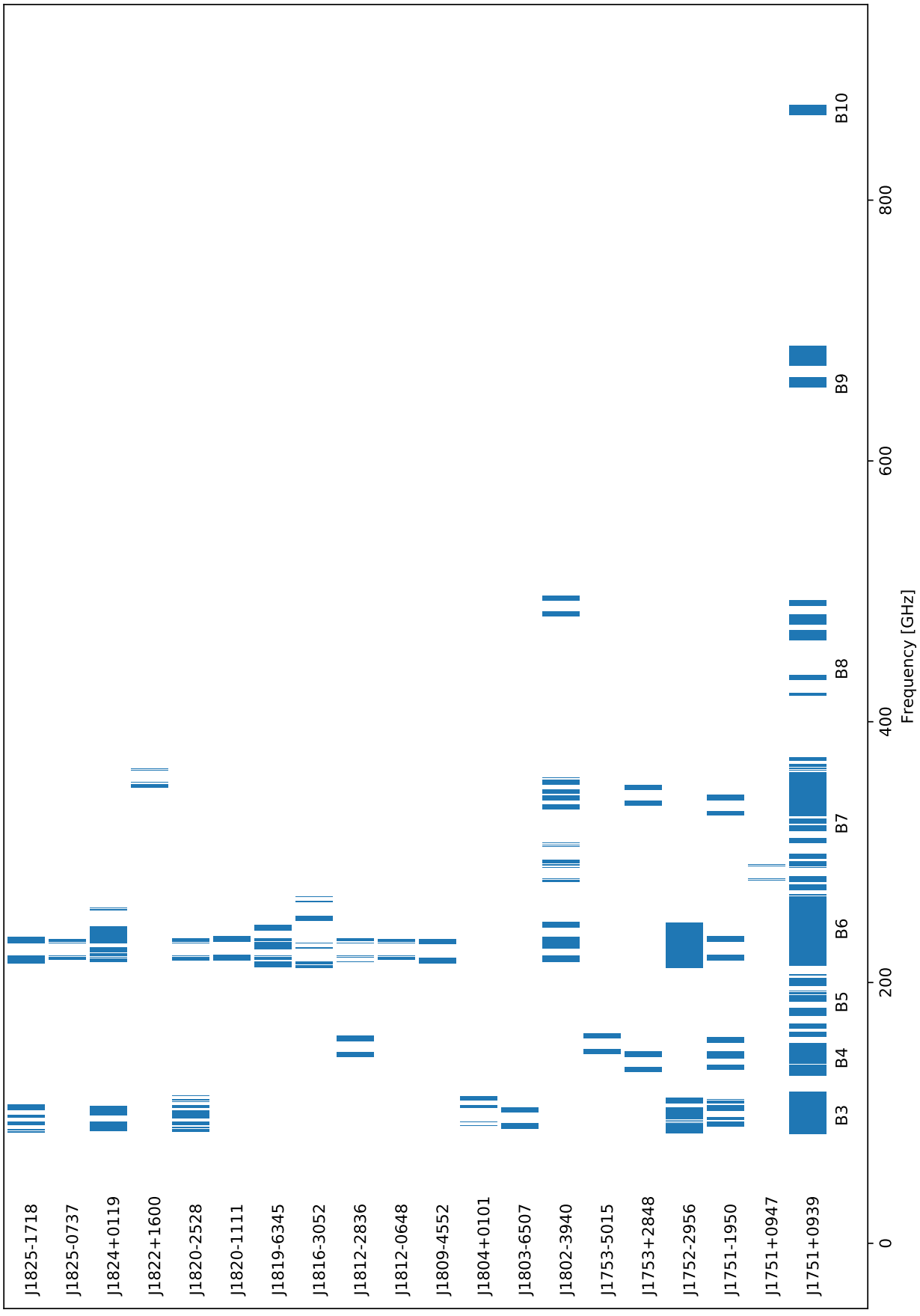
J1825-1718
J1825-0737
J1824+0119
J1822+1600
J1820-2528
J1820-1111
J1819-6345
J1816-3052
J1812-2836
J1812-0648
J1809-4552
J1804+0101
J1803-6507
J1802-3940
J1753-5015
J1753+2848
J1752-2956
J1751-1950
J1751+0947
J1751+0939
B3
B4
B5
B6
B7
B8
B9
B10
0
200
400
600
800
Frequency [GHz]

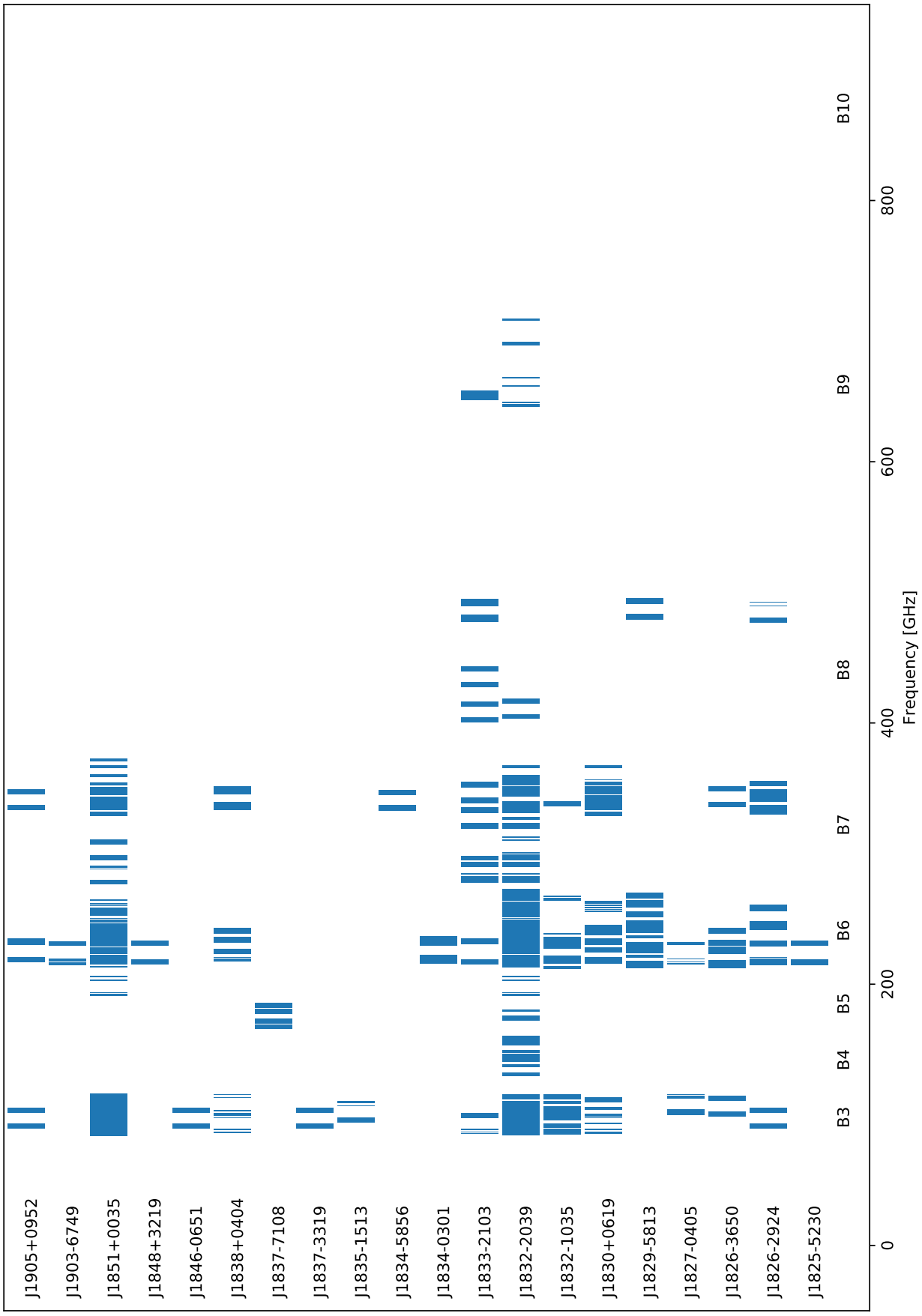
J1905+0952
J1903-6749
J1851+0035
J1848+3219
J1846-0651
J1838+0404
J1837-7108
J1837-3319
J1835-1513
J1834-5856
J1834-0301
J1833-2103
J1832-2039
J1832-1035
J1830+0619
J1829-5813
J1827-0405
J1826-3650
J1826-2924
J1825-5230
B3
B4
B5
B6
B7
B8
B9
B10
0
200
400
600
800
Frequency [GHz]

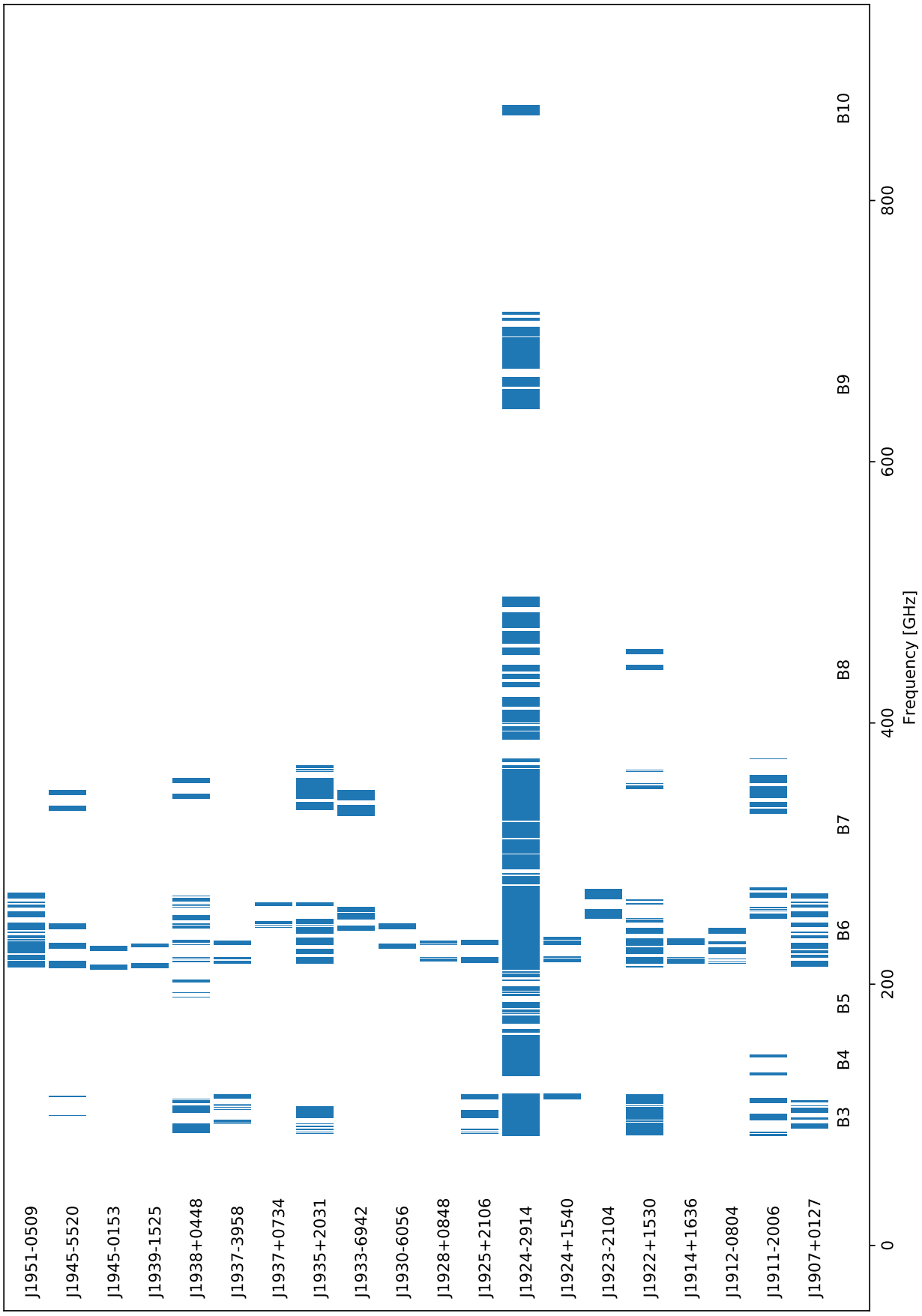
J1951-0509
J1945-5520
J1945-0153
J1939-1525
J1938+0448
J1937-3958
J1937+0734
J1935+2031
J1933-6942
J1930-6056
J1928+0848
J1925+2106
J1924-2914
J1924+1540
J1923-2104
J1922+1530
J1914+1636
J1912-0804
J1911-2006
J1907+0127
B3
B4
B5
B6
B7
B8
B9
B10
0
200
400
600
800
Frequency [GHz]

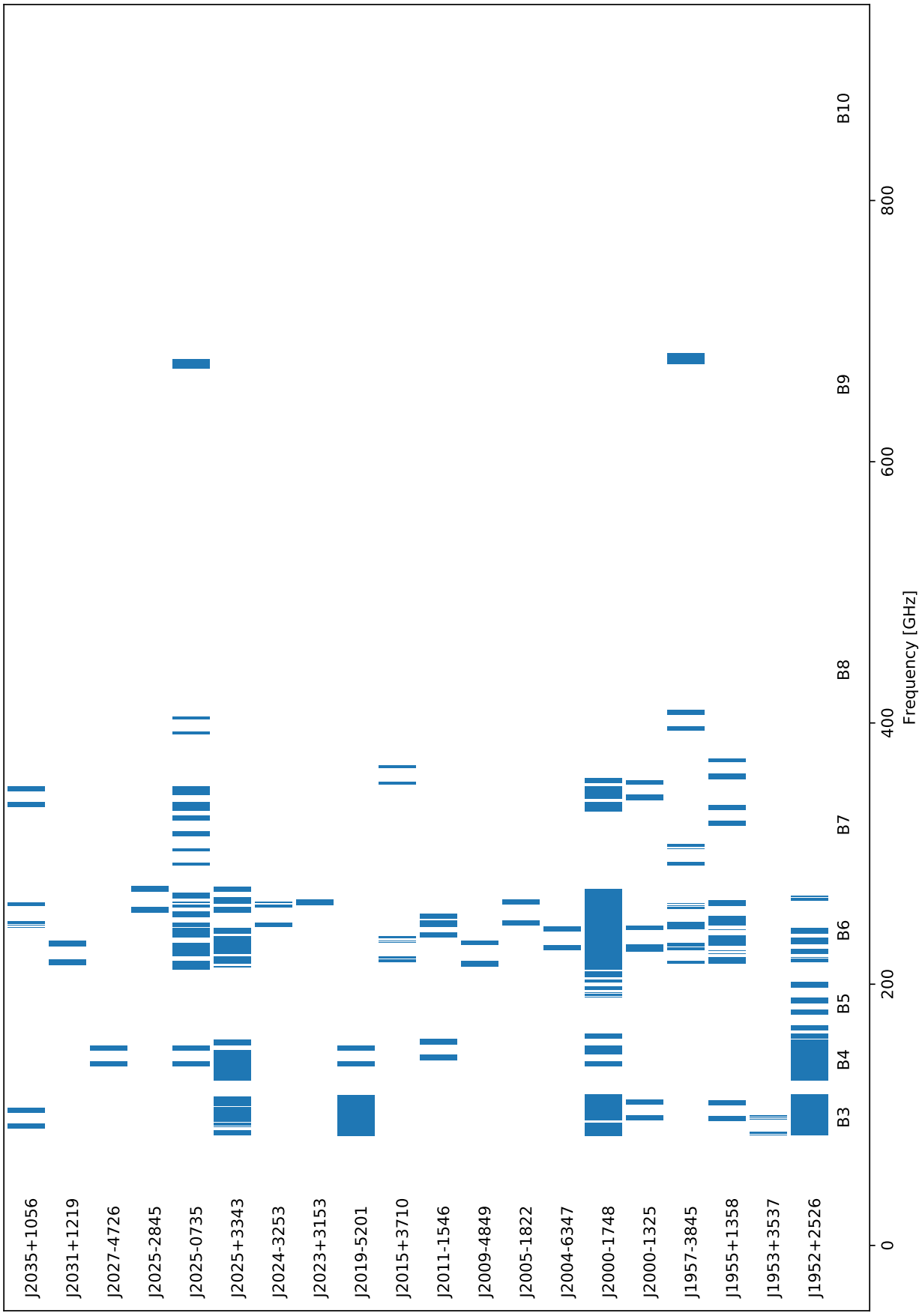
J2035+1056
J2031+1219
J2027-4726
J2025-2845
J2025-0735
J2025+3343
J2024-3253
J2023+3153
J2019-5201
J2015+3710
J2011-1546
J2009-4849
J2005-1822
J2004-6347
J2000-1748
J2000-1325
J1957-3845
J1955+1358
J1953+3537
J1952+2526
B3
B4
B5
B6
B7
B8
B9
B10
0
200
400
600
800
Frequency [GHz]

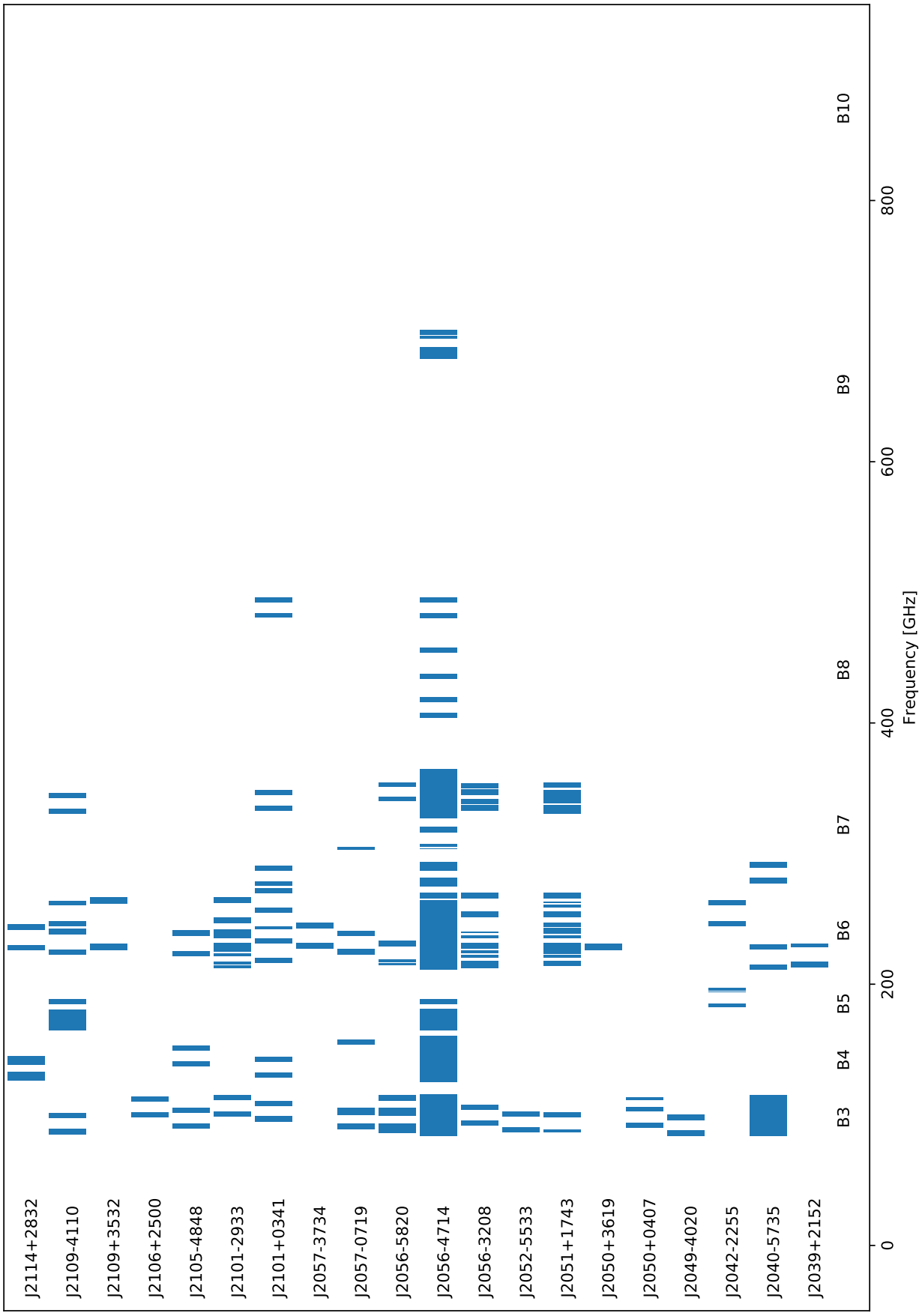
J2114+2832
J2109-4110
J2109+3532
J2106+2500
J2105-4848
J2101-2933
J2101+0341
J2057-3734
J2057-0719
J2056-5820
J2056-4714
J2056-3208
J2052-5533
J2051+1743
J2050+3619
J2050+0407
J2049-4020
J2042-2255
J2040-5735
J2039+2152
B3
B4
B5
B6
B7
B8
B9
B10
0
200
400
600
800
Frequency [GHz]

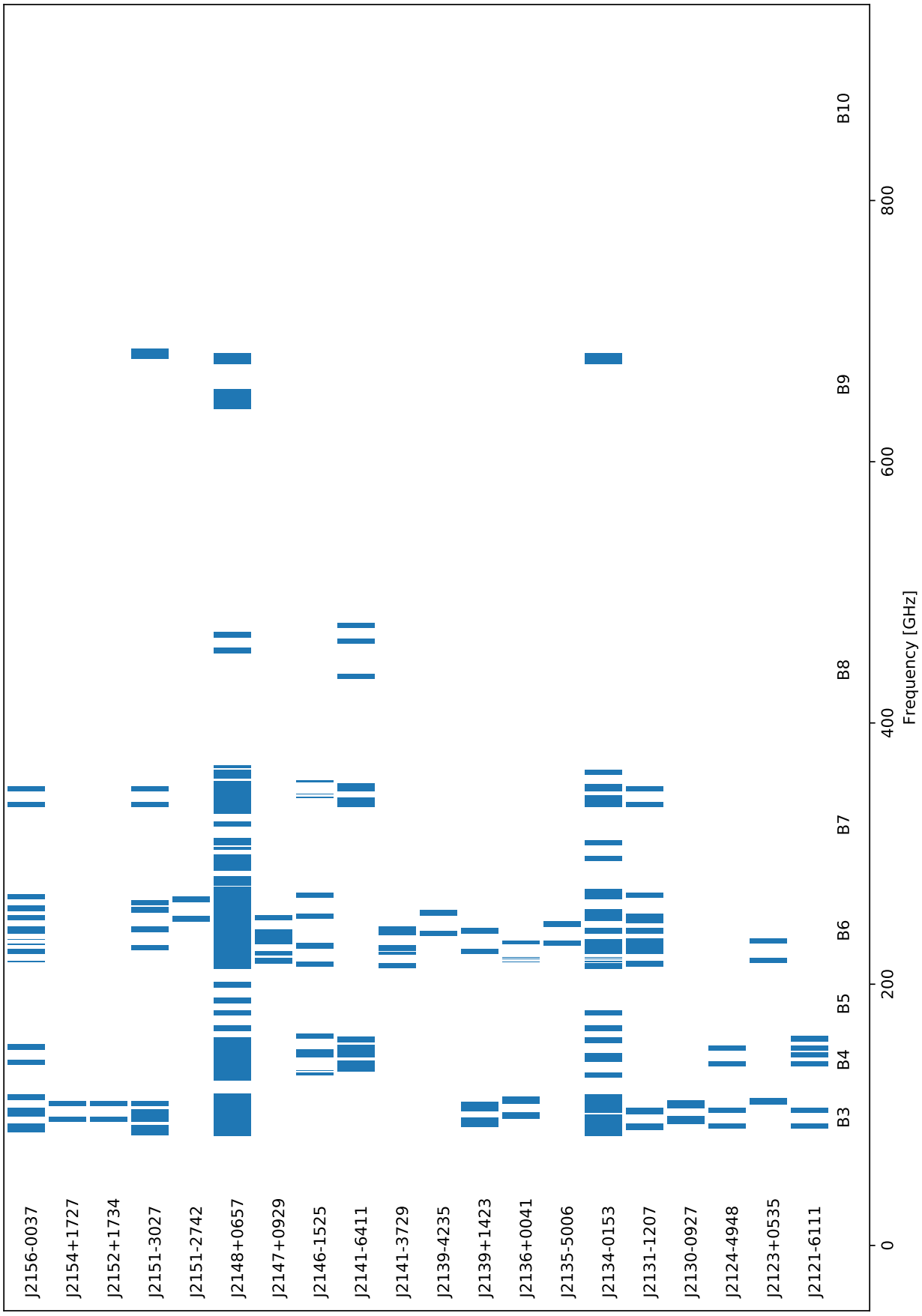
J2156-0037
J2154+1727
J2152+1734
J2151-3027
J2151-2742
J2148+0657
J2147+0929
J2146-1525
J2141-6411
J2141-3729
J2139-4235
J2139+1423
J2136+0041
J2135-5006
J2134-0153
J2131-1207
J2130-0927
J2124-4948
J2123+0535
J2121-6111
B3
B4
B5
B6
B7
B8
B9
B10
0
200
400
600
800
Frequency [GHz]

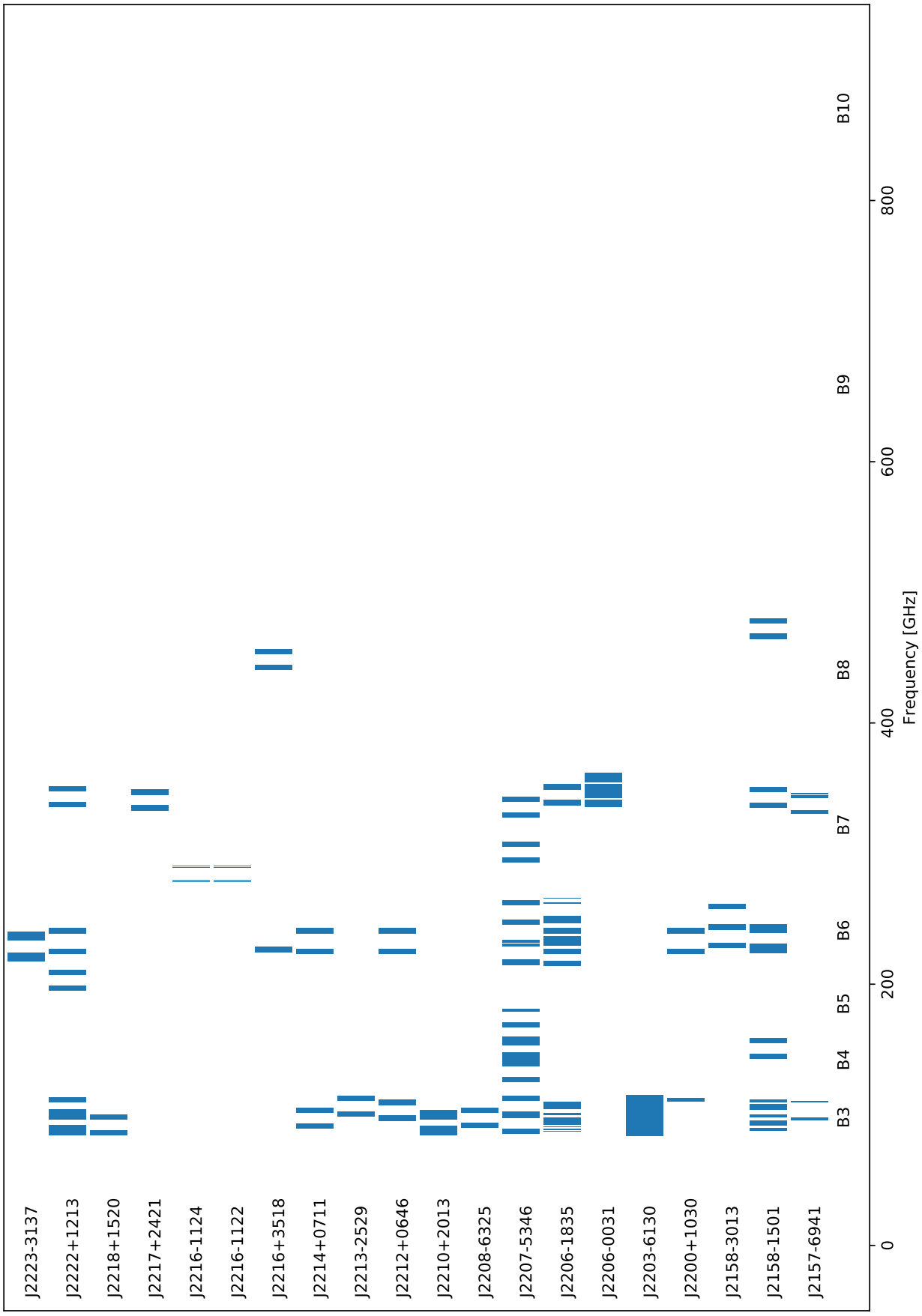
J2223-3137
J2222+1213
J2218+1520
J2217+2421
J2216-1124
J2216-1122
J2216+3518
J2214+0711
J2213-2529
J2212+0646
J2210+2013
J2208-6325
J2207-5346
J2206-1835
J2206-0031
J2203-6130
J2200+1030
J2158-3013
J2158-1501
J2157-6941
B3
B4
B5
B6
B7
B8
B9
B10
0
200
400
600
800
Frequency [GHz]

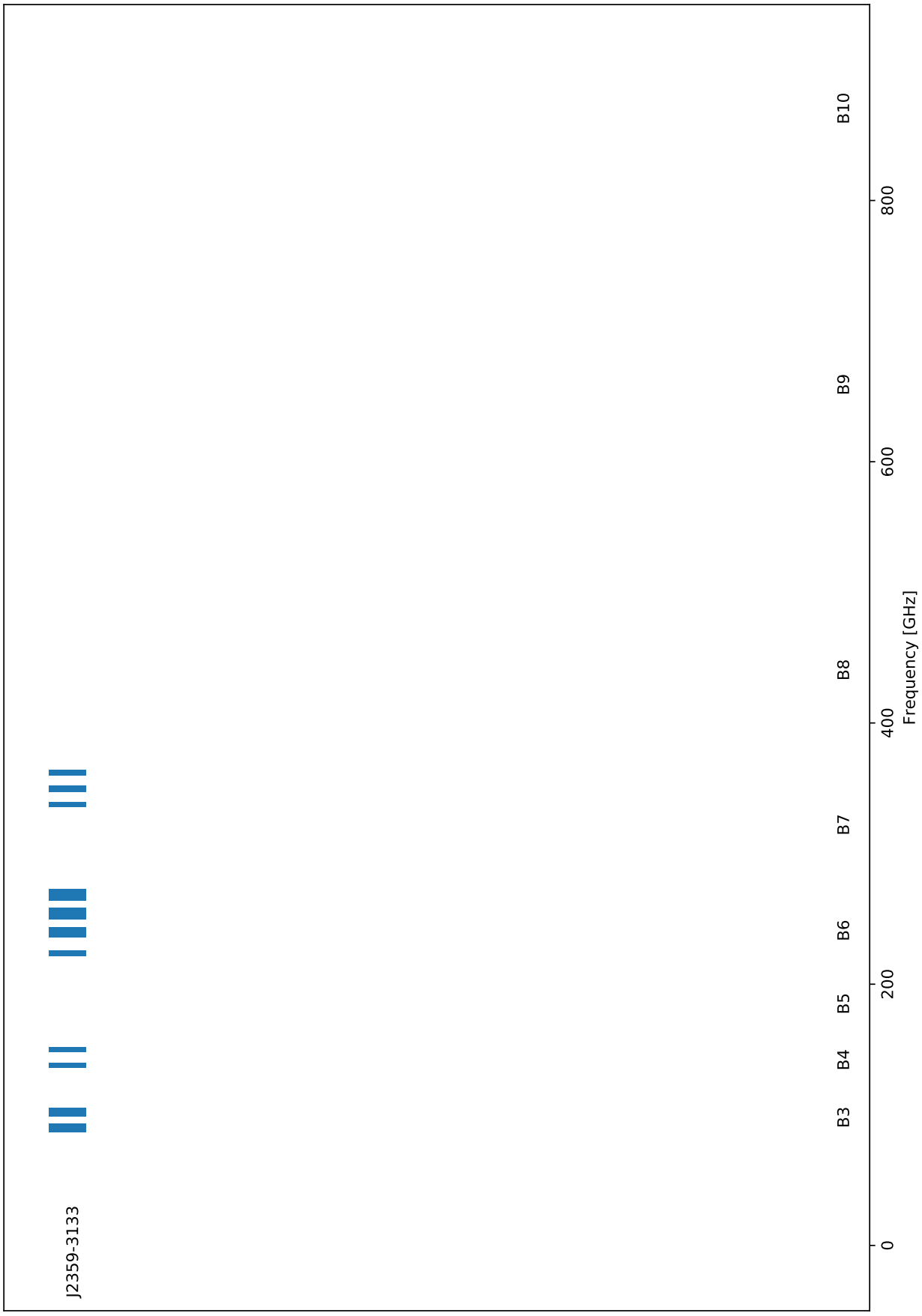
J2359-3133
B3
B4
B5
B6
B7
B8
B9
B10
0
200
400
600
800
Frequency [GHz]